

©2012 Jessica René Creveling
All rights reserved.

Dissertation Advisor
Andrew H. Knoll

Author
Jessica René Creveling

SEDIMENTOLOGY, GEOCHEMISTRY, AND GEOPHYSICS OF THE CAMBRIAN EARTH SYSTEM

ABSTRACT

Within this dissertation, I document how—and hypothesize why—the quirks and qualities of the Cambrian Period demarcate this interval as fundamentally different from the preceding Proterozoic Eon and succeeding periods of the Phanerozoic Eon.

To begin, I focus on the anomalous marine deposition of the mineral apatite. Sedimentary sequestration of phosphorus modulates the capacity for marine primary productivity and, thus, the redox state of the Earth system. Moreover, sedimentary apatite minerals may entomb and replicate skeletal and soft-tissue organisms, creating key aspects of the fossil record from which paleontologists deduce the trajectory of animal evolution. I ask what geochemical redox regime promoted the delivery of phosphorus to Cambrian seafloors and conclude that, for the case of the Thornton Limestone, apatite nucleation occurred under anoxic, ferruginous subsurface water masses. Moreover, I infer that phosphorus bound to iron minerals precipitated from the water column and organic-bound phosphorus were both important sources of phosphorus to the seafloor. Petrographic observations allow me to reconstruct the early diagenetic pathways that decoupled phosphorus from these delivery shuttles and promoted the precipitation of apatite within the skeletons of small animals. Together, mechanistic understandings of phosphorus delivery to, and retention within, seafloor sediment allow us to constrain hypotheses for the fleeting occurrence of widespread apatite deposition and exquisite fossil preservation within Cambrian sedimentary suc-

cessions.

Next, I describe and quantify the nature of carbonate production on a marine platform deposited at the hypothesized peak of Cambrian skeletal carbonate production. I find that fossils represent conspicuous, but volumetrically subordinate components of early Cambrian carbonate reef ecosystems and that despite the evolution of mineralized skeletons, Cambrian carbonate platforms appear similar to their Neoproterozoic counterparts, primarily reflecting abiotic and microbial deposition.

Finally, I investigate the geodynamic mechanism responsible for rapid, oscillatory true polar wander (TPW) events proposed for the Neoproterozoic and Phanerozoic Earth on the basis of paleomagnetic data. Using geodynamic models, I demonstrate that elastic strength in the lithosphere and stable excess ellipticity of Earth's figure provided sufficient stabilization to return the pole to its original state subsequent to convectively-driven TPW.

CONTENTS

ABSTRACT	iii
CONTENTS	v
LIST OF FIGURES	vii
LIST OF TABLES	ix
ACKNOWLEDGEMENTS	x
DEDICATION	xii
1 INTRODUCTION	1
2 SOURCES OF PHOSPHORUS FOR PHOSPHATIC CARBONATE DEPOSITION: A CASE STUDY OF THE CAMBRIAN THORNTONIA LIMESTONE, SOUTHERN GEORGINA BASIN, AUSTRALIA	10
2.1 Introduction	11
2.2 Geologic Background	13
2.2.1 Basin history	13
2.2.2 Drill core NTGS 99/1	16
2.3 Methods	22
2.4 Results	25
2.5 Discussion	31
2.5.1 Stratigraphic Correlation and Temporal Continuity	33
2.5.2 The Relationship Between P and C	36
2.5.3 The Fe-P Shuttle	38
2.5.4 Source(s) of P to the sediment column	44
2.6 Conclusions	57
2.7 References Cited	61
3 TAPHONOMY OF PHOSPHATIC SMALL SHELLY FOSSILS: A CASE STUDY OF THE CAMBRIAN THORNTONIA LIMESTONE, SOUTHERN GEORGINA BASIN, AUSTRALIA	72
3.1 Introduction	72
3.2 The Ediacaran–Cambrian Phosphatization Window	73

3.3	Phosphatic Fossils in the Thornton Limestone: Stratigraphic Context	75
3.4	Petrography of Skeletal Fossil Preservation	77
3.5	Mechanistic Understanding of Skeletal Fossil Preservation	85
3.6	Dimensions of the Ediacaran–Cambrian Phosphatization Taphonomic Window	90
3.7	Conclusions	93
3.8	References Cited	94
4	GEOBIOLOGY OF A LOWER CAMBRIAN CARBONATE PLATFORM, PEDROCHE FORMATION, SPAIN	99
4.1	Introduction	100
4.2	Geologic Setting	101
4.3	Methods	103
4.4	Carbon Isotopic Chemostratigraphy	105
4.5	Lithofacies Descriptions and Paleoenvironmental Interpretations . . .	108
4.5.1	Lithofacies Descriptions	108
4.5.2	Lithofacies Associations	118
4.5.3	Depositional Environments	121
4.6	Pedroche Platform Development	125
4.6.1	Point counts	125
4.6.2	Skeletal Contributions to the Pedroche Formation	131
4.6.3	Carbonate Production on the Pedroche Platform	136
4.7	Conclusions	138
4.8	References Cited	140
5	A MECHANISM FOR OSCILLATORY TRUE POLAR WANDER IN DEEP TIME	146
5.1	Introduction: The Paleomagnetic Record	147
5.2	The Rotational Stability of the Earth	151
5.2.1	The Figure of the Earth	151
5.2.2	The Physics of TPW	152
5.2.3	A Non-Linear Rotational Stability Theory	155
5.3	Results	160
5.3.1	The Numerical Model	160
5.3.2	Sensitivity Analyses	165
5.3.3	Modelling Paleomagnetically-Inferred TPW	172
5.3.4	Miscellaneous Numerical Tests	173
5.4	Final Remarks	180

LIST OF FIGURES

Figure 2.1	Generalized geology and map of the study area.	15
Figure 2.2	Lithofacies of the Thornton Limestone and Arthur Creek Formation in NTGS 99/1.	18
Figure 2.3	Photomicrograph of phosphatization within the Thornton Limestone, NTGS 99/1.	21
Figure 2.4	Lithology and stable isotope chemostratigraphy of the Thornton Limestone and lower Arthur Creek formations within drill core NTGS 99/1.	27
Figure 2.5	Phosphorus and iron speciation geochemistry, molar C:P ratios, and correlations between P and other geochemical metrics within the Thornton Limestone and Arthur Creek formations.	28
Figure 2.6	Iron speciation geochemistry.	30
Figure 2.7	Elemental ratios normalized to aluminum.	31
Figure 2.8	Bioessential trace element concentrations.	32
Figure 2.9	Relationship between siliciclastics, iron speciation phases, and total organic carbon.	41
Figure 2.10	Schematic of the calculations for the estimate of phosphorus delivery to the sea floor and loss from the sediment column.	46
Figure 3.1	Generalized stratigraphy of the Thornton Limestone.	76
Figure 3.2	Photomicrographs of apatite distribution within lithologies of the middle Thornton Limestone.	78
Figure 3.3	Photomicrographs of apatite steinkerns of small skeletal fossils.	79
Figure 3.4	SEM-EDX analysis of steinkerns within packstone, middle Thornton Limestone.	80
Figure 3.5	Photomicrographs of fossil preservation within apatite cement, Thornton Limestone.	82
Figure 3.6	Photomicrographs of apatite distribution within wackestone, Thornton Limestone.	83
Figure 3.7	SEM-EDX analysis of authigenic, allocthonous phosphatic grains within mud-dominated lithologies of the Thornton Limestone.	84
Figure 4.1	Generalized geology and map of the study area.	101

Figure 4.2	Lithostratigraphy and $\delta^{13}C_{carb}$ chemostratigraphy of the Pedroche Formation.	106
Figure 4.3	Lithologic and petrographic character of the interbedded carbonate mudstone, bioclastic wackestone, archaeocyathan floatstone–packstone–rudstone and siliciclastic siltstone lithofacies.	109
Figure 4.4	Photomicrographs of archaeocyath-bearing lithofacies and mode of archaeocyath preservation.	111
Figure 4.5	Photomicrographs of small skeletal fossil preservation.	112
Figure 4.6	Lithologic character of the ooid/oncoid/peloid grainstone lithofacies.	114
Figure 4.7	Petrography of the ooid/oncoid/peloid grainstone lithofacies.	115
Figure 4.8	Photomicrographs of the modes of biological preservation within the ooid/oncoid/peloid grainstone and thrombolite boundstone lithofacies.	116
Figure 4.9	Lithologic character of the thrombolite boundstone lithofacies.	117
Figure 4.10	Percent skeletal contribution within the Pedroche Formation as determined from point counts of representative petrographic thin-sections.	130
Figure 4.11	Percent constituent components of the carbonate lithofacies of Pedroche Formation.	132
Figure 4.12	Comparison of the percent skeletal contribution to archaeocyath-bearing reef and inter-reef lithologies between the Pedroche Formation and other reef/inter-reef localities.	134
Figure 5.1	TPW, supercontinent phases and the Earth’s figure in deep time.	148
Figure 5.2	The physics underlying the standard and revised rotational stability theories.	153
Figure 5.3	Modelling paleomagnetically-inferred TPW during the Mesozoic.	161
Figure 5.4	Modelling paleomagnetically-inferred TPW during the Neoproterozoic	164
Figure 5.5	TPW predictions: Numerical experiments.	166
Figure 5.6	Sensitivity of numerical predictions of convectively-driven TPW to variations in standard model parameters.	168
Figure 5.7	Sensitivity of numerical predictions of t_{max} as a function of convective forcing and viscosity.	170
Figure 5.8	Sensitivity of numerical predictions of convectively-driven TPW to variations in model parameters.	171
Figure 5.9	Bounding the effective elastic thickness of a broken lithosphere.	176

LIST OF TABLES

Table 4.1	Percent contribution of carbonate lithofacies to stratigraphic sections of the Pedroche Formation.	126
Table 4.2	Point-count data of constituent components to lithologies of the Pedroche Formation.	127
Table 4.3	Average percent of constituent components of carbonate lithofacies of the Pedroche Formation.	129

ACKNOWLEDGEMENTS

This dissertation represents five years of focused work that was possible only with the guidance, encouragement, and generosity of numerous colleagues and friends. I would like to express my gratitude for the scientific vision and mentorship of my advisor, Andy Knoll. The opportunities provided to me by Andy have been enumerable and invaluable, and for these extraordinary experiences and, equally, for his unflinching daily support, I am forever grateful. I thank Dave Johnston for his mentorship and kindness, beginning during his time as a post-doctoral fellow and continuing through to his role as a committee member and advisor. I also thank the various faculty who participated in my thesis committees, Dan Schrag, Sam Bowring, and Sujoy Mukhopadhyay.

My graduate experience was enriched by the tutelage of Jerry Mitrovica. I thank both Dan Schrag and Ann Pearson for encouraging me to become a more ambitious geoscientist. I am grateful for conversations with Paul Hoffman and Peter Huybers.

My friends and colleagues in the Knoll lab—Jon Wilson, Phoebe Cohen, Ben Kotrc, Tony Rockwell, Dave Johnston, Nick Tosca, Ben Gill, Tais Dahl, Tinker Green, David Hewitt, Erik Sperling, Rowan Martindale, and Suzanne Costanza—provided equal measures of scientific inspiration and distraction.

Most lastingly, my thesis brought me a lifelong friend and confidant, Ben Kotrc. Ben, words are not repayment enough for coaxing me to this finish line.

Thanks to my cohort in EPS—Karin Louzada, Andy Masterson, Rita Parai, Kate

Dennis, Sierra Petersen, Wil Leavitt, Allie Gale, Greg Santoni, Hilary Close, Tom Laakso, Roderick Bovee, Rick Kraus, Justin Strauss, and Uyanga Bold—for laughter and support.

To the Mitrovica group, Eric Morrow, Erick Chan, Carling Hay, Natalya Gomez, Jacky Austermann, and Ken Ferrier, for graciously accepting me into the fold.

Greg Eischeid provided technical assistance with a healthy dose of humor. Likewise, this work would not be possible without the support of numerous administrative staff, including Sarah Colgan, Chenoweth Moffat, Paul Kelly, Diane Sheridan, Sabinna Cappo and Marisa Reilly. Erin Beirne kept my chin up towards the very end.

I thank Paul Myrow for his enthusiasm and support. In addition to Paul, I thank Francis Macdonald and John Abelson/The Agouron Institute for field experiences. I thank David Fike, Jochen Brocks, Simon Poulton, Sara Pruss, Bob Gaines, Jose de la Torre, Scott Dawson, and Frank Corsetti for a series of conversations, both intellectual and personal, that altered my academic trajectory.

I am so lucky to have Nick Crandall, Emily Taplin, Sierra Ewert, Liza Murray, Casey Avaunt, and Kerri Kuhn as beacons of fun. I thank Lorraine for her wisdom and empathy. I thank Tim and Liz Morningstar, Pete and Emilie Valle, and Daria Perreault for their warmth, generosity, and humor.

Finally, I am humbled by the support and love of my family—particularly my dad, mom, Michael, the Mouser clan, Grandpa Bob and Susan, and Grandma Babette.

For my mother, Linda. For my father, Brad.

CHAPTER 1

INTRODUCTION

The Cambrian Explosion colloquially describes the evolutionary diversification of animals as viewed through the lens of the fossil record (Knoll and Carroll, 1999; Marshall, 2006; Erwin et al., 2011). Much paleontological research has focused on cataloguing the Cambrian succession of morphological innovation and inferred taxonomic diversity (reviewed, for example, in Maloof et al., 2010 and Kouchinsky et al., 2012). Such studies contribute to a narrative of animal evolution, but do not generally address the central issue of causality. More recently, however, the burgeoning field of geobiology—which integrates information from geology, geochemistry, and evolutionary/developmental biology—has begun to inspire new interpretations the Cambrian paleontological record within a framework of both environmental opportunity (‘permissive ecology’) and genetic potential (Knoll, 2003). What has emerged from these studies is an understanding that the Cambrian Explosion has roots that extend well into the Proterozoic Eon, and that its effects reverberated throughout the Phanerozoic Earth system.

The Cambrian Explosion followed a period in Earth’s history marked by critical and interwoven changes in tectonics, climate, biogeochemical cycles, and atmospheric composition (Knoll and Carroll, 1999). As an example, the disaggregation of the supercontinent Rodinia and subsequent amalgamation of the Gondwana superterrane

define the evolving paleogeographic landscape that preceded the Cambrian (Li et al., 2008). Cryogenian glaciations provide examples of non-uniformitarian fluctuations in all aspects of the Earth system that must have presented an extreme challenge for eukaryotic life in the oceans (Hoffman et al., 1998). Moreover, these Snowball Earth events were accompanied by dramatic perturbations to the carbon cycle that persisted through to the early Cambrian (Halverson et al., 2005; Maloof et al., 2005). Throughout this interval, geological and geochemical proxies suggest that low atmospheric oxygen concentrations permitted persistent ocean anoxia (Canfield et al., 2008; Gill et al., 2011). Thus, the Cambrian Explosion did not unfold in an Earth system that largely mirrored the modern, save for one or two conditions—rather, it unfolded over an interval with only limited semblance to the world we see today.

Many tools can be brought to bear on this interval of Earth history. This dissertation begins with an exploration of the phosphorus cycle. On geological timescales, reactive phosphorus availability regulates marine primary production (Tyrrell, 1999). In turn, the burial efficiency of the organic matter generated by primary producers—and the associated phosphorus within organic compounds—modulates molecular oxygen production (see, for instance, Van Cappellen and Ingall, 1996). The reservoir size and residence time of reactive phosphorus in the ocean relates to the relative magnitudes of sources and sinks. These fluxes are difficult to constrain, in large part because phosphorus has no stable isotopes. However, the sedimentary record suggests that there were intervals in Earth history when phosphorus retention within seafloor sediment was significantly greater than today (Cook and McElhenny, 1979). This heterogeneous temporal distribution remains enigmatic. From a geobiological standpoint, an understanding of the environmental and geochemical mechanisms controlling the marine phosphorus cycle may thus illuminate both the history of Earth’s biological productivity and redox trajectory during this interval.

In Chapter 2, I present sedimentological, petrographic, and geochemical data from the Cambrian Series 2–3 Thornton Limestone, Georgina Basin, Australia, one of the youngest Cambrian localities displaying widespread apatite nucleation (Southgate, 1988). I integrate sedimentological and geochemical data (iron and phosphorus speciation data, stable carbon isotopes and trace element concentrations) to investigate the basin-scale environmental context of phosphate deposition. This research was guided by two overarching questions: what were the shuttles of phosphorus to the seafloor, and what physical, biological and chemical variables decoupled phosphorus from these delivery shuttles and promoted retention within the sediment column? To this end, my research reveals that phosphorus deposition occurred during times of expanded anoxic, ferruginous conditions in subsurface water masses. This suggests that, in addition to organic matter delivery, phosphorus adsorbed to, and co-precipitated with, iron minerals forming in the water column provided a significant shuttle to the seafloor. The remineralization of this sedimentary organic matter, which drove pore waters anoxic, remobilized phosphorus within accumulating carbonates. Petrology reveals that early diagenetic processes redistributed phosphate within sediments, forming internal molds of selected skeletons. While the conclusions drawn from these data address fundamental questions of the necessary conditions of phosphatic carbonate deposition, these data invite further research into the underlying source of this phosphorus reservoir.

Beyond information gained from quantifying the magnitude of sedimentary phosphorus removal, the nature of this removal provides a different set of insights into the Cambrian Earth system. Specifically, when sedimentary phosphorus retention occurs through the precipitation of the calcium phosphate mineral apatite, it often entombs animal fossils with remarkable fidelity (see Butterfield, 2003, and Porter, 2004, and references therein). Thus, the early-diagenetic replication of animal skele-

tons by phosphate minerals provides an important taphonomic window through which paleontologists view the foundational events of animal evolution. For unknown reasons, however, this window on early animal diversity shutters in the middle of the Cambrian Period (Porter, 2004). Building on the results of Chapter 2, I describe in Chapter 3 a case study of Cambrian exceptional preservation of small skeletal fossils by apatite minerals. In this research, I identify the processes that contributed to the phosphatization of skeletal elements and explore which, if any, of these processes were characterized by a time-variability consistent with the closure of the phosphatization taphonomic window.

The repercussions of the Cambrian explosion raise questions just as intriguing as those that arise from an examination of its historical context. One such effect was on the nature and distribution of marine carbonate deposition. Archean and Proterozoic carbonate platforms comprised lithologies and textures produced by abiotic and microbially mediated precipitation (Grotzinger, 1989; Knoll and Swett, 1990; Grotzinger and James, 2000). In contrast, most Phanerozoic carbonate platforms developed through the aggradation of skeletal carbonates (Schlager, 2003). To date, research quantifying the contribution of skeletal production to early Cambrian carbonate has suggested a protracted increase that did not mirror the explosion in the diversity of skeletonizing organisms (Hicks and Rowland, 2009; Pruss et al., 2010, 2012). In Chapter 4, I describe a new case study that addresses the question: what was the nature of marine carbonate production at the apex of Cambrian skeletal biomineralization? I find that skeletons contributed at most 20% to biohermal carbonate reef facies while thrombolite boundstone and coated-grainstone comprise the majority of carbonate production. This predominance of microbial carbonate textures over skeletal carbonates supports the conclusions of previous research that Cambrian carbonate production more closely resembles earlier, Neoproterozoic carbonates. Nev-

ertheless, the nature of these microbial carbonates—dominated by thrombolites, not stromatolites—reflects an important transition in the mode of Cambrian carbonate production.

Sedimentology and geochemistry are not the only disciplines to provide insight into the Neoproterozoic and Cambrian Earth system. In the final chapter of my dissertation, I demonstrate how geophysics can be brought to bear on enigmas of the Earth system during this critical transition interval. Paleomagnetic studies of this period indicate that Earth’s rotation axis may have experienced large, oscillatory shifts relative to the surface geography. These episodes of true polar wander appear to correlate with supercontinent phases and, in some instances, with large perturbations to both the carbon cycle and global-scale sea level. A framework for understanding these disparate observations has only partially been constructed. For instance, studies of mantle convection show that supercontinent aggregation leads to an elongation of the Earth’s equatorial form that strongly favors rotational instability (Evans, 2003). The reorientation of continentals relative to the rotation axis perturbs Earth’s centrifugal potential and leads to large-scale sea-level changes with a distinct and predictable geometry (Mound and Mitrovica, 1998). With regard to biogeochemical cycles, the inferred translation of continents from equatorial to high latitudes may have diminished organic carbon burial efficiency, which would alter the carbon isotope composition of carbonates and organic matter (Maloof et al., 2006). But other elements of the framework are missing. Most notably, what aspect of the Earth system leads to a propensity for oscillatory motion in which the pole repeatedly returns close to its original state? In Chapter 5, I introduce geophysical models for the Earth’s rotational state designed to explore this issue. To this end, I hypothesize that both elasticity in the lithosphere and a stable background excess ellipticity of the Earth’s figure provide an intrinsic mechanism for the oscillatory return of the rota-

tion pole. I describe the physical preconditions necessary to permit a large amplitude TPW event on the timescale of millions of years.

Together, the chapters of this dissertation demonstrate how the application of research tools from multiple disciplines can elucidate the context of—and the processes responsible for—fundamental geobiological events archived in the Neoproterozoic and Paleozoic stratigraphic record.

REFERENCES CITED

- Butterfield, N.J., 2003, Exceptional fossil preservation and the Cambrian Explosion: Integrative and Comparative Biology, v. 43, p. 166-177.
- Canfield, D.E., Poulton, S.W., Knoll, A.H., Narbonne, G.M., Ross, G., Goldberg, T., and Strauss, H., 2008, Ferruginous conditions dominated later Neoproterozoic deep-water chemistry: Science, v. 321, p. 949-952.
- Cook, P.J., and McElhinny, M.W., 1979, A re-evaluation of the spatial and temporal distribution of sedimentary phosphate deposits in the light of plate tectonics: Economic Geology and the Bulletin of the Society of Economic Geologists, v. 74, p. 315-330.
- Erwin, D.E., Laflamme, M., Tweedt, S.M., Sperling, E.A., Pisani, D., and Peterson, K.J., 2011, The Cambrian conundrum: Early divergence and later ecological success in the early history of animals: Science, v. 334, p. 1091-1097.
- Evans, D.A.D., 2003, True polar wander and supercontinents: Tectonophysics, v. 362, p. 303-320.
- Gill, B.C., Lyons, T.W., Young, S.A., Kump, L.R., Knoll, A.H., and Saltzman, M.R., 2011, Geochemical evidence for widespread euxinia in the Later Cambrian ocean: Nature, v. 469, p. 80-83.
- Grotzinger, J.P., 1989, Facies and evolution of Precambrian carbonate depositional systems: emergence of the modern platform archetype: Society of Economic Paleontologists and Mineralogists Special Publication 44, p. 79-106.
- Grotzinger, J.P., and James, N.P., 2000, Precambrian carbonates: Evolution of understanding: Society for Sedimentary Geology (SEPM) Special Publication, v. 67, p. 3-22.
- Halverson, G.P., Hoffman, P.F., Schrag, D.P., Maloof, A.C., and Rice, A.H.N., 2005, Toward a Neoproterozoic composite carbon-isotope record: Geological Society of America Bulletin, v. 117, p. 1181-1207.
- Hicks, M., and Rowland, S.M., 2009, Early Cambrian microbial reefs, archaeocyathan inter-reef communities, and associated facies of the Yangtze Platform: Palaeogeography, Palaeoclimatology, Palaeoecology, v. 281, p. 137-153.
- Hoffman, P.F., Kaufman, A.J., Halverson, G.P., and Schrag, D.P., 1998, A Neoproterozoic Snowball Earth: Science, v. 281, p. 1342-1346.

-
- Knoll, A. H. Life on a Young Planet: *The First Three Billion Years of Evolution on Earth*. Princeton: Princeton University Press, 2003.
- Knoll, A.H., and Carroll, S.B., 1999, Early animal evolution: Emerging views from comparative biology and geology: *Science*, v. 284, p. 2129-2137.
- Knoll, A.H., and Swett, K., 1990, Carbonate deposition during the late Proterozoic Era: an example from Spitsbergen: *American Journal of Science*, v. 290-A, p. 104-132.
- Kouchinsky, A., Bengtson, S., Runnegar, B., Skovsted, C., Steiner, M., and Vendrasco, M., 2012, Chronology of early Cambrian biomineralization: *Geological Magazine*, v. 149, p. 221-251.
- Li, Z.X., Bogdanova, S.V., Collins, A.S., Davidson, A., De Waele, B., Ernst, R.E., Fitzsimons, I.C.W., Fuck, R.A., Gladkochub, D.P., Jacobs, J., Karlstrom, K.E., Lu, S., Natapov, L.M., Pease, V., Pisarevsky, S.A., Thrane, K., and Vernikovskiy, V., 2008, Assembly, configuration, and break-up history of Rodinia: A synthesis: *Precambrian Research*, v. 160, p. 179–210.
- Maloof, A.C., Schrag, D.P., Crowley, J.L, and Bowring, S.A., 2005, An expanded record of Early Cambrian carbon cycling from the Anti-Atlas Margin, Morocco: *Canadian Journal of Earth Sciences*, v. 42, p. 2195-2216.
- Maloof, A.C., Halverson, G.P., Kirschvink, J.L., Schrag, D.P., Weiss, B.P., and Hoffman, P.F., 2006, Combined paleomagnetic, isotopic, and stratigraphic evidence for true polar wander from the Neoproterozoic Akademikerbreen Group, Svalbard, Norway: *Geological Society of America Bulletin*, v. 118, p. 1099-1124.
- Maloof, A.C., Porter, S.M., Moore, J.L., Dudás, F.Ö., Bowring, S.A., Higgins, J.A., Fike, D.A., and Eddy, M.P., 2010, The earliest Cambrian record of animals and ocean geochemical change: *Geological Society of America Bulletin*, v. 122, p. 1731-1774.
- Marshall, C.R., 2006, Explaining the Cambrian “explosion” of animals: *Annual Review of Earth and Planetary Science*, v. 34, p. 355–84.
- Mound, J.E., and Mitrovica, J.X., 1998, True polar wander as a mechanism for second-order sea-level variations: *Science*, v. 279, p. 534-537.
- Porter, S.M., 2004, Closing the phosphatization window: testing for the influence of taphonomic megabias on the pattern of small shelly fossil decline: *Palaios*, v. 19, p. 178-183.
- Pruss, S.A., Clemente, H., and Laflamme, M., 2012, Early (Series 2) Cambrian archaeocyathan reefs of southern Labrador as a locus for skeletal carbonate production: *Lethaia*, v. 45, p. 401-410.

- Pruss, S.A., Finnegan, S., Fischer, W.W., and Knoll, A.H., 2010, Carbonates in skeleton-poor seas: New insights from Cambrian and Ordovician strata of Laurentia: *Palaios*, v. 25, p. 73-84.
- Schlager, W., 2003, Benthic carbonate factories of the Phanerozoic: *International Journal of Earth Sciences*, v. 92, p. 445-464.
- Southgate, P.N., 1988, A model for the development of phosphatic and calcareous lithofacies in the Middle Cambrian Thornton Limestone, northeast Georgia Basin, Australia: *Australian Journal of Earth Sciences*, v. 35, p. 111-130.
- Tyrrell, T., 1999, The relative influences of nitrogen and phosphorus on oceanic primary production: *Nature* v. 400, p. 525–531.
- Van Cappellen, P., and Ingall, E.D., 1996, Redox stabilization of the atmosphere and oceans by phosphorus-limited marine productivity: *Science*, v. 271, p. 493-496.

CHAPTER 2

SOURCES OF PHOSPHORUS FOR PHOSPHATIC CARBONATE DEPOSITION: A CASE STUDY OF THE CAMBRIAN THORNTONIA LIMESTONE, SOUTHERN GEORGINA BASIN, AUSTRALIA

ABSTRACT

The templating of organic remains and replication of shell material by mineral phosphate provides an illuminating, but time-bounded, taphonomic window into Ediacaran—Cambrian animal evolution. For reasons that remain unknown, this taphonomic window closed significantly through Cambrian Series 2. Here we present sedimentological, petrographic, and geochemical data from the Cambrian Series 2–3 Thornton Limestone, Australia, some of the youngest Cambrian strata displaying exceptional phosphatic preservation of small shelly fossils. Phosphorus enrichment occurred during times of expanded anoxic, ferruginous conditions in subsurface water masses, suggesting that phosphorus adsorption to iron minerals precipitating from the water column provided a significant source of phosphorus to the sediment column. Nevertheless, accounting for the observed phosphorus enrichment by invoking phosphorus delivery associated with either organic carbon or iron minerals alone presents a mass-balance challenge. Within Thornton sediments, phosphate was remobilized by organic decay and bacterial iron reduction, with subsequent reprecipitation largely in the form

of steinkerns of small shelly fossils. Together, these data suggest that an overarching basin redox regime, combined with specific pore-water features, set the probability space for phosphatic carbonate deposition and phosphatization taphonomy.

2.1 INTRODUCTION

Phosphorite and phosphatic carbonate define a spectrum of sedimentary lithologies enriched in the authigenic calcium phosphate mineral apatite (Kazakov, 1937; Baturin and Bezrukov, 1979; Riggs, 1986; Cook and Shergold, 1986; Cook et al., 1990; Föllmi, 1996; Trappe, 2001). The punctuated temporal distribution (Cook and McElhinny, 1979; Cook and Shergold, 1984, 1986) and evolving spatial distribution (Brasier and Callow, 2007) of phosphatic lithologies through Earth history suggest that unique and restrictive physical and/or chemical conditions govern phosphate deposition in time and space.

There are many reasons to want to understand this distribution. Perhaps foremost is the practical concern for understanding how ore-grade sedimentary phosphorites form (e.g., Cook and Shergold, 1986). As with petroleum, phosphate ores are approaching peak production, while global demand continues to rise (Cordell et al., 2009; Filippelli, 2011). At the same time, biogeochemists increasingly invoke perturbations to the ancient phosphorus cycle to explain inferred fluctuations in biological productivity, organic carbon burial and oxidant accumulation over geological time-scales (Tyrrell, 1999; Bjerrum and Canfield, 2002; Saltzman, 2005; Holland et al., 2006; Konhauser et al., 2007; Algeo and Ingall, 2007; Planavsky et al., 2010; Swanson-Hysell et al., 2012). Finally, phosphatic deposits provide a direct window into evolutionary history through the exceptional preservation of fossils (Cook, 1992;

A version of this chapter is intended for publication at the *Geological Society of America Bulletin* with co-authors: David T. Johnston, Simon W. Poulton, Benjamin Kotrc, Christian März, Daniel P. Schrag, and Andrew H. Knoll.

Bengtson and Zhao, 1997; Xiao and Knoll, 2000; Butterfield, 2003; Porter, 2004a).

Research on phosphogenesis has focused primarily on aspects of the physical oceanographic (e.g., Riggs, 1986; Cook and Shergold, 1986) and sedimentological environment of deposition (see review by Föllmi, 1996). Stratigraphically, phosphorite and phosphatic carbonate occur within transgressive and highstand sequence tracts, often above unconformities and hiatal surfaces. With regard to lithology, authigenic apatite is most commonly hosted by shale/siltstone and carbonate. Finally, within a single bed, phosphatization may be so limited spatially that it occurs only as nodules and/or apatite-replaced fossils.

A global phosphogenic window, encompassing these stratigraphic and depositional patterns, coincides with major evolutionary innovation during the Ediacaran and Cambrian (Cook and Shergold, 1984; 1986; Cook, 1992). Much of our knowledge of early animal diversification derives from biomineralized and soft-bodied metazoans replicated and/or templated by phosphate minerals (Bengtson et al., 1990; Xiao and Knoll, 1999; 2000; Donoghue et al., 2006; Dornbos et al., 2006; Kouchinsky et al., 2012). Phosphatization taphonomy is tied to the biogeochemical cycle of phosphorus and, for reasons that remain unknown, a major decline in the incidence of phosphatic lithologies and phosphatic fossil preservation occurs in Cambrian Series 2 (Cook and McElhinny, 1979; Porter, 2004b; Donoghue et al., 2006). This observation prompts two fundamental questions: what physical, biological and/or chemical variables dictated the locus of phosphogenesis within a basin, and which of these variables changed to (largely) end the incidence of phosphogenesis and phosphatization taphonomy at this time?

Geochemistry provides one avenue to address these questions. One commonly held view is that anomalous delivery of reactive phosphorus (i.e., phosphorus that may undergo biogeochemical transformations within the sediment column) to the

sea floor is the primary variable governing enhanced sedimentary phosphorus sequestration (e.g., see Föllmi 1996 and references therein; Papineau, 2010). In modern marine environments, reactive phosphorus delivery to the sea floor occurs predominantly in association with two phases (e.g., Delaney et al., 1998; Benitez-Nelson, 2000): phosphorus bound within organic matter (Redfield, 1958) and/or phosphorus adsorbed to/co-precipitated with particulate iron minerals (herein referred to as the ‘Fe-P shuttle’) (Bernier, 1973; Shaffer, 1986; Feely et al., 1991; Feely et al., 1998; Poulton and Canfield, 2006). To examine the extent to which these reactive phosphorus sources contributed to ancient phosphatic deposits, we report high-resolution sedimentological and geochemical data from the phosphatic Thornton Limestone, Georgina Basin, Australia (Cambrian Series 2–3; Southgate, 1988; Southgate and Shergold, 1991), and for comparison, the overlying non-phosphatic Arthur Creek Formation. In particular, we report iron and phosphorus speciation data, stable carbon isotope measurements, and trace element concentrations across the transition from a carbonate platform to an outer-ramp depositional setting. We combine basin-scale environmental context, provided by sedimentology, geochemistry, and petrography, to assess the source of phosphorus for phosphatic carbonate deposition.

2.2 GEOLOGIC BACKGROUND

2.2.1 BASIN HISTORY

The Centralian Superbasin is a laterally extensive intracratonic basin initiated during Neoproterozoic transcontinental rifting of Rodinia. Regional tectonic events subsequently dissected the superbasin into a mosaic of discrete, asymmetric, polyphase foreland basins (Fig. 1a; Walter et al., 1995; Lindsay, 2002; Dunster et al., 2007). The major constituent basins—Officer, Amadeus, Ngalia, Daly and Georgina—display

broadly similar megasequence architecture, but show important differences in the lithologies of depositional sequences (Lindsay, 2002). In particular, phosphate deposition developed variably and diachronously across the basins (Howard, 1986; Cook and Shergold, 1986; Southgate, 1988; Southgate and Shergold, 1991; Dunster et al., 2007). Here, we focus on the Cambrian stratigraphy of the southern Georgina Basin (Fig. 1b; Cook and Shergold, 1986; Southgate, 1988; Southgate and Shergold, 1991).

The Shadow Group encompasses all Cambrian Series 1 (Terreneuvian) stratigraphy of the southern Georgina Basin (Fig. 1b; Dunster et al., 2007). The lower bounding unconformity of the Shadow Group is the expression of distal uplift and erosion during the late Ediacaran–early Cambrian Petermann Orogeny adjacent to the southwest margin of the Amadeus Basin (Ambrose and Putnam, 2006). Formations comprising the lower Shadow Group encompass a spectrum of (predominantly) siliclastic depositional environments—from proximal alluvial fan facies (Mount Baldwin Formation) to distal marine siltstone and shale (Adam Shale)—derived from the uplifted, subjacent Arunta Province (Ambrose and Putnam, 2006). As Petermann orogenesis terminated, tectonic quiescence coincided with marine transgression and deposition of the upper Shadow Group Red Heart Dolostone within half-grabens and structure-bound topographic lows (Ambrose and Putnam, 2006). Ichnofacies from the Mount Baldwin Formation, and archaeocyathans and small shelly fossils from the Red Heart Dolostone, indicate that the Shadow Group spans the Terreneuvian Series and possibly includes lowermost Cambrian Series 2, Stage 3 (Fig. 1b; Dunster et al., 2007; Peng and Babcock, 2011).

The Narpa Group encompasses Cambrian Series 2 and Series 3 stratigraphy of the southern Georgina Basin (Fig. 1b; Ambrose et al., 2001; Dunster et al., 2007). Deposition of its lowermost member, the *Thorntonia* Limestone, reflects a major transgression and expansion of the Georgina Basin. For this reason, the basal contact

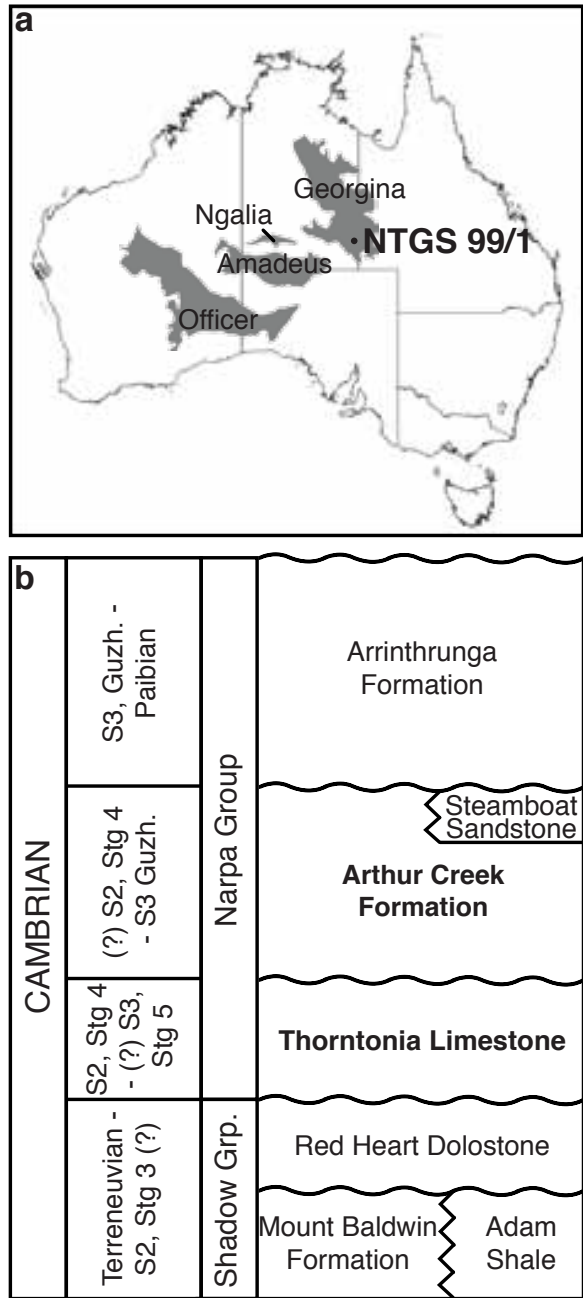


Figure 2.1: (A) Areal extent of the constituent basins of the Neoproterozoic Centralian Superbasin. The black dot marks the drill locality for core NTGS 99/1 in the southern Georgina Basin. (B) Biostratigraphy and lithostratigraphic nomenclature for the Northern Territory outcroppings of Cambrian strata within the southern Georgina Basin (modified from Dunster et al., 2007). Abbreviations S and Stg stand for Series and Stage, respectively. Guz. denotes the Guzhangian Stage. The symbol “(?)” reflects uncertainties in correlating regional Australian trilobite Zones with International Cambrian System designations.

of the Thornton Limestone can unconformably overlie the Shadow Group, conformably and gradationally overlie the Shadow Group, or can overlie and re-work igneous basement. The rest of the Narpa Group records a basin-wide, shallowing-upward succession that transitions from outer ramp (lower Arthur Creek Formation), middle ramp (upper Arthur Creek Formation) and inner ramp (Steamboat Sandstone) depositional environments into a flat-topped carbonate platform (Arrinhrunga Formation) (Ambrose et al., 2001; Dunster et al., 2007).

Trilobite biostratigraphy assigns the Thornton Limestone to the Ordian and early Templetonian stages of Australian chronostratigraphy (Fig. 1b; Laurie, 2004a,b; Dunster et al., 2007), correlative to Cambrian Series 2, Stage 4 and, possibly, lowermost Series 3, Stage 5 (Fig. 1b; Babcock and Peng, 2007; Peng and Babcock, 2011). Trilobites biozones within the Arthur Creek Formation are diagnostic of the Australian regional Ordian, Templetonian, Floran, Undillan, and Boomerangian stages (Laurie, 2004a,b; Dunster et al., 2007), correlative to the uppermost Stage 4 (?) of Cambrian Series 2 through to the Guzhangian Stage of Cambrian Series 3 (Fig. 1b; Babcock and Peng, 2007; Peng and Babcock, 2011).

2.2.2 DRILL CORE NTGS 99/1

We examined the sedimentology and lithofacies associations of the Thornton and Arthur Creek formations from a drill core repositied at the Northern Territory Geological Survey: NTGS 99/1. Markings on this core assign 598.4–580.1 meters core depth (mcd), 580.1–558.7 mcd, and 558.7–554.7 mcd to the informal lower, middle, and upper members, respectively, of the Thornton Limestone (previously Hay River Formation), and 554.7–103.2 mcd to the Arthur Creek Formation (previously Marqua Formation; Ambrose et al., 2001; Dunster et al., 2007). Isopach maps of the Arthur Creek Formation indicate that it is ~260 m thick within drillcore NTGS 99/1 (Dun-

ster et al., 2007). We characterized the sedimentology and geochemistry of the entire Thornton and the lowermost ~200 m of the lower Arthur Creek.

THORNTONIA LIMESTONE

The Shadow Group is absent from NTGS 99/1. In this locality, the Thornton transgressed directly over Paleoproterozoic granite basement. The basal meters of the lower Thornton member include lithic fragments and sand grains within dolomudstone, with minor cubic pyrite crystals (Fig. 2a). More generally, the lower Thornton is comprised of dolomudstone and bioclast dolowackestone with pervasive structural dissolution textures (Fig. 2b). Dissolution is inferred from a spectrum of morphologies broadly characterized as: swarms of anastomosing non-sutured, wispy dissolution seams creating a micro-nodular fabric with millimeter scale idens; swarms and sub-parallel sets of non-sutured dissolution seams creating a stylolaminated to stylobedded fabric; and irregular to hummocky sutured dissolution seams and stylolites that create a sharp to diffuse stylonodular fabric with centimeter-scale idens preserving dolomudstone and bioclastic dolowackestone lithologies. Thin section petrography reveals a mosaic of equigranular, xenotopic calcite with scattered dolomite rhombs. Iron oxides, clay, pyrite crystals, and lingulate brachiopod fragments occur as cumulate along stylolites and dissolution seams. The interstitial condensation of iron oxides and clays suggests primary interbedding of siliciclastic-rich carbonate with mudstone and wackestone (Dunster et al., 2007). Lithofacies of the lower Thornton within drill core NTGS 99/1 are consistent with previous interpretations of a carbonate platform depositional environment (Dunster et al., 2007), as well as with sequence stratigraphic designations of the basal, arkosic, terrigenous unit as a low-stand system tract, and the overlying stylolitic carbonate as a condensed transgressive / high-stand system tract (Southgate and Shergold, 1991).

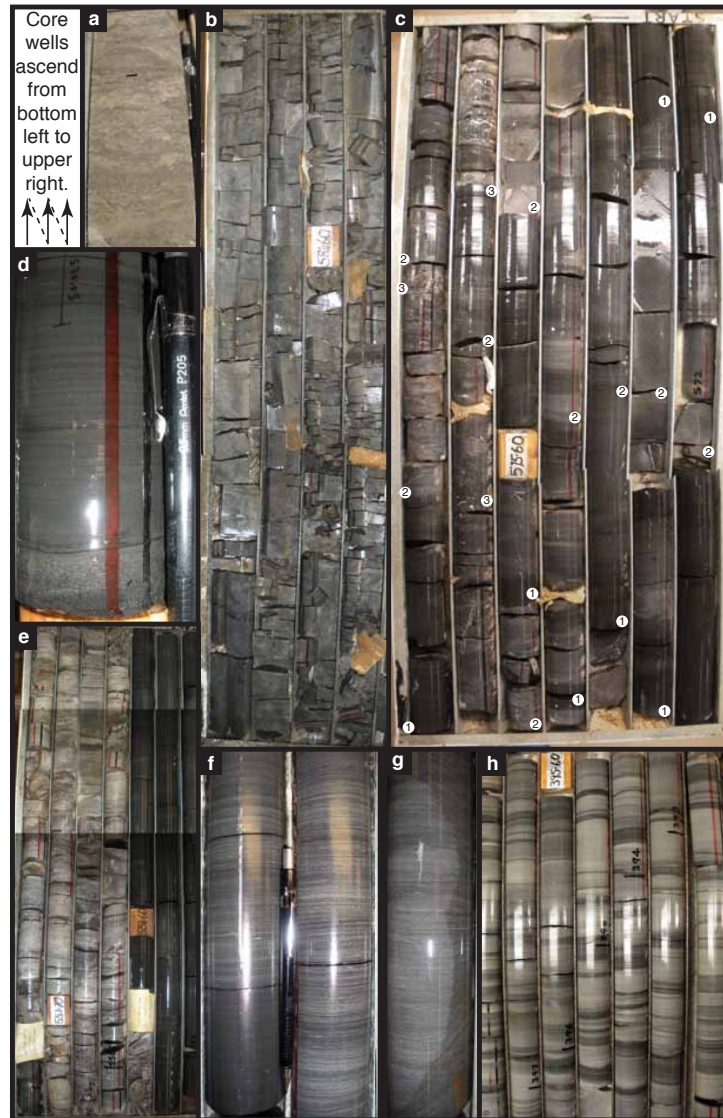


Figure 2.2: Lithofacies of the Thornton Limestone and Arthur Creek Formation in NTGS 99/1. (A) Carbonate with sand-sized lithic fragments above the contact between the Thornton Limestone and underlying Paleoproterozoic granite basement (~595.8–595.6 mcd). (B) General character of the mottled to stylonodular lower Thornton Limestone (584–580.5 mcd). (C) Characteristic meter to sub-meter scale lithology alternations and color variation within the middle Thornton Limestone. (1) Denotes black and dark gray carbonate mudstone; (2) lighter gray mudstone, wackestone and packstone; and (3) grainstone lithologies. Note the general up-package coarsening and lightening, often without cyclic or predictable variation. (D) Bioclastic grainstone to mudstone transition from 570.15–570.05 mcd (middle Thornton Limestone). (E) Appearance of the vuggy, bioclastic grainstone of the upper Thornton Limestone (left) and the overlying basal ‘hot shale’ of the lower Arthur Creek Formation (right). Contact at 554.7 mcd. (F) The laminated facies of the lower Arthur Creek Formation. (G) Light-gray early diagenetic nodule (dolomudstone) displacing dark-gray laminations within the lower Arthur Creek Formation at 532.8–532.65 mcd. (H) General appearance of the interbedded siliciclastic mudstone/siltstone and carbonate mudstone (neomorphosed to microspar) facies of the lower Arthur Creek Formation above ~430 mcd.

The middle Thorntonian consists of four interbedded and interlaminated lithofacies that occur within generally coarsening-upward meter- to sub-meter-scale packages (Fig. 2c). These lithofacies include: (1) black to medium gray carbonate mudstone; (2) dark to medium gray peloidal, bioclastic, and, occasionally, intraclastic wackestone; (3) medium to light gray peloidal and bioclastic packstone; and (4) medium to light gray bioclastic grainstone. Carbonate mudstone or wackestone lithofacies define the base of each package, and interlamine, or alternate gradationally, on a centimeter to decimeter scale. These mud-dominated lithologies typically grade upward into, and may contact sharply with laminae and beds of packstone. Thin beds of bioclastic grainstone may overlie packstone beds. Grainstone beds display basal erosional contacts with millimeter to half-centimeter-scale topography. Upper contacts appear as either (1) sharp and overlain by beds of black to medium-gray carbonate mudstone, or diffuse and conformable with beds of medium-gray packstone or wackestone (Fig. 2d). There is a broad up-core trend: packages initiate with progressively coarser lithologies and terminate with progressively thicker grainstone beds. As recorded within the NTGS 99/1 core, the middle Thorntonian comprises a progradational parasequence set. The nature of deposition for the Thorntonian Limestone within NTGS 99/1 is consistent with the phosphatic lithofacies model from the northeast Georgina Basin (Cycle mP of Southgate, 1988). Southgate and Shergold (1991) assign these shallowing-upward cycles to the transgressive system tract.

The lithologic association of the middle Thorntonian reflects deposition within a subtidal to intertidal depositional environment. Mudstone, wackestone, and packstone beds accumulated from suspension sedimentation in calm settings that lack significant tide, wave, and storm activity. The coarser grain size and subtle current-generated stratification observed in grainstone beds reflect a higher energy depositional environment. Grainstone beds reveal no internal grading, but do show evidence

for amalgamation and winnowing of carbonate mud by either currents or waves. Deposition under the influence of waves is also manifest in rosettes of brachiopod and trilobite shell fragments along basal scour surfaces of bioclastic grainstone beds (Fig. 2d).

In NTGS 99/1, the upper *Thorntonia* encompasses a 4 meter-thick vuggy, fossiliferous dolopackstone with laminae, beds, and pockets of bioclastic dolograinstone (Fig. 2e). When present, dolospar crystals are inequigranular, non-rhombic, anhedral to subhedral, and form a mosaic around bioclasts (primarily of lingulate brachiopods). In addition to representing a prominent matrix constituent, bioclasts are enriched as cumulate along dissolution seams.

PETROGRAPHY OF APATITE DISTRIBUTION

Apatite enrichment displays three predominant modes within the middle and upper *Thorntonia*. First, within bioclast-rich carbonate lithologies, apatite occurs as the internal molds (steinkerns) of conical small shelly fossils and as lingulate brachiopod skeletal debris (Fig. 3a). Apatite may also occlude gaps between, and template the exterior of, silica-replaced skeletons (Fig. 3a). Second, in rare instances, apatite occurs as cement within bioclastic grainstone lithologies (Fig. 3b). Third, within mud-supported, suspension-deposited carbonate, apatite occurs as sub-angular to sub-rounded coarse-silt to medium-sand-size grains, and as silt- to fine-sand-size, tabular or undulose grains within well-sorted, thin beds (Fig. 3c). Due to the textural maturity and fine grain-size of these lithologies, we cannot say conclusively whether these grains are eroded, transported and winnowed from a site of apatite authigenesis (i.e., allocthonous apatite grains) or whether these grains were sourced with a detrital siliciclastic influx. We favor the interpretation that these grains represent re-worked authigenic grains (i.e., intraclasts of authigenic cement and steinkern bioclasts) be-

cause we observe no comparable-size detrital siliciclastic grains.

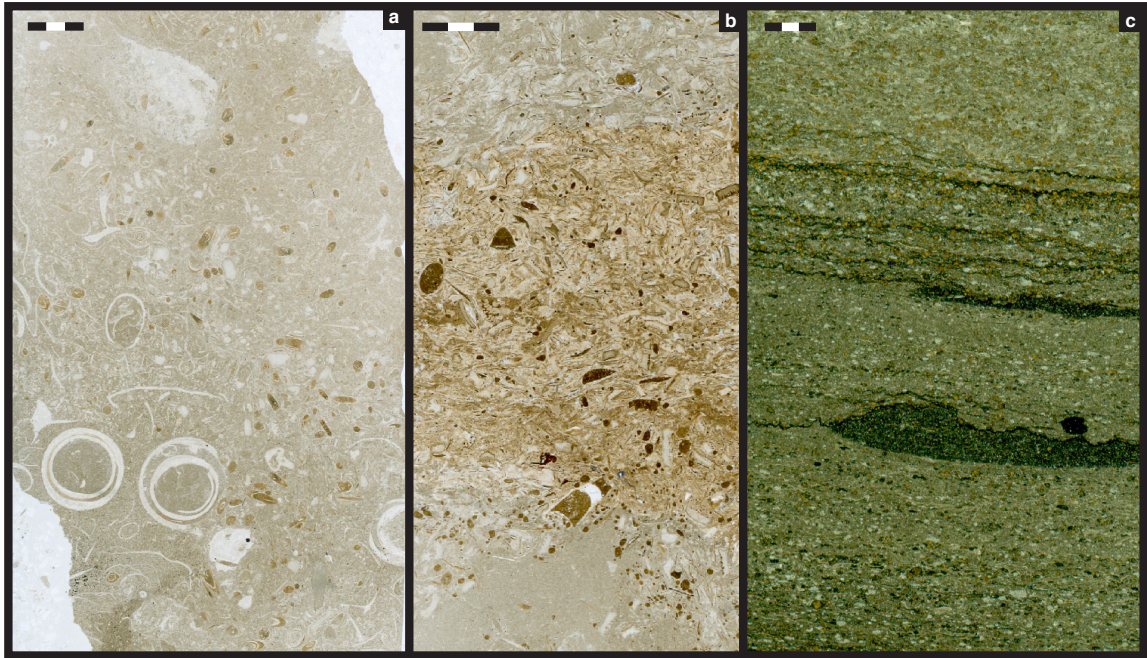


Figure 2.3: Photomicrograph of 570.35 mcd (middle Thornton Limestone). (A) Plane-polarized light image of a packstone with characteristic apatite replacement specifically targeting conical small shelly fossil elements. (B) Wholesale matrix and grain phosphatization in 575.17 mcd. (C) Dispersed, allochthonous grains of authigenic origin in 560.69 mcd. Scale bar within each frame is 3 mm.

ARTHUR CREEK FORMATION

Within NTGS 99/1, the basal 10 m of the lower Arthur Creek encompasses a petroleum-generating, massive black shale (Fig. 2e) succeeded by planar, undulose, and corrugated interlaminae of black to dark gray organic matter- and clay-rich shale, as well as siltstone with medium to light gray calcimudstone and dolomudstone. The shale also contains rare interbeds of very fine-grained bioclastic packstone and grainstone (Fig. 2f). Clay- and iron-oxide-rich laminae include sub-rounded to angular, very well sorted, monocrystalline quartz and authigenic pyrite crystals, the latter of which often

occlude pore space. Horizontal alignment of clay minerals indicates that compaction enhanced the physical expression of lamination. Commonly below ~ 490 mcd, and only rarely above, decimeter-scale light gray limestone nodules displace and retain faint remnants of laminations, indicating nodular development during compaction, but before lithification (Fig. 2g). We interpret individual laminae to reflect the gravitational settling of fine particles suspended by dilute turbidity currents, and wafted towards the basin interior, consistent with an outer-ramp depositional environment (Dunster et al., 2007).

In the upper meters of the measured lower Arthur Creek, a second lithofacies interbeds with the laminated facies (Fig. 2h). This facies includes interbeds of light gray lime mudstone and siliciclastic siltstone. Rare, undulatory laminae truncation indicates intermittent deposition under the influence of currents. Millimeter-scale compacted burrows are present within siltstone-dominated beds. This facies is a harbinger of the more proximal ramp depositional environment of the overlying upper Arthur Creek, which was not measured in this study. Southgate and Shergold (1991) assign the lower Arthur Creek to a transgressive system tract.

2.3 METHODS

We completed detailed sedimentological observation of the Thornton and lower Arthur Creek formations from drill core NTGS 99/1 housed at the Northern Territory Core Library, Alice Springs, Australia. With a water-cooled saw, we cut 534 three-cm-long, quarter-core samples perpendicular to bedding at ~ 10 -25 cm resolution between 597.58 and 347.98 mcd. Each sample was again divided (perpendicular to bedding) into two subsamples, one half designated as a hand-sample or thin-section billet, the other half pulverized with a steel ring mill. The resulting powders were

divided for the following carbon, phosphorus, iron, and trace element geochemical analyses aimed at diagnosing the sediment- and water-column geochemistry at the time of phosphatic carbonate deposition.

Carbon geochemistry targeted both carbonate and organic carbon isotopic compositions and mass fractions. Each hand-sample billet was micro-drilled along individual laminations for carbonate carbon ($\delta^{13}\text{C}_{\text{carb}}$) and carbonate oxygen ($\delta^{18}\text{O}_{\text{carb}}$) isotopic analysis. Samples were measured against an in-house reference gas on a VG Optima dual-inlet mass spectrometer attached to a VG Isocarb preparation system. All isotopic values are reported in the V-PDB per mil (‰) notation with a standard reproducibility of $1\sigma = 0.1\text{‰}$, and 0.33‰ for $\delta^{13}\text{C}_{\text{carb}}$ and $\delta^{18}\text{O}_{\text{carb}}$, respectively.

To determine carbon mass fractions, we acidified 5-10 g of powdered sample with cold, 2.5M hydrochloric acid. The resulting insoluble residue, which represents a combination of silicate minerals and organic matter, was isolated by filtration, rinsed thoroughly with de-ionized water, then dried and weighed. Total inorganic carbon (TIC) was estimated as the weight percent difference between the bulk sample and the insoluble residue. To determine the weight percent of total organic carbon (TOC) and its isotopic composition ($\delta^{13}\text{C}_{\text{org}}$), aliquots of the insoluble residue were combusted within a Carlo Erba NA 1500 Analyzer attached to a Thermo Scientific Delta V Advantage isotope ratio mass spectrometer. Reproducibility of $\delta^{13}\text{C}_{\text{org}}$ for an acetanilide standard was 0.16‰ (1σ). Of the 100 samples processed, 29 were analyzed in duplicate and yielded an analytical reproducibility of $1\sigma = 0.07$ weight percent (wt.%) TOC. Finally, we estimated the wt.% of silicate phases (either siliciclastic or authigenic) as the wt.% of the insoluble fraction minus the wt.% of the TOC fraction.

In this study we employ two operationally defined elemental extraction techniques. The speciation of phosphorus (P) was determined with a modified sequential extraction methodology for marine sediments (Ruttenberg, 1992). Here, 150-200 mg of rock

powder was sequentially extracted with 10 mL each of (1) 0.3M sodium-citrate/1M sodium bicarbonate/0.14M sodium dithionite (pH = 7.5) for P bound to iron minerals (P_{Fe}), (2) 1M sodium acetate (pH = 4.0) for carbonate fluorapatite, biogenic hydroxyapatite, and carbonate-bound P ($P_{\text{auth+carb}}$), (3) 1.2M cold HCl for crystalline fluorapatite (P_{x1}), and (4) 1.2M cold HCl after a 2 hour ignition at 550°C for organic P (P_{org}). To prevent P readsorption during the first two extraction steps, two 5 mL 1M MgCl_2 washes were performed post-extraction. Phosphorus in extracts and wash solutions (except P_{Fe}) was analyzed spectrophotometrically (Thermo Genesys 6) with the addition of molybdate-blue (Strickland and Parsons, 1972; Ruttenberg, 1992); P_{Fe} was measured by inductively coupled plasma optical emissions spectrometry (ICP-OES; Varian Vista-MPX). We note that Ruttenberg (1992) considers extraction phase (3), P_{x1} as detrital fluorapatite of igneous and metamorphic origin. We abbreviate this phase as P_{x1} for ‘crystalline’ apatite so as to remove reference to a genetic mechanism (i.e., detrital) for a chemically operationally-defined phase. We discuss this in greater detail in the discussion.

To confirm that the sequential extraction method was fully extracting P, total P (P_{T}) values were determined independently (SGS Mineral Services Group) by inductively coupled plasma atomic emissions spectrometry (ICP-AES) after a standard four acid digestion ($\text{HF-HClO}_4\text{-HCl-HNO}_3$). These analyses also provide the additional major and trace metal concentrations reported below. To account for variable dilution by siliciclastic influx, we report element concentrations normalized to aluminum (Al). Element/Al ratios are reported in wt.%/wt.% and ppm/wt.% units for major and trace elements, respectively.

To determine the speciation of iron within our samples, we applied a modified version of the sequential extraction method of Poulton and Canfield (2005). Here, 80-100 mg of rock powder was sequentially extracted with 10 mL each of (1) 1M

sodium-acetate, adjusted to pH 4.5 with acetic acid to extract Fe associated with carbonate phases such as siderite and ankerite (Fe_{carb}); (2) 0.28M sodium dithionite, adjusted to pH = 4.8 with 0.2M acetic acid/0.25M tri-sodium citrate, for iron oxides such as hematite and goethite (Fe_{ox}); and (3) 0.2M ammonium oxalate/0.17M oxalic acid (pH = 3.2) for magnetite (Fe_{mag}). The boiling chromium reduction distillation of Canfield et al. (1986) was used to quantify sulfur (S) within pyrite from the insoluble residues derived from the TIC dissolutions. We used a pyrite stoichiometry (FeS_2) to relate the extracted S back to iron (Fe_{py}). Total Fe (Fe_{T}), which comprises the sum of the diagenetically highly reactive phases ($\text{Fe}_{\text{HR}} = \text{Fe}_{\text{carb}} + \text{Fe}_{\text{ox}} + \text{Fe}_{\text{mag}} + \text{Fe}_{\text{py}}$), as well as unreactive Fe (Fe_{U} ; predominately silicate-bound Fe), was determined via a boiling HF-HNO₃-HClO₄ extraction on an additional aliquot of sample powder. All iron concentrations were measured by atomic absorption spectrometry (AAS). Eight replicates of one sample, 572.64 mcd, yield a RSD of 2%, 13%, and 71% for Fe_{carb} , Fe_{ox} , and Fe_{mag} , respectively. The high RSD of the latter two phases result from measured quantities close to the instrument detection limit; that is, the average wt.% $\pm 1\sigma$ for the eight Fe-speciation replicates is 0.110 ± 0.002 , 0.016 ± 0.002 , and 0.001 ± 0.001 for Fe_{carb} , Fe_{ox} , and Fe_{mag} , respectively. At higher Fe concentrations for each fraction, the RSD is <5% for each stage, and this is also the case for Fe_{py} and Fe_{T} (Poulton and Canfield, 2005).

2.4 RESULTS

A generalized stratigraphic column of the Thornton and lower Arthur Creek is shown in Figure 4a. The isotopic composition of carbonate carbon ($\delta^{13}\text{C}_{\text{carb}}$) varies throughout the Thornton and lower Arthur Creek, with coherent excursions between -3 and 2‰ below ~ 474.5 mcd preceding a slight decrease in $\delta^{13}\text{C}_{\text{carb}}$ values from ~ 425

m to the top of the measured core interval (Fig. 4b). Generally, $\delta^{18}\text{O}_{\text{carb}}$ values range from -5 to -13‰ and display coherent variation, save for a 3‰ discontinuity in $\delta^{18}\text{O}_{\text{carb}}$ values between 560.88 and 560.05 mcd (above a grainstone bed), not associated with the formation or informal member boundaries (Fig. 4c). Cross-plots of $\delta^{13}\text{C}_{\text{carb}}$ and $\delta^{18}\text{O}_{\text{carb}}$ display no statistically significant co-variation (Fig. 4e). TOC varies from 0.1-2.9 wt.% in the Thornton, displaying a general increasing trend in the lower Thornton and high variance in the middle Thornton; TOC ranges from 0.1 to 2.5 wt.% in the lower Arthur Creek, with higher values at the base of the formation, decreasing towards a mean of 0.1 wt.% TOC in the upper 100 m of the measured section (Fig. 4d). $\delta^{13}\text{C}_{\text{org}}$ values vary coherently between -36 and -24‰ (Fig. 4d), but display no co-variation with $\delta^{13}\text{C}_{\text{carb}}$ within either the middle/upper Thornton or the Arthur Creek formations (Fig. 4f; lower Thornton: $R^2 = 0.75$; middle/upper Thornton: $R^2 = 0.04$; Arthur Creek: $R^2 = 0.2$).

Total phosphorus (P_{T}) within the Thornton ranges up to 3.9 wt.% (Fig. 5a). P_{T} increases systematically within the lower Thornton and the lower middle Thornton, followed by a significant increase around 575 mcd. The overlying meters of the middle Thornton and upper Thornton display high variance in P_{T} . In contrast, the maximum value of P_{T} within the Arthur Creek is 0.4 wt.%, but is typically much lower with an average of $0.04 \pm 0.04\%$ (Fig. 5a).

We tested the fidelity of the SEDEX method by comparing the sum of the operationally defined pools ($P_{\text{T,se dex}} = \Sigma P_{\text{x l}} + P_{\text{auth+carb}} + P_{\text{org}} + P_{\text{Fe}}$) to total phosphorus content determined by ICP-AES analysis. The consistency between these two measurement techniques (slope of linear regression = 1.1, $R^2 = 0.88$; Fig. 5e) increases confidence in the values of the constituent SEDEX P-speciation phases. In both the Thornton and Arthur Creek, the operationally-defined $P_{\text{x l}}$ and $P_{\text{auth+carb}}$ phases dominate $P_{\text{T,se dex}}$, while P_{org} and P_{Fe} contribute a negligible fraction (Fig. 5b). The

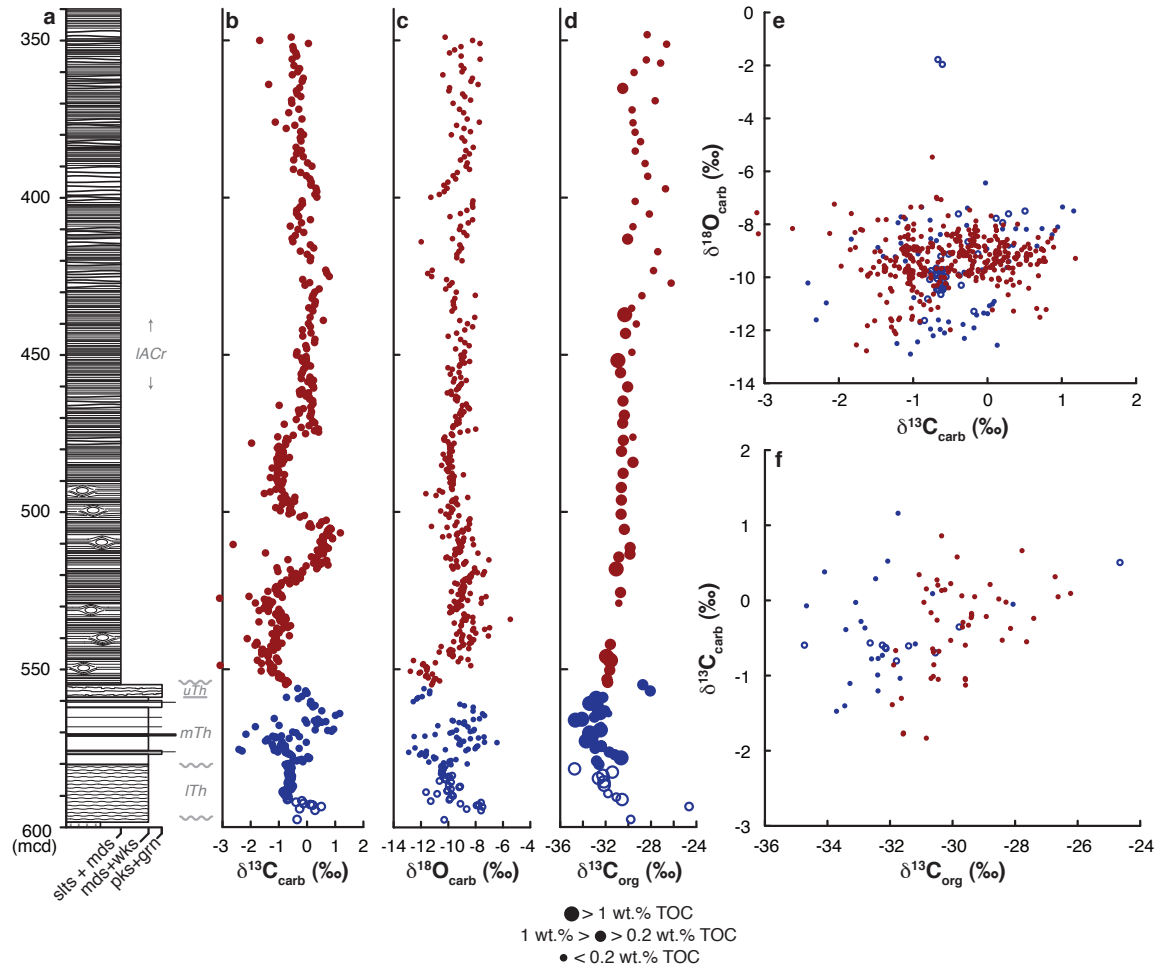


Figure 2.4: Lithology and stable isotope chemostratigraphy of the Thornton Limestone and lower Arthur Creek formations within drill core NTGS 99/1. For all panels, data for the lower and middle/upper Thornton Limestone are plotted in open and solid blue circles, respectively, while data for the Arthur Creek Formation are plotted in solid red circles. (A) Generalized stratigraphic column depicting the lithology of the lower, middle, and upper Thornton Limestone and the lower Arthur Creek Formation. Lithologic abbreviations: Siliciclastics: slts = siltstone; Carbonates: mds = mudstone; wks = wackestone; pks = packstone; grn = grainstone. Vertical axis reflects meters of core depth from surface (mcd). (B) Carbonate carbon isotopic composition. (C) Carbonate oxygen isotopic composition. (D) Total organic carbon isotopic composition (symbol size scaled to wt.% TOC). (E) Cross-plot of carbonate carbon and carbonate oxygen isotopic composition. (F) Cross-plot of organic carbon and carbonate carbon isotopic composition.

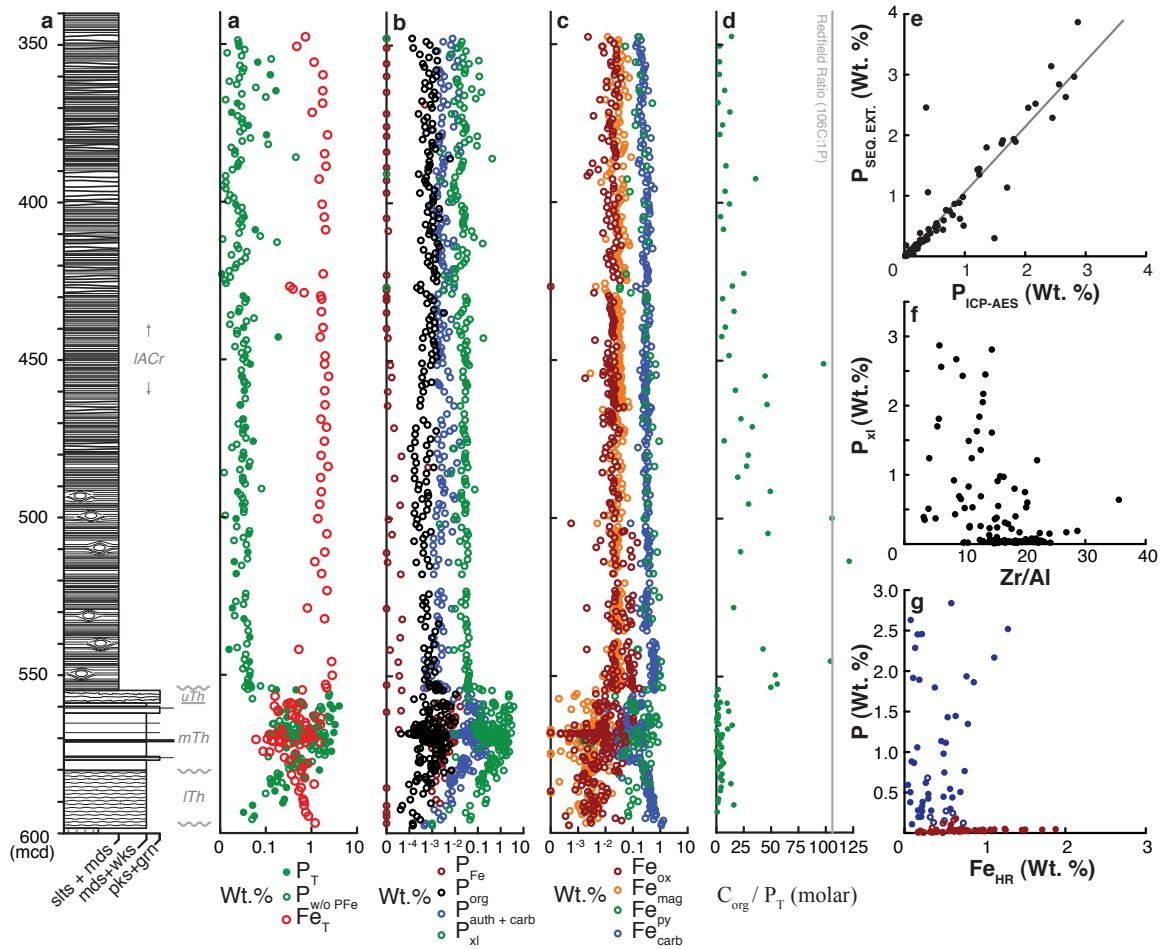


Figure 2.5: Phosphorus and iron speciation geochemistry, molar C:P ratios, and correlations between P and other geochemical metrics within the Thornton Limestone and Arthur Creek formations. (A) Weight percent total phosphorus (filled green circles) and subtotal phosphorus (open green circle) for those samples whose P_{Fe} concentrations were not determined from P-speciation geochemistry. Weight percent total Fe (open red circle) from Fe-speciation geochemistry. Note the logarithmic scale to emphasize, in particular, P enrichment in the middle and upper Thornton Limestone. (b) Weight percent of operationally-defined phosphorus phases as determined by phosphorus speciation geochemistry. Note the logarithmic scale emphasizing the dominance of detrital phosphate minerals (P_{x1}; see text for discussion) and authigenic and carbonate-bound mineralogies (P_{auth+carb}) over organic-bound (P_{org}) and iron-bound phosphorus (P_{Fe}). (c) Weight percent of iron phases as determined by iron speciation geochemistry. Note the logarithmic scale emphasizing the dominance of pyrite (Fe_{py}) and iron carbonate mineralogies (Fe_{carb}) over iron oxides (Fe_{ox}) and magnetite (Fe_{mag}). (D) Molar ratio of organic carbon to total phosphorus. Grey line intersects the axis at C:P = 106:1, the canonical Redfield ratio. (E) Correlation between the weight percent phosphorus within individual samples as determined from ICP-AES versus that determined by the sequential extraction method (see Methods section). Slope of linear regression = 1.1; R² = 0.88. (F) Correlation between the zirconium to aluminum ratio (ppm/%) and operationally-defined P_{x1}. (G) Cross-plot of the weight percent of highly reactive iron species (Fe_{HR}) determined from iron-speciation geochemistry versus the weight percent of P_T determined from phosphorous-speciation geochemistry.

maximum and mean $\pm 1\sigma$ percent contribution to P_T are: $P_{xl} = 98.1\%$ (81.8 ± 20.2), $P_{\text{auth+carb}} = 98.3$ (16.4 ± 19.5), and $P_{\text{org}} = 15.6$ (1.5 ± 2.5). P_{Fe} was measured only on a subset of samples, but this phase contributes minimally to P_T (a maximum of 2.3% and a mean $0.28\pm 0.4\%$).

Total iron (Fe_T) varies from 0.06-1.49 wt.% in the Thorntonia and from 0.32-2.71 wt.% in the Arthur Creek (Fig. 5a). In general, Fe_T is lowest where P_T is highest. Based on the slope of linear regression, 88% of Fe_T resides in Fe_{HR} phases within the Thorntonia ($R^2 = 0.92$; Fig. 6a). In contrast, within the Arthur Creek, $\sim 48\%$ of Fe_T resides in Fe_{HR} ($R^2 = 0.57$; Fig. 6a), and this lower coefficient of determination reflects a secular decrease in $\text{Fe}_{\text{HR}}/\text{Fe}_T$ from 0.66 at the base of the formation to ~ 0.3 near the top of the measured section. Reduced iron phases, Fe_{py} and Fe_{carb} , dominate Fe_{HR} in both formations, while oxidized and partially oxidized iron phases, Fe_{ox} and Fe_{mag} , contribute a minimal fraction (Fig. 5c). Based on the slope of the linear regression, 82 wt.% of Fe_{HR} resides as Fe_{carb} within the lower Thorntonia ($R^2 = 0.62$; Fig. 6c) while Fe_{py} accounts for only a minor contribution that has no statistically significant correlation with Fe_{HR} (Fig. 6b). As such, the gradual decrease in Fe_{HR} within the lower Thorntonia reflects a systematic decrease in Fe_{carb} from 1.3 wt.% to ~ 0.3 wt.%. In the middle and upper Thorntonia, 64% of Fe_{HR} resides as Fe_{py} ($R^2 = 0.95$; Fig. 6b) and 31% resides as Fe_{carb} ($R^2 = 0.82$; Fig. 6c). For the lower Arthur Creek, $\sim 73\%$ and 26% of Fe_{HR} reside in Fe_{py} ($R^2 = 0.94$; Fig. 6b) and Fe_{carb} ($R^2 = 0.72$; Fig. 6c), respectively.

Within NTGS 99/1, the mean $\pm 1\sigma$ acid insoluble fraction (i.e., silicates) within the Thorntonia is 12.4 ± 10.7 as compared to 42.6 ± 15.3 for the Arthur Creek (Fig. 7). TOC/Al ratios are higher and more variable in the Thorntonia than for the Arthur Creek (Fig. 7). Ti/Al ratios remain nearly invariant throughout the measured core interval, whereas both Fe/Al ratios and Mn/Al ratios decline throughout

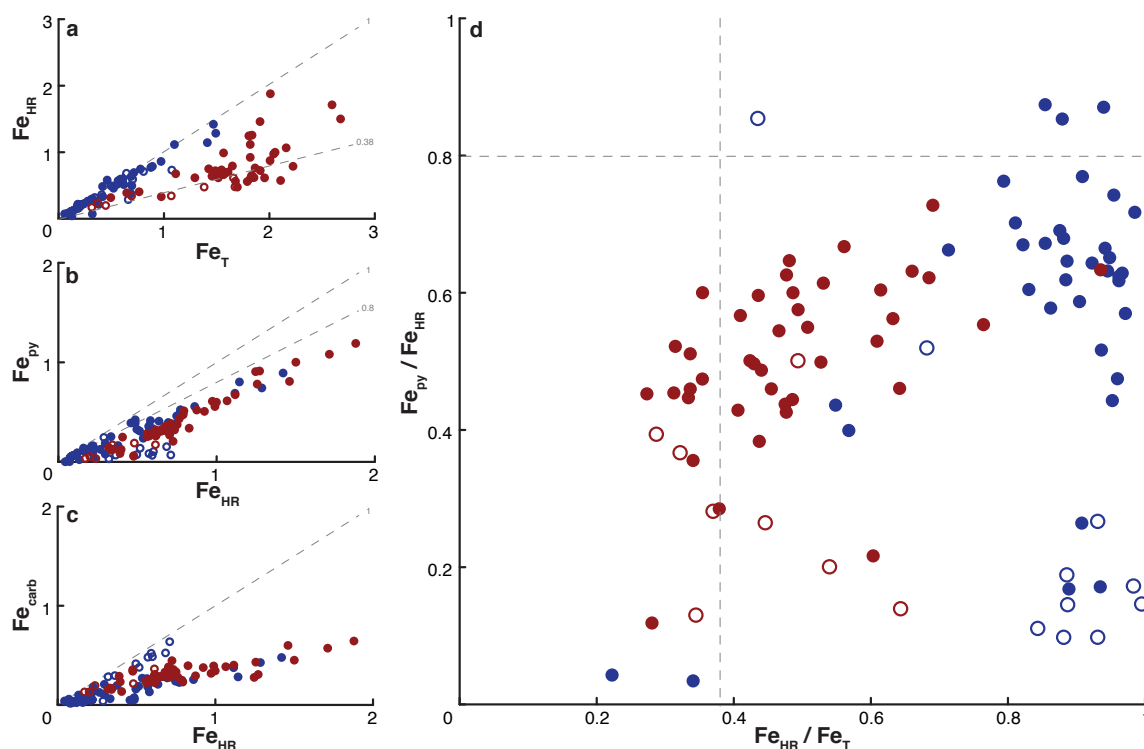


Figure 2.6: Iron speciation geochemistry. For all panels, data for the lower and middle/upper Thornton Limestone are plotted in open and solid blue circles, respectively, while data for the laminated and interbedded facies of the Arthur Creek Formation are plotted in solid and open red circles, respectively. Slopes of regression (not plotted, but provided below) reflect the percentage of the phase of the vertical axis contributing to the phase on the horizontal axis. We plot slopes of 1 and 0.38 as a reference for comparing these carbonate data to previously published iron-speciation data, but we do not advocate interpreting these data within the canonical siliciclastic framework (see (D)). (A) Cross-plots of weight percent total iron (Fe_T) versus weight percent iron within highly reactive phases (Fe_{HR} ; oxides, magnetite, pyrite, and iron carbonates). Lower Thornton = 57%, $R^2 = 0.53$; middle/upper Thornton = 89%, $R^2 = 0.95$; laminated facies of the Arthur Creek = 53%, $R^2 = 0.44$; interbedded facies of the Arthur Creek = 26%, $R^2 = 0.90$). (B) Cross-plots of weight percent highly reactive iron (Fe_{HR}) versus weight percent iron within pyrite (Fe_{py}). Lower Thornton = 17%, $R^2 = 0.07$; middle/upper Thornton = 64%, $R^2 = 0.95$; laminated facies of the Arthur Creek = 75%, $R^2 = 0.95$; interbedded facies of the Arthur Creek = 30%, $R^2 = 0.50$). (C) Cross-plots of weight percent iron carbonate versus weight percent highly reactive iron (Fe_{HR}) versus iron carbonate (Fe_{carb}). Lower Thornton = 82%, $R^2 = 0.62$; middle/upper Thornton = 31%, $R^2 = 0.82$; laminated facies of the Arthur Creek = 25%, $R^2 = 0.68$; interbedded facies of the Arthur Creek = 52%, $R^2 = 0.73$). (D) A translation of frames (A) and (B) into the typical visualization of siliciclastic-derived iron speciation data. Within the iron-speciation interpretative framework for siliciclastic units, a sedimentary Fe_{HR}/Fe_T ratio greater than 0.38 reflects deposition under an anoxic water-column, while a ratio below this value indicates oxic depositional conditions.

the lower Thorntonian (save for a couple of high values in the upper Thorntonian; Fig. 7). Mn/Sr values decay through the lower Thorntonian to a ratio consistently below 1 above ~ 575 mcd, coincident with the increase in P_T . Zr/Al is low and variable within the Thorntonian compared to the Arthur Creek (Zr/Al) and increases abruptly across the middle/upper Thorntonian boundary. Figure 8 presents variation in the aluminum-normalized concentrations of the redox sensitive and bioessential trace metals. Broadly, these elements display high and variable Al-normalized concentrations in the Thorntonian relative to the lower, and stable values observed within the Arthur Creek.

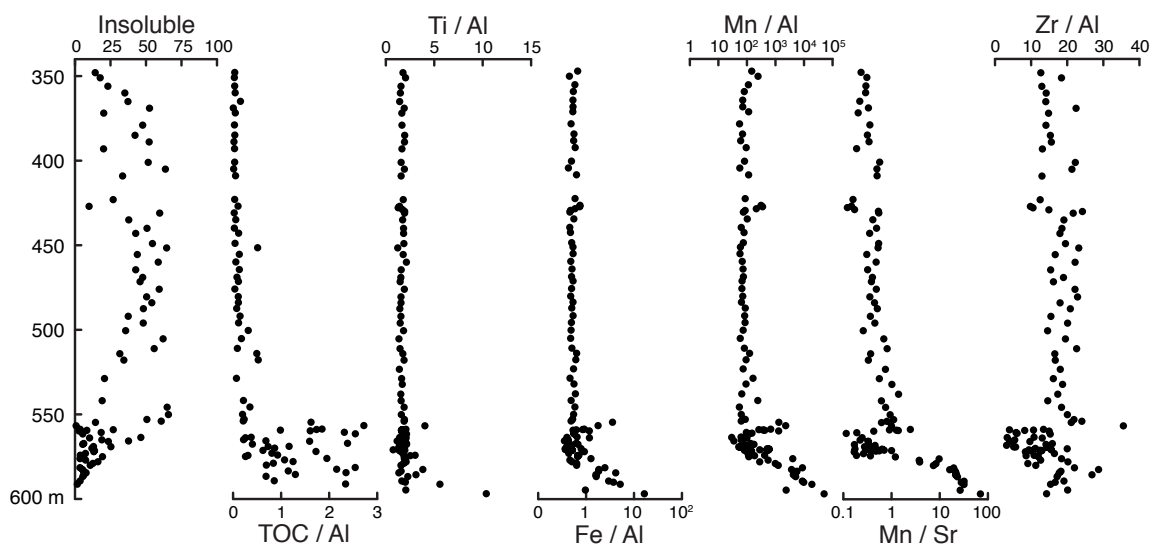


Figure 2.7: Acid insoluble (i.e., siliciclastic), total organic carbon content, and element concentrations normalized to aluminum (Al), and Mn/Sr ratios. From left to right: acid insoluble content (%; see Methods); total organic carbon/Al (%/Al); iron/Al (%/Al); Mn/Al (ppm/Al); Mn/Sr (ppm/ppm); and zirconium/Al (ppm/Al).

2.5 DISCUSSION

To evaluate the processes that contribute to phosphogenesis, and to develop mass balance models for the delivery of phosphorus to phosphatic lithologies, one must ac-

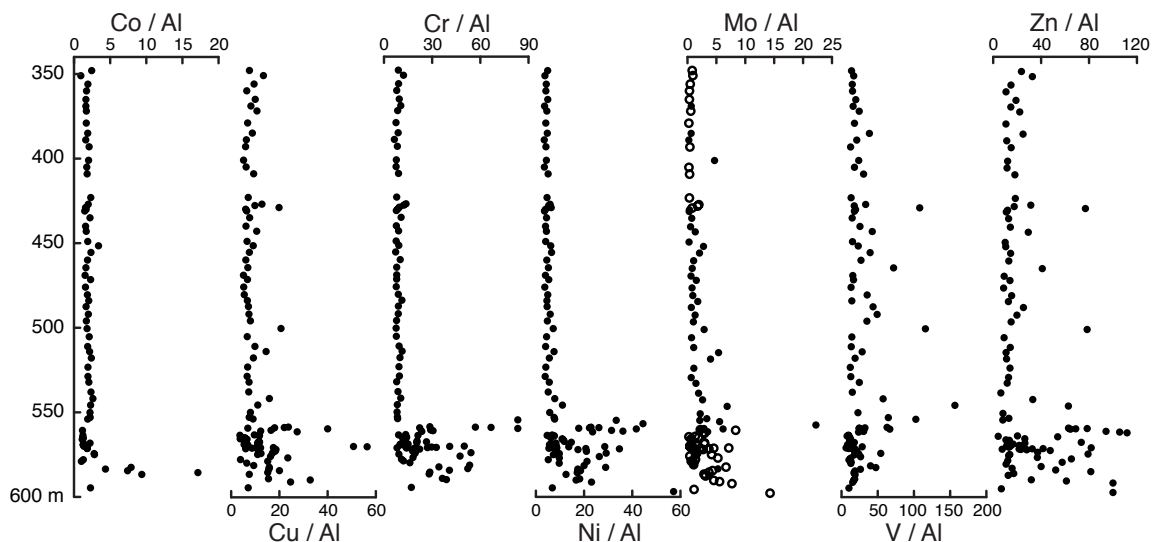


Figure 2.8: Bioessential trace element concentrations. From left to right: cobalt/Al (ppm/%); copper/Al (ppm/%); chromium/Al (ppm/%); nickel/Al (ppm/%); molybdenum/Al (ppm/%; note open circles represent maximum values for samples with concentrations below the detection limit of 1 ppm); vanadium/Al (ppm/%); and zinc/Al (ppm/%).

count for the magnitude of sedimentary phosphorus retention across a reconstructed paleogeographic spatial scale throughout a biostratigraphically constrained temporal interval (Filippelli and Delaney, 1992). Unfortunately, strong lateral variations in the lithofacies of phosphatic lithologies and complex sequence architecture complicate the correlation of phosphatic lithologies within the southern Georgina Basin and between structural domains of the basin as a whole (Southgate, 1988; Southgate and Shergold, 1991). Integrated trilobite biostratigraphy and $\delta^{13}\text{C}_{\text{carb}}$ chemostratigraphy can provide high-resolution temporal bounds on the timing of phosphatic carbonate and phosphorite deposition within the Georgina Basin. As a first attempt at such a quantitative mass-balance model, this study constrains the timing and magnitude of phosphorus deposition from the locality of phosphatic carbonate deposition intercepted by drill core NTGS 99/1.

2.5.1 STRATIGRAPHIC CORRELATION AND TEMPORAL CONTINUITY

Within the southern Georgina Basin, both the Thornton and, in particular, the basal black shale of the Arthur Creek are known petroleum source rocks. As such, strata in proximity to these units may be susceptible to diagenetic alteration of their primary $\delta^{13}\text{C}_{\text{carb}}$ signal due to re-equilibration with an isotopically-depleted, petroleum-bearing fluid derived from the thermal maturation of organic matter (e.g., Derry et al., 2010). Indeed, high Mn/Al ratios, particularly in the lower Thornton would seem to suggest a fluid-interaction (Derry et al., 1992). Here we show that $\delta^{13}\text{C}_{\text{carb}}$ variation in the Thornton and Arthur Creek is coherent within biostratigraphically well-resolved temporal intervals within the southern Georgina Basin, and thus discount the possibility that localized pore fluids altered $\delta^{13}\text{C}_{\text{carb}}$ values. This observation provides the basis for applying carbon isotope chemostratigraphy as a stratigraphic correlation tool and using chemostratigraphic discontinuity as a means to assess missing time.

The $\delta^{13}\text{C}_{\text{carb}}$ curve generated for NTGS 99/1 displays two positive peaks, the first in the middle Thornton (563.92 mcd) and the second in the Arthur Creek (506.51 mcd). Consistent with trilobite biostratigraphy (Laurie, 2004a,b; Fig. 4b), we correlate the middle Thornton excursion to the Ordian–early Templetonian Event and the Arthur Creek excursion to the Late Templetonian–Floran Event. This assignment corroborates regional isotopic variation in the southern Georgina, Amadeus, and Daly Basins (Lindsay et al., 2005) and, further afield, to the Argentine Pre-cordillera (Gomez et al., 2007), the Great Basin, U.S.A. (Saltzman, 2005), South China (Zhu et al., 2004; Guo et al., 2010), and northwest China (Wang et al., 2011).

Sedimentology reveals that candidate horizons for missing time include the Thornton–Arthur Creek boundary and informal member contacts within the Thornton Lime-

stone (Fig. 4a). For each of these candidate surfaces, we use the (dis)continuity of $\delta^{13}\text{C}_{\text{carb}}$ stratigraphy to assess this possibility. A positive inflection in $\delta^{13}\text{C}_{\text{carb}}$ values marks the informal lower–middle Thornton contact (Fig. 4b). In addition, a $\sim 0.5\%$ discontinuity between the informal middle–upper Thornton members is consistent with the observed disconformable contact (Fig. 4b). Notably, an increase in Zr/Al occurs across the middle/upper Thornton contact (Fig. 7). Elevated Zr/Al ratios define erosional surfaces where high-energy currents winnow fine-grained, low-density siliciclastic minerals (proxied by Al input), thereby concentrating high-density minerals (proxied by Zr; Vine and Tourtelot, 1970). Unlike carbon isotopes, secondary fluid migration does not affect the Zr/Al ratio. Thus, this proxy confirms sediment winnowing associated with the upper Thornton. Regionally, the Thornton Limestone—Arthur Creek Formation contact represents a sequence boundary, with karstification developed along this surface in the western margin of the basin (Dunster et al., 2007). While the formation boundary within NTGS 99/1 represents a major lithologic break, $\delta^{13}\text{C}_{\text{carb}}$ values display general continuity across this boundary (Fig. 4b), suggesting either relative temporal continuity or fortuitous resumption of deposition with similar carbon isotopic composition. Isopach maps of the Arthur Creek show that the formation thickens to the east-southeast, where the NTGS 99/1 drill core intercepted the maximum depocenter of the preserved basin margin (Dunster et al., 2007). Thus, under the former scenario, the Thornton Limestone—Arthur Creek Formation boundary within NTGS 99/1 would represent a near correlative conformity of the regional sequence boundary, with limited time missing across this lithologic contact.

Small-magnitude discontinuities in $\delta^{13}\text{C}_{\text{carb}}$, together with constraints from trilobite biostratigraphy, suggest that hiatuses across the informal Thornton Limestone member boundaries, and across the Thornton—Arthur Creek formation bound-

ary, were of relatively short duration. This conclusion is relevant to the mechanism for phosphatic carbonate deposition. Stratigraphic sections reflect variation in depositional environment through time. Naïvely, one might assume that the increase in phosphorus content within the middle Thornton— in a depositional sequence recording similar depositional environment throughout— must speak to an extrinsic mechanism of P delivery to the seafloor, or retention within sediments, specific to that window in time at this locality. In contrast, the cessation of this enrichment at the Thornton—Arthur Creek contact, which reflects an abrupt transition in depositional environment, could reflect either a mechanism discontinuous in time, or one specific to a depositional setting. While it is hard to deconvolve the relative importance of these variables through analysis of just one stratigraphic location, $\delta^{13}\text{C}_{\text{carb}}$ suggests that if the mechanism for phosphatic carbonate deposition toggled on and off through time, it did so rather abruptly.

In theory, carbonate isotopic values make a prediction for the $\delta^{13}\text{C}_{\text{org}}$ value of organic matter produced from a contemporaneous dissolved inorganic carbon reservoir (Knoll et al., 1986). In practice, ancient environmental records, including those for the studied time period, commonly display small-scale variability and/or a lack of co-variation between $\delta^{13}\text{C}_{\text{carb}}$ and $\delta^{13}\text{C}_{\text{org}}$ (e.g., Maloof et al., 2010; Jiang et al., 2012). Within NTGS 99/1, the absolute magnitude of variation in $\delta^{13}\text{C}_{\text{org}}$ is greater than in $\delta^{13}\text{C}_{\text{carb}}$, with no statistically significant co-variation between δ -values in either the Thornton or the Arthur Creek (Fig. 4d,f). Despite the lack of covariance, one trend emerges: high (> 1.0 wt.%), medium ($0.2 < \text{wt.\%} < 1.0$), and low (< 0.2 wt.%) TOC correlates with light, intermediate, and heavy $\delta^{13}\text{C}_{\text{org}}$ values, respectively (Fig. 4d; e.g., Bartley et al., 1998; Johnston et al., 2012). Furthermore, these bins correlate with lithostratigraphy; the lightest $\delta^{13}\text{C}_{\text{org}}$ values occur in the most organic rich facies, the middle Thornton Limestone. The latter two TOC bins generally

correspond to samples from the Arthur Creek below and above ~ 430 mcd, respectively, which is the transition between the laminated facies and the first appearance of the interbedded carbonate mudstone–siliciclastic mudstone facies. Notably, the most phosphatic strata retain the lightest $\delta^{13}\text{C}_{\text{org}}$ values preserved within the succession.

2.5.2 THE RELATIONSHIP BETWEEN P AND C

Phosphorus speciation geochemistry provides a (semi)quantitative measure of the chemical fraction of phosphorus within a sedimentary succession. The majority of P extracted from NTGS 99/1 is operationally classified as fluorapatite of detrital igneous and/or metamorphic origin (P_{x1}) and accounts for $81 \pm 20.2\%$ of P_{T} . However, as described above, petrographic observations reveal an authigenic origin of the apatite grains, with apatite occurring predominantly as the internal molds of small shelly fossils (Fig. 3a) or, occasionally, within the matrix of bioclastic grainstones (Fig 3b). Given the thermal history of the Georgina Basin, which reached temperatures necessary to develop Type II kerogen (Dunster et al., 2007), burial diagenesis should have increased the crystallinity of authigenic phosphate minerals (Shemesh, 1990). It is thus no surprise that authigenic apatite formed within marine sediment during the Cambrian are operationally classified as crystalline igneous and metamorphic apatite. Much like zircon, fluorapatite is a heavy mineral. If P_{x1} comprised fluorapatite sourced to the basin along with a detrital siliciclastic influx, we would predict it should correlate with the Zr/Al ratio. We observe no correlation between P_{x1} and the Zr/Al ratio (Fig. 7). Consistent with petrographic observations (Figure 3), we consider that the P_{x1} pool largely represents authigenic apatite.

What was the source of P for the phosphatic carbonate of the *Thorntonia* Limestone? Perhaps the simplest model for sedimentary P delivery is to assume that organic matter arrives at the sea floor with a C:P ratio that reflects the Redfield ratio

of $C_{\text{org}}:P_{\text{org}} \sim 106:1$ (Redfield, 1958). This simplistic assumption can be violated in two ways: (1) P can be preferentially remineralized within the water-column (Clark et al., 1998) or within anoxic zones of the sediment column (Ingall et al., 1993, 1997; Van Cappellen and Ingall, 1996; Jilbert et al., 2011), and (2) organic-bound P can 'sink-switch' and end up preserved within authigenic phases (Ruttenberg and Berner, 1993). $C_{\text{org}}:P_{\text{org}}$ molar ratios within the Thorntonian vary up to 17,000:1. From this we infer that at least one of these two processes influenced the measured C:P.

The C:P ratio of organic matter entering the sediment column commonly departs from the Redfield ratio, and may be much higher (see Algeo and Ingall, 2007 and references therein). While this delivery ratio could contribute to high $C_{\text{org}}:P_{\text{org}}$ values, we must assess the potential role of 'sink-switching' by comparing C_{org} to total phosphorus (P_{T}) under the assumption that all P derives originally from organic matter (Ingall et al., 1993; Anderson et al., 2001; Algeo and Ingall, 2007). $C_{\text{org}}:P_{\text{T}}$ typically fall well below the canonical Redfield ratio (Fig. 5d). In the Thorntonian, $C_{\text{org}}:P_{\text{T}}$ is low, ranging from 0.1-16:1. In the Arthur Creek Formation (up to a depth of ~ 450 mcd), the $C_{\text{org}}:P_{\text{T}}$ is scattered but much higher (up to 157:1). Continuing upsection, the variation in molar $C_{\text{org}}:P_{\text{T}}$ is again muted, ranging between 1.6-36:1. From this perspective, the Thorntonian and Arthur Creek formations retain more P than would be expected based on organic delivery with a Redfield stoichiometry. Further, realistic departures from this ratio ($C:P > 106$) of organic matter delivered to the sediment column would make it even more difficult to reconcile the observed $C:P_{\text{T}}$ with P derived from organic deposition alone.

What other mechanism(s) could explain these $C_{\text{org}}:P_{\text{T}}$ values? One possibility is preferential C_{org} remineralization. However, $\delta^{13}C_{\text{carb}}$ values are not distinctly light as might be expected if pore-water carbonate precipitation incorporated carbon derived from organic matter remineralization. Alternatively, an additional source of phos-

phorus could have augmented organic-bound P delivered to the sea floor. We explore this possibility in the following section.

2.5.3 THE FE-P SHUTTLE

Phosphorus adsorbed onto and/or co-precipitated with metal oxide particles provides a second source of P to the sediment column whose importance depends, in part, on the magnitude of the flux of metal oxides (e.g., iron-oxyhydroxides) to the sediment column (Shaffer, 1986; Feely et al., 1990; Feely et al., 1998; Poulton and Canfield, 2006). In the modern, oxygenated ocean, iron mobility is generally limited to particulate fluxes of insoluble Fe^{3+} mineralogies (Martin and Meybeck, 1979; Poulton and Raiswell, 2002). In contrast, under anoxic conditions the reductive dissolution and solubilization of iron-oxyhydroxides by dissimilatory iron reduction or dissolved sulfide production during early diagenesis, generates soluble Fe^{2+} that is subsequently redistributed to anoxic slope and basinal environments (Canfield et al., 1996; Severmann et al., 2008; 2010; see review in Lyons and Severmann, 2006). This ‘intrabasin iron shuttle’ provides a mechanism for decoupling iron delivery to the seafloor from siliciclastic sources, and is manifest as an increase in the Fe_T/Al ratio, and as an increase in syngenetic, highly-reactive (Fe_{HR}) phases, of distal sediment deposited under anoxic conditions (Canfield et al., 1996; Lyons and Severmann, 2006).

We assay the behavior of the ancient iron cycle—and, for our purposes, the operation and strength of the Fe-P shuttle—through the speciation and enrichment of sedimentary iron minerals throughout the Thornton and Arthur Creek formations. These geochemical methods are most commonly applied to fine-grained siliciclastic lithologies, where the ratios of various mineralogical phases are interpreted to reflect specific and calibrated environmental redox conditions (Canfield et al., 1992; Raiswell and Canfield, 1998; Raiswell et al., 2001; Poulton and Raiswell, 2002). Appreciating

that these formations comprise carbonate-dominated lithologies, we do not interpret iron-speciation data within the siliciclastic-derived framework; instead, we use the wt.% abundances and cation oxidation states (i.e., ferric or ferrous) of iron mineralogies as a qualitative indicator of redox environment.

Fe_T within the Thornton and Arthur Creek ranges up to 1.5 wt.%, suggesting a significant soluble enrichment of iron to these lithofacies at the time of deposition (Fig. 5a). For the P-enriched middle and upper Thornton units, $\sim 90\%$ of sedimentary Fe resides within highly reactive phases, specifically the ferrous iron constituents pyrite and iron carbonate (Fig. 6a-c). Likewise, while the Arthur Creek shows an up-core decrease in the ratio of $\text{Fe}_{\text{HR}}/\text{Fe}_T$, almost all measured highly reactive iron resides in reduced iron mineralogies (Fig. 6b,c). The petrographic observation that pyrite crystals occlude pore-space within the matrix of fine-grained carbonate requires, at the minimum, that sulfide production occurred within anoxic sediment pore-water. Nonetheless, weight percent enrichments of iron in carbonate lithologies, as well as the dominance of iron mineralogies with a ferrous oxidation state, suggest that these lithologies were deposited from an anoxic, ferruginous water column.

Next, we examine Fe_T/Al to see how well this ratio adheres to predictions for the operation of the intrabasin Fe shuttle (Lyons and Severmann, 2006). Within the lower Thornton, Fe_T/Al ratios are high and variable, decaying towards values of ~ 2 below the lower-middle Thornton informal member contact (Fig. 7). Fe_T/Al values in the remainder of Thornton generally range from ~ 0.2 – 1.2 except for two high values in the upper Thornton. In contrast, the Arthur Creek has a largely invariant Fe_T/Al , ranging from 0.45–0.6, similar to average shale (Taylor and McLennan, 1985). Within the Thornton, Fe_T/Ti confirms that iron introduces the variability within the Fe_T/Al ratio. This is supported by direct analysis of the proportions of iron phases through time; for instance, the high Fe_T/Al near the base of the Thornton

is largely controlled by Fe-carbonate content, which declines up-section, giving way to a pyrite-dominated Fe_{HR} -pool in the middle and upper Thornton. Attributing such variance to iron, rather than siliciclastic associated Al and Ti, is expected, given the mobility of ferrous iron in anoxic fluids. High $\text{Fe}_{\text{T}}/\text{Al}$ ratios within the middle and upper Thornton suggests a decoupling of Fe delivery from siliciclastic influx, further supporting the hypothesis that soluble iron was delivered from within anoxic subsurface water masses.

Nevertheless, within samples from NTGS 99/1, we observe a linear correlation between Fe_{T} and the insoluble mineralogical fraction (comprised of siliciclastics and acid resistant authigenic minerals) (Fig. 9a). This relationship is commonly interpreted to reflect iron delivery associated with a siliciclastic influx (Poulton and Raiswell, 2002). However, upon closer inspection, the constituent authigenic mineralogical phases that dominate Fe_{T} , Fe_{py} and Fe_{carb} , also track the insoluble fraction (Fig. 9b,c). These latter relationships would be unexpected if Fe_{T} derived from a siliciclastic influx. There is no a priori reason why authigenic mineral production should track siliciclastic fluxes, nor is there an expectation that the ratio of Fe_{py} to Fe_{carb} should remain fixed over variable wt.% Fe_{HR} between the middle/upper Thornton and the Arthur Creek (Fig. 6b,c). We suggest that the necessary link between these correlations is organic carbon. TOC content displays a weak correlation with the insoluble (i.e., siliciclastic) fraction (Fig. 9d). Additionally, TOC displays a weak correlation with Fe_{py} in the middle and upper Thornton (Fig. 9e), but not with Fe_{carb} (Fig. 9f). These data suggest that sedimentary TOC content dictated the extent to which sulfate reduction (and, therefore, sulfide production) controlled the pore-water Fe cycle through the nucleation of iron sulfide minerals (Johnston et al., 2010).

Determining the source of iron to these formations requires consideration of regional stratigraphic architecture. In the southern Georgina Basin, the Cambrian

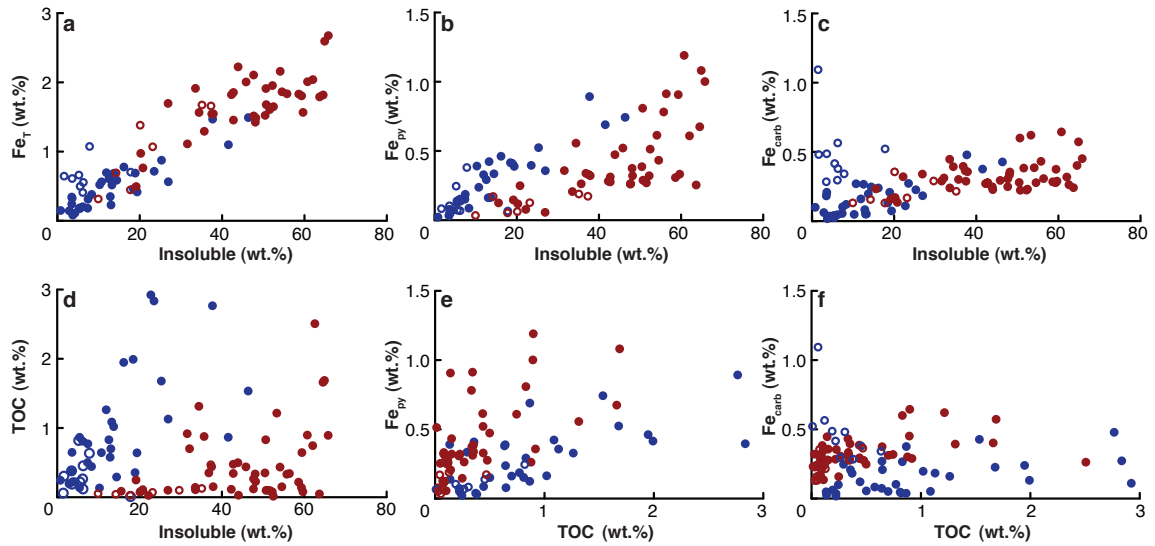


Figure 2.9: Relationship between acid-insoluble fraction (i.e., siliciclastics), iron speciation phases, and total organic carbon. (A) Correlation between highly reactive iron and insoluble phases. (B) Correlation between pyrite and insoluble phases. (C) Correlation between iron carbonate mineralogies and insoluble phases. (D) Correlation between total organic carbon and insoluble phases. (E) Correlation between pyrite and total organic carbon. (F) Correlation between iron carbonate mineralogies and total organic carbon.

Series 1 Mount Baldwin—Adam shale formations record sedimentation by alluvial fans denuding uplifted cratonic blocks during the Petermann orogeny (Ambrose and Putnam, 2006). Ferruginous carbonates of either the Red Heart Dolostone or, in some localities, the Thorntonia Limestone, overlie these alluvial fan systems and/or granitic basement (Fig. 1b). As described above, and consistent with this generalized stratigraphic architecture, within drillcore NTGS 991/1 the Thorntonia transgressed directly over Paleoproterozoic granitic basement. Enrichments in highly reactive iron require anoxic fluid and, given this geologic setting, we envision one of two scenarios for the sourcing of iron to the ferruginous carbonates of the Red Heart Dolostone and the Thorntonia Limestone. The alluvial fan system and/or continental regolith could provide a potential source of iron for the overlying ferruginous carbonates. Indeed, both sources have been invoked to reconcile the ubiquity of iron-enriched lithologies within the late Neoproterozoic and Cambrian (Peters and Gaines, 2012; Swanson-Hysell et al., 2010). We note, however, that Fe_T/Al ratios of the Thorntonia require that delivery of this hypothesized alluvial Fe must occur decoupled from Al (that is, a siliciclastic influx), implying that this iron must have been chemically leached during transgression over the alluvial strata and/or continental regolith. Alternatively, iron enrichments within the Thorntonia may have no genetic relationship to underlying strata, but rather reflect deposition from an Fe^{2+} -rich marine water mass, with that iron sourced more broadly within the Georgina Basin.

In assessing iron speciation data, we note that lithostratigraphic units generally fall within distinct regions of $\text{Fe}_{\text{HR}}/\text{Fe}_T\text{-Fe}_{\text{py}}/\text{Fe}_{\text{HR}}$ space (Fig. 6d). For example, the highest values of $\text{Fe}_{\text{HR}}/\text{Fe}_T$ and $\text{Fe}_{\text{py}}/\text{Fe}_{\text{HR}}$ within this data set characterize the phosphorus enriched middle and upper Thorntonia. In contrast, within a lithostratigraphic unit, lithofacies and/or depositional texture may or may not further bin into distinct $\text{Fe}_{\text{HR}}/\text{Fe}_T\text{-Fe}_{\text{py}}/\text{Fe}_{\text{HR}}$ space. Within the middle and upper Thorntonia, for

example, individual carbonate textures cannot be distinguished within $\text{Fe}_{\text{HR}}/\text{Fe}_{\text{T}}-\text{Fe}_{\text{py}}/\text{Fe}_{\text{HR}}$ space; in contrast, the lithofacies of the Arthur Creek broadly splay into distinct subclasses (Fig. 6d). $\text{Fe}_{\text{HR}}/\text{Fe}_{\text{T}}$ values for both the laminated facies and the interbedded carbonate and siliciclastic mudstone facies falls within both the anoxic, ferruginous quadrant in $\text{Fe}_{\text{HR}}/\text{Fe}_{\text{T}}-\text{Fe}_{\text{py}}/\text{Fe}_{\text{HR}}$ space and within the equivocal redox range between the modern average for oxic deposition and anoxia ($0.26 < \text{Fe}_{\text{HR}}/\text{Fe}_{\text{T}} < 0.38$).

$\text{Fe}_{\text{HR}}/\text{Fe}_{\text{T}}$ data within the equivocal redox zone likely results from the homogenization of fluctuating oxic and anoxic deposition through current re-working. Macroscopic sedimentary structures observed within this lithofacies of the Arthur Creek Formation allow for the possibility that currents stirred the seafloor such that sediment deposited during oxic intervals (light-colored carbonates; no Fe_{HR} enrichment) mixed with sediment deposited during anoxia (dark gray, organic rich marly siltstones; Fe_{HR} enrichment). Such a process would yield an $\text{Fe}_{\text{HR}}/\text{Fe}_{\text{T}}$ signal that does not by itself give a clear indication of oxic deposition, and instead gives a more intermediate $\text{Fe}_{\text{HR}}/\text{Fe}_{\text{T}}$ signal than sediments deposited during more persistent times of anoxia. Thus, we hypothesize that $\text{Fe}_{\text{HR}}/\text{Fe}_{\text{T}}$ data of the Arthur Creek, particularly the upper interbedded member, suggest variable redox conditions—from anoxic to fully oxic—consistent with sedimentology (Fig. 2h). Nonetheless, the nature of redox chemistry during deposition of these formations should be further tested by iron speciation methods applied to time-equivalent siliciclastic facies within the basin, or calibrated to carbonate depositional environments within a framework of detailed sedimentology and micropaleontology.

Together, the enrichment in Fe_{HR} , the high $\text{Fe}_{\text{T}}/\text{Al}$, and the identity of Fe_{HR} phases as ferrous iron mineralogies suggest that an intrabasin iron shuttle operated within the southern Georgina Basin during the time of deposition of the Thornton

and Arthur Creek. Given this, then the associated flux of phosphorus adsorbed onto iron minerals formed as dissolved Fe precipitated in the water column provides a second, potentially significant source of phosphorus to augment organic-bound P delivery. However, the limited contribution of Fe_{ox} to Fe_{HR} in both the Thornton and Arthur Creek (Fig. 5c), the low P_{Fe} values (Fig. 5b), and the present distribution of P within the Thornton decoupled from Fe phases (Fig. 5g), suggests that any P delivered to Thornton sediments via this Fe-P shuttle was subsequently remobilized. Such a decoupling would be expected, given that anoxic sediment pore waters induce the reductive dissolution of iron (oxyhydr)oxides, and organic carbon laden sediments spur both microbial and non-biological iron redox cycling. This distribution confounds easy attribution of P within the Thornton Limestone to primary source vectors. In the following section we integrate C, Fe, and P geochemical data to explore the contribution of P from each of the potential delivery sources.

2.5.4 SOURCE(S) OF P TO THE SEDIMENT COLUMN

Within NTGS 99/1, neither the Fe_{ox} pool determined from iron speciation geochemistry, nor the P_{Fe} pool determined from phosphorus speciation geochemistry, speak directly to a large Fe-bound P flux to the sea floor. Instead, the relatively high wt.% TOC suggests that organic-bound P is a likely source for apatite formation. In contrast, values of $\text{C}:\text{P}_{\text{T}}$ below the Redfield ratio require either significant remineralization of the organic matter that delivered P, or a second source of P to the seafloor.

To begin, we estimate whether organic matter degradation alone could provide sufficient phosphorus for the observed apatite enrichment in the Thornton Limestone. We then quantify how much of this estimated organic carbon would have been lost through remineralization to reconcile the observed concentration in these strata.

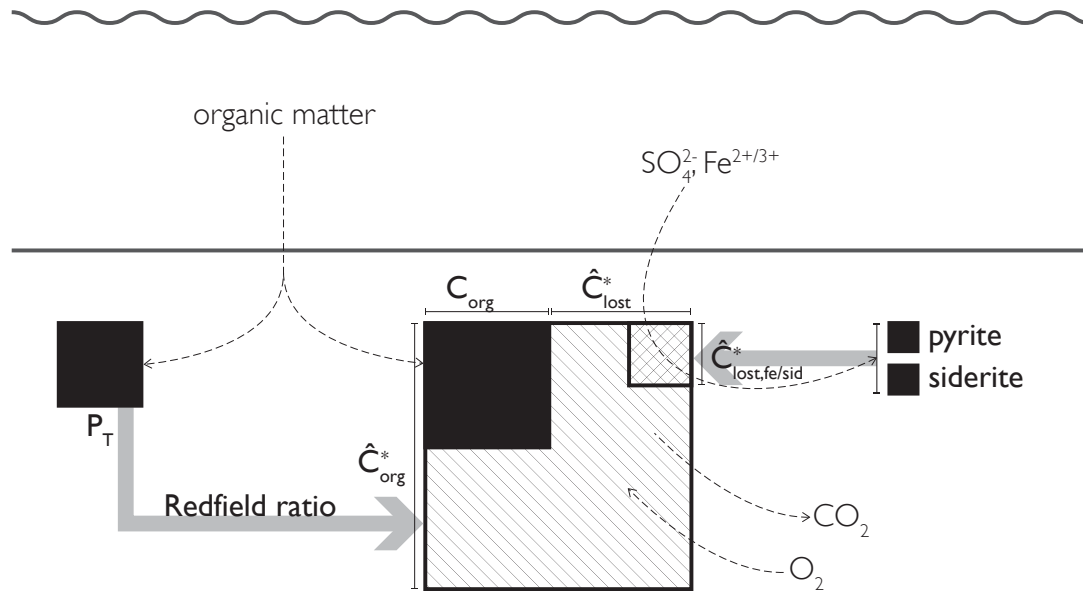
To do so, we use a Redfield stoichiometry (Redfield, 1958) to relate the measured sedimentary weight percent phosphorus to the associated flux of organic carbon necessary for this phosphorus delivery (Fig. 10a). The integrated ecological Redfield stoichiometry varies in space and time due to, for instance, taxonomic variability in biomolecule and cellular composition and nutrient availability regulating biosynthetic allocation (e.g., Geider and LaRoche, 2002). Moreover, water-column heterotrophy increases the C:P ratio of particulate organic carbon delivered to the sediment-water interface (Clark et al., 1998). To be conservative, we assume no water-column remineralization and adopt the canonical Redfield ratio (106C:1P) in the calculations below. We also adopt the combined organic-bound and authigenic phosphorus phases determined from the phosphorus speciation extraction as an estimate of the original flux of phosphorus delivered via organic carbon. This simplistic calculation provides a conservative estimate because we neglect the iron-adsorbed or carbonate-bound P as potential sources for authigenic apatite (as these can represent primary sources of phosphorus to the sediment column), and we assume no diffusive loss of phosphate from pore-water contemporaneous with sedimentary apatite authigenesis.

Following the above arguments, our estimate for the weight percent organic carbon delivered to the sediment column (\widehat{C}_{org}^*) consistent with the observed weight percent phosphorus is given by:

$$\widehat{C}_{org}^* = (P_{auth+carb} + P_{org}) \times R \times \frac{\alpha_c}{\alpha_p}, \quad (2.1)$$

where R is the adopted Redfield ratio and α_C and α_P represent the molar weights of carbon and phosphorus, respectively (Slomp et al., 2004). We estimate the percentage of organic carbon remineralization necessary to reconcile the difference between the delivery estimate, \widehat{C}_{org}^* , and the measured wt.% organic carbon (C_{org}) within

(A) Phosphorus from organic matter



(B) Phosphorus from the “iron shuttle”

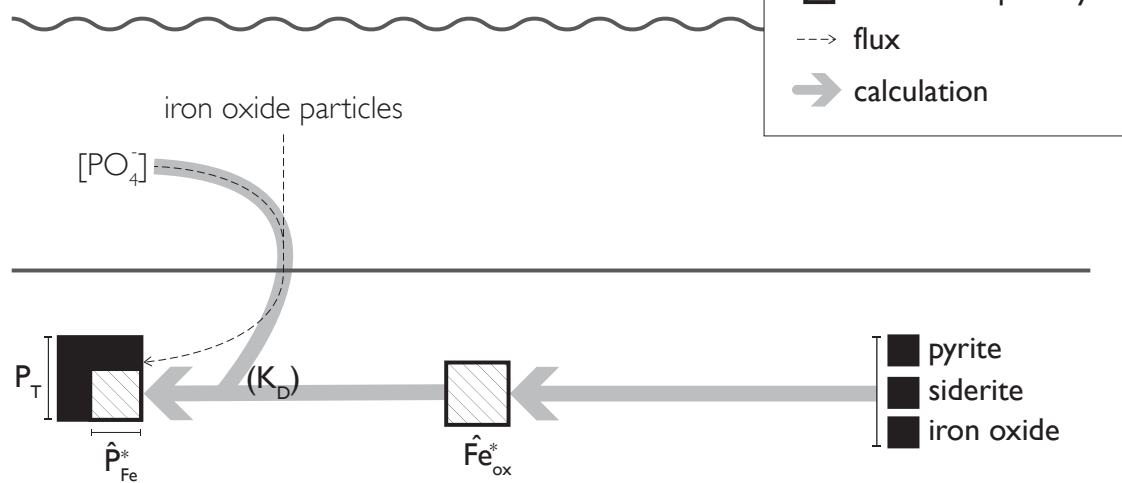


Figure 2.10: Schematic of the calculations for the estimate of phosphorus delivery to the sea floor, and loss from the sediment column, during deposition and before lithification of the Thornton Limestone and Arthur Creek Formations. (A) Phosphorus delivered bound to organic matter versus (B) phosphorus delivered bound to iron oxide particles.

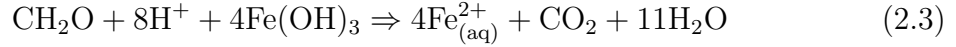
Thorntonia and Arthur Creek rocks (Slomp et al., 2004):

$$\% \hat{C}_{org}^* \text{ loss} = \left(\frac{\hat{C}_{org}^* - C_{org}}{\hat{C}_{org}^*} \right) \times 100. \quad (2.2)$$

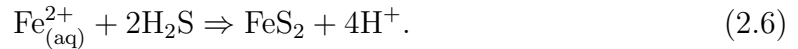
This value represents an estimate of organic carbon remineralization in the time between delivery to the sediment-water interface and lithification. Applying these equations to samples within the phosphorus enriched middle and upper Thorntonia yields a median \hat{C}_{org}^* of 18.6 wt.% and a median loss of 97.8% of this estimated delivery flux. For comparison, applying these equations to samples from the Arthur Creek indicates a high median organic carbon loss estimate (74.0%) from a median organic carbon delivery estimate, \hat{C}_{org}^* , of only 1.1 wt.%. If, instead, we consider more typical ratios of $C_{org}:P_{org}$ delivered to the sediment column, that is, $C:P \gg 106:1$ (Ingall et al., 1993; Van Cappellen and Ingall, 1996, Algeo and Ingall, 2007), then the required C_{org} delivery (\hat{C}_{org}^*) increases proportionately, and so does the estimated % C_{org} loss. Likewise, any diffusive/advective loss of phosphate from the sediment column prior to lithification (Ingall et al., 1993; Slomp et al. 2002; 2004) would increase the delivery estimate and, thus, the inferred % C_{org} loss.

If organic carbon represented the sole delivery source of phosphorus to the sediment column, what would have been the oxidant demand for the organic carbon remineralization estimated above? Dissimilatory microbial metabolisms couple the remineralization of sedimentary organic carbon to the reduction of an oxidant (primarily O_2 , NO_3^- , SO_4^{2-} , and Fe^{3+} ; Konhauser, 2007). Thus, a portion of the estimated organic carbon loss can be accounted for in the early diagenetic mineralogies pyrite and siderite, which form from microbial dissimilatory sulfate and ferric iron respiration, respectively, using organic matter as the electron donor. In the following calculations, we assume the stoichiometry of Fe-(oxyhydr)oxide reduction, where one

mole of organic carbon is remineralized per four moles of siderite produced:



and sulfate reduction, where four moles of organic carbon are remineralized per mole of pyrite produced:



To correct for the presence of siderite within samples, we relate the measured molar quantity of siderite to the Fe^{3+} respiration stoichiometries of Eqns. 3 and 4 to estimate the necessary weight percent of organic carbon consumed to produce this siderite (C_{siderite}):

$$C_{\text{siderite}} = \left(\frac{\text{measured siderite (mols)} \times \left[\frac{1 \text{ mol } C_{\text{org}}}{4 \text{ mol } C_{\text{siderite}}} \right] \times \gamma}{\text{sample weight (g)}} \right), \quad (2.7)$$

where γ converts measured values in moles to wt.%. Likewise, to correct for the presence of pyrite, we relate the measured molar quantity of pyrite within each sample to the stoichiometry of SO_4^{2-} respiration (Eqns. 5 and 6) in order to estimate the weight percent of organic carbon remineralized to produce this pyrite (C_{pyrite}):

$$C_{\text{pyrite}} = \left(\frac{\text{measured pyrite (mols)} \times \left[\frac{4 \text{ mol } C_{\text{org}}}{1 \text{ mol } C_{\text{siderite}}} \right] \times \gamma}{\text{sample weight (g)}} \right). \quad (2.8)$$

With these estimates, we augment Eqn. (2) as:

$$\% \widehat{C}_{org}^* \text{ loss} = \left(\frac{\widehat{C}_{org}^* - (C_{org} + C_{pyrite} + C_{siderite})}{\widehat{C}_{org}^*} \right) \times 100. \quad (2.9)$$

This exercise yields a corrected median loss (96.2%) for the middle and upper Thornton members, not significantly different than the estimate from Eqn. (2). In contrast, and with the exception of phosphorus enriched samples in the uppermost measured meters, the corrected median loss for the Arthur Creek indicates that there is an excess wt.% of organic carbon to account for the observed wt.% phosphorus.

With sulfate and ferric iron accounted for, the only quantitatively important remaining oxidant is molecular oxygen (Konhauser, 2007). In this regard, and if the above assumptions hold, the implication is that the majority of the hypothesized organic carbon loss was through respiration using molecular oxygen. As a thought exercise, we define a ratio of the estimate of organic matter consumed through anoxic respiration (that is, with Fe^{3+} and SO_4^{2-} to form $C_{siderite}$ and C_{pyrite} , respectively) to the estimate of C_{org} loss not accounted for by this estimated anoxic remineralization. We calculate the ratio of anoxic to oxic respiration as:

$$\frac{\text{anoxic}}{\text{oxic}} \text{rem mineralization} = \frac{C_{pyrite} + C_{siderite}}{\widehat{C}_{org}^* - (C_{org} + C_{pyrite} + C_{siderite})}. \quad (2.10)$$

We obtain a mean value of 0.03 ± 0.03 (1σ) for the middle and upper Thornton members. This is to say that, on average, 3% of the estimated organic carbon delivery required to source the observed phosphorus content was remineralized through anoxic pathways—97% must have been remineralized with molecular oxygen to explain the absence of this organic carbon from measured samples. If, however, one assumes a diffusive loss of either sulfide or ferrous iron from the sediment column (i.e., the

numerator underestimates the organic carbon consumed by anoxic remineralization), the estimated percent of anoxic remineralization becomes a minimum. If such diffusive loss occurred, then the proportion of C_{org} remineralized through oxic respiration would be less than 97% and approach 0% as the sedimentary production of sulfide and/or Fe^{2+} through microbial dissimilatory redox reactions quantitatively consumed $\widehat{C}_{\text{org}}^*$. While we cannot determine the diffusive flux of reductants from Thornton or Arthur Creek sediments based on preserved geochemical signatures, we note that such a diffusive loss is possible if the redox boundary resided within the water-column, as suggested by iron-speciation geochemical data.

While such low organic carbon preservation efficiencies (or, as we describe, high % C_{org} loss estimates) commonly occur within modern marine environments, they typify oxygenated shelf settings ($> 20 \mu\text{M}$ bottom-water O_2 ; Canfield, 1994; Hedges and Keil, 1995), not the anoxic depositional environment interpreted for the Thornton Limestone and Arthur Creek formations. Moreover, the calculated weight percent of organic carbon required to deliver the observed phosphorus is notable; the median value, 18.6 wt.%, exceeds organic carbon export to the sea floor in modern marine environments (Hedges and Keil, 1995). Thus, the oxidant demand to efficiently remineralize this magnitude of organic carbon is difficult to reconcile with Cambrian oxygen concentrations, perhaps just 15–50% of the present atmospheric levels (Dahl et al., 2010; Bergman et al., 2004; for alternative views, see Berner, 2006; Garrels and Lerman, 1984).

If organic carbon alone provides an implausible source of phosphorus to the sediment column, then an additional source of P must have augmented the sedimentary P inventory during deposition of the Thornton. A growing body of literature calls upon P adsorbed to the surface of metal oxides, particularly iron (oxyhydr)oxide particles, as an important shuttle of phosphorus to the sea floor (Berner, 1973; Shaffer,

1986; Feely et al., 1991; Feely et al., 1998; Poulton and Canfield, 2006). Additionally, under anoxic conditions, Fe(II)-phosphates (e.g., vivianite, strengite) may have played a more important role for marine P cycling than previously considered (e.g., März et al., 2008; Dellwig et al., 2010). Dissolution of these Fe phases releases adsorbed/co-precipitated P to sediment pore water, potentially leading to sedimentary apatite nucleation (Krom and Berner, 1981; Schuffert et al., 1994, 1998; Slomp et al., 1996; Shen et al., 2000; März et al., 2008). Accordingly, we next estimate phosphorus delivery under the assumption of an appreciable iron-bound P flux, for simplicity based entirely on P adsorbed to iron (oxyhydr)oxides (Fig. 10b). The molar ratio of the co-precipitation of phosphorus onto iron (oxyhydr)oxide particles conforms to a distribution coefficient (K_D) model that scales linearly to the ambient seawater phosphate concentration ($[P_{sw}]$) (Feely et al., 1991; 1998; Konhauser et al., 2007):

$$\left(\frac{P}{Fe}\right)_{molar} = K_D \times [P_{sw}]. \quad (2.11)$$

Thus, to estimate the delivery of iron-bound phosphorus, \hat{P}_{Fe}^* , we multiply an estimate of iron oxide delivery ($\hat{F}_{e_{ox}}^*$) by the adsorption coefficient of phosphorus to iron oxides (K_D) for a given estimate of seawater phosphate concentration ($[P_{sw}]$):

$$\hat{P}_{Fe}^* = \gamma \hat{F}_{e_{ox}}^* \times K_D \times [P_{sw}], \quad (2.12)$$

where γ converts measured values (in wt.%) to moles as required in the definition of the adsorption coefficient.

We use iron-speciation measurements to estimate the total delivered to the sediment column. Under anoxic conditions, a fraction of the iron oxides delivered to the sediment column will be reduced by dissimilatory iron reduction and converted

to ferrous iron, and these ions will either precipitate as pyrite or iron carbonate, or advect/diffuse to the overlying anoxic water column. Accordingly, a full accounting of would include all of these conservation and loss terms. The estimate becomes a lower bound on \widehat{P}_{Fe}^* if we ignore the ferrous iron loss flux, which in any event is unconstrained, and include only the measured iron-oxide (Fe_{ox}), pyrite (Fe_{py}) and iron-carbonate phases (Fe_{carb}). We note also that magnetite may form through the reductive dissolution of ferric oxide phases (e.g., Zegeye et al., 2012), and, as such, could be considered in the summation of primary iron oxide mineralogies; however, magnetite may also form during prograde metamorphism, in which case inclusion of this phase would over-estimate the primary ferric iron flux to the sediment column. We include Fe_{mag} within our calculation because the authigenic pathway likely exceeds weathering and metamorphic overprints for this depositional environment. (Regardless, within NTGS 99/1 magnetite represents a negligible component of Fe_T , therefore this assumption does not alter the estimate for \widehat{P}_{Fe}^* .) In this case, we can rewrite Eqn (12) in the approximate form:

$$\widehat{P}_{Fe}^* = \gamma(Fe_{ox} + Fe_{py} + Fe_{carb} + Fe_{mag}) \times K_D \times [P_{sw}]. \quad (2.13)$$

A host of seawater ions—silica, trace metals and rare earth elements—compete with phosphorus for adsorption sites on the surface of iron oxide particles (e.g., Berner, 1973; Trocine and Trefry, 1988; Olivarez and Owen, 1989; Trefry and Metz, 1989; Feely et al., 1991; Feely et al., 1998; German et al., 1990; Konhauser et al., 2007). Thus, the choice of K_D depends on the assumption of the seawater composition of Cambrian oceans. As these concentrations are broadly unknown for the Paleozoic, we focus here only on the role of the major seawater constituent dissolved silica in competition for iron-surface anion sites. Following the Siever (1992) observation of cristo-

balite saturation throughout the early Phanerozoic ($[Si_{SW}] = 0.67 \text{ mM}$), Konhauser et al. (2007) determined experimentally $K_D = 0.0108$ for ferrihydrite at this silicon saturation state. Notably, the linear range of the K_D model depends on the phosphorus concentration of ambient seawater. At cristobalite saturation, the linearity of the K_D model saturates above $\sim 5 \mu\text{M}$ $[P_{SW}]$. This is to say that the co-precipitation and, thus, delivery of phosphorus bound to iron-oxides remains constant at and above this ambient seawater phosphate concentration. Hence, we adopt $[P_{SW}] = 5 \mu\text{M}$ to calculate a maximum estimate for \hat{P}_{Fe}^* at the adopted $[Si_{SW}]$. The adopted phosphate concentration is consistent with modern anoxic environments, including the Black Sea, Cariaco Basin, and Framvaren Fjord (Shaffer, 1986; Dryssen, 1999, Scranton et al., 2006). Nevertheless, the simplistic assumptions regarding the composition of Cambrian seawater chemistry make the following estimates speculative.

Applying Eqn. (13) to samples from the middle and upper Thornton members yields a median estimate for iron-bound P of 0.1 wt.% as compared to a median estimate of 0.2 wt.% for the Arthur Creek. In this formulation, phosphorus delivery by iron-oxides is proportional to the highly reactive iron phases (Fe_{HR}) determined from iron speciation geochemistry. While Fe_{HR}/Fe_T decreases between the P-enriched middle and upper Thornton members and the Arthur Creek, the observed increase in Fe_T within the Arthur Creek compensates such that the molar estimate of $\hat{F}e_{ox}^*$, and, thus, \hat{P}_{Fe}^* remains roughly constant between the two formations. As such, and if the above assumptions hold, this implies that the relative contribution of the Fe-P shuttle to the observed weight percent of sedimentary P is much greater in the Arthur Creek because of the lower wt.% P_T measured throughout this formation. Indeed, the median estimate of $\hat{P}_{Fe}^* = 0.2 \text{ wt.}\%$ for the Arthur Creek greatly exceeds the median measured P_T (0.03 wt.%). In contrast, the median estimate of $\hat{P}_{Fe}^* = 0.1 \text{ wt.}\%$ for the middle and upper Thornton members provides only $\sim 10\%$ of the median measured

P_T (0.98 wt.%), and proportionally less for samples with the highest measured P_T approaching 4 wt.%. Likewise, any diffusive loss of P from the sediment column prior to lithification would increase the requisite \widehat{P}_{Fe}^* and, in the case of the Thornton, increase the deficiency between the observed P_T and P hypothesized to have been delivered associated with Fe_{ox} .

In the following discussion, we address ways in which estimates of the magnitude of the Fe-P shuttle could deviate from the simplistic formulation of equations 11 through 13. First, we ask whether the measured Fe_{HR} provides an accurate proxy for the contribution of Fe_{ox} to the sediment column, or whether it could underestimate the original Feox flux ($\widehat{F}e_{ox}^*$), and, thus, \widehat{P}_{Fe}^* to the sediment column? One can envision a spectrum of scenarios for the relative magnitudes of Fe_{ox} delivery to and Fe^{2+} loss flux from the sediment column. These scenarios fall within three generalized categories: Fe_{ox} delivery less than, (nearly) equal to, or greater than Fe^{2+} diffusive/advective loss. In the following discussion we neglect the case of a loss term greater than a delivery term as such an imbalance defines an unsustainable Fe cycle.

To begin, we consider the scenario that (1) Fe_{ox} delivery exceeds Fe^{2+} loss. This can result from two opposing redox regimes. (1a) If the majority of Fe_{ox} delivered to the sediment column were stabilized within oxygenated pore-water then this would preclude widespread iron reduction. In this instance, only a small amount of P would be liberated from the Fe_{ox} delivery shuttle, and Fe_{ox} would dominate Fe_{HR} . Iron speciation data from NTGS 99/1 does not support this scenario. (1b) Alternatively, if sedimentary electron donors (e.g., C_{org}) contributed to pore-water anoxia, some fraction of the delivered Fe_{ox} would be reduced to Fe^{2+} , and any P bound to these Fe_{ox} particles would be released to pore-waters. To maintain the low Fe^{2+} loss fraction defining this scenario, any Fe^{2+} ions produced must be captured quantitatively within authigenic ferrous iron mineralogies. In this instance, sedimentary Fe would

be partitioned amongst Fe_{ox} , Fe_{carb} , and Fe_{py} phases, and the dominance of the latter two mineralogies would imply that much of the original Fe_{ox} flux was reduced. Iron speciation data from NTGS 99/1 allow for this anoxic sediment column Fe-cycle scenario with Fe^{2+} capture within pyrite and iron carbonate (Fig. 6b,c). Notably, with regard to P delivery, either scenario for high Fe_{ox} delivery relative to Fe^{2+} loss predicts that our measurement of sedimentary Fe_{HR} represents a close approximation of the magnitude of P delivery associated with the Fe-P shuttle (\widehat{P}_{Fe}^*). Thus, if the Fe cycle were operating in this manner at the time of deposition of the middle and upper Thornton members then, under the above assumptions, the Fe-shuttle is constrained to have contributed a median of $\sim 10\%$ P_{T} and, therefore, could not represent the dominant source of P for the observed quantities.

Next, we consider scenario (2) in which Fe_{ox} delivery to the sediment column marginally exceeds Fe^{2+} loss. Like scenario (1b) above, scenario (2) necessitates a redox environment that facilitates the reductive dissolution of the majority of Fe_{ox} delivered to the sediment column, regardless of the size of this flux. In contrast, scenario (2) is distinguished from scenario (1) by the condition that the majority of the sedimentary Fe^{2+} produced must escape to the overlying water column, resulting in less capture of Fe^{2+} ions in authigenic mineralogies. Such diffuse loss requires anoxia within the water-masses overlying the sediment column. As above, Fe retained within the sediment can reside in any combination of Fe_{ox} , Fe_{carb} , and/or Fe_{py} phases. Iron speciation data from NTGS 99/1 allows for a sedimentary Fe-cycle with both significant Fe^{2+} diffusive loss and retention of some Fe^{2+} in authigenic ferrous minerals (Fig. 6b,c). However, our iron speciation data cannot distinguish between this and scenario (1b) of anoxia with quantitative capture of Fe^{2+} within authigenic minerals. Scenario (2) allows for the measured Fe_{HR} value to significantly underestimate iron-oxide delivery to the sea floor ($\widehat{F}_{\text{ox}}^*$) and, therefore, to underestimate the Fe-P shuttle

(\widehat{P}_{Fe}^*). As such, if the Fe cycle were operating with an extensive benthic flux of Fe^{2+} to the water column, and if a mechanism existed to preferentially retain the delivered P, then the Fe-shuttle could provide a significant proportion of the P retained within phosphatic carbonate of the middle and upper Thornton members.

From these calculations, we conclude that the Arthur Creek had sufficient delivery sources (C_{org} and Fe_{ox}) to account for the observed P_T . In contrast, the Thornton requires exceptional delivery of organic-bound phosphorus, iron-bound phosphorus, or both, to account for the high observed sedimentary phosphorus content. Estimates of phosphorus delivery to the Arthur Creek by the iron-shuttle may significantly overestimate observed phosphorus values for two reasons. First, our equations reflect an assumed K_D given best estimates of contemporaneous seawater silicon concentrations, and use a seawater phosphate concentration to maximize the potential for phosphorus delivery by the iron shuttle. However, the Fe-shuttle need not be operating at this hypothesized maximum. If, instead, we presumed a higher seawater silicon concentration (that is, decreased K_D), or if, for an assumed $[Si_{SW}]$, we also assumed a lower $[P_{SW}]$, then we would calculate a lower P delivery flux per unit Fe_{ox} , and, thus, derive an estimate of \widehat{P}_{Fe}^* more consistent with observed P_T values for the Arthur Creek.

The capacity for iron minerals to scavenge and deliver phosphorus to the sea floor also depends on the number of adsorption sites—a function of mineral surface area. In this regard, amorphous to poorly crystalline phases will scavenge more P ions than highly crystalline phases. Here we assume ferrihydrite as the carrier phase (Konhauser et al., 2007), however, a range of other iron minerals form during anaerobic Fe^{2+} oxidation (e.g., Kappler and Newman, 2004; Zegeye et al., 2012). For instance, carbonated green rust (‘fougerite’) and magnetite form from a precursor of ferrihydrite in the ferruginous water column of Lake Matano, Indonesia (Zegeye et al., 2012). While this depositional environment is not strictly comparable to Cambrian oceans

(e.g., Lake Matano has low [Si]), such a finding does highlight the need to consider multiple and varied carrier phases for the ancient Fe-P shuttle. If, for instance, the adsorption coefficient (K_D) of these minerals with respect to P were higher than for ferrihydrite, we could envisage a more effective Fe-P shuttle to Thornton sediments for a given iron flux to the sea floor.

The discrepancy between the need to invoke a large iron-bound P shuttle to the Thornton and a diminished shuttle to the Arthur Creek prompts two questions: Did a new geochemical regime associated with the change in depositional environment terminate phosphorus delivery to the seafloor? Or could there have been a variable intrinsic to the sedimentology of these two formations that affected their capacity to retain phosphorus with the sediments? Inasmuch as iron-speciation geochemistry allows us to reconstruct the redox condition between these depositional environments, this proxy enables us to address the first question of these questions. While Fe_{HR}/Fe_T decreases between formations, reflecting an increase in siliciclastic-derived (unreactive) Fe, the apportioning of Fe_{HR} to Fe_{py} and Fe_{carb} remains remarkably constant across the boundary (Fig. 6a-c). This constancy argues against the hypothesis for a major change in iron cycling between deposition of the Thornton and Arthur Creek and, thus, casts doubt that a diminution of the flux of P from the Fe-P shuttle drove a change in phosphatic carbonate deposition at this formation boundary.

2.6 CONCLUSIONS

Within drill core NTGS 99/1, phosphorus enrichment is confined to the middle and upper members of the Thornton Limestone, and petrographic observation reveals that this enrichment reflects authigenic apatite mineral nucleation primarily associated with the interior of bioclasts and, more rarely, as cement in bioclastic packstone

and grainstone lithologies. Under the canonical model that phosphorus bound within organic matter represents the only significant delivery flux of phosphorus to the sediment column, total organic carbon concentration and, to a lesser degree, carbon isotopic values provide a means of whether organic carbon remineralization reactions can account for the observed phosphorus content of strata. In the case of the Thornton Limestone, if significant organic carbon remineralization did occur, then the resultant isotopically light CO_2 did not contribute to pore-water authigenic carbonate precipitation, as $\delta^{13}\text{C}_{\text{carb}}$ values retain a basin-wide consistent secular variation.

Interpreted together, sedimentological observations and reduced-iron mineralogical phases suggest that deposition within the southern Georgina occurred under anoxic conditions. Weight percent total iron contents, and the predominance of this iron in the reduced phases of pyrite and iron carbonate, suggest that this anoxia extended into the overlying water column. While mineralogical phases point towards anoxia, we stop short of using siliciclastic-calibrated iron-speciation thresholds for quantifying anoxia in these carbonate-dominated lithologies. It is nevertheless noteworthy that data from these formations fall predominately within the anoxic, ferruginous redox quadrant of Fe-speciation diagrams and that differences in the $\text{Fe}_{\text{HR}}/\text{Fe}_{\text{T}} - \text{Fe}_{\text{py}}/\text{Fe}_{\text{HR}}$ space may reflect differences in lithology. This redox diagnosis is consistent with previous research documenting the propensity for anoxic, ferruginous conditions in the late Neoproterozoic and Cambrian (Canfield et al., 2008) driven by the relative flux of electron donors (organic carbon) to electron acceptors (reactive Fe, sulfate) into a basin (Johnston et al., 2010). Our interpretation of the redox environment of the southern Georgina Basin during deposition of the Thornton and Arthur Creek Formations is testable by either calibrating iron-speciation proxies to carbonate depositional environments or by analyzing time-equivalent siliciclastic deposits within the southern Georgina Basin.

If correct, the conclusion of an active iron redox cycle contemporaneous with the deposition of the Thornton and Arthur Creek Formation provides a second mechanism for augmenting sedimentary phosphorus delivery—phosphorus adsorbed to particulate iron minerals. The stoichiometry of delivery estimates and remineralization reactions indicates that the phosphorus content within the Arthur Creek Formation is easily accounted for by any combination of phosphorus associated with organic matter and/or iron oxide fluxes. However, the observed and quantified phosphorus content within the Thornton is difficult to reconcile with reasonable fluxes of either source of phosphorus alone.

Regardless of the relative proportion of the vectors for phosphorus delivery, organic carbon remineralization plays the central role in liberating phosphorus from delivery sources. Specifically, remineralization liberates phosphorus directly from the electron donor, organic matter. Moreover, anoxic remineralization can additionally liberate P from the electron acceptor, iron-oxides, either directly through dissimilatory iron reduction, or indirectly, if pore-water anoxia facilitates abiotic reductive dissolution of Fe^{3+} by sulfide, and subsequent P liberation. Although complementary, one release mechanism links phosphorus to a redox active reductant (organic matter), whereas the other vector is an available oxidant (Fe^{3+}) for heterotrophy or inorganic reactions.

The discontinuous nature of phosphorite and phosphatic carbonate through Earth history speaks to a discontinuous mechanism for formation. Of the variables enumerated here—phosphorus delivery or the development of a suitable sedimentary micro-environment—the delivery of phosphorus is generally considered the primary variable dictating phosphogenesis. Here, we suggest that the phosphorus delivery mechanism through the Fe-P shuttle, rather than a discontinuous organic carbon flux, provides the more intermittent mechanism for punctuated intervals of phosphogenesis and phosphatization taphonomy throughout Earth history. In concert with pore water

anoxia that would remobilize P within sediments, this discontinuous delivery shuttle, reflecting the incidence of anoxic, ferruginous basin chemistry through time and space, may explain the punctuated temporal record of phosphogenesis and the limited temporal windows for phosphatization taphonomy throughout Earth history.

ACKNOWLEDGEMENTS

We thank the Northern Territory Geological Survey and Max Heckenberg and Jay Carter of the Alice Springs Core Library for generous access to core material. The Agouyon Institute and NASA Astrobiology provided financial support. We thank Paul Myrow for discussions of sedimentology and Eric Morrow for a data compilation script.

2.7 REFERENCES CITED

- Algeo, T.J., and Ingall, E., 2007, Sedimentary C_{org}:P ratios, paleocean ventilation, and Phanerozoic atmospheric pO₂: *Palaeogeography, Palaeoclimatology, Palaeoecology* v. p. 130–155, doi:10.1016/j.palaeo.2007.02.029.
- Ambrose, G., and Putnam, P., 2006, The Georgina Basin 2006: Northern Territory of Australia onshore hydrocarbon potential, Northern Territory Geological Survey, Record 2006-003.
- Ambrose GJ, Kruse PD and Putman PE, 2001, Geology and hydrocarbon potential of the southern Georgina Basin, Australia: *Australian Petroleum Production and Exploration Association Journal*, v. 41, p. 139–163.
- Anderson L. D., Delaney M. L. and Faul K. L., 2001, Carbon to phosphorus ratios in sediments: implications for nutrient cycling: *Global Biogeochemical Cycles*, v. 15, p. 65–79, doi:10.1029/2000GB001270.
- Babcock, L.E., and Shanchi Peng, 2007, Cambrian chronostratigraphy: Current state and future plans: *Palaeogeography, Palaeoclimatology, Palaeoecology*, v. 254, p. 62–66, doi:10.1016/j.palaeo.2007.03.011.
- Bartley, J.K., Pope, M., Knoll, A.H., Semikhatov, M.A., and Petrov, P.Yu., A Vendian—Cambrian boundary succession from the northwestern margin of the Siberian Platform: stratigraphy, palaeontology, chemostratigraphy and correlation: *Geological Magazine*, v. 135, p. 473-494, doi:10.1017/S0016756898008772.
- Baturin, G. N., and Bezrukov, P. L., 1979, Phosphorites on the sea floor and their origin: *Marine Geology*, v. 31, p. 317–332, doi: 10.1016/0025-3227(79)90040-9.
- Bengtson, S. & Yue Zhao, 1997, Fossilized metazoan embryos from the earliest Cambrian: *Science*, v. 277, p. 1645-1648, doi:10.1126/science.277.5332.1645.
- Benitez-Nelson, C.R., 2000, The biogeochemical cycling of phosphorus in marine systems: *Earth-Science Reviews*, v. 51, p. 109-135, doi: 10.1016/S0012-8225(00)00018-0.
- Bergman, N.M., Lenton, T.M., and Watson, A.J., 2004, COPSE: A new model of biogeochemical cycling over Phanerozoic time: *American Journal of Science*, v. 304, p. 397-437, doi: 10.2475/ajs.304.5.397.

- Berner, R. A., 1973, Phosphate removal from sea water by adsorption on volcanogenic ferric oxides: *Earth and Planetary Science Letters*, v. 18, p. 77–86, doi: 10.1016/0012-821X(73)90037-X.
- Berner, R.A., 2006, GEOCARBSULF: A combined model for Phanerozoic atmospheric O₂ and CO₂: *Geochimica et a Cosmochimica Acta*, v. 70, p. 5653-5664, doi: 10.1016/j.gca.2005.11.032.
- Bjerrum, C.J., and Canfield, D.E., 2002, Ocean productivity before about 1.9 Gyr ago limited by phosphorus adsorption onto iron oxides: *Nature*, v. 417 p. 159–162, doi:10.1038/417159a.
- Brasier, M.D. and Callow, R.H.T., 2007, Changes in the Patterns of Phosphatic Preservation across the Proterozoic-Cambrian Transition: *Memoirs of the Association of Australasian Palaeontologists*, No. 34, p. 377-389.
- Butterfield, N.J., 2003, Exceptional fossil preservation and the Cambrian explosion: *Integrative and Comparative Biology*, v. 43, p. 166–177, doi: 10.1093/icb/43.1.166.
- Canfield, D.E., Lyons, T.W., Raiswell, R., 1996, A model for iron deposition to euxinic Black Sea sediments: *American Journal of Science*, v. 296, p. 818–834.
- Canfield, D.E., 1994, Factors influencing organic carbon preservation in marine sediments: *Chemical Geology*, v. 114 p. 315–329, doi: 10.1016/0009-2541(94)90061-2.
- Canfield D. E., Raiswell R., Westrich J. T., Reaves C. M. and Berner R. A., 1986, The use of chromium reduction in the analysis of reduced inorganic sulfur in sediments and shales: *Chemical Geology*, v. 54, p., 149–155, doi: 10.1016/0009-2541(86)90078-1.
- Canfield D. E., Raiswell R. and Bottrell S., 1992, The reactivity of sedimentary iron minerals towards sulfide: *American Journal of Science* v. 292, p. 659– 683.
- Canfield, D.E., Poulton, S.W., Knoll, A.H., Narbonne, G.M., Ross, G., Goldberg, T., and Strauss, H., 2008, Ferruginous conditions dominated later Neoproterozoic deep-water chemistry: *Science*, v. 321, p. 949-952, doi: 10.1126/science.1154499.
- Clark, L.L., Ingall, E.D., Benner, R., 1998, Marine phosphorus is selectively remineralized: *Nature*, v. 393, p. 426-426 doi:10.1038/30881.
- Cook, P.J., 1992, Phosphogenesis around the Proterozoic-Phanerozoic transition: *Journal of the Geological Society of London*, v. 149, p. 615-620, doi: 10.1144/gsjgs.149.4.0615

- Cook, P.J., and McElhinny, M.W., 1979, A re-evaluation of the spatial and temporal distribution of sedimentary phosphate deposits in the light of plate tectonics: *Economic Geology and the Bulletin of the Society of Economic Geologists*, v. 74, p. 315–330, doi: 10.2113/gsecongeo.74.2.315.
- Cook, P and Shergold, J.H., 1984, Phosphorus, phosphorites and skeletal evolution at the Precambrian–Cambrian boundary: *Nature* v.10, p. 231–236, doi: 10.1038/308231a0.
- Cook, P.J., and Shergold, J.H., 1986, Proterozoic and Cambrian phosphorites – nature and origin: *in* Cook, P.J., and Shergold, J.H., eds., *Phosphate deposits of the world: Proterozoic and Cambrian phosphorites*, Volume 1: Cambridge, UK, Cambridge University Press, p. 369-386.
- Cook, P.J., Shergold, J.H., Burnett, W.C., and Riggs, S.R., 1990, Phosphorite research: a historical overview: *Geological Society, London, Special Publication*, v. 52, p. 1-22, doi: 10.1144/GSL.SP.1990.052.01.02.
- Cordell, D., Drangert, J.-O., and White, S., 2009, The story of phosphorus: Global food security and food for thought: *Global Environmental Change*, v. 19, p. 292-305, doi: 10.1016/j.gloenvcha.2008.10.009.
- Dahl, T.W., Hammarlund, E.U., Anbar, A.D., Bond, D.P.G., Gill, B.C., Gordon, G.W., Knoll, A.H., Nielsen, A.T., Schovsbo, N.H., Canfield, D.E., 2010, Devonian rise in atmospheric oxygen correlated to the radiations of terrestrial plants and large predatory fish, v. 107, p. 17911-17915, doi: 10.1073/pnas.1011287107.
- Delaney M.L., 1998, Phosphorus accumulation in marine sediments and the oceanic phosphorus cycle: *Global Biogeochemical Cycles*, v. 12, p. 563–572, doi:10.1029/98GB02263.
- Dellwig, O., Leipe, T., März, C., Glockzin, M., Pollehne, F., Schnetger, B., Yakushev, E.V., Böttcher, M.E., and Brumsack, H.-J., 2010, A new particulate Mn-Fe-P-shuttle at the redoxcline of anoxic basins: *Geochimica et Cosmochimica Acta*, v. 74, p. 7100-7115.
- Derry, L.A., 2010, A burial diagenesis origin for the Ediacaran Shuram-Wonoka carbon isotope anomaly: *Earth and Planetary Science Letters*, v. 294, p. 152–162, doi: 10.1016/j.epsl.2010.03.022.
- Derry, L.A., Kaufman, A.J., and Jacobsen, S.B., 1992, Sedimentary cycling and environmental change in the late Proterozoic: Evidence from stable and radiogenic isotopes: *Geochimica et Cosmochimica Acta*, v. 56, p. 1317-1329, doi: 10.1016/0016-7037(92)90064-P.

- Donoghue, P., Kouchinsky, A., Waloszek, D., Bengtson, S., Dong, X.-p., Val'kov, A.K., Cunningham, J.A., and Repetski, J.E., 2006, Fossilized embryos are widespread but the record is temporally and taxonomically biased: *Evolution & Development*, v. 8, p. 232–238, doi: 10.1111/j.1525-142X.2006.00093.x.
- Dornbos, S.Q., Botjer, D.J., Chen, J.-Y., Gao, F., Oliveri, P., and Li, C.-W., 2006, Environmental controls on the taphonomy of phosphatized animals and animal embryos from the Neoproterozoic Doushantuo Formation, southwest China: *Palaios*, v. 21, p. 3-14, doi: 10.2110/palo.2004.p04-37.
- Dunster, J.N., Kruse, P.D., Duffett, M.L., and Ambrose, G.J., 2007, Geology and resource potential of the southern Georgina Basin: Northern Territory Geological Survey, Digital Information Package DIP007.
- Dyrssen, D.W., 1999, Framvaren and the Black Sea – Similarities and differences: *Aquatic Geochemistry*, v. 5, p. 59-73.
- Filippelli, G.M., 2011, Phosphate rock formation and marine phosphorus geochemistry: the deep time perspective: *Chemosphere*, v. 84, p. 759-766, doi: 10.1016/j.chemosphere.2011.02.019.
- Filippelli, G.M., and Delaney, M.L., 1992, Similar phosphorus fluxes in ancient phosphorite deposits and a modern phosphogenic environment: *Geology*, v. 20, p. 709-712, doi: 10.1130/0091-7613(1992)020<070.
- Feely, R.A., Trefry, J.H., Massoth, G.J., Metz, S., 1991, A comparison of the scavenging of phosphorus and arsenic from seawater by hydrothermal iron oxyhydroxides in the Atlantic and Pacific Oceans: *Deep Sea Research*, v. 38, p., 617-623, doi: 10.1016/0198-0149(91)90001-V.
- Feely, R.A., Trefry, J.H., Lebon, G.T., and German, C.R., 1998, The relationship between P/Fe and V/Fe ratios in hydrothermal precipitates and dissolved phosphate in seawater: *Geophysical Research Letters*, v. 25, p. 2253-2256, doi:10.1029/98GL01546.
- Froelich, P.N., Arthur, M.A., Burnett, W.C., Deakin, M., Hensley, V., Jahnke, R., Kaul, L., Kim, K.-H, Roe, K., Soutar, A., Vathakanon, C., 1988, Early diagenesis of organic matter in Peru continental margin sediments: Phosphorite precipitation: *Marine Geology*, v. 80, p. 309-343.
- Föllmi, K.B., 1996, The phosphorus cycle, phosphogenesis and marine phosphate-rich deposits: *Earth-Science Reviews*, v. 40, p. 55–124, doi: 10.1016/0012-8252(95)00049-6.

- Garrels, R.M., and Lerman, A., 1984, Coupling of the sedimentary sulfur and carbon cycles; an improved model: *American Journal of Science*, v. 284, p. 989-1007, doi: 10.2475/ajs.284.9.989.
- Geider, R., and La Roche, J., 2002, Redfield revisited: variability of C:N:P in marine microalgae and its biochemical basis: *European Journal of Phycology*, v. 37, p. 1-17, doi:10.1017/S0967026201003456.
- German, C.R., Klinkhammer, G.P., Edmond, J.M., Mitra, A., Elderfield, H., 1990. Hydrothermal scavenging of rare earth elements in the ocean: *Nature*, v. 345, p. 516–518, doi:10.1038/345516a0.
- Gomez, F.J., Ogle, N., Astini, R.A., and Kalin, R.M., 2007, Paleoenvironmental and Carbon-Oxygen Isotope Record of Middle Cambrian Carbonates (La Laja Formation) in the Argentine Precordillera: *Journal of Sedimentary Research*, v. 77, p. 826-842, doi: 10.2110/jsr.2007.079.
- Guo, Q., Strauss, H., Liu, C., Zhao, Y., Yang, X., Peng, J., and Yang, H., 2010, A negative carbon isotope excursion defines the boundary from Cambrian Series 2 to Cambrian Series 3 on the Yangtze Platform, South China: *Palaeogeography, Palaeoclimatology, Palaeoecology*, v. 285, p. 143–151, doi:10.1016/j.palaeo.2009.11.005.
- Howard, P.F., 1990, The distribution of phosphatic facies in the Georgina, Wiso and Daly River Basins, Northern Australia: *Geological Society, London, Special Publications*, v. 52, p. 261-272, doi: 10.1144/GSL.SP.1990.052.01.19
- Hedges, J.I, and Kiel, R.G., 1995, Sedimentary organic matter preservation: an assessment and speculative synthesis: *Marine Chemistry*, v. 49, p.81-115, doi: 10.1016/0304-4203(95)00008-F.
- Holland, H.D., 2006, The oxygenation of the atmosphere and oceans: *Philosophical Transactions of the Royal Society–B*, v. 361, p. 903-915, doi: 10.1098/rstb.2006.1838.
- Ingall, E.D., Bustin, R.M., and Van Cappellen, P., 1993, Influences of water column anoxia on the burial and preservation of carbon and phosphorus in marine shales: *Geochimica et Cosmochimica Acta*, v. 57, p. 303–316, doi: 10.1016/0016-7037(93)90433-W.
- Ingall E. D. and Jahnke R. A., 1997, Influence of water- column anoxia on the elemental fractionation of carbon and phosphorus during sediment diagenesis: *Marine Geology*, v. 139, p. 219–229, doi: 10.1016/S0025-3227(96)00112-0.

- Jahnke, R. A., Emerson, S.R., Roe, K.K., and Burnett, W.C., 1983, The present day formation of apatite in Mexican continental margin sediments: *Geochimica et Cosmochimica Acta*, v. 47, p. 259-266, doi: 10.1016/0016-7037(83)90138-2.
- Jiang, G., Wang, X., Shi, X., Xiao, S., Zhang, Z., and Dong, J., 2012, The origin of decoupled carbonate and organic carbon isotope signatures in the early Cambrian (ca. 542–520 Ma) Yangtze platform: *Earth and Planetary Science Letters*, v. 317-318, p. 96-110, doi: 10.1016/j.epsl.2011.11.018.
- Jilbert, T., Slomp, C.P., Gustafsson, B.G., and Boer, W., 2011, Beyond the Fe-P-redox connection: preferential regeneration of phosphorus from organic matter as a key control on Baltic Sea nutrient cycles: *Biogeosciences*, v. 8, p. 1699-1720, doi: 10.5194/bg-8-1699-2011.
- Johnston, D.T., Poulton, S.W., Dehler, C., Porter, S., Husson, J., Canfield, D.E., and Knoll, A.H., 2010, An emerging picture of Neoproterozoic ocean chemistry: Insights from the Chuar Group, Grand Canyon, USA: *Earth and Planetary Science Letters*, v. 290, p. 64-73, doi: 10.1016/j.epsl.2009.11.059.
- Kappler, A., and Newman, D.K., 2004, Formation of Fe(III)-minerals by Fe(II)-oxidizing photoautotrophic bacteria: *Geochimica et Cosmochimica Acta*, v. 68, p. 1217–1226, doi:10.1016/j.gca.2003.09.006.
- Kazakov, A.V., 1937, The phosphate facies: Origin of phosphorites and geological factors of deposit formation: *Proceedings of the Scientific Institute of Fertilizers and Insectofungicides*, v. 145, p. 1–106.
- Knoll, A. H., Hayes, J. M., Kaufman, A. J., Swett K., and Lambert, I. B., 1986, Secular variation in carbon isotope ratios from Upper Proterozoic successions of Svalbard and East Greenland: *Nature* v. 321, 832 - 838, doi:10.1038/321832a0.
- Konhauser, K.O., 2007, *Introduction to Geomicrobiology*: Oxford, Blackwell Science, 425 p.
- Konhauser, K.O., Lalonde, S.V., Amskold, L., and Holland, H.D., 2007, Was There Really an Archean Phosphate Crisis?: *Science*, v. 315, p. 1234, doi: 10.1126/science.1136328.
- Kouchinsky, A., Bengtson, S., Runnegar, B., Skovsted, C., Steiner, M., and Vendrasco, M., 2012, Chronology of early Cambrian biomineralization: *Geological Magazine*, v. 149, p. 221-251, doi: 10.1017/S0016756811000720.
- Krom, M.D. and Berner, R.A., 1981, The diagenesis of phosphorus in a nearshore marine sediment: *Geochimica et Cosmochimica Acta*, v. 45, p. 207–216, doi: 10.1016/0016-7037(81)90164-2.

- Laurie, J.R., 2000, Macrofossils from NTGS 99/1 corehole, southern Georgina Basin, Northern Territory: Professional Opinion, Australian Geological Survey Organisation.
- Laurie, J.R., 2004a, Early Middle Cambrian trilobites from Pacific Oil & Gas Baldwin 1 well, southern Georgina Basin, Northern Territory: *Memoirs of the Association of Australasian Palaeontologists* v. 32, p. 127-204.
- Laurie, J.R., 2004b, Early Middle Cambrian trilobite faunas from NTGS Elkedra 3 corehole, southern Georgina Basin, Northern Territory: *Memoirs of the Association of Australasian Palaeontologists*, v. 30, p. 221-260.
- Lindsay, J.F., 2002, Supersequences, superbasins, supercontinents – evidence from the Neoproterozoic–Early Palaeozoic basins of central Australia: *Basin Research*, v. 14, p. 207-223, doi: 10.1046/j.1365-2117.2002.00170.x.
- Lindsay, J.F., Kruse, P.D., Green, O.R., Hawkins, E., Brasier, M.D., Cartlidge, J., Corfield, R.M., 2005, The Neoproterozoic–Cambrian record in Australia: a stable isotope study: *Precambrian Research*, v. 143, p. 113–133, doi: 10.1016/j.precamres.2005.10.002.
- Lyons, T.W., and Severmann, S., 2006, A critical look at iron paleoredox proxies: New insights from modern euxinic marine basins: *Geochimica et Cosmochimica Acta*, v. 70, p. 5698–5722, doi: 10.1016/j.gca.2006.08.021.
- Maloof, A.C., Porter, S.M., Moore, J.L., Dudás, F.Ö., Bowring, S.A., Higgins, J.A., Fike, D.A., and Eddy, M.P., 2010, The earliest Cambrian record of animals and ocean geochemical change: *Geological Society of America Bulletin*, v. 122, p. 1731-1774, doi: 10.1130/B30346.1.
- Martin, J.-M., and Meybeck, M., 1979, Elemental mass-balance of material carried by major world rivers: *Marine Chemistry*, v. 7. P. 173-206, doi:10.1016/0304-4203(79)90039-2.
- März, C., Poulton, S.W., Beckmann, B., Küster, K., Wagner, T., and Kasten, S., 2008, Redox sensitivity of P cycling during marine black shale formation: Dynamics of sulfidic and anoxic, non-sulfidic bottom waters: *Geochimica et Cosmochimica Acta*, v. 72, p. 3703–3717, doi: 10.1016/j.gca.2008.04.025.
- Moore, P.A., and Reddy, K.R., 1994, Role of Eh and pH on phosphorous geochemistry in sediments of lake Okeechobee, Florida: *Journal of Environmental Quality*, v. 23, p. 955-964.

- Olivarez, A.M., Owen, R.M., 1989. REE/Fe variations in hydrothermal sediments: Implications for the REE content of seawater. *Geochimica et Cosmochimica Acta*, v. 53, p. 757–762.
- Papineau, D., 2010, Global biogeochemical changes at both ends of the Proterozoic: Insights from phosphorites: *Astrobiology*, v. 10, p. 165–181, doi:10.1089/ast.2009.0360.
- Peng, Shanchi, and Babcock, L.E., 2011, Continuing progress on chronostratigraphic subdivision of the Cambrian System: *Bulletin of Geosciences*, doi: 10.3140/bull.geosci.1273.
- Peters, S.E., and Gaines, R.R., 2012, Formation of the ‘Great Unconformity’ as a trigger for the Cambrian explosion: *Nature*, v. 484, p. 363–366, doi:10.1038/nature10969.
- Planavsky, N.J., Rouxel, O.J., Bekker, A., Lalonde, S.V., Konhauser, K.O., Reinhard, C.T., and Lyons, T.W., 2010, The evolution of the marine phosphate reservoir: *Nature*, v. 467, p. 1088–1090, doi:10.1038/nature09485
- Porter, S.M., 2004a, Halkieriids in Middle Cambrian phosphatic limestones from Australia: *Journal of Paleontology*, v. 78, p. 574–590, doi: 10.1666/0022-3360(2004)078<0574:HIMCPL>2.0.CO;2.
- Porter, S.M., 2004b, Closing the phosphatization window: testing for the influence of taphonomic megabias on the pattern of small shelly fossil decline: *Palaios*, v. 19, p. 178–183, doi: 10.1669/0883-1351(2004)019<0178.
- Poulton, S.W. and Canfield, D.E., 2005, Development of a sequential extraction procedure for iron: implications for iron partitioning in continentally derived particulates: *Chemical Geology*, v. 214, p. 209–221, doi: 10.1016/j.chemgeo.2004.09.003.
- Poulton, S. W., and Canfield, D. E., 2006, Co-diagenesis of iron and phosphorus in hydrothermal sediments from the southern East Pacific rise: implications for the evaluation of paleoseawater phosphate concentrations: *Geochimica et Cosmochimica Acta*, v. 70, p. 5883–5898, doi: 10.1016/j.gca.2006.01.031.
- Poulton S. W. and Raiswell R, 2002, The low-temperature geochemical cycle of iron: from continental fluxes to marine sediment deposition: *American Journal of Science*, v. 302, p. 774–805, doi: 10.2475/ajs.302.9.774.
- Raiswell, R., Canfield, D.E., 1998, Sources of iron for pyrite formation in marine sediments: *American Journal of Science*, v. 298, p. 219–245, doi: 10.2475/ajs.298.3.219.

- Raiswell, R., Newton, R.J., and Wignall, P.B., 2001, An indicator of water-column anoxia: resolution of biofacies variations in the Kimmeridge Clay (Upper Jurassic, U.K.): *Journal of Sedimentary Research*, v. 71, p. 286–294, doi: 10.1306/070300710286.
- Redfield, A.C., 1958, The biological control of chemical factors in the environment: *American Scientist*, v. 64, p. 205-221.
- Riggs, S.R., 1986, Proterozoic and Cambrian phosphorites – specialist studies: phosphogenesis and its relationship to exploration for Proterozoic and Cambrian phosphorites: in Cook, P.J., and Shergold, J.H., eds., *Phosphate deposits of the world: Proterozoic and Cambrian phosphorites*, Volume 1: Cambridge, UK, Cambridge University Press, p. 352-368.
- Ruttenberg, K.C., 1992, Development of a sequential extraction method for different forms of phosphorus in marine sediments: *Limnology and Oceanography*, v. 37, p. 1460–1482, doi: 10.4319/lo.1992.37.7.1460.
- Ruttenberg, K.C., and Berner, R.A., 1993, Authigenic apatite formation and burial in sediments from non-upwelling, continental margin environments: *Geochimica et Cosmochimica Acta*, v. 57, p. 991-1007.
- Saltzman, M.R., 2005, Phosphorus, nitrogen, and the redox evolution of the Paleozoic oceans: *Geology* v. 33, p. 573–576, doi: 10.1130/G21535.1.
- Schuffert, J.D., Kastner, M., and Jahnke, R.A., 1998, Carbon and phosphorus burial associated with modern phosphorite formation: *Marine Geology*, v. 146, p. 21-31.
- Schuffert, J.D., Jahnke, R.A., Kastner, M., Leather, J., Sturz, A., and Wing, M.R., 1994, Rates of formation of modern phosphorite off western Mexico: *Geochimica et Cosmochimica Acta*, v. 58, p. 5001–5010, doi: 10.1016/0016-7037(94)90227-5.
- Scranton, M.I., McIntyre, M., Astor, Y., Taylor, G.T., Mueller-Karger, F., and Fanning, K., 2006, Temporal variability in the nutrient chemistry of the Cariaco Basin: in Neretin, L.N. (ed.), *Past and Present Water Column Anoxia*: Springer Berlin Heidelberg New York, p. 139-160.
- Severmann, S., Lyons, T.W., Anbar, A., McManus, J., and Gordon, G., 2008, Modern iron isotope perspective on the benthic iron shuttle and the redox evolution of ancient oceans: *Geology*, v. 36, p. 487-490, doi: 10.1130/G24670A.1.
- Severmann, S., McManus, J., Berelson, W.M., and Hammond, D.E., 2010, The continental shelf benthic iron flux and its isotopic composition: *Geochimica et Cosmochimica Acta*, v. 74, p. 3984-4004, doi: 10.1016/j.gca.2010.04.022.

- Shaffer, G., 1986, Phosphate pumps and shuttles in the Black Sea: *Nature*, v. 321, p. 515-517, doi:10.1038/321515a0.
- Shemesh, A., 1990, Crystallinity and diagenesis of sedimentary apatites: *Geochimica et Cosmochimica Acta*, v. 54, p. 2433-2438, doi: 10.1016/0016-7037(90)90230-I.
- Shen, Y., Schidlowski, M., and Chu, X., 2000, Biogeochemical approach to understanding phosphogenic events of the terminal Proterozoic to Cambrian: *Palaeogeography Palaeoclimatology Palaeoecology*, v. 158, p. 99–108, doi: 10.1016/S0031-0182(00)00033-X.
- Siever, R., 1992, The silica cycle in the Precambrian: *Geochimica et Cosmochimica Acta*, v. 56, p. 3265-3272, doi: 10.1016/0016-7037(92)90303-Z.
- Slomp, C.P., Epping, E.H.G., Helder, W., and Van Raaphorst, W., 1996, A key role for iron-bound phosphorus in authigenic apatite formation in North Atlantic continental platform sediments: *Journal of Marine Research*, v. 54, p. 1179-1205, doi: 10.1357/0022240963213745.
- Slomp C. P., Thomson J., and De Lange G. J., 2004, Controls on phosphorus regeneration and burial during formation of eastern Mediterranean sapropels: *Marine Geology*, v. 203, p. 141–159, doi: 10.1016/S0025-3227(03)00335-9.
- Southgate, P.N., 1988, A model for the development of phosphatic and calcareous lithofacies in the Middle Cambrian Thornton Limestone, northeast Georgina Basin, Australia: *Australian Journal of Earth Sciences*, v. 35, p. 111-130, doi: 10.1080/08120098808729443.
- Southgate, P.N., and Shergold, J.H., 1991, Application of sequence stratigraphic concepts to Middle Cambrian phosphogenesis, Georgina Basin, Australia: *Journal of Australian Geology and Geophysics*, v. 12, p. 119–144.
- Strickland, J.D.H., and Parsons, T.R., 1972, *A Practical Handbook of Seawater Analysis*: Fish Research Board of Canada.
- Swanson-Hysell, N.L., Rose, C.V., Calmet, C.C., Halverson, G.P., Hurtgen, M.T., and Maloof, A.C., 2010, Cryogenian glaciation and the onset of carbon-isotope decoupling: *Science*, v. 328, 608-611, doi:10.1126/science.1184508.
- Taylor, S.R., McLennan, S.M., 1985, *The Continental Crust: Its Composition and Evolution*: Blackwell Scientific, Boston, MA, U.S.A., 312 p..
- Trappe, J., 2001, A nomenclature system for granular phosphate rocks according to depositional texture: *Sedimentary Geology*, v. 145, p. 135–150, doi: 10.1016/S0037-0738(01)00103-8.

- Trefry, J.H., Metz, S., 1989. Role of hydrothermal precipitates in the geochemical cycling of vanadium: *Nature*, v. 342, p. 531–533, doi:10.1038/342531a0.
- Trocine, R.P., Trefry, J.H., 1988. Distribution and chemistry of suspended particles from an active hydrothermal vent site on the Mid-Atlantic Ridge at 26°N: *Earth and Planetary Science Letters*, v. 88, p. 1–15, doi:10.1016/0012-821X(88)90041-6.
- Tyrrell, T., 1999, The relative influences of nitrogen and phosphorus on oceanic primary production: *Nature* v. 400, p.525–531, doi:10.1038/22941.
- Van Cappellen, P., and Ingall, E.D., 1996, Redox stabilization of the atmosphere and oceans by phosphorus-limited marine productivity: *Science*, v. 271, p. 493-496, doi: 10.1126/science.271.5248.493.
- Vine, J.D., and Tourtelot, E.B., 1970, Geochemistry of black shale deposits; a summary report: *Economic Geology*, v. 65 no. 3 p. 253-272, doi: 10.2113/gsecongeo.65.3.253.
- Walter, M.R., Veevers, J.J., Calver, C.R., and Grey, K., 1995, Neoproterozoic stratigraphy of the Centralia Superbasin, Australia: *Precambrian Research*, v. 73, p. 173-195, doi: 10.1016/0301.9268(94)00077-5.
- Wang, X., Hu, W., Yao, S., Chen, Q., and Xie, X., 2011, Carbon and strontium isotopes and global correlation of Cambrian Series 2-Series 3 carbonate rocks in the Keping area of the northwestern Tarim Basin, NW China: *Marine and Petroleum Geology*, v. 28, p. 992-1002, doi:10.1016/j.marpetgeo.2011.01.006.
- Xiao, S. H. and Knoll, A. H., 1999, Fossil preservation in the Neoproterozoic Doushantuo phosphorite Lagerstätte, South China: *Lethaia*, v. 32, p. 219 – 240, doi:10.1111/j.1502-3931.1999.tb00541.x
- Xiao, S. and Knoll, A.H., 2000, Phosphatized animal embryos from the Neoproterozoic Doushantuo formation at Weng'an, Guizhou, south China: *Journal of Paleontology* v. 74, p. 767–788, doi:10.1666/0022-3360(2000)074,0767:PA EFTN.2.0.CO;2.
- Zegeye, A., Bonneville, S. Benning, L.G., Sturm, A., Fowle, D.A., Jones, C. Canfield, D.E., Ruby, C., MacLean, L.C, Nomosatryo, S., Crowe, S.A., and Poulton, S.W., Green rust formation controls nutrient availability in a ferruginous water column: *Geology*, v. 40, p. 599-602, doi:10.1130/G32959.1.
- Zhu, M.-Y., Zhang, J.-M., Li, G.-X., and Yang, A.-H., 2004, Evolution of C isotopes in the Cambrian of China: implications for Cambrian subdivision and trilobite mass extinctions: *Geobios*, v. 37, p. 287-301, doi: 10.1016/j.geobios.2003.06.001.

CHAPTER 3

TAPHONOMY OF PHOSPHATIC SMALL SHELLY FOSSILS: A CASE STUDY OF THE CAMBRIAN THORNTONIA LIMESTONE, SOUTHERN GEORGINA BASIN, AUSTRALIA

3.1 INTRODUCTION

Fossils record the history of life, but interpretation of this record depends in part on the nature of the preservational windows through which we view past organisms. Both the benefits and limitations of differing preservational modes are apparent for the Ediacaran and Cambrian periods, during which distinct and time-bounded taphonomic processes documented the initial diversification of animals (e.g., Butterfield, 2003). Drawing paleobiological conclusions from this record requires that we understand the biases imparted by specific taphonomic modes. To this end, we wish to know both the mechanisms by which fossilization occurred and the environmental or biological circumstances that opened and subsequently closed specific preservational windows.

In this paper, we ask what defines the Ediacaran–Cambrian taphonomic window for phosphate replication. To address this question, we examine one instance of skeletal fossil preservation from the Cambrian Series 2 Thornton Limestone, southern Georgina Basin, Australia (Southgate, 1988). Sequence stratigraphy places phosphatized fossils in physical environmental context, and geochemical analyses further

constrain both redox environment and sources of phosphate to sediments. With these in mind, petrographic observations allow us to develop a mechanistic understanding of skeletal replication by phosphate minerals. This, in turn, prompts us to ask which of the processes and circumstances necessary for phosphatization taphonomy vary through time in a pattern consistent with the temporal dimensions of the taphonomic window. Understanding the Ediacaran–Cambrian phosphate window will thus contribute to our understanding of both biological and environmental history. Moreover, insofar as phosphates constitute a critical and diminishing resource for fertilizers applied globally in agriculture, as well as a principal source of the rare Earth elements critical to 21st century technologies, there is practical benefit to understanding the circumstances under which phosphate deposition waxed and waned during the Ediacaran and Cambrian periods.

3.2 THE EDIACARAN–CAMBRIAN PHOSPHATIZATION WINDOW

Phosphatized microfossils occur sporadically in Proterozoic rocks, both marine (Edwards et al., 2012; Bengtson et al., 2009; Knoll and Vidal, 1980) and lacustrine (Battison and Brasier, 2012). The phosphatization taphonomic window, however, opens widely only during the middle of the Ediacaran Period, preserving a range of small, soft-bodied remains that includes multicellular algae (Zhang et al., 1998) and animal embryos (Xiao and Knoll, 1999; Hagadorn et al., 2006) or basal holozoans (Hultgren et al., 2011). Undisputed embryos occur relatively widely in lower Cambrian (Tommotian) deposits and sporadically in younger rocks up to the Lower Ordovician (Donoghue et al., 2006). Curiously, fossil embryos younger than Tommotian are limited to *Markeulia*, whose ‘precocious development of cuticle’ evidently predisposed it to phosphatic replication (Briggs, 2003; Butterfield, 2003; Donoghue et al., 2006,

p. 233). As such, the soft-tissue taphonomic window may reflect time-restricted biological factors, such as the innovation of tissue and/or shell material particularly amenable to phosphatization superimposed on geochemical conditions conducive to authigenic apatite precipitation. Cuticle also appears to have played a critical role in so-called ‘Örsten-style’ preservation, which provides a high-fidelity window into small arthropods and other invertebrates throughout the Cambrian Period (Maas and Waloszek, 2001; Waloszek, 2003; Maas et al., 2006).

In contrast, the phosphatization window for skeletonizing organisms opens with the first appearance of macroscopic skeletons in the late Ediacaran (Bengtson and Zhao, 1992), or possibly earlier (Cohen et al., 2011, Cohen and Knoll, 2012), and expands in the earliest Cambrian (Terreneuvian Series) with the radiation of skeleton-forming animals (e.g., Bengtson et al., 1990; Maloof et al., 2010). Porter (2004) examined the distribution of Cambrian phosphatic lithologies and the consequent taphonomic bias contributing to the pattern of small shelly fossil decline during this interval. These data indicate that phosphatic lithologies declined significantly through the period, from 75% of total taphonomic lithologies in the earliest Cambrian to a low of 40% through Cambrian Series 2–3.

The record of Furongian phosphorite and phosphatic carbonate is minor relative to earlier Cambrian deposits (Cook and Shergold, 1984). Moreover, with regard to the spatial dimensions of the phosphatization taphonomic window, Brasier and Callow (2007) report a secular change in the environment of phosphatization within a basin—from shallow marine, photic zone phosphatization in Ediacaran deposits towards outer shelf/slope environments of the later Phanerozoic. These authors report a concomitant change in the taxonomy of organisms preserved in these depositional environments, from photic zone flora/fauna in the Ediacaran to the earliest Cambrian, shifting to preservation of the exoskeletons of deeper-water organisms from the

middle Cambrian forward. Finally, they note a decline through time in the fidelity of phosphatic fossil preservation, from high quality cellular and sub-cellular preservation of the Ediacaran and earliest Cambrian towards low quality preservation in younger rocks.

3.3 PHOSPHATIC FOSSILS IN THE THORNTONIA LIMESTONE: STRATIGRAPHIC CONTEXT

The Cambrian Series 2–3 Thornton Limestone, southern Georgina Basin, hosts phosphorite and phosphatized skeletal (Porter, 2004b) and soft-bodied (Waloszek et al., 1993) fossils. Broadly, Southgate (1988) describes the Thornton Limestone as stacked shallowing-upward parasequences. We examined the Thornton Limestone within drill-core NTGS 99/1. In this locality, we find that the Thornton Limestone comprises three distinct carbonate lithologic units (consistent with brief descriptions by Dunbar et al., 2007).

Within NTGS 99/1, the Thornton Limestone sits atop Paleoproterozoic granitic basement. The lowermost Thornton unit (598.4–580.1 m) consists of dolomudstone and dolowackestone with pervasive structural dissolution textures. The medial Thornton unit consists of four interbedded lithofacies that occur within generally coarsening-upward meter- to sub-meter-scale packages (Fig. 1; 580.1–558.7 m). These lithofacies include black to medium grey carbonate mudstone and wackestone, bioclastic packstone and grainstone, and minor bioclastic grainstone. There is a broad up-core trend: packages initiate with progressively coarser lithologies and terminate with progressively thicker grainstone beds. A four-meter thick, vuggy, bioclastic dolopackstone comprises the upper Thornton unit (558.7–554.7).

Phosphorus speciation geochemistry of samples from NTGS 99/1 indicate that

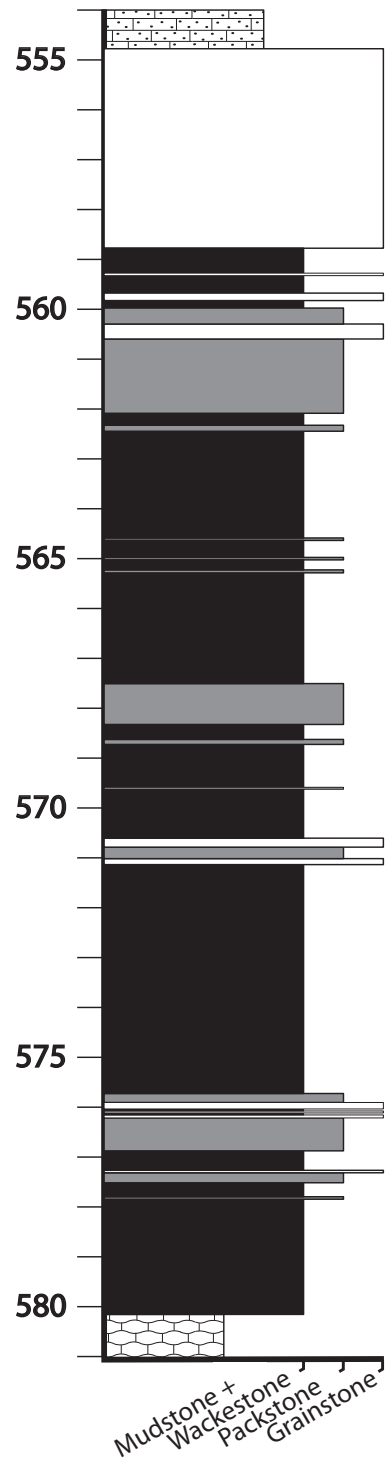


Figure 3.1: Generalized stratigraphic column of the middle and upper units of the Thornton Limestone from drillcore NTGS 99/1, southern Georgina Basin.

phosphorus ranges from 0–4 weight percent (wt.%), with values within the medial and upper units of the Thornton Limestone consistently above ~ 0.2 wt.%. Iron speciation geochemistry reveals that the Thornton has 1–2 wt.% total iron, and nearly 90% of this resides within the biogeochemically highly reactive phases pyrite and iron carbonate. Highly reactive iron enrichment requires anoxia. Thus, we interpret the phosphorus-rich Thornton carbonates to record deposition from anoxic subsurface water masses.

3.4 PETROGRAPHY OF SKELETAL FOSSIL PRESERVATION

Within the Thornton Formation, apatite occurs in four modes. First, lingulid brachiopods with impunctate shells of primary dahllite comprise a significant fraction of bioclasts. As this is not an early diagenetic phase, we do not discuss it further.

Second, within bioclastic wackestone and packstone, apatite occurs frequently as the internal molds (steinkerns) of ovoid, conical, and, rarely, campanulate or pentate small shelly fossils (Figs. 2 and 3a-i). Apatite may also occlude the small volume bound by concentric, nested shells, but never the central cavity of the organism (Fig. 2a, lower left, and 3j). Elemental analysis by scanning electron microscope energy-dispersive X-ray spectroscopy (SEM-EDX) supports the petrographic observation that apatite precipitation occurred only in focused microenvironments, specifically the interiors of small shelly fossils (Fig. 4a,c). Generally, apatite does not occur as a matrix phase or as cement surrounding grains (Fig. 4b). Petrographic observation also reveals that many skeletal elements were at least partially filled with micrite and finer-grained calcitic bioclasts prior to phosphatization; apatite nucleation occurred within this matrix and phosphate expanded locally at the expense of this pre-existing carbonate (Fig. 3a,d,h). When present, the enveloping carbonate

skeleton is preserved as a neomorphosed, drusy calcite spar (Fig. 3a-i).

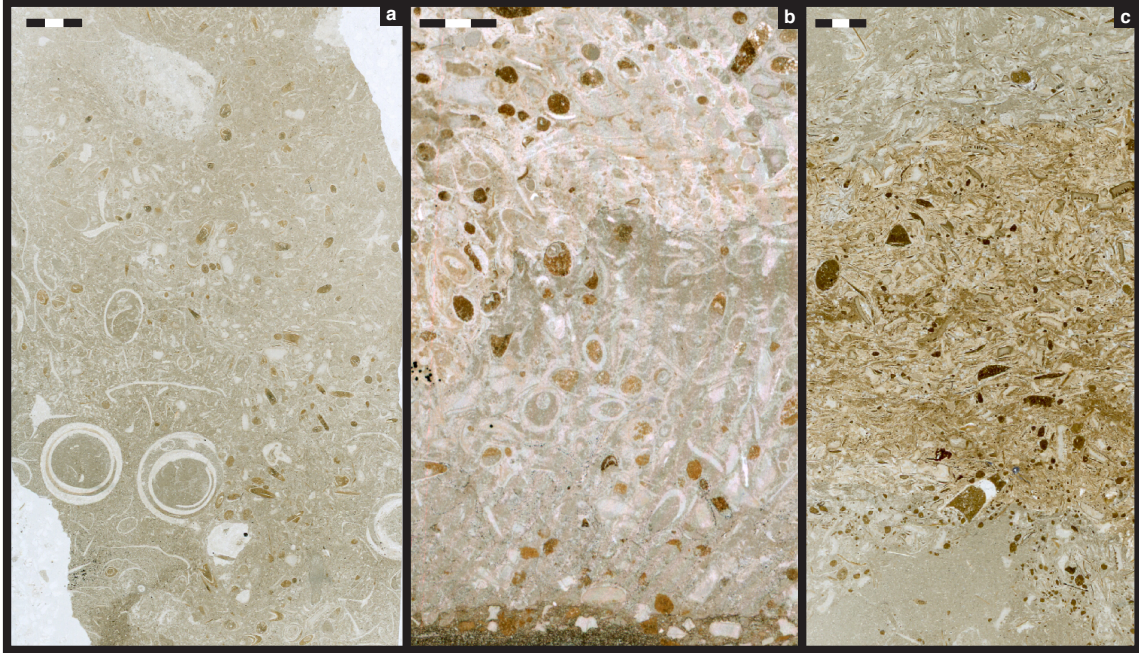


Figure 3.2: Photomicrographs of apatite distribution within lithologies of the middle Thornton Limestone. (A) NTGS 570.35 m, wackestone with apatite steinkerns of small skeletal fossils. (B) NTGS 570.5 m, packstone with apatite steinkerns and apatite cement (see upper third of thin-section). (C) NTGS 575.17 m, a grainstone with apatite cement. Scale bar in each frame is 3 mm.

The petrographic observation that steinkerns replace carbonate infill and entomb calcite bioclasts indicates that the skeletons were transported to their depositional site as bioclasts; soft tissue decay predated deposition and so cannot have provided a local source of phosphate. From skeletons displaying incomplete molding by apatite, we infer that phosphatization proceeded from the vertex towards the aperture of skeletons with conical morphologies, and from the exterior to the interior of spherical/oblate morphologies (Fig. 3b,c,f). The internal molding of skeletons occurred prior to any dissolution of the bounding skeleton, as evidenced by the sharp margins of steinkerns (Fig. 3c,f).

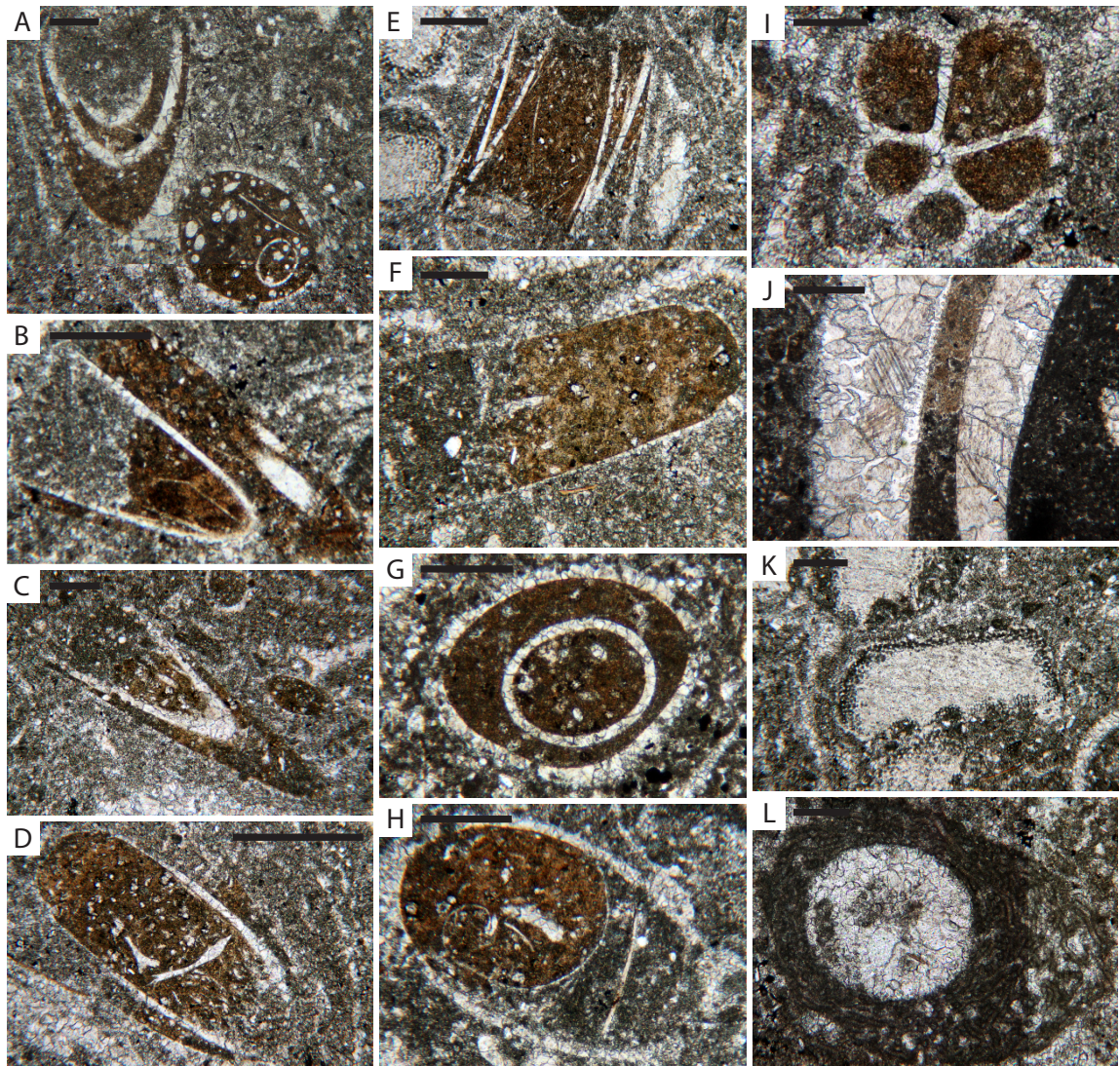


Figure 3.3: Photomicrographs of apatite steinkerns of small skeletal fossils from sample NTGS 99/1 570.35 m. Scale bar in each frame is 400 μ m.

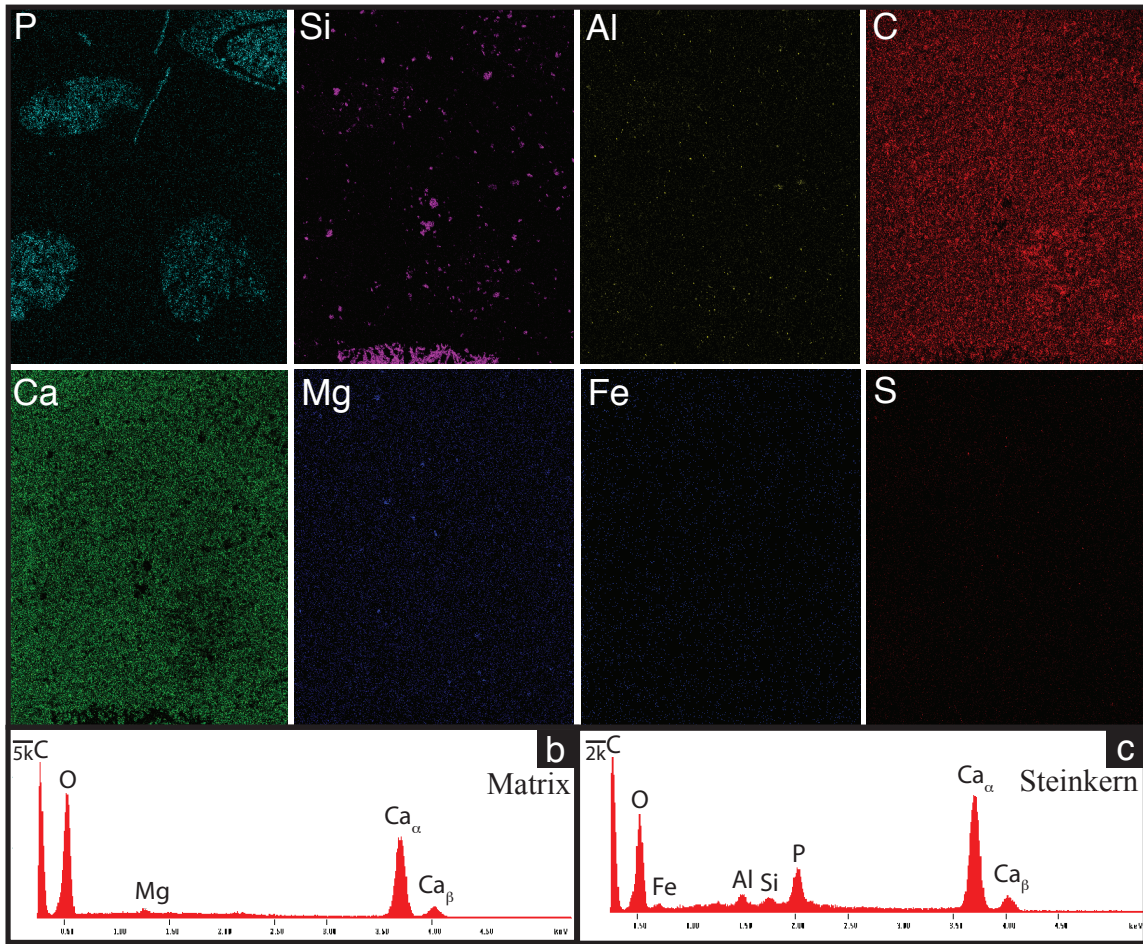


Figure 3.4: SEM-EDX analysis of NTGS 99/1 570.35 mcd, middle Thornton limestone (see Fig. 2a for petrographic character). (A) Elemental maps of phosphorus (P), silicon (Si), aluminum (Al), carbon (C), calcium (Ca), magnesium (Mg) iron (Fe) and sulfur (S). (B) Consistent with elemental maps, spot analysis indicates a pure carbonate matrix (note absence of P peak on this spectrum). (C) Spot analysis of a steinkern reveals large calcium and phosphorus peaks.

The retention of carbonate depositional textures in phosphatic steinkerns is consistent with localized apatite nucleation within the shell interior followed by carbonate dissolution along a front of expanding phosphate. Maliva and Siever (1988) showed how the force of crystallization in early diagenetic cherts would promote carbonate dissolution along the growth front, preserving textures even as mineralogy changed. Force of crystallization not only provides an explanation for observed petrographic textures within steinkerns, it could also source of calcium ions. Presumably, carbonate and phosphate anions would compete for liberated Ca^{2+} , with apatite forming preferentially because of its lower solubility. The skeletons themselves appear to have provided a relative impermeable barrier that both governed microenvironmental conditions favoring apatite precipitation and constrained the spatial expansion of authigenic phosphate minerals.

In rare instances, apatite occurs as a cryptocrystalline cement within bioclastic grainstone (Fig. 2b,c). Within these lithologies, echinoderm ossicles appear with greater abundance and, generally, with higher fidelity preservation (Fig. 5a); nevertheless, ossicles often display neomorphic microspar interiors with patches of phosphatization (Fig. 5b). Steinkerns of conical, ovate, and campanulate small shelly fossils appear less frequently than in packstone without apatite matrix or grainstone without apatite cement (Figs. 2c and 5c,d).

Finally, within mud-supported, suspension-deposited carbonate, apatite appears as sub-angular to sub-rounded coarse-silt to medium sand-sized grains, and as silt- and fine sand-sized, tabular and undulose grains within well-sorted laminae (Fig. 6). Due to the textural maturity and fine grain-size of these lithologies, it is difficult to determine definitively the origin of this phase. Tabular and undulose grains likely comprise lingulid brachiopod shell fragments. Likewise, rounded grains may comprise eroded and transported authigenic apatite, such as steinkern bioclasts and/or intra-

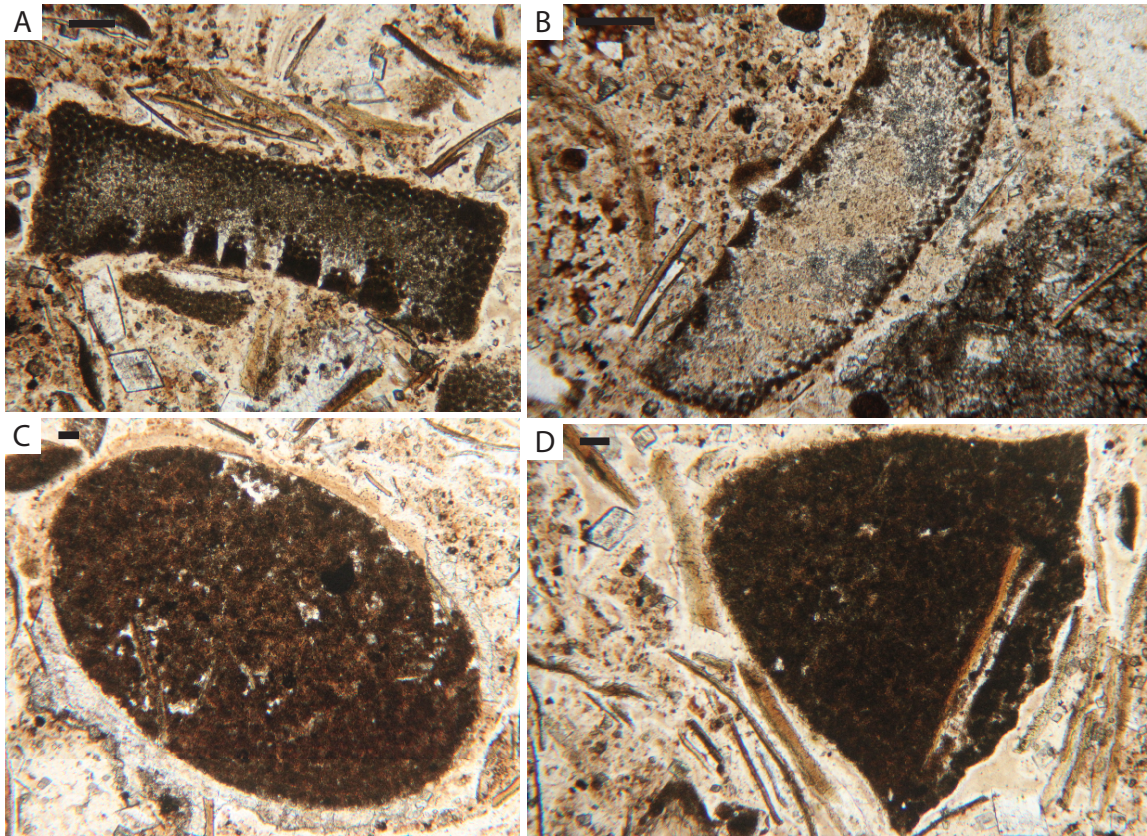


Figure 3.5: Photomicrographs of fossil preservation within apatite cement, sample NTGS 99/1 575.17 m. (A) Echinoid ossicle replaced by apatite. (B) Echinoid ossicle with neomorphosed carbonate spar in interior subsequently replaced by apatite cement. (C) Apatite steinkern of an ovate small skeletal fossil. (D) Apatite steinkern of a campanulate small skeletal fossil. Scale bar in each frame is 100 μm .

clasts of cement/hardgrounds. Alternatively, rounded grains may represent apatite of igneous or metamorphic origin derived from an influx of detrital siliciclastic sediment to the basin. However, we favor the former interpretation because we observe no comparable-size siliciclastic grains. For carbonate mud-supported lithologies, SEM-EDX elemental analysis confirms that phosphorus is a rare component of the matrix, and is (mostly) confined to these allocthonous, authigenic grains (Fig. 7).

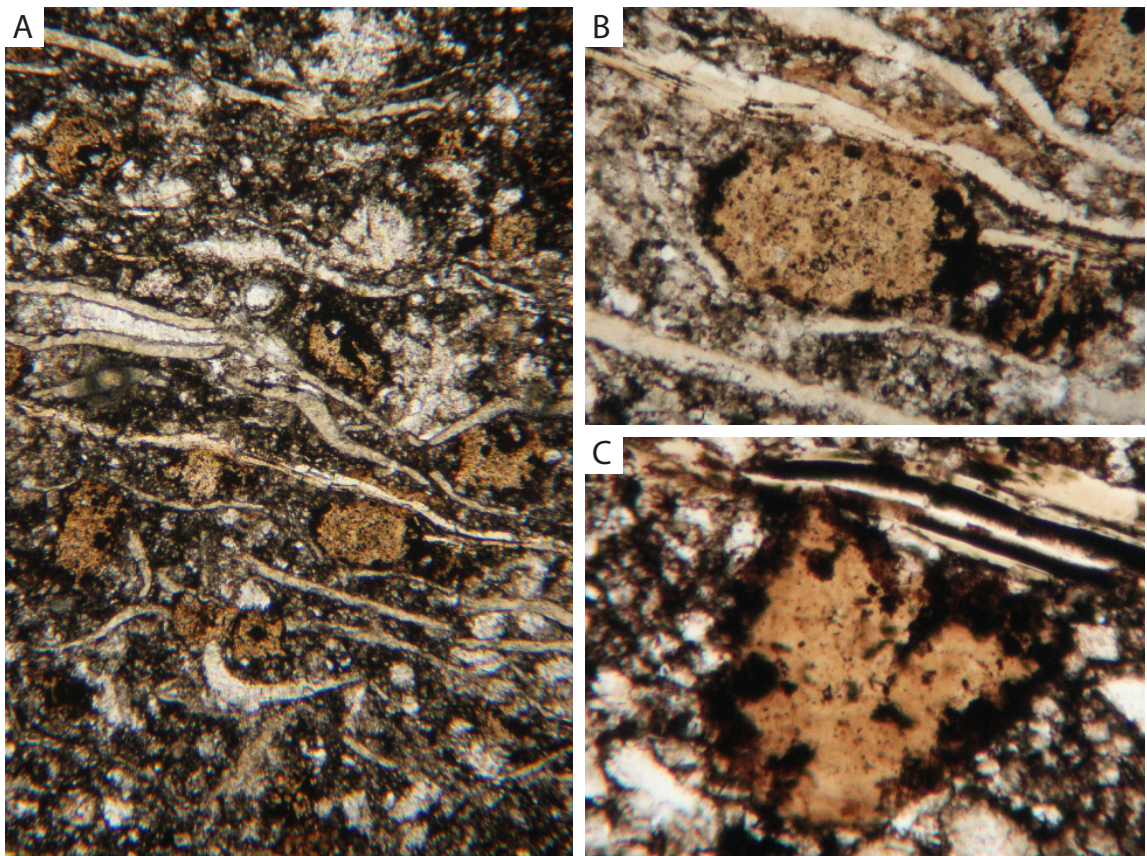


Figure 3.6: Photomicrographs of apatite distribution within wackestone of the middle Thornton Limestone sample NTGS 99/1 560.69 m.

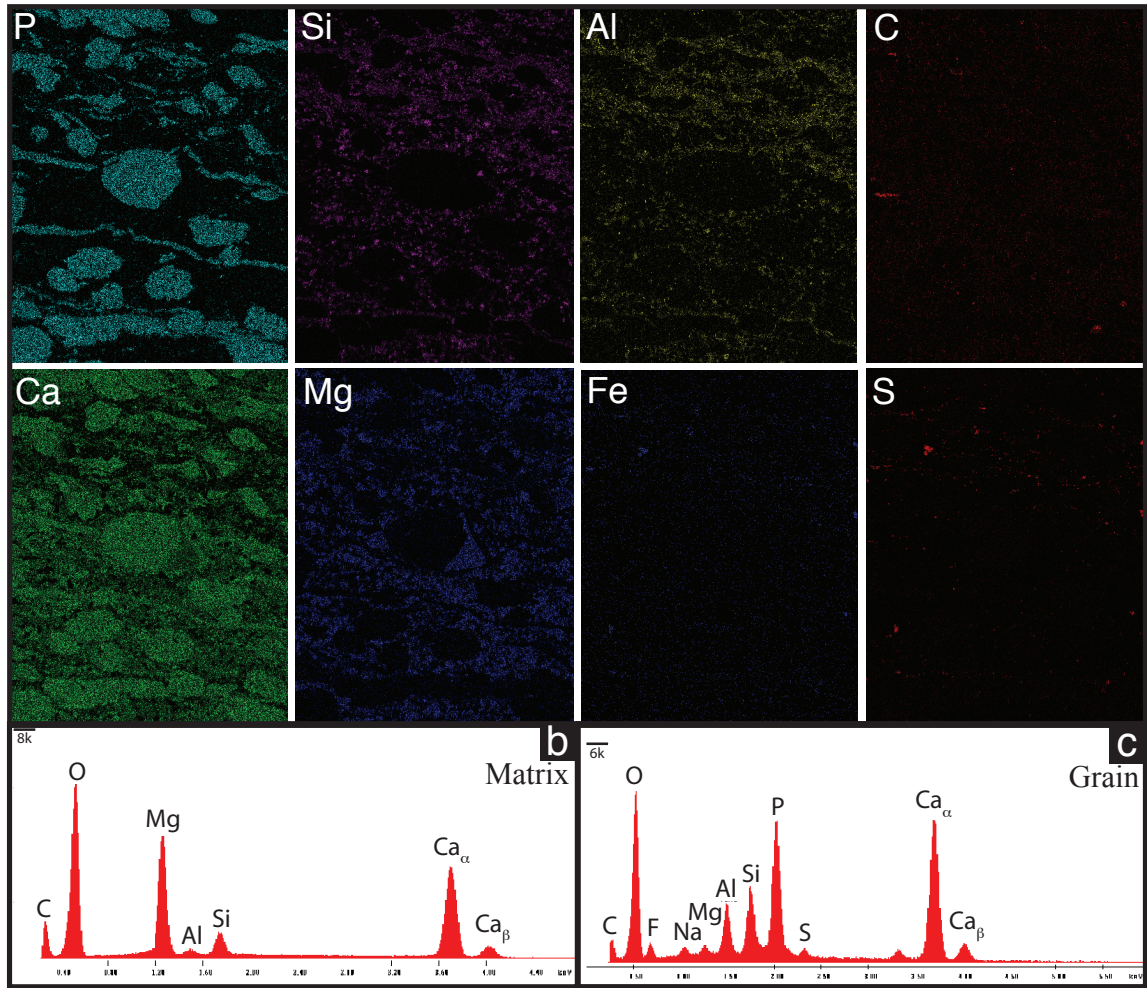


Figure 3.7: SEM-EDX analysis of 560.69 m, middle Thornton Limestone. (A) Elemental distribution (see caption for Fig. 4 for element symbols) of this sample reveals a dolomitic (Ca, Mg) and siliciclastic (Si, Al) matrix with grains of apatite (P, Ca) and minor pyrite (S). (B) Spot analysis of the matrix confirms this distribution, and emphasizes the absence of phosphorus. (C) Spot analysis of a constituent grain reveals large Ca and P peaks, consistent with apatite mineralogy, as well as an apparent close association between siliciclastic (Al, Si) and pyrite (S) minerals.

3.5 MECHANISTIC UNDERSTANDING OF SKELETAL FOSSIL PRESERVATION

Three circumstances were necessary for Thorntonite steinkerns to form: a source of phosphate, remobilization of phosphate within sediment pore-waters, and the localized reprecipitation of apatite within skeleton interiors.

At the most fundamental level, phosphatization requires a sufficient quantity of phosphorus for apatite replication of biological remains. What was the source of phosphorus for this instance of phosphatization taphonomy? In a previous study, we used iron-speciation and trace element geochemistry to constrain the sources of phosphate to Thorntonite sediments (see Chap. 2). We compared the preserved organic carbon quantity within these sediments to the quantity of organic matter predicted to source the observed phosphorus if that organic matter were delivered with a Redfield stoichiometry. From these calculations, we concluded that organic matter degradation alone could not provide sufficient phosphorus for the observed apatite enrichment in the Thorntonite Limestone. Based on iron geochemical data from the Thorntonite Limestone, we concluded that phosphorus deposition occurred during times of anoxic, ferruginous conditions in subsurface water masses, suggesting that phosphorus adsorption to iron minerals precipitating from the water column provided an additional source of phosphorus to the seafloor. Our calculations indicate that, under a redox regime in which the iron cycle operates with an extensive benthic flux of Fe^{2+} to the water column, phosphorus bound to iron minerals could have provided a significant source for phosphatic carbonate of the Thorntonite Limestone.

For two reasons, we conclude that phosphorus sourced from the oxidation of the soft tissue of skeletonizing organisms could not provide sufficient phosphorus for steinkern precipitation. First, specific to the Thorntonite Limestone, the observation that bioclastic carbonate sediment filled conical/ovate skeletons prior to phosphatiza-

tion requires soft-tissue remineralization and loss of associated phosphate ions. Second, in regard to mass-balance constraints for phosphatization, in order for apatite to replace a volume previously occupied by organic matter, the amount of phosphorus within both phases must be similar. However, both the mass fraction of phosphorus (f_P) within apatite ($\text{Ca}_{10}(\text{PO}_4)_5(\text{CO}_3)\text{F}$) and the density (ρ) of apatite exceed those of organic matter with a Redfield stoichiometry ($\text{C}_{106}\text{H}_{212}\text{O}_{106}\text{N}_{16}\text{P}$):

$$f_{P,\text{apatite}}(\rho_{\text{apatite}} \times \nu) \gg f_{P,\text{orgC}}(\rho_{\text{orgC}} \times \nu), \quad (3.1)$$

where ν represents the volume surrounded by a skeleton. Thus, to precipitate a steinkern of pure apatite composition, an additional source of phosphorus must augment that derived from the organic tissue of that organism. We note, however, that imperfections in the apatite lattice and/or micro-scale secondary mineral phases (such as a carbonate) would decrease the amount of phosphorus necessary for apatite steinkern development. Despite this, the large difference between the mass fractions of phosphorus in apatite versus organic matter ($\sim 16\%$ versus $\sim 0.9\%$, respectively) suggests that such secondary mineral phases would be a dominant component of the steinkern mineralogy, and, therefore, visible by petrography.

A corollary to this conclusion is that phosphate must have occurred as a mobile phase, which is in turn consistent with the rare observation of apatite precipitation in the matrix of grainstones (Fig. 2). We return to this issue later in the text.

Regardless of whether phosphate entered the Thornton sediments bound to organic matter or adsorbed/co-precipitated with iron oxides, petrological observation makes it clear that phosphorus is no longer associated with these delivery phases, but rather has been redistributed to local microenvironments within the sediment column. Thus, a full description of phosphatization taphonomy requires not simply

an explanation for a sufficient delivery source, but also a mechanism to decouple phosphorus ions from these delivery shuttles.

Redistribution would be unlikely in oxic porewaters. Phosphate would remain bound to iron oxides, and although PO_4^{3-} would be liberated during aerobic respiration, this metabolism would act to decrease pH, increasing apatite solubility (Moore and Reddy, 1994). In this regard, the anaerobic remineralization of organic carbon provides a more likely mechanism for remobilization of both organic- and iron-bound phosphorus. Anaerobic remineralization can liberate phosphorus bound to the electron acceptor, iron-phosphorus minerals, either directly through dissimilatory iron reduction, or indirectly, if pore-water anoxia facilitates the abiotic reductive dissolution of Fe^{3+} . Although complementary, one release mechanism links phosphorus to a redox-active reductant (organic matter), whereas the other vector is an available oxidant (Fe^{3+}) for heterotrophy or inorganic reactions.

We note that authigenic apatite frequently occurs in association with organic-rich limestone and fine-grained siliciclastic lithologies (e.g., Dornbos et al., 2006; Föllmi et al., 2005; März et al., 2008). While this observation is usually discussed in terms a phosphorus source for phosphogenesis, mass balance constraints indicate that weight percent phosphorus enrichments require hundred-fold more organic carbon if this phosphorus derived originally from organic matter with a (near) Redfield stoichiometry. Indeed, for phosphatic lithologies with $\text{C}_{\text{org}}:\text{P}$ values at or below the Redfield ratio (e.g., Föllmi et al., 2005; Chap. 2), including the Thornton Limestone, a second source of phosphorus was necessary to augment organic-bound phosphorus. Thus, we suggest that the significance of the association of phosphatic lithologies with high organic carbon content lies in the role that organic matter remineralization played in governing the sedimentary redox environment that facilitates phosphorus remobilization from delivery shuttles.

Nevertheless, while ample phosphorus delivery to the seafloor and a mechanism for remobilization from these shuttles are both necessary, they are insufficient to explain the incidence of phosphatic skeletal preservation. We turn again to petrographic observations of preservation that show the close spatial association of authigenic phosphate with the interiors of (mainly) conical small shelly fossils. To fully address the phosphatic preservation of *Thorntonia* fossils, we must ask: what factors predispose the interior of SSFs to targeted apatite precipitation?

Mineral precipitation involves both pore-water saturation with respect to apatite and favorable kinetics for nucleation. In this regard, understanding why marine phosphate minerals precipitate requires that we fully constrain the relative budgets of calcium, phosphorus, and fluorine ions; carbonate alkalinity; and the pH of pore-water environments (Jahnke et al., 1983; Froelich et al., 1988). These factors can be difficult to ascertain in modern phosphogenic environments, and thus determining them in ancient samples, where diagenesis may have obscured primary geochemical signals, proves challenging. Nevertheless, a combination of petrographic observations and geochemical data provide clues to these variables.

Iron geochemistry and trace element systematics of the *Thorntonia* Limestone indicate deposition under an anoxic, ferruginous water column (Chap. 2). Therefore, within the anoxic sediment of the *Thorntonia* Limestone, anaerobic respiration would have freed phosphorus from organic matter, and iron respiration in particular would have reduced the iron minerals on which phosphorus was adsorbed. Thus, remobilization of phosphorus within the sediment column presents no difficulties. Apatite precipitation, in turn, would depend on apatite solubility, which, in anoxic environments, is a function of $[\text{Ca}^{2+}]$ and pH (Moore and Reddy, 1994).

Petrography aids in the identification of the source of calcium for apatite precipitation. In the case of small shelly fossil preservation in the *Thorntonia* Limestone,

we propose that Ca^{2+} derives from the dissolution of a previously infilling micritic matrix. Whatever their proximal sources, the required calcium and phosphate ion loads were available, and thus the pore-waters of the *Thorntonia* were poised for apatite precipitation. What, then, dictated the spatial specificity of mineral nucleation within the cavities defined by skeletons?

If not limited by ion availability, perhaps then the micro-environment within and in the proximity of bioclasts may have circumvented typical kinetic barriers to apatite nucleation. For instance, by stagnating fluid flow, ion advection and/or diffusion, these sites could have maintained carbonate phosphate mineral saturation over the time necessary for mineral nucleation. In support of this argument, the maximum diameter of apatite steinkerns is about 2-3 mm; this size is comparable to the maximum size noted for Örsten-style preservation of the carapace of micro-arthropods (Butterfield, 2003). We also note that while phosphatization is absent from the central cavity of larger-sized shells (Fig. 2a), it is often present in the smaller volume bounded by concentric shell-structures (Fig. 3j). The hypothesis for a regulated micro-environment does not dismiss the need for the ion activity product to favor saturation, but rather acknowledges the fact that kinetic factors, not simply saturation states, dictate apatite mineral precipitation. Such a mechanism could also operate over a larger spatial-scale of fluid flow stagnation, accounting for the instances when apatite is observed to have nucleated as the cement within high porosity bioclastic lithologies (Fig. 2b,c). If, indeed, phosphatization occurred as the force of crystallization dissolved proximal carbonate ions (*sensu* Maliva and Siever, 1988), this mechanism provides a positive feedback on apatite nucleation, with dissolving carbonate providing a local source of calcium ions.

3.6 DIMENSIONS OF THE EDIACARAN–CAMBRIAN PHOSPHATIZATION TAPHONOMIC WINDOW

Research on *Thorntonia* materials indicates that three factors were necessary for the formation of phosphatic fossils: (1) delivery of phosphorus to the sediment column through a combination of organic- and iron-bound shuttles, (2) remobilization of phosphorus from these delivery shuttles via microbial metabolic pathways in anoxic porewaters, and (3) re-precipitation of the phosphorus as apatite in small-scale, discrete geochemical environments, predominantly defined by the remains of small skeletal fossils. Conditions 1 and 2 should apply more generally to phosphatic preservation. The specific circumstances of reprecipitation will, of course, vary depending on whether the fossils are steinkerns, phosphatic replicates precipitated on an organic template, or skeletal replacements. We evaluate each of these three factors in light of the limited temporal duration, and varying spatial distribution, of the phosphatization taphonomic window.

If one supposes that a conical to tubular small skeletal fossil—in contrast to larger shells—provides the physical environment that facilitates apatite precipitation, then one might conclude that the presence of these organisms helps to define the boundaries of the phosphatization taphonomic window. That is, while phosphate minerals are necessary to preserve small skeletal fossils, small skeletal fossils may themselves facilitate the nucleation of phosphate minerals. Following this logic, if the average size of conical to tubular skeletons increased through the Phanerozoic Eon, then one might expect the formation of phosphatic steinkerns to decline through time. Shell size in mollusks, brachiopods and conical problematica increased from the Cambrian to the Ordovician (and beyond; Finnegan and Droser, 2008; Novack-Gottshall, 2008), but small skeletons continued to form and accumulate in sediments. If skeletal size

were the only variable dictating the dimensions of the phosphatization taphonomic window, then this might predict that the window should shift through time towards preservation of small or juvenile morphologies, rather than disappearing entirely.

We next turn to the possibility that a change in the efficiency of phosphorus remobilization was key to controlling the phosphatization taphonomic window. As discussed above, anoxia is a necessary precondition for remobilizing phosphorus from both organic matter and iron-minerals. This cannot, however, explain why phosphatization is uncommon in pre-Ediacaran sedimentary rocks that routinely accumulated in anoxic environments (e.g., Holland, 2006). The Ediacaran–Cambrian phosphatization window appears to open widely as pO_2 increases (e.g., Canfield et al., 2008; Fike et al., 2008; Scott et al., 2008; Johnston et al., 2011), perhaps indicating a somewhat different phosphate chemistry from the low-oxygen world of the Proterozoic Eon (Laakso and Schrag, *in review*). Bioturbation has been invoked to explain the cessation of Burgess Shale-type preservation (Orr et al., 2003), and increasing sediment irrigation could contribute to the spatial and temporal patterns of phosphate mineralization observed in Cambrian rocks (Brasier and Callow, 2007). A general Paleozoic increase in pO_2 (Bergmann et al., 2004; Berner, 2006; Dahl et al., 2010) might also have contributed to a shuttering of the phosphatization window, but the continual recurrence of anoxic, organic-rich shales in Paleozoic and Mesozoic basins argues that by itself, this would not explain observed patterns of phosphatization. This is not to discount the possibility that Cambrian oxidation drove the closure of the phosphatization taphonomic window. Indeed, this connection is supported by the observation that phosphatization taphonomy progressed into deeper-water environments since shallow-shelf environments would have been the first to become sufficiently oxygenated to preclude phosphorus remobilization.

Finally, delivery mechanisms may have played an important role in the opening

and closure of the Ediacaran–Cambrian phosphatization window. The geologic record indicates that high fluxes of organic carbon into sediments began in the Archean (e.g., Hayes and Waldbauer, 2006) and continued well after the Cambrian Period. Therefore, one cannot appeal to variations in organic matter delivery through time as an explanation for the temporal bounds of the phosphatization window. In contrast, the delivery of phosphorus adsorbed onto and co-precipitated with iron minerals depends on the redox state of subsurface water masses. Perhaps, then, the closure of the taphonomic window can be understood, as in the case of remineralization above, as a consequence of the increased oxidation of the ocean–atmosphere system, including the build-up of marine sulfate levels (Canfield and Farquhar, 2011) that helped to change anoxic water masses from ferruginous to sulfidic.

The nature of organisms, both skeleton-forming and burrowing invertebrates, may thus have contributed to the closure of the Ediacaran–Cambrian phosphatization window, as did a transition in the distribution and chemical nature of anoxic water masses and pore waters. How the window opened, however, is another matter. A hypothesized return to anoxic, ferruginous conditions in the Neoproterozoic–Cambrian (Canfield et al., 2008; Papineau, 2010) provides one explanation for the opening of the taphonomic window because it allows for iron-bound phosphorus delivery at a time when geochemical and biological conditions favored retention of this phosphorus within the sediment column. However, more recent observations suggest that the Earth system was subject to intermittent episodes of anoxic, ferruginous conditions prior to the Neoproterozoic and Cambrian (Johnston et al., 2010; Kendall et al., 2010, Poulton et al., 2010). These episodes are not consistent with the Ediacaran onset of the phosphatization taphonomic window. Instead, the opening of the taphonomic window may reflect the overcoming of an insufficient source of phosphorus rather than the onset of an intermittent mechanism to shuttle phosphorus from that source

to the seafloor. One possibility in this regard is that throughout the Proterozoic phosphorus was sequestered in fluvial environments until oxygenation became sufficient to deliver phosphate into open marine environments (Laakso and Schrag, *in review*).

3.7 CONCLUSIONS

Petrology makes clear that not all small shelly fossils were equally likely to fossilize by steinkern formation; conical fossils are commonly filled by phosphatic steinkerns while other skeletons remain phosphate mineral-free. Thus, phosphatization appears to impart a selectivity to fossil preservation, complicating efforts to understand patterns of diversity, biomass distribution or ecological organization in the Thornton Limestone.

We posit that an anoxic, ferruginous redox regime sets the probability space for the occurrence of the Cambrian phosphatization pathways, but that the alignment of a number of additional levers—from biological shell-size to pore-water saturation state—dictates the instantiation of individual occurrences of phosphatic preservation.

The delineation of both morphological biases and spatio-temporally restrictive geochemical regimes in phosphatization taphonomic processes places important constraints on evolutionary biological conclusions drawn from the phosphatic fossil record of Cambrian skeletal organisms.

3.8 REFERENCES CITED

- Battison, L. and Brasier, M. D., 2012, Remarkably preserved prokaryote and eukaryote microfossils within 1 Ga-old lake phosphates of the Torridon Group, NW Scotland: *Precambrian Research*, v. 196, p. 204-217, doi: 10.1016/j.precamres.2011.12.012.
- Bengtson, S., and Zhao, Y., 1992, Predatorial borings in late Precambrian mineralized exoskeletons: *Science*, v. 257, p. 367-369, doi:10.1126/science.257.5068.367.
- Bengtson, S., Belivanova, V., Rasmussen, B., and Whitehouse, M., 2009, The controversial "Cambrian" fossils of the Vindhyan are real but more than a billion years older: *Proceedings of the National Academy of Sciences*, v. 106, p. 7729-7734, doi: 10.1073/pnas.0812460106.
- Bengtson, S., Conway Morris, S., Cooper, B. J., Jell, P. A. & Runnegar, B. N, 1990, Early Cambrian fossils from South Australia: *Memoirs of the Association of Australian Palaeontologists*, v. 9, p. 1-364.
- Bergman, N.M., Lenton, T.M., and Watson, A.J., 2004, COPSE: A new model of biogeochemical cycling over Phanerozoic time: *American Journal of Science*, v. 304, p. 397-437, doi: 10.2475/ajs.304.5.397.
- Berner, R.A., 2006, GEOCARBSULF: A combined model for Phanerozoic atmospheric O₂ and CO₂: *Geochimica et a Cosmochimica Acta*, v. 70, p. 5653-5664, doi: 10.1016/j.gca.2005.11.032.
- Brasier, M.D. and Callow, R.H.T., 2007, Changes in the Patterns of Phosphatic Preservation across the Proterozoic-Cambrian Transition: *Memoirs of the Association of Australasian Palaeontologists*, No. 34, p. 377-389.
- Briggs, D.E.G., 2003, The role of decay and mineralization in the preservation of soft-bodied fossils: *Annual Review of Earth and Planetary Science*, v. 31, p. 275-301.
- Butterfield, N.J., 2003, Exceptional fossil preservation and the Cambrian Explosion: *Integrative and Comparative Biology*, v. 43, p. 166-177.
- Canfield, D.E., and Farquhar, J., 2011, Animal evolution, bioturbation, and the sulfate concentrations of the oceans: *Proceedings of the National Academy of Sciences*, v. 106, p. 8123-8127.

- Canfield, D.E., Poulton, S.W., Knoll, A.H., Narbonne, G.M., Ross, G., Goldberg, T., and Strauss, H., 2008, Ferruginous conditions dominated later Neoproterozoic deep-water chemistry: *Science*, v. 321, p. 949-952, doi: 10.1126/science.1154499.
- Cohen, P.A., Schopf, W., Butterfield, N.J., Kudryavtsev, A., and Macdonald, F.A., 2011, Phosphate biomineralization in mid-Neoproterozoic protists: *Geology*, v. 39, p. 539-542.
- Cohen, P.A., and Knoll, A.H., in press, Expanded diversity of scale microfossils from the mid Neoproterozoic Fifteenmile Group, Yukon: *Journal of Paleontology*.
- Cook, P and Shergold, J.H., 1984, Phosphorus, phosphorites and skeletal evolution at the Precambrian–Cambrian boundary: *Nature* v.10, p. 231–236..
- Dahl, T.W., Hammarlund, E.U., Anbar, A.D., Bond, D.P.G., Gill, B.C., Gordon, G.W., Knoll, A.H., Nielsen, A.T., Schovsbo, N.H., Canfield, D.E., 2010, Devonian rise in atmospheric oxygen correlated to the radiations of terrestrial plants and large predatory fish, v. 107, p. 17911-17915, doi: 10.1073/pnas.1011287107.
- Donoghue, P.C.J., Kouchinsky, A., Waloszek, D., Bengtson, S., Dong, X-P., Val'kov, A.K., Cunningham, J.A., and Repetski, J.E., 2006, Fossilized embryos are widespread but the record is temporally and taxonomically biased: *Evolution and Development*, v. 8, p., 232-238.
- Dornbos, S.Q., Botjer, D.J., Chen, J.-Y., Gao, F., Oliveri, P., and Li, C.-W., 2006, Environmental controls on the taphonomy of phosphatized animals and animal embryos from the Neoproterozoic Doushantuo Formation, southwest China: *Palaios*, v. 21, p. 3-14.
- Dunster, J.N., Kruse, P.D., Duffett, M.L., and Ambrose, G.J., 2007, Geology and resource potential of the southern Georgina Basin: Northern Territory Geological Survey, Digital Information Package DIP007.
- Edwards, C.T., Pufahl, P.K., Hiatt, E.E., Kyser, T.K., 2012, Paleoenvironmental and taphonomic controls on the occurrence of Paleoproterozoic microbial communities in the 1.88 Ga Ferriman Group, Labrador Trough, Canada: *Precambrian Research*, v. 212-213, p. 91-106, doi: 10.1016/j.precamres.2012.04.020.
- Fike, D.A., and Grotziner, J.P., 2008, A paired sulfate–pyrite $\delta^{34}\text{S}$ approach to understanding the evolution of the Ediacaran–Cambrian sulfur cycle: *Geochimica et Cosmochimica Acta*, v. 72, p. 2636–2648.

- Finnegan, S. and Droser, M.L., 2008, Body size, energetics, and the Ordovician restructuring of marine ecosystems: *Paleobiology*, v. 34, p. 342-359, doi: 10.1666/07074.1.
- Föllmi, K.B., Badertscher, C., de Kaenel, E., Stille, P., John, C.M., Adatte, T., and Steinmann, P., 2005, Phosphogenesis and organic-carbon preservation in the Miocene Monterey Formation at Naples Beach, California—The Monterey hypothesis revisited: *Geological Society of America Bulletin*, v. 117, p. 589-619.
- Froelich, P.N., Arthur, M.A., Burnett, W.C., Deakin, M., Hensley, V., Jahnke, R., Kaul, L., Kim, K.-H., Roe, K., Soutar, A., Vathakanon, C., 1988, Early diagenesis of organic matter in Peru continental margin sediments: Phosphorite precipitation: *Marine Geology*, v. 80, p. 309-343.
- Hagadorn, J.W., Xiao, S., Donoghue, P.C.J., Bengtson, S., Gostling, N.J., Pawlowska, M., Raff, E.C., Raff, R.A., Turner, F.R., Chongyu, Y., Zhou, C., Yan, X., McFeely, M.B., Stampanoni, M., and Nealson, K.H., 2006, Cellular and subcellular structure of Neoproterozoic animal embryos: *Science*, v. 314. P. 291-294, doi: 10.1126/science.1133129.
- Hayes, J.M. and Waldbauer, J.R., The carbon cycle and associated redox processes through time: *Philosophical transactions of the Royal Society B*, v. 361, p. 931-950.
- Holland, H.D., 2006, The oxygenation of the atmosphere and oceans: *Philosophical transactions of the Royal Society B*, v. 361, p. 903-915.
- Huldtgren, T., Cunningham, J.A., Yin, C., Stampanoni, M., Marone, F., Donoghue, P.C.J., and Bengtson, S., 2011, Fossilized Nuclei and Germination Structures Identify Ediacaran "Animal Embryos" as Encysting Protists: *Science*, v. 334, p.1696-1699, doi: 10.1126/science.1209537.
- Jahnke, R. A., Emerson, S.R., Roe, K.K., and Burnett, W.C., 1983, The present day formation of apatite in Mexican continental margin sediments: *Geochimica et Cosmochimica Acta*, v. 47, p. 259-266.
- Johnston, D.T., Poulton, S.W., Dehler, C., Porter, S., Husson, J., Canfield, D.E., and Knoll, A.H., 2010, An emerging picture of Neoproterozoic ocean chemistry: Insights from the Chuar Group, Grand Canyon, USA: *Earth and Planetary Science Letters*, v. 290, p. 64-73.
- Kendall, B., Reinhard, C.T., Lyons, T.W., Kaufman, A.J., Poulton, S.W., and Anbar, A., 2010, Pervasive oxygenation along late Archaean ocean margins: *Nature Geoscience*, v. 3, p. 647-652.

- Knoll, A.H., and Vidal, G., 1980, Late Proterozoic vase-shaped microfossils from the Visingsö Beds, Sweden: *Geologiska Foreningens i Stockholm Forhandlingar*, v. 102, p. 207-211.
- Laakso, T.A., and Schrag, D.P., in review, Regulation of atmospheric oxygen during the Proterozoic: *Proceedings of the National Academy of Sciences*.
- Maliva, R.G., and Siever, R., 1988, Diagenetic replacement controlled by force of crystallization: *Geology*, v. 16, p. 688-691.
- Maloof, A.C., Porter, S.M., Moore, J.L., Dudás, F.Ö., Bowring, S.A., Higgins, J.M., Fike, D.A., Eddy, M.P., 2010. The earliest Cambrian record of animals and ocean geochemical change. *Geological Society of America* 122, 1731–1774.
- März, C., Poulton, S.W., Beckmann, B., Küster, K., Wagner, T., and Kasten, S., 2008, Redox sensitivity of P cycling during marine black shale formation: Dynamics of sulfidic and anoxic, non-sulfidic bottom waters: *Geochimica et Cosmochimica Acta*, v. 72, p. 3703–3717.
- Maas, A. and Waloszek, D., 2001, Cambrian derivatives of the early arthropod stem lineage, pentastomids, tardigrades and lobopodians—an ‘Orsten’ perspective: *Zoologischer Anzeiger*, v. 240, p. 451–459.
- Maas A., Braun A., Dong X.-P., Donoghue P.C.J., Müller K.J., Olempska, E., Repetski, J.E., Siveter, D.J., Stein, M., and Waloszek, D., 2006, The ‘Orsten’—More than a Cambrian Konservat-Lagerstätte yielding exceptional preservation: *Palaeoworld*, v. 15, p. 266–282.
- Moore, P.A, and Reddy, K.R., 1994, Role of Eh and pH on phosphorous geochemistry in sediments of lake Okeechobee, Florida: *Journal of Environmental Quality*, v. 23, p. 955-964.
- Novack-Gottshall, P.M., 2008, Ecosystem-wide body-size trends in Cambrian-Devonian marine invertebrate lineages: *Paleobiology*, v. 34, p. 210-228, doi: 10.1666/0094-8373(2008)034[0210:EBTICM]2.0.CO;2.
- Orr, P.J., Benton, M.J., and Briggs, D.E.G., 2003, Post-Cambrian closure of the deep-water slope-basin taphonomic window: *Geology*, v. 31, p. 769-772.
- Porter, S.M., 2004a, Closing the phosphatization window: testing for the influence of taphonomic megabias on the pattern of small shelly fossil decline: *Palaios*, v. 19, p. 178–183.

- Porter, S.M., 2004b, Halkieriids in Middle Cambrian phosphatic limestones from Australia: *Journal of Paleontology*, v. 78, p. 574-590.
- Poulton, S.W., Fralick, P.W., and Canfield, D.E., 2010, Spatial variability in oceanic redox structure 1.8 billion years ago: *Nature Geoscience*, v. 3, p. 486-490.
- Scott, C., Lyons, T.W., Bekker, A., Shen, Y., Poulton, S.W., Chu, X., and Anbar, A.D., 2008, Tracing the stepwise oxidation of the Proterozoic ocean: *Nature*, v. 452, p. 456-459.
- Southgate, P.N., 1988, A model for the development of phosphatic and calcareous lithofacies in the Middle Cambrian Thornton Limestone, northeast Georgina Basin, Australia: *Australian Journal of Earth Sciences*, v. 35, p. 111-130.
- Waloszek, D., Hinz, I., Shergold, J.H., and Müller, K.J., 1993, Three-dimensional preservation of arthropod soft integument from the Middle Cambrian of Australia: *Lethaia*, v. 26, p. 7-15.
- Waloszek D., 2003, The 'Orsten' Window—a three-dimensionally preserved Upper Cambrian meiofauna and its contribution to our understanding of the evolution of Arthropoda: *Paleontological Research*, v. 7, p. 71-88.
- Xiao, S., and Knoll, A.H., 1999, Fossil preservation in the Neoproterozoic Doushantuo phosphorite Lagerstätte: *Lethaia*, v. 32, p. 219-240.
- Zhang, Y., Yin, L., Xiao, S., and Knoll, A.H., 1998, Permineralized fossils from the terminal Proterozoic Doushantuo Formation, south China: *Memoir 50 (The Paleontological Society)*, 52 p.

CHAPTER 4

GEOBIOLOGY OF A LOWER CAMBRIAN CARBONATE PLATFORM, PEDROCHE FORMATION, SPAIN

ABSTRACT

The Cambrian Series 2 Pedroche Formation comprises a mixed siliciclastic–carbonate succession recording subtidal deposition on a marine platform. Thrombolites comprise ~60% of carbonate-normalized stratigraphy and coated-grains another ~10%. Skeletons contribute at most 20% to biohermal, inter-reef, and reef-flank lithologies, of which an average of 70% are archaeocyath clasts. In contrast, skeletons comprise a negligible volume of other carbonate lithofacies. As such, archaeocyathan bioherms represent a specific and limited locus of skeletal carbonate deposition. Consistent with data from other lower Cambrian successions, this supports the view that early Cambrian carbonates have more in common with earlier, Neoproterozoic deposits than with younger carbonates dominated by skeletal accumulation.

This chapter is intended for publication at the journal *Palaeogeography, Palaeoclimatology, Palaeoecology* with co-authors: Andrew H. Knoll, David Fernández-Remolar, Kristin D. Bergmann, Benjamin C. Gill, Bethany L. Ehlmann, Kathryn M. Stack, Diego C. García-Bellido, Christian Hallmann, John P. Grotzinger, Silvia Menendez, Marta Rodríguez-Martínez, Ricardo Amils, and John Abelson.

4.1 INTRODUCTION

Today, skeletons account for most carbonate accumulation in the oceans (e.g., Sarmiento and Gruber, 2006). The geological record, however, shows that this was not the case for most of Earth history; Archean and Proterozoic succession contain thick packages of shallow-marine carbonates deposited via abiotic and microbially-mediated precipitation (e.g., Grotzinger, 1989; Knoll and Swett, 1990; Grotzinger and James, 2000). With this in mind, a canonical view holds that the Cambrian diversification of skeletal animals (Maloof et al., 2010a; Kouchinsky et al., 2012) was a watershed event in the evolution of platform and shelf carbonate deposition (e.g., Zeebe and Westbroek, 2003). Yet, this sense that the nature of carbonate production irrevocably changed with the advent of skeletal biomineralization is hard to reconcile with uppermost Neoproterozoic and Cambrian carbonates whose textures resemble Proterozoic platform archetypes despite a quantifiable skeletal contribution.

Where, then, do Cambrian carbonates fall along the spectrum of non-skeletal to skeletal control? Might the Cambrian Period represent a time when organisms had evolved biomineralized skeletons but not yet transformed ecosystem ecology? Analysis of upper Cambrian and earliest Ordovician carbonates from Laurentia provides support for this view; in successions from Newfoundland and the Cordillera, skeletal material rarely exceeds 25% of bulk carbonate volume and is commonly much less (Pruss et al., 2010). Upper Cambrian rocks, however, might understate the case for skeletal input to Cambrian carbonates, in large part because archaeocyaths, the most conspicuous Cambrian reef animals, had nearly disappeared by 510 Ma (Debrenne, 2007). Preliminary research on earlier Cambrian carbonates suggests that skeletons contributed up to ~20% of total carbonate production, with archaeocyathan material dominating skeletal input (Hicks and Rowland, 2009; Pruss et al., 2012).

Here we provide a new case study of carbonate production on an early Cambrian carbonate platform that hosted archaeocyath-bearing reefs, focusing on carbonate deposition and skeletal abundance within the Cambrian Series 2 Pedroche Formation, Andalusia, Spain. We follow the methodology of Pruss et al. (2010) and use nested scale observations, from outcrop stratigraphy to petrographic analysis of carbonate microfacies, to quantify the contribution of skeletal material to carbonate lithofacies and assess more broadly the nature of carbonate production across the platform.

4.2 GEOLOGIC SETTING

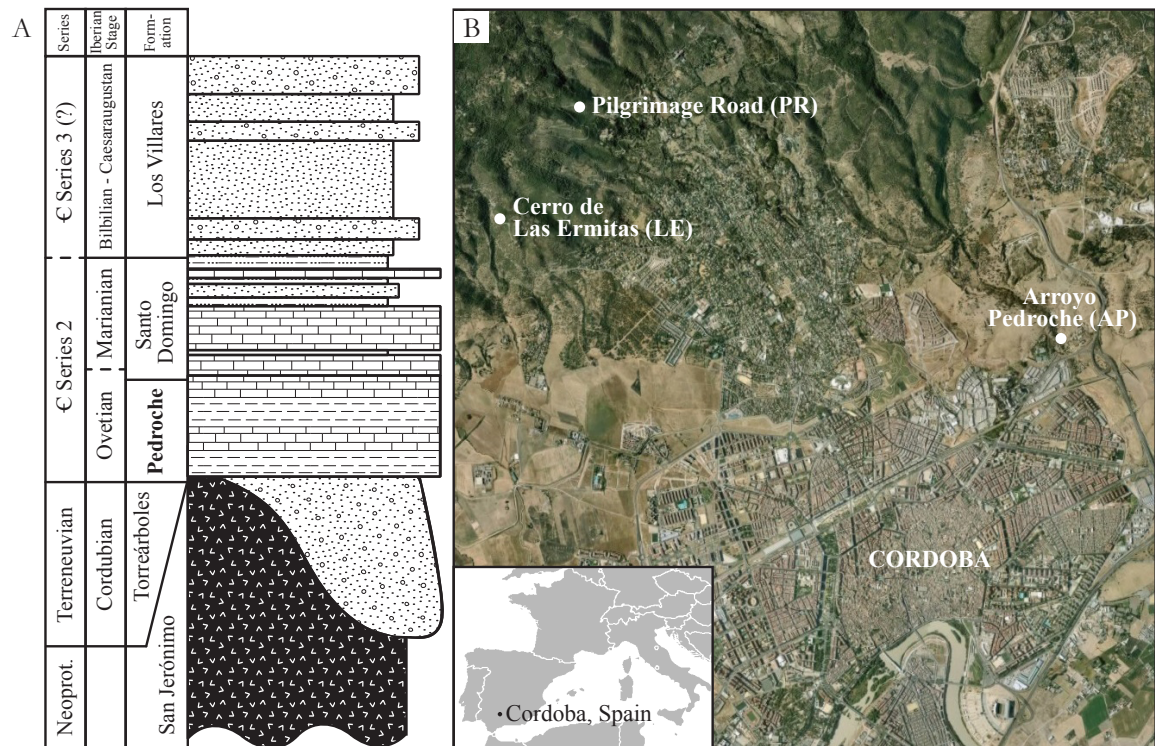


Figure 4.1: Geology and map of the study area. A) Generalized Neoproterozoic to Cambrian stratigraphy of the Ossa Morena geotectonic zone, Iberian massif (adapted from Gubanov et al., 2004). B) Locations (white dots) of the three measured stratigraphic sections around the city of Cordoba, Andalusia, Spain.

The Iberian Massif is divided into five geotectonic zones (Dallmeyer and Martínez García, 1990). Our study focuses on strata cropping out within the Ossa-Morena zone, which records a complex history of Neoproterozoic and Paleozoic extension, sedimentation and orogenesis resulting from the geodynamic interactions among Gondwana, Laurentia, Baltica, and proximal micro-continents, including Iberia (see, for example, Eguíluz et al., 2000; Dallmeyer and Martínez García, 1990). Broadly, the tectonostratigraphy of the Ossa-Morena zone documents Neoproterozoic Cadomian and middle-to-late Paleozoic Hercynian orogeny, each followed by sedimentation during rift-to-drift (passive margin) transition (Eguíluz et al., 2000). Figure 1a summarizes the rift succession developed in the wake of Cadomian orogeny. In ascending stratigraphic order this includes the Neoproterozoic San Jerónimo Formation, a volcano-sedimentary complex; the siliciclastic-dominated Terreneuvian Torresárboles Formation; the carbonate-dominated Cambrian Series 2 Pedroche and Santo Domingo formations; and the predominantly siliciclastic Cambrian Series 2 (?) to Series 3 Los Villares Formation (Fig. 1a; Liñán et al., 1993). Here we focus on fossiliferous carbonates of the Pedroche Formation.

Pedroche rocks record the first stable carbonate platform development after Cadomian rifting (Liñán and Quesada, 1990). Trilobite (Liñán et al., 2005; Liñán et al., 2008), archaeocyath (Perejón, 1986; 1989; 1994; Perejón et al., 2008), and small shelly fossil (Fernández-Remolar, 2001; Gubanov et al., 2004; Hinz-Schallreuter et al., 2008) biostratigraphy assign the Pedroche succession to the early Ovetian Stage of the Iberian chronostratigraphic framework (Liñán et al., 1993 and references therein). Biostratigraphic interpretations variably correlate the Ovetian Stage to the latest Tommotian through to the earliest Botomian stages of Siberia, but all agree that the Ovetian encompasses the Atdabanian Stage. As such, the Pedroche Formation records deposition correlative to Cambrian Series 2, Stage 3 of the international chronostratig-

raphy for the Cambrian System (Fig. 1a; Jensen et al., 2012; Peng and Babcock, 2011; Babcock and Peng, 2007).

4.3 METHODS

Detailed sections of the Pedroche Formation were measured at three localities in the vicinity of Cordoba, Andalusia, Spain (Fig. 1b). The type section for the formation, Arroyo Pedroche (Section AP; 37°54'26.67"N, 4°45'29.07"W), crops out along the east embankment of an arroyo just north of the dam. Additionally, the Pedroche Formation is exposed north-northeast of the city, within the Sierra de Córdoba, where strata crop out along the north side of a hairpin turn on CO-110, herein referred to as Pilgrimage Road (Section PR; 37°55'45"N, 4°49'02"W), as well as on the east side of road CV-79 leading to Cerro de Las Ermitas (Section LE; 37°55'05.25"N, 4°49'34.66"W), just above the fifth station of the cross.

We collected hand samples of carbonate lithofacies at ~1 to 2 meter resolution. The samples were cut with a water-cooled saw perpendicular to bedding to create slabs and thin-section billets. Each slab or billet was micro-drilled with a 1 mm dental bit for carbonate carbon ($\delta^{13}C_{carb}$) and carbonate oxygen ($\delta^{18}O_{carb}$) isotopic analysis. Carbonate powder reacted in a common phosphoric acid bath at 90°C for 7 minutes. Evolved CO₂ was cryogenically concentrated and measured against an in-house reference gas on a VG Optima dual-inlet mass spectrometer attached to a VG Isocarb preparation system. All isotopic values are reported in the V-PDB per mil (‰) notation with a standard reproducibility of $1\sigma \approx 0.1\text{‰}$ and 0.3‰ for $\delta^{13}C_{carb}$ and $\delta^{18}O_{carb}$, respectively.

Point-counts of petrographic thin-sections enabled us to quantify the proportional contributions of constituent components to carbonate volume (e.g., Flügel, 2004;

Payne et al., 2006; Pruss et al., 2010; Pruss and Clemente, 2011). The statistical robustness of such a frequency analysis depends on the density of the point array (spacing) with respect to the size and percent contribution of individual components (Van der Plas and Tobi, 1965; Flügel, 2004). Generally, the width of the chosen grid-spacing relative to the largest diameter of the constituent components (e.g., micrite, ooids, or archaeocyaths) dictates whether the counting procedure over-represents large grains (dense grid) or under-represents small grains (sparse grid) (Van der Plas and Tobi, 1965; Flügel, 2004). Here, we use transmitted light microscopy to classify ~ 200 points per thin-section, corresponding to a 2 x 2 mm width grid spacing. This point-density translates to 2σ errors of ~ 2 , 4, and 5.5% for constituent components calculated to comprise ~ 3 , 9, and 20% of the sample, respectively. In other words, a sample determined to have 9% skeletal content by point-count analysis should be considered to have $9 \pm 4\%$ with 95% confidence (Van der Plas and Tobi, 1965; Flügel, 2004).

Lithologies and microtextures of the Pedroche, particularly the archaeocyath-bearing reef facies, consist of submicron- to centimeter-scale crystals and grains. As such, the use of a fixed grid spacing introduces a potential bias towards grains larger than 2 x 2 mm width / circumference. We note, however, that the true skeletal component of large skeletal grains, such as archaeocyaths, comprise only a fraction of the total encompassing volume. For this reason, we employ the grain-solid method of point counting wherein only the solid fraction of a skeleton is classified as skeletal contribution; any primary inter-skeletal void space, such as the central cavity of an archaeocyath, is counted separately under relevant textural classifications, such as micrite or sparry cement (Flügel, 2004). As such, we believe the chosen grid spacing should not over represent the largest diameter constituents.

4.4 CARBON ISOTOPIC CHEMOSTRATIGRAPHY

Figure 2 presents a 3-point moving average of carbon isotope chemostratigraphy for the AP and PR sections, and un-averaged data for the LE section. Carbonate C-isotopes from the Arroyo Pedroche section display a positive trend from 1.9 to 3.3‰ from 32–37 m that precedes a negative excursion to a nadir of -1.3‰ at 67 m. Above the covered interval from ~68.1–81 m, $\delta^{13}C_{carb}$ values resume at -2.0‰, plateau at ~ -1.4‰ between 82.9–119.1 m, and increase to -0.5‰ by 129 m. At the Pilgrimage Road section, $\delta^{13}C_{carb}$ values show a broadly similar pattern of stratigraphic variation, increasing from -1.8 to 1.0‰ from the base of the section to 30.5 m, declining to a nadir of -2.9‰ at 52 m, and then rebounding toward values of -1 to -2‰ in the upper part of the section (but showing a transient negative excursion to -2.9‰ at 89 m). The carbon isotope composition of archaeocyath-bearing carbonates of the Las Ermitas section remains invariant at ~ -1.5‰.

The architecture and magnitude of $\delta^{13}C_{carb}$ variation within the three measured stratigraphic sections suggests they record overlapping but not entirely equivalent time intervals (Fig. 2). Specifically, isotopes imply that deposition of the Las Ermitas section correlates only with the upper half of the succession at Arroyo Pedroche. Detailed correlation with the Pilgrimage Road section is less clear. Many of the isotopic values reported from Pilgrimage Road are more negative than those reported from either Arroyo Pedroche or Las Ermitas, consistent with the observation that carbonates at Pilgrimage Road are often nodular, massively recrystallized, and/or interbedded with siliciclastic strata; these textures and facies associations often result from, or are susceptible to, diagenetic recrystallization which, in the presence of organic remineralization, can result in more negative isotopic values. Broadly, however, the stratigraphic trends measured at Pilgrimage Road resemble those at Arroyo

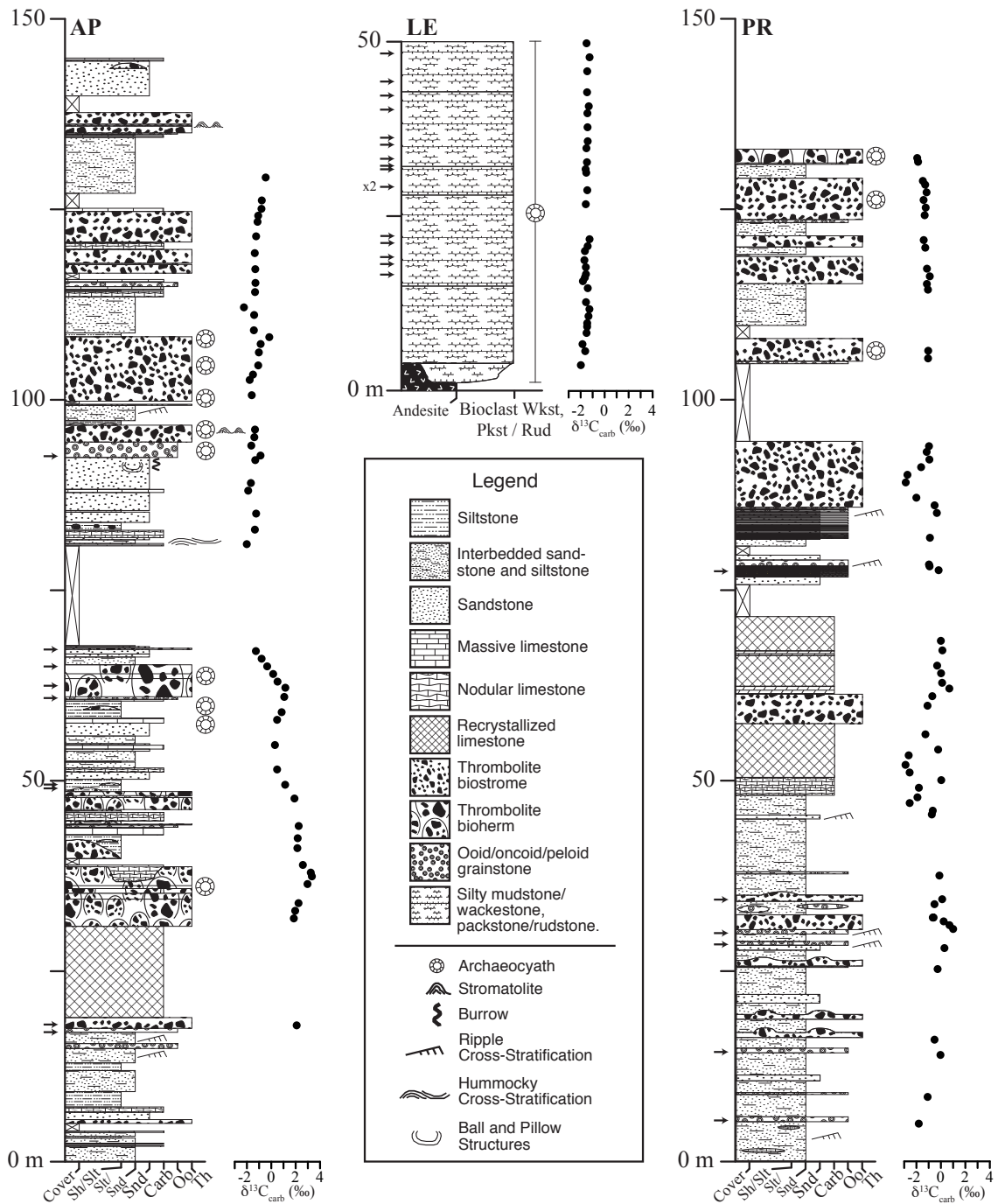


Figure 4.2: Lithostratigraphy and $\delta^{13}C_{carb}$ chemostratigraphy of the Pedroche Formation. AP = Arroyo Pedroche section; LE = Cerro de Las Ermitas section; PR = Pilgrimage Road section. Samples of lithologies point-counted for percent constituent components are denoted with a small arrow next to the stratigraphic height.

Pedorche. In any event, the Pedroche Formation, as defined by lithostratigraphy, encompasses diachronous carbonate deposition.

The biostratigraphic assignment of Pedroche carbonates to the early Ovetian makes a prediction for their C-isotopic composition. Consistent with this, $\delta^{13}C_{carb}$ values from Arroyo Pedroche appear to capture the apex of a positive excursion, with absolute values like those of the early Atdabanian Stage IV excursion in Siberia (Brasier et al., 1994; Kouchinsky et al., 2007). Within the Arroyo Pedroche section, these positive $\delta^{13}C_{carb}$ values precede a plateau of -1.5‰ , further consistent with values recorded from expanded sections of early Atdabanian age (Maloof et al., 2005; Kouchinsky et al., 2007). Thus, chemostratigraphy supports the assignment of the Pedroche Formation to the lower part of Cambrian Series 2, Stage 3. Moreover, correlation of the Pedroche $\delta^{13}C_{carb}$ values to a radiometrically calibrated Cambrian Terreneuvian—Series 2 $\delta^{13}C_{carb}$ curve suggests an absolute depositional age between 520.93 ± 0.14 Ma and 517.0 ± 1.5 Ma (Maloof et al., 2010b; Landing et al., 1998).

The global boundary stratotype section and point (GSSP) for the Cambrian Terreneuvian—Series 2 boundary remains under consideration by the International Subcommittee on Cambrian Stratigraphy (Peng and Babcock, 2011). Most workers propose to define this boundary at the first appearance datum of trilobites (Zhu et al., 2006; Babcock and Peng, 2007; Peng and Babcock, 2011) or various SSF taxa (Rožanov et al., 2011; Steiner et al., 2011). However, the concept of the first appearance datum has been criticized for potential globally diachroneity (Landing and Geyer, *in review*), due either to lithofacies-/sequence stratigraphic-bound fossil distribution (see, for instance, Holland, 1995) or provincialism and delayed ecological dispersion. For these reasons, Landing and Geyer (*in review*) propose to tie the Terreneuvian—Series 2 boundary to the positive $\delta^{13}C_{carb}$ excursion IV within the lower Atdabanian Stage of Siberia. The chemostratigraphic framework developed

here for the trilobite, archaeocyath, and small shelly fossil bearing Pedroche Formation will assist in the correlation of the Ovetian Stage to other regions in which high-resolution biostratigraphy can be linked to chemostratigraphy. However, the difficulty in making detailed correlations between the Pilgrimage Road section to the Arroyo Pedroche type section—just kilometers away—provides a note of caution in applying chemostratigraphy to boundary definition; without question the strongest correlations—and, hence, boundary definition—will occur when bio- and chemostratigraphic data are considered together.

4.5 LITHOFACIES DESCRIPTIONS AND PALEOENVIRONMENTAL INTERPRETATIONS

4.5.1 LITHOFACIES DESCRIPTIONS

INTERBEDDED CARBONATE MUDSTONE, BIOCLASTIC WACKESTONE, ARCHAEOCYATHAN FLOATSTONE–PACKSTONE–RUDSTONE AND SILICICLASTIC SILTSTONE

This facies consists of massive, neomorphosed carbonate mudstone, bioclastic wackestone and archaeocyathan packstone–floatstone–rudstone, with abundant crenulated-to-stylolitic, parallel, sub-parallel, and anastomosing laminae and beds of red siliciclastic siltstone imparting an amalgamated stylonodular to stylobedded fabric (Fig. 3a-c). Individual fabrics occur either with gradational-to-sharp contacts over a mm-to-cm scale, or as discrete beds and micronodules delineated by dissolution seams enriched in siliciclastic stylocumulate. Generally, carbonate comprises ~50–80% of this lithofacies, averaging 60–70%; however, for short stratigraphic intervals, siltstone laminae and beds may comprise up to ~80% of rock volume. These lithologies also comprise the clasts of intraclastic breccias. Archaeocyathan clasts, ranging from 0.5–3 cm in diameter, are oriented randomly, aligned along their elongate axis, or, rarely, found in life position (Fig. 3b,c).

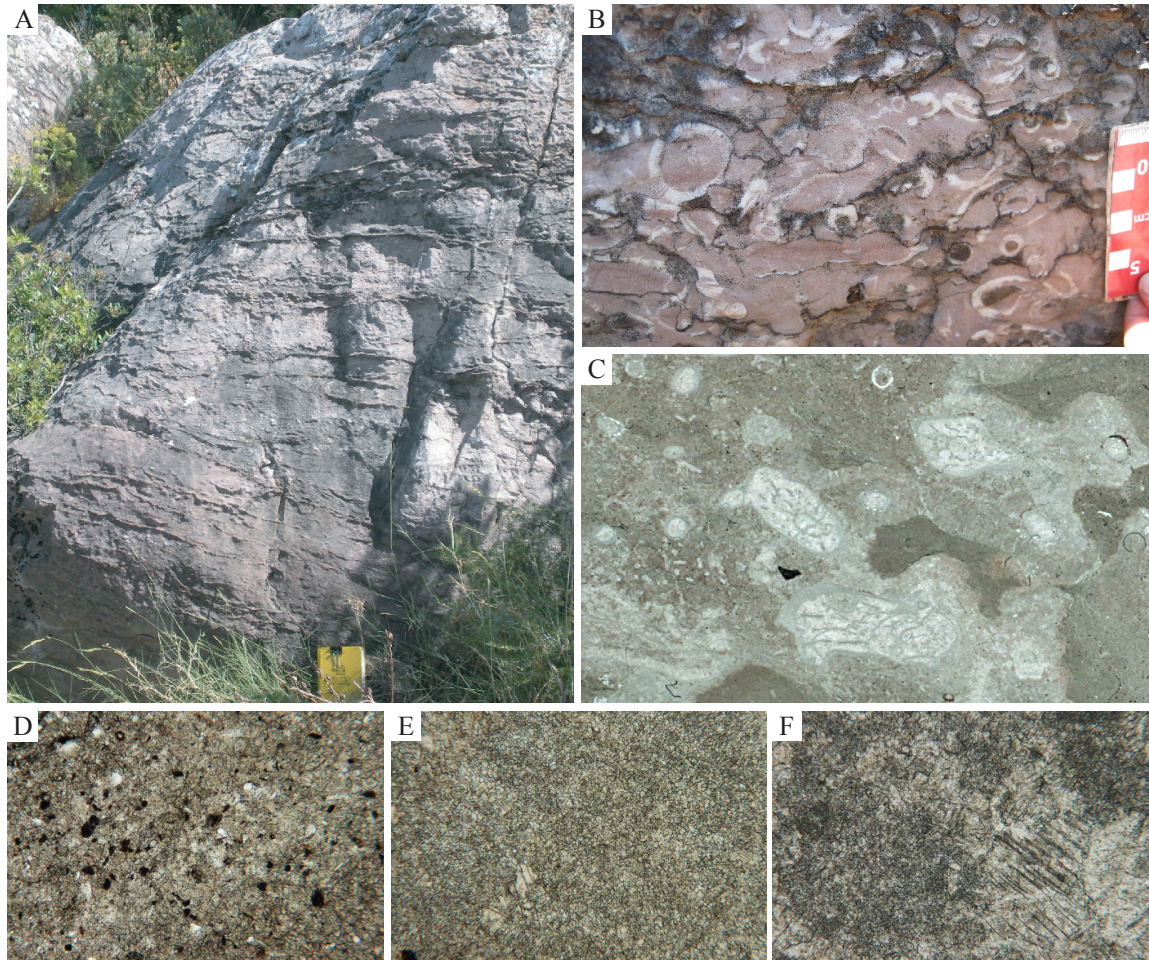


Figure 4.3: Lithologic and petrographic character of the interbedded carbonate mudstone, bioclastic wackestone, archaeocyathan floatstone–packstone–rudstone and siliclastic siltstone lithofacies comprising the Las Ermitas section. A) Outcrop appearance of the lithofacies. B) Bioclast orientation within the archaeocyathan rudstone. C) Photomicrograph of archaeocyathan rudstone (LE 31.5 m). Photomicrographs of the matrix micro-fabrics D) mcr1, E) mcr2, and the late-stage cement F) Sp (as described in the main text).

Petrography reveals three distinct carbonate microfabrics. In the first, the matrix is an inequigranular, xenotopic microspar hosting 5–10% brown-to-opaque, rectangular, silt-sized clay mineral grains and sub-rounded Fe-oxide crystals, perhaps after pyrite (fabric mcr1; Fig. 3d). This fabric is interpreted as a neomorphosed silt-bearing micrite. A second common matrix fabric comprises a drusy-to-equant mosaic of xenotopic microspar lacking siliciclastic grains but, at times, hosting < 5% light-green, rectangular lathes of glauconite (fabric mcr2; Fig. 3e). This fabric represents a variably fabric destructive to fabric retentive early burial cement. Less commonly, a third matrix microfacies—equigranular, hypidiotopic-to-idiotopic coarse spar with twinned-lamellae—is found as pockets within fabric mcr2, forming recrystallization halos around archaeocyath skeletal clasts, or as veins that cross-cut other matrix fabrics (fabric Sp; Fig. 3f). We interpret this microfabric in terms of later stage fluid flow that neomorphosed the drusy cement, with flow preferentially running through high porosity conduits provided by archaeocyath skeletons.

Archaeocyath skeletal preservation occurs through multiple pathways (Fig. 4). Drusy microspar (mcr2) typically molds the outer wall, inner wall and septa of individual archaeocyaths (Fig. 4b-d). Rarely, microcrystalline hematitic overgrowths, known as Frutexites, rim the exterior of the outer wall. Commonly, a slightly coarser drusy microspar (mcr2) or an optically twinned, coarse spar (Sp) molds the intervallum (Fig. 4c,d); more rarely, the intervallum may be filled with reddish-pink microspar (mcr1; Fig. 4b) or include both mcr1 and mcr2 within the same specimen (Fig. 4c). Likewise, the central cavity may be infilled by mcr1 (Fig. 4b,c); however, more commonly among smaller specimens, the central cavity is molded by drusy microspar (mcr2; Fig. 4d). The petrogenesis of archaeocyath preservation is apparent from Figure 4. Post-mortem, the intervallum and central cavity of archaeocyathan clasts are filled, to varying degrees, by siliciclastic-bearing carbonate

silt (mcr1). Subsequently, primary skeletal porosity is occluded by a drusy cement or coarse spar (mcr2, Sp).

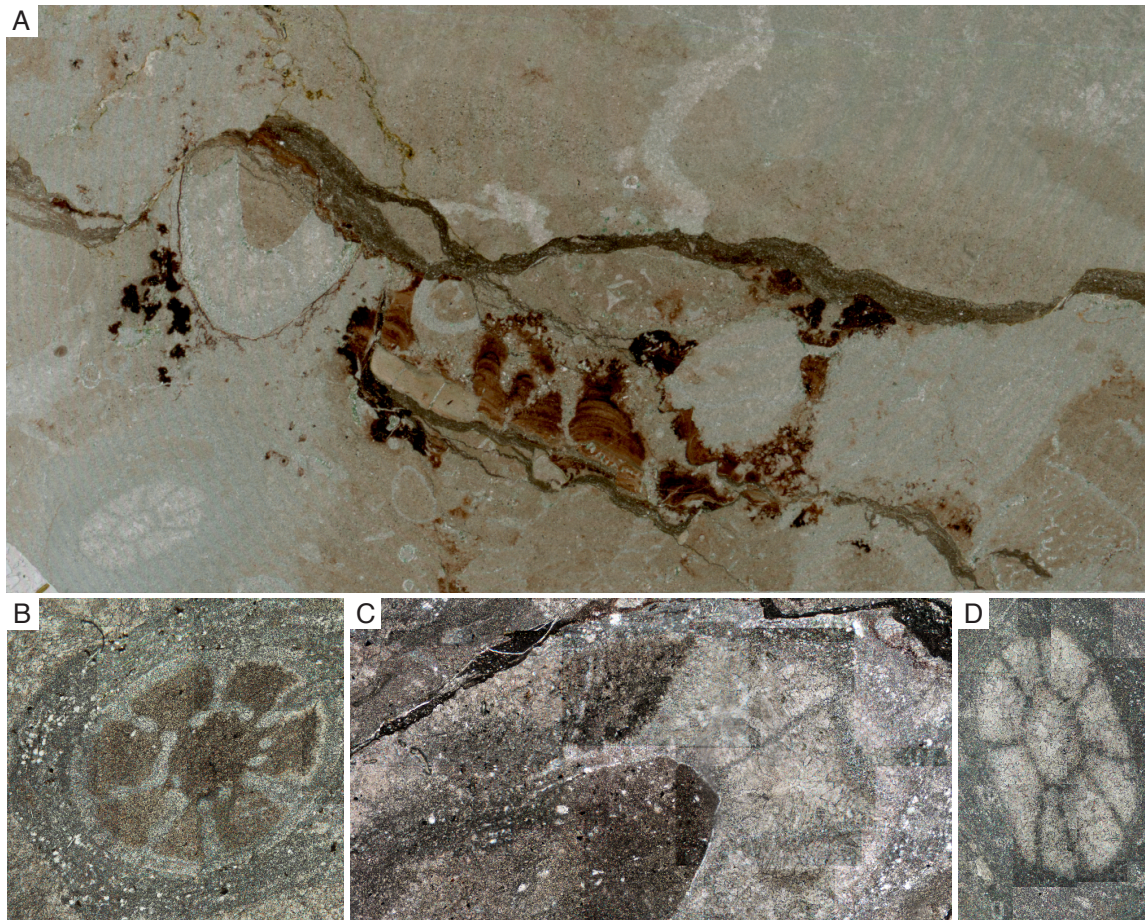


Figure 4.4: Photomicrographs of archaeocyath-bearing lithofacies and mode of archaeocyath preservation. A) Thin-section LE 18.0 m. B) Archaeocyath with mcr1 infilling the central cavity and intervallum (LE 48.0 m). C) Archaeocyath with mcr1 infilling the central cavity and mcr1 infilling, and mcr2/Sp molding, the intervallum (LE 29.0 m). D) Archaeocyath with mcr2 molding the central cavity and intervallum (LE 18.0 m).

In contrast to archaeocyathan preservation, small shelly fossils are always molded by a drusy microspar (mcr2) and never occur as single calcite crystals (Fig. 5). Within this lithofacies, microbial fabrics are rare but, when present, include mm-scale stromatolites (Fig. 4a) and filamentous, oncolitic halos around archaeocyathan

bioclasts (Fig. 4b). No echinoderm ossicles, and few trilobite carapaces, were observed within representative thin-sectioned samples of this lithofacies.

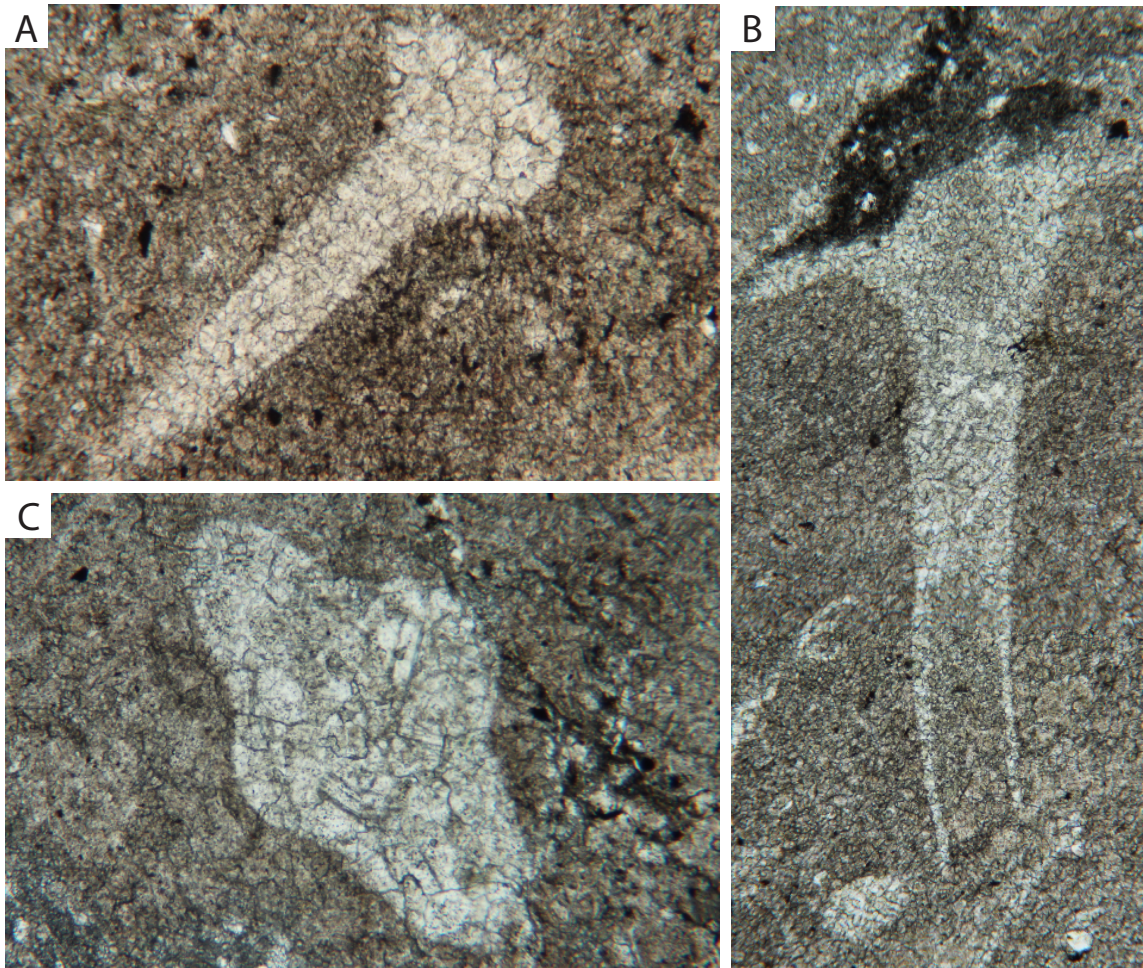


Figure 4.5: Photomicrographs of small skeletal fossil preservation. Small skeletal fossil from sample A) LE 18.0 m, B) LE 33.0 m, and C) LE 48.0 m.

OID, ONCOID AND PELOID GRAINSTONE

This facies consists of light grey to mauve weathering, medium-to-thick beds of well-sorted ooid, oncoïd, and peloid grainstone (Fig. 6). Individual ooid grains range from 0.5–1.0 mm in diameter (Fig. 6a). Petrographic examination reveals three distinct

cortical fabrics. Most commonly, ooids display a fabric-destructive dolomitization by euhedral crystals (Fig. 7a-c). This texture indicates dissolution of the primary cortical mineralogy, leaving casts of nearly circular morphology later filled with cement (oomolds). More rarely, ooids have a micritized cortex (Fig. 7d). In some instances, these reveal faint concentric laminations and/or the ghosts of radially oriented crystals (Fig. 7e), suggesting that micritization occurred at the expense of the primary cortical fabric. Under cross-nichols, micritic ooids display a (pseudo-uniaxial) extinction cross. Regardless of preservation texture, few ooid grains retain discernable nuclei (Fig. 7). Such an absence suggests a nucleus of carbonate that dissolved along with the primary cortices. Rarely, the interiors of dolomitized ooids include a cluster of equant, anhedral microspar crystals, suggesting, perhaps, that ooids nucleated from peloids (Fig. 7b).

We observe a second set of structureless, micritized grains, 0.1–1.0 mm in diameter, with morphologies that deviate from spherical. We classify these as peloids. Peloids are generally ovoid, whereas coarse-grained peloids appear nephroid and, rarely, irregular in outline (Fig. 7f). Given the history of fabric-destructive recrystallization apparent from ooid textures, it is possible that grains classified as peloids based on preservational texture originated as oncolites. Unambiguous oncoids are present as mm-cm, oblate-to-irregular shaped, sub-rounded micritized grains (Fig. 6b). A fibrous, isopachous cement often envelopes individual grains, displacing an inferred primary grain-to-grain contact (Fig. 7).

Skeletal clasts are rare within the ooid/oncoid/peloid grainstone facies (Fig. 8). Within all samples thin-sectioned from sections AP and PR, only trilobites (Fig. 8a) calcitic brachiopods (Fig. 8b) and small skeletal fossils (Fig. 8c), were identified within grainstone facies; archaeocyaths were absent from bioclastic debris. When present, skeletons and bioclasts are molded by an equant, microspar, and are com-

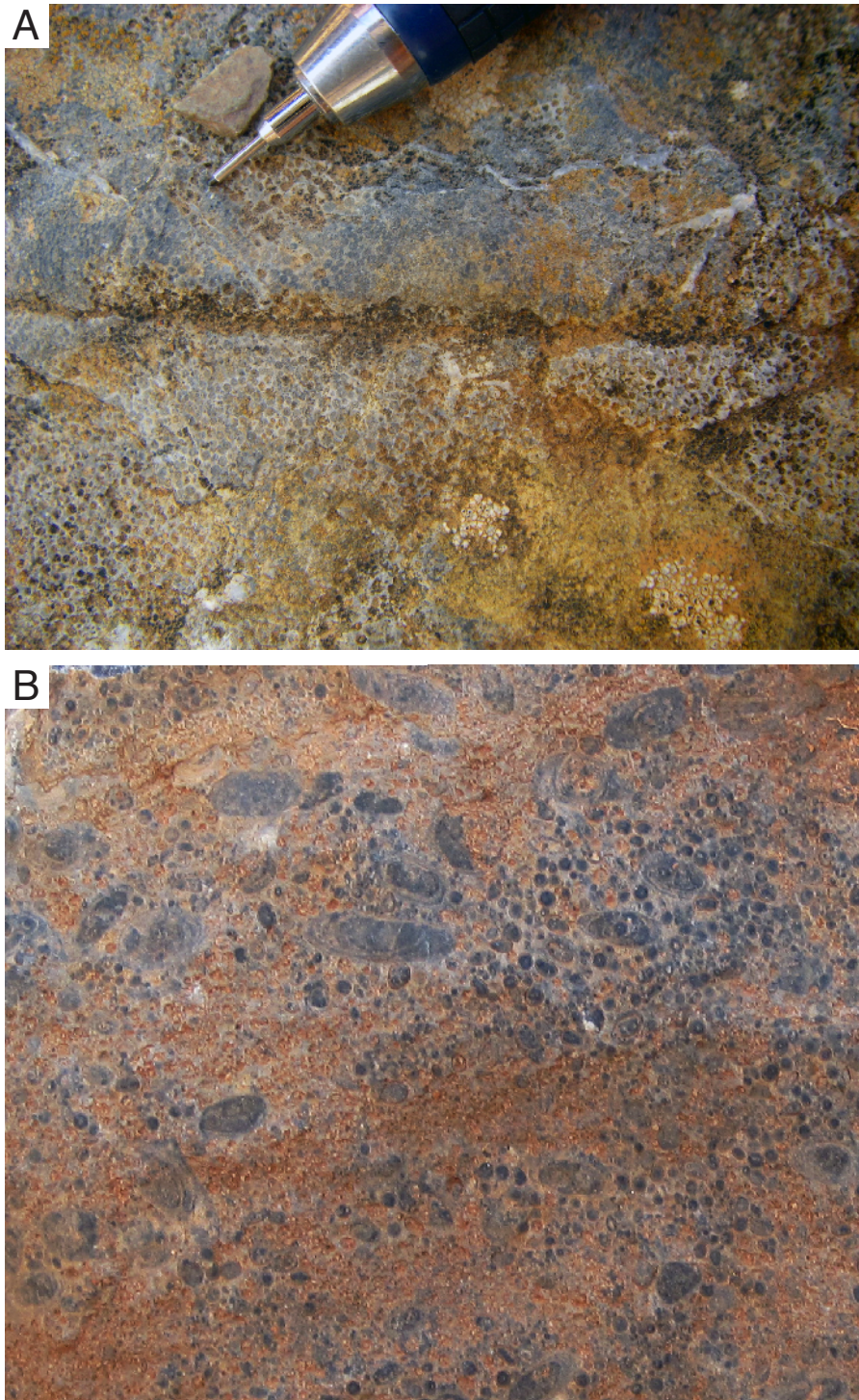


Figure 4.6: Lithologic character of the ooid/oncoid/peloid grainstone lithofacies. A) Fine-grained, well-sorted ooid grainstone (AP 61 m). Ooids are commonly replaced by ferroan dolomite (oomolds). B) Poorly-sorted ooid/oncoid/peloid grainstone.

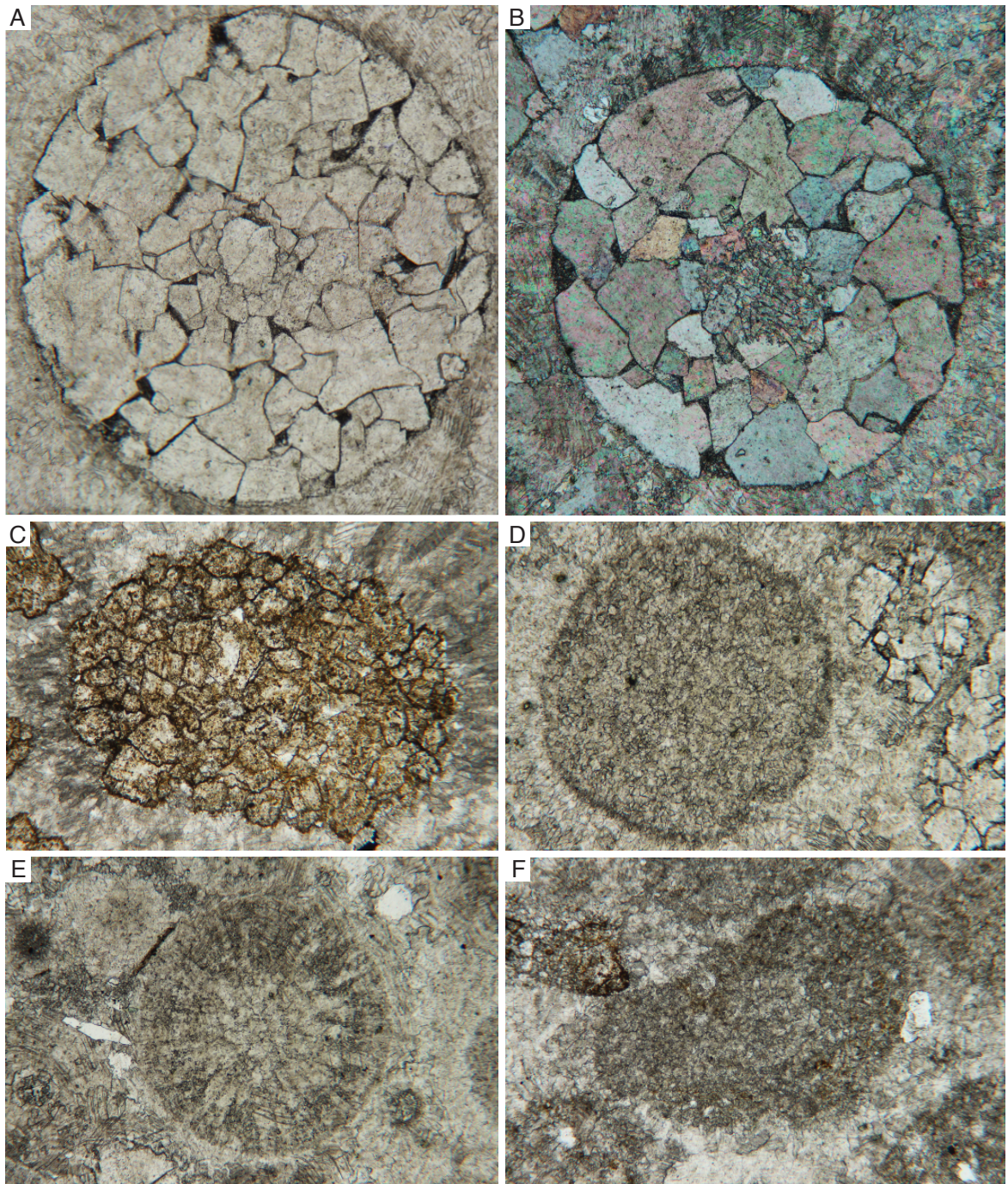


Figure 4.7: Petrography of the ooid/oncoid/peloid grainstone lithofacies. Photomicrograph of ooid replaced by dolomite rhombs (oomold) in A) plane-polarized light and B) cross-polarized light. C) Photomicrograph of peloid replaced by ferroan dolomite rhombs. D) Photomicrograph of ooid with micritic cortoid fabric. E) Photomicrograph of ooid with micritic cortoid fabric retaining faint radial arrangement of neomorphosed crystals. F) Nephroid peloid.

monly enveloped by isopachous cements (Fig. 8). Trilobite carapaces and cortoids of trilobite incurved margins are preserved by rectangular-to-blocky dolomite (Fig. 8a).

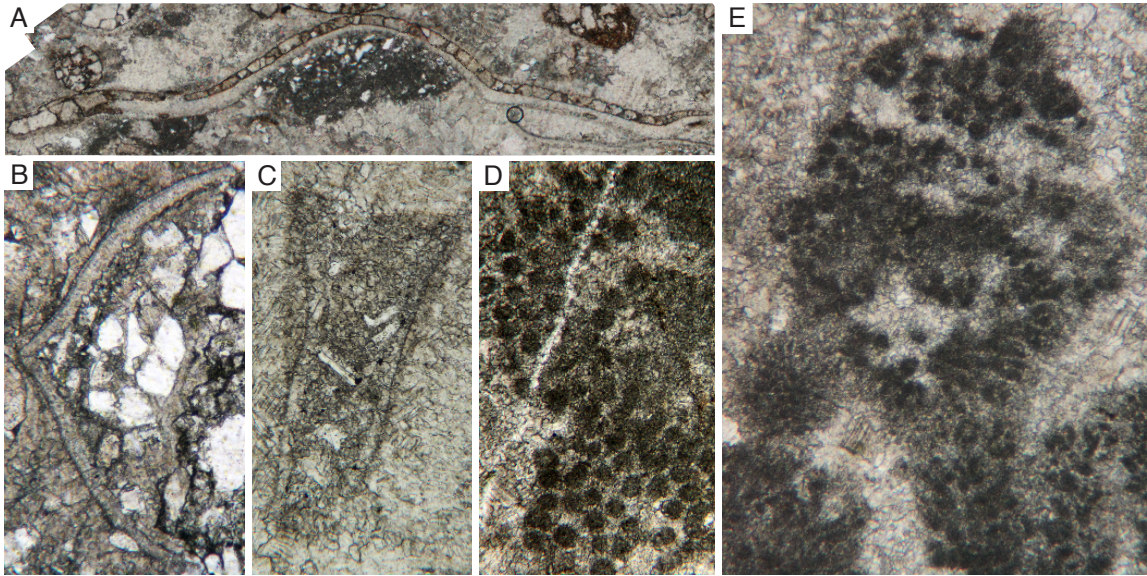


Figure 4.8: Photomicrographs of the modes of biological preservation within the ooid/oncoid/peloid grainstone and thrombolite boundstone lithofacies, Arroyo Pedroche and Pilgrimage Road sections. A) Dolomitized trilobite carapace. B) Calcitic brachiopod. C) Small shelly fossil. D) Epiphyton comprising a thrombolite boundstone mesoclot. E) Arboreal thrombolite boundstone mesoclot texture.

THROMBOLITE BOUNDSTONE

This facies consists of (1) thick to very thick tabular beds (biostromes) of massive thrombolite boundstone; (2) thick to very thick beds of 10-cm to meter-scale, amalgamated, columnar, lobate, and digitate thrombolite heads and mounds; and (3) meter-scale, isolated, kalyprate bioherms of thrombolite boundstone (Fig. 9). All thrombolite boundstones include a significant component of interlaminated, interbedded, or draping siliciclastic siltstone (Fig. 9b,c). The characteristic thrombolitic mesoscale clots occur in isolation, or coalesce to form botryoidal and dendritic textures. In areas of exceptional fabric retention, petrography reveals that these mesostructures are

composed of Epiphyton, Renalcis, and, rarely, Girvanella, that occur as both intergradations and intergrowths from one morphotype to another at a sub-mm scale (Fig. 8e; Pratt, 1984). Aggrading neomorphism and/or secondary dolomitization obscures the primary texture of the matrix between micritic mesoclots. Crenulated-to-wispy dissolution seams with siliciclastic and iron-oxide stylocumulate are common to this lithofacies. Millimeter-scale veins of coarse calcite spar often dissect the thrombolite boundstone lithofacies. Archaeocyath fossils may occur within the matrix of thrombolite boundstone (Fig. 9d).

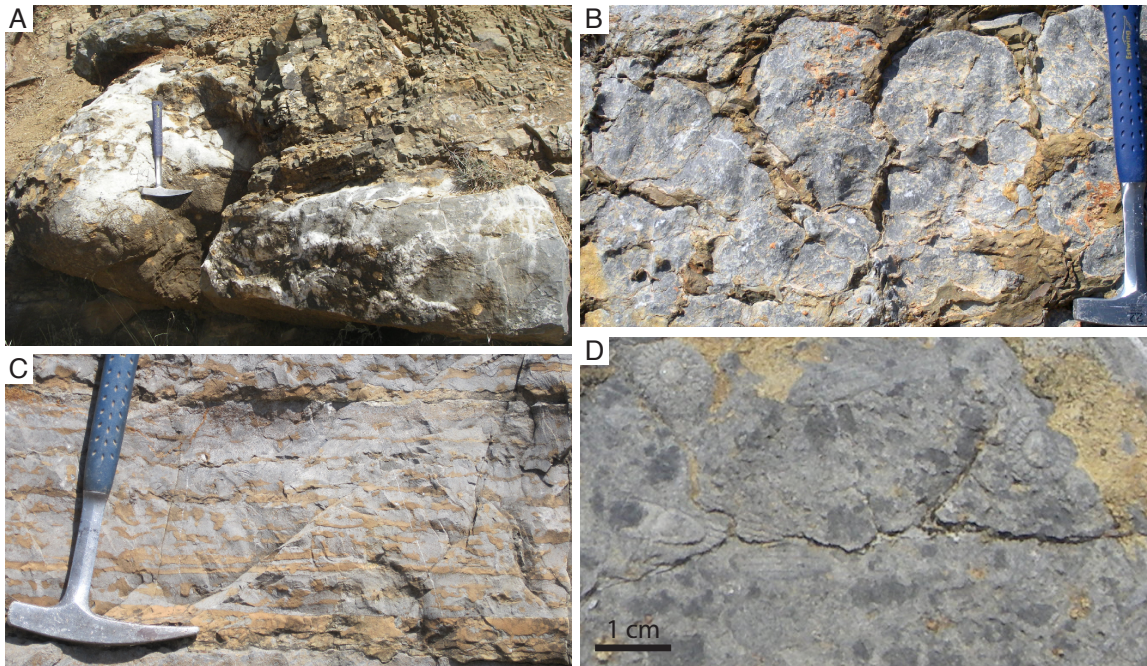


Figure 4.9: Lithologic character of the thrombolite boundstone lithofacies. A) Isolated, bioherm surrounded by bedded carbonate and siliciclastics. B) Columnar heads (separated by siliciclastic siltstone). C) Thrombolite biostrome with interbeds and drapes of siltstone. D) Archaeocyath clasts within thrombolitic boundstone.

MASSIVE GRAINSTONE AND RECRYSTALLIZED CARBONATE

This facies consists of thin to thick beds of very fine to medium grain tabular or irregular-to-wavy bedded grainstone, nodular carbonate and thick to very thick beds of massive, and finely-to-coarsely recrystallized and/or vuggy dolomitized carbonate.

FINE-GRAINED SILICICLASTIC ROCKS

This facies consists of very thin to thin beds of planar laminated and/or ripple cross-laminated shale and siltstone; and thin to medium, planar-to-undulose beds of massive, planar laminated, ripple cross-laminated, or swaley-to-hummocky cross-laminated and cross-stratified, very fine to medium-grained, micaceous quartz sandstone.

4.5.2 LITHOFACIES ASSOCIATIONS

ARROYO PEDROCHE

The Arroyo Pedroche section comprises mixed siliciclastic and carbonate lithologies, both non-cyclically and meter- to decameter-scale cyclically (serially repeated) bedded. (Here, we use the term cycle to describe repetition of lithologies, not to invoke a particular time-scale or depositional mechanism (*sensu* Myrow et al., 2012).) At Arroyo Pedroche, the lowermost ~19 m of the Pedroche Formation consists of shale and siltstone with minor intercalations of bedded thrombolite boundstone and nodular limestone. Towards the top of this interval, ripple and hummocky cross-stratified, siltstone and fine- to medium-grained sandstone beds occur along with rare beds of massive ooid grainstone. A massive, recrystallized carbonate crops out between 19 and 31 m.

From 31–68.1 m, the Pedroche Formation is characterized by the non-cyclic in-

tercalation of: (1) planar laminated shale and siltstone, and planar laminated to ripple cross-laminated very fine-grained sandstone, (2) irregularly bedded carbonate, (3) ooid/oncoid/peloid grainstone beds and channels, and (4) isolated and amalgamated mounds and bioherms of thrombolite boundstone typically surrounded by bedded, fine-grained siliciclastic lithologies. While all facies were observed to grade laterally and vertically into thrombolitic boundstone, the ooid/oncoid/peloid grainstone facies occurs most frequently as erosive, channelized infill between thrombolite bioherms. Biohermal morphologies most commonly develop within fine-grained siliciclastic lithologies, while digitate morphologies preferentially develop in grainstone troughs. Bioherms comprise discrete heads composed of mesoclots of thrombolite. Thrombolite boundstone lacking discernable synoptic-relief occurs in association with carbonate mudstone.

Above a covered interval from 68.1–80 m, cyclic interbedding of lithologies is more strongly developed. These cycles consist of a basal siliciclastic-dominated component and an upper carbonate-dominated component. The generalized succession of siliciclastic lithologies within cycles includes: (1) interbeds of laminated shale and siltstone and/or (2) interbeds of laminated-to-swaley siltstone and very fine-grained sandstone grading into (3) swaley, hummocky, or ripple cross-laminated, very fine- to medium-grained, amalgamated sandstone. In turn, the coarser, cross-stratified siliciclastic lithologies are commonly interbedded with, or overlain by, carbonate lithologies that may include: (4) nodular and/or irregular beds of carbonate with and without grains and/or (5) cross-bedded or massive ooid/peloid/oncoid grainstone atop which (6) biohermal and biostromal thrombolite boundstones nucleate and grow. Thrombolite biostromes and bioherms are nearly always succeeded by beds of the fine-grained siliciclastics (predominately siltstone), but may also underlie beds of massive/nodular carbonate or grade laterally and vertically into the ooid/oncoid/peloid grainstone

lithofacies. Common variations on this generalized theme include: interbedding of siliciclastic lithologies without a discernable coarsening-upward succession (or a distinct shaling-upward succession); isolated thrombolitic boundstone bioherms or amalgamated thrombolite heads within siliciclastic lithologies; and/or the absence of the nodular/irregular carbonate lithofacies. Inasmuch, mixed siliciclastic-carbonate cycles represent upward-coarsening cycles.

PILGRIMAGE ROAD

Planar and ripple cross-laminated siltstone and very fine- to fine-grained micaceous quartz sandstone with and without lime mudstone nodules comprise the majority of the basal ~45 m of the Pilgrimage Road section. Beds of massive and cross-bedded fine- to medium-grained quartz sandstone, beds and lenses of massive and cross-bedded ooid/oncoid/peloid grainstone, and mounds and bioherms of thrombolite boundstone intercalate with these fine-grained siliciclastic lithologies. At ~45 m, the carbonate mudstone nodules within a 2.5 meter-thick siltstone/sandstone bed increase in abundance, grading into a carbonate interval from 47.5 – ~71 m. Carbonates textures within this interval include: interbedded massive recrystallized limestone; vuggy, coarse-crystalline dolomite; and one ~3 meter-thick massive, recrystallized thrombolite boundstone biostrome.

Cyclic interbedding of lithofacies occurs from ~71 m to the top of the measured section. At Pilgrimage Road, cycles include: (1) a covered interval, (2) micaceous siltstone and very fine-grained quartz sandstone, and (3) massive to cross-bedded ooid/oncoid/peloid grainstone capped by (4) a very thick, massive thrombolite boundstone biostrome interlaminated, interbedded and draped with siltstone. Thrombolite beds contain rare archaeocyath bioclasts. The basal cycle deviates from this pattern in that interbeds of massive and cross-bedded fine- to medium-grained sandstone and

oid grainstone underlie the thrombolite biostrome. Other variations on this theme include the absence of either the fine-grained siliciclastic or the ooid/oncoid/peloid grainstone lithofacies.

CERRO DE LAS ERMITAS

At the Cerro de Las Ermitas section, Pedroche carbonates transgress over and in-fill meter-scale paleotopographic relief incised into andesites of the underlying San Jer nimo volcano-sedimentary complex (Fig. 2). A complex cavity-dwelling calcimicrobial and skeletal community found on this paleosurface is described thoroughly by Vennin et al. (2003). Atop this nonconformity, the Pedroche succession consists of discrete archaeocyath-bearing, decameter-scale bioherms surrounded by, and interbedded with, the carbonate mudstone, bioclastic wackestone and archaeocyathan packstone–floatstone–rudstone lithofacies.

4.5.3 DEPOSITIONAL ENVIRONMENTS

ARROYO PEDROCHE AND PILGRIMAGE ROAD

Within the Arroyo Pedroche section, strata below ~19 m record an upward-shoaling succession from a calm, deep-water setting to one influenced by tide, wave, and storm activity. The interlaminated and interbedded shale, siltstone, and fine sandstones without macroscopic sedimentary structures record suspension deposition of fine-grained siliciclastic particles entrained in dilute turbidity currents. We therefore interpret these lithologies to record sediment accumulation in an offshore shelf or distal ramp setting. In contrast, the development of macroscopic sedimentary structures—including hummocky, swaley, or ripple cross-lamination—within siltstone and sandstone record traction deposition from gravity waves. Such sedimentary structures

within well-sorted, amalgamated beds are common to shoreface depositional environments.

Above the massive recrystallized carbonate (for which we do not provide a depositional environment), the non-cyclic arrangement of siliciclastic and carbonate lithofacies with thrombolite boundstone—particularly between 31–49.5 m at Arroyo Pedroche—defines a thrombolite mound-and-channel facies. In this interval, thrombolite aggradations develop with decimeter- to meter-scale synoptic relief. Bedded carbonate and siliciclastic lithologies onlap onto thrombolites, or, in some instances, scour the margins of bioherms. Massive, planar-laminated and ripple cross-laminated, undulatory-bedded carbonate grainstone, and massive carbonate without discernable texture, record a combination of traction transport and suspension deposition. These lithologies are common in shallow, subtidal depositional environments. Well-sorted, cross-bedded ooid/oncoid/peloid grainstone reflects traction deposition from high-energy flow capable of winnowing carbonate and siliciclastic mud, silt and fine sand grains. We interpret these lithologies as migrating shoals and/or sheets that prograde onto deeper subtidal lithologies (i.e., siliciclastic sands and thrombolite boundstone bioherms).

The interfingering and interbedding of these lithologies within the mound-and-channel environment speaks to a contiguous spatial distribution of these lithofacies along an ancient mixed siliciclastic–carbonate shoreface. Evidence for exposure is uncommon in the section, indicating entirely subaqueous deposition. From this we interpret that sediment influx did not consistently outpace the creation of accommodation space. Likewise, the common occurrence of macroscopic sedimentary structures formed from traction deposition indicates that the creation of accommodation space did not significantly outpace sediment accumulation, which would result in shoreface retrogradation and transition into an offshore depositional environment. Thus, we

interpret the alternation between siliciclastic-dominated and carbonate-dominated sedimentation within the mound-and-channel facies to reflect the lateral migration of lithofacies rather than major changes in accommodation space and facies belts.

In contrast, when mixed siliciclastic-carbonate lithologies occur together in continuous, upward-coarsening cycles (as above 81 m at Arroyo Pedroche), we interpret these as upward-shoaling successions. Above the major covered interval, the basal medium-grained sandstone of the cyclic-interbedded section includes hummocky cross-stratification. The re-introduction of this sedimentary structure indicates a deepening to a storm-dominated shoreface. Above this cycle, the transgressive siliciclastics that define the base of each cycle and ooid grainstone beds include ripple cross-stratification, indicative of deposition above fair-weather wave base. We note, however, that deviations from upward-coarsening siliciclastic successions, such as fining-upward patterns or frequent alternations between suspension and traction deposited lithologies, reflect a more complex sediment accumulation pattern than simple shoreface progradation.

Facies associations of the Pedroche Formation at Pilgrimage Road record similar depositional environments as the Arroyo Pedroche type-section. At Pilgrimage Road, the predominance of well-sorted, very fine-grained sandstone with siltstone intercalations throughout the basal ~45 m of the section record a shoreface depositional environment. Minor interbeds of massive ooid grainstone represent the maximum advance of the carbonate system into the siliciclastic-dominated depositional setting. Likewise, above a thick, recrystallized carbonate interval, whose depositional environment is difficult to discern, strata display a well-developed cyclic arrangement. Similar to the AP section, we interpret these (broadly) coarsening-upward sequences as shallowing upward-sequences.

The geometry of thrombolite boundstone beds changes significantly between the

lower and upper portions of both the Arroyo Pedroche and Pilgrimage Road sections. Within the basal ~ 71 m at AP, and the basal ~ 45 m of PR, both intervals of siliciclastic-dominated lower shoreface deposition, thrombolites occur as mounds and biostromes with significant synoptic relief. In contrast, in the upper, cyclically bedded stratigraphy, beds of thrombolite boundstone occur in planar, biostromal geometries, often interbedded with siltstone. Biohermal thrombolites can aggrade when water depth exceeds synoptic relief. As a corollary, the development of biostromal morphologies could reflect limited accommodation space, characteristic of very shallow to nearly emergent depositional environments. However, the common occurrence of siliciclastic silt interlaminae and drapes that disrupt the aggradation of thrombolite boundstone bioherms and biostromes suggests that the morphology of thrombolite accretion is also controlled by the relative rates of carbonate precipitation versus siliciclastic influx (see analogous discussion of stromatolite aggradation in Grotzinger and Knoll, 1999; Cowan and James, 1993). Thus, rather than strictly associate thrombolite boundstone morphology with a flow-regime or water depth, we acknowledge that siliciclastic influx influences the morphology of thrombolite accretion. The common occurrence of ooid/oncoid/peloid grainstone and sandstone underlying beds of thrombolite boundstone suggests that a stable substrate is a prerequisite for thrombolite growth.

CERRO DE LAS ERMITAS

The interlaminated finer-grained carbonate (mudstone and wackestone) and siliciclastic siltstone lithologies accumulated predominately by settling of suspended fine-grains during very low energy conditions. The changing abundance of carbonate versus siliciclastic silt reflects the temporally-variably influx of terrigenous material diluting and/or suppressing background carbonate production. In contrast, coarser-

grained carbonate lithologies reflect higher-energy depositional episodes that entrained reef organisms, re-worked, and winnowed them, as evidenced by deposits of parallel-oriented whole and partial archaeocyath clasts (Fig. 3b). We interpret this lithofacies as inter-reef and reef-flank (talus) deposits. While the measured LE section did not directly transect an archaeocyath framework reef, bioherms were observed above the section. These are not included in the measured section because dense vegetation precluded confident stratigraphic placement.

4.6 PEDROCHE PLATFORM DEVELOPMENT

Table 1 summarizes the proportional contributions of carbonate lithofacies to the three stratigraphic sections measured through of the Pedroche Formation. Thrombolite boundstone comprises 27% and 26% of the Arroyo Pedroche and Pilgrimage Road sections, respectively. Ooid/oncoid/peloid grainstone comprise 3% and 6% of the AP and PR sections, respectively. Other carbonates (i.e., massive grainstone and recrystallized strata) comprise 14% and 15% of the AP and PR sections, respectively. On a carbonate-normalized basis, the thrombolite boundstone, ooid/oncoid/peloid grainstone, and other carbonate lithofacies make up 60%, 8%, and 32%, respectively, of the AP section and 55%, 13%, and 31%, respectively, of the PR section. The entirety of the Las Ermitas section comprises the interbedded carbonate mudstone, bioclastic wackestone, archaeocyathan floatstone–packstone–rudstone and siliciclastic siltstone lithofacies.

4.6.1 POINT COUNTS

Of the 74 thin-sections examined for lithofacies description, we point counted 30 thin sections for quantitative analysis of constituent components, with 16 represent-

Carbonate Lithofacies	Arroyo Pedroche	Pilgrimage Road	Las Ermitas
Inter-reef/Reef-flank Facies	0%	0%	100%
Thrombolite Boundstone	27% (60%)	26% (55%)	0%
Ooid/Oncoid/Peloid Grainstone	3% (8%)	6% (23%)	0%
Other Carbonate	14% (32%)	15% (31%)	0%

Table 4.1: Percent contribution of carbonate lithofacies (rows) to the total meterage of measured stratigraphic sections (columns) of the Pedroche Formation. Percent normalized to only the measured carbonate lithofacies meters presented in parentheses.

ing the archaeocyathan biohermal reef facies, 9 representing the ooid/oncoid/peloid grainstone facies, and 5 representing the thrombolite boundstone facies (Fig. 2). Point-count data are summarized in Table 2. In the following discussion, we report the calculated average percentage of a constituent fabric component $\pm 1\sigma$ unless otherwise noted (summarized in Table 3).

Table 4.2: Raw point-count data from representative samples of the Cambrian Series 2, Stage 3 Pedroche Formation, Andalusia, Spain. Numerical values in the table represent the abundance of identified components counted within a given thin-section. Lithological abbreviations represent: Mdst = mudstone, Wkst = wackestone, Grnst = grainstone, Rud = rudstone, and Th = thrombolite boundstone. Constituent component abbreviations represent: A. = archaeocyath, Biocl. = bioclastic, Oo. = ooid, On. = oncoid, Pel. = peloid, and SSF = small shelly fossil.

Sample	Lithology	Mcr.	Sp.	Si./Sty.	Vein	Oo.	On./Pel.	Archaeo.	Tri.	SSF	Microb.	Other	Total
LE 16.5 m	Mdst	202	2	4	0	0	0	0	0	1	0	1	210
LE 18.0 m	A. Rud	114	27	11	6	0	0	20	0	12	19	1	210
LE 19.0 m	Mdst	169	7	3	9	0	0	0	0	1	0	0	189
LE 21.0 m	Mdst	197	0	11	1	0	0	1	0	3	0	0	213
LE 22.0 m	A. Wkst	84	94	19	0	0	0	10	0	0	0	5	212
LE 29.0 m (1)	Biocl. Wkst/A. Rud	122	6	33	0	0	0	22	0	12	0	3	198
LE 29.0 m (2)	Biocl. Wkst/A. Rud	132	1	32	0	0	0	12	0	4	0	0	181
LE 31.5 m	A. Rud	109	46	9	1	0	0	27	0	7	0	3	202
LE 32.0 m	A. Rud	149	9	31	0	0	0	1	0	11	0	4	205
LE 33.0 m	Biocl. Wkst	72	98	2	0	0	0	33	0	11	0	2	218
LE 35.0 m	Biocl. Wkst	153	0	20	2	0	0	1	0	9	0	5	190
LE 36.0 m	Biocl. Wkst/A. Rud	103	17	55	0	0	0	3	0	8	0	2	188
LE 40.0 m	Wkst/Mdst	160	4	11	2	0	0	1	0	6	0	5	189
LE 42.0 m	Mdst	204	9	0	2	0	0	0	0	2	0	0	217
LE 44.0 m	Mdst	152	2	20	0	0	0	0	0	0	0	0	174
LE 48.0 m	Biocl./A. Wkst	160	23	2	1	0	0	1	0	8	1	2	198

Table 4.2: continued

Sample	Lithology	Mcr.	Sp.	Si./Sty.	Vein	Oo.	On./Pel.	Archaeo.	Tri.	SSF	Microb.	Other	Total
AP 17.0 m	On./Pel. Grnst	96	6	5	2	0	0	0	0	0	53	35	197
AP 18.0 m	Th	101	5	5	3	0	0	0	0	0	82	35	231
AP 49.0 m	Th	110	0	10	0	0	0	0	0	0	93	6	219
AP 49.5 m	Th	100	3	5	8	0	0	0	0	0	94	5	215
AP 61.0 m	On./Pel. Grnst	65	4	7	9	68	0	0	0	0	28	5	186
AP 62.2 m	Th	128	0	8	0	0	0	0	0	0	72	10	218
AP 65.0 m	Th	97	0	36	1	0	0	0	0	0	69	17	220
AP 92.6 m	Oo. Grnst	87	2	25	0	51	5	0	4	0	5	2	181
PR 5.0 m	Oo. Grnst	62	4	4	2	112	0	0	0	0	0	2	186
PR 14.0 m	Oo. Grnst	125	3	0	1	77	0	0	0	0	0	6	212
PR 28.0 m	Pel./Oo. Grnst	77	2	0	6	27	72	0	0	0	0	2	186
PR 30.0 m	Pel./Oo. Grnst	64	51	4	0	20	66	0	0	0	0	5	210
PR 34.4 m	Pel./Oo. Grnst	112	4	0	4	16	74	0	0	0	0	1	211
PR 77.5 m	Oo. Grnst	67	2	4	0	88	0	0	0	0	0	3	164

Carbonate Lithofacies	Skeletons	Micrite	Microbial	Ooids/Peloids
Reef Complex	7.6	82.1	0.6	0
Thrombolite Boundstone	0	49.4	37.2	0
Ooid/Oncoid/Peloid Grainstone	0.2	47.3	0	44.0

Table 4.3: Average percent of the constituent components (columns) of carbonate lithofacies (rows) of the Pedroche Formation.

Figure 10 presents the percentage of skeletal material contributing to carbonate lithofacies of the Pedroche Formation, as determined from the point count data in Table 2. Total skeletal contribution peaks at 21% in the archaeocyathan floatstone–packstone–rudstone facies ($16\pm 5\%$; Fig. 10a). Total skeletal contributions to bioclastic wackestone and carbonate mudstone range from 3–7% and 0.5–2%, respectively (Fig. 10a). Within the archaeocyathan floatstone–packstone–rudstone lithofacies, archaeocyaths are more abundant than SSFs (Fig. 10b), with archaeocyaths averaging $11\pm 3\%$ and SSFs averaging $4\pm 2\%$. In contrast, within bioclastic wackestone and carbonate mudstone lithofacies, archaeocyaths are less abundant than SSFs (Fig. 10c). No thin sections of the thrombolite boundstone lithofacies included a quantifiable skeletal contribution (Fig. 10a). Likewise, of the ooid/oncoid/peloid grainstone samples analyzed, only one revealed a discernable skeletal contribution (2%; Fig. 10a).

Figure 11 depicts the percent composition of all quantitatively important (i.e., $>1\%$) constituents of each carbonate lithofacies found in the Pedroche Formation. In addition to the variable skeletal contribution discussed above, micrite ($82\pm 11\%$) and siliciclastic clay and/or silt ($8\pm 8\%$) dominate the composition of the archaeocyathan-bearing biohermal reef lithofacies (Fig. 11a); in contrast, microbial textures (e.g., stromatolitic laminae and fruticities) contribute a maximum of 9%, but typically much less ($0.7\pm 2\%$; Fig. 11a; see photomicrograph in Fig. 3). The thrombolite litho-

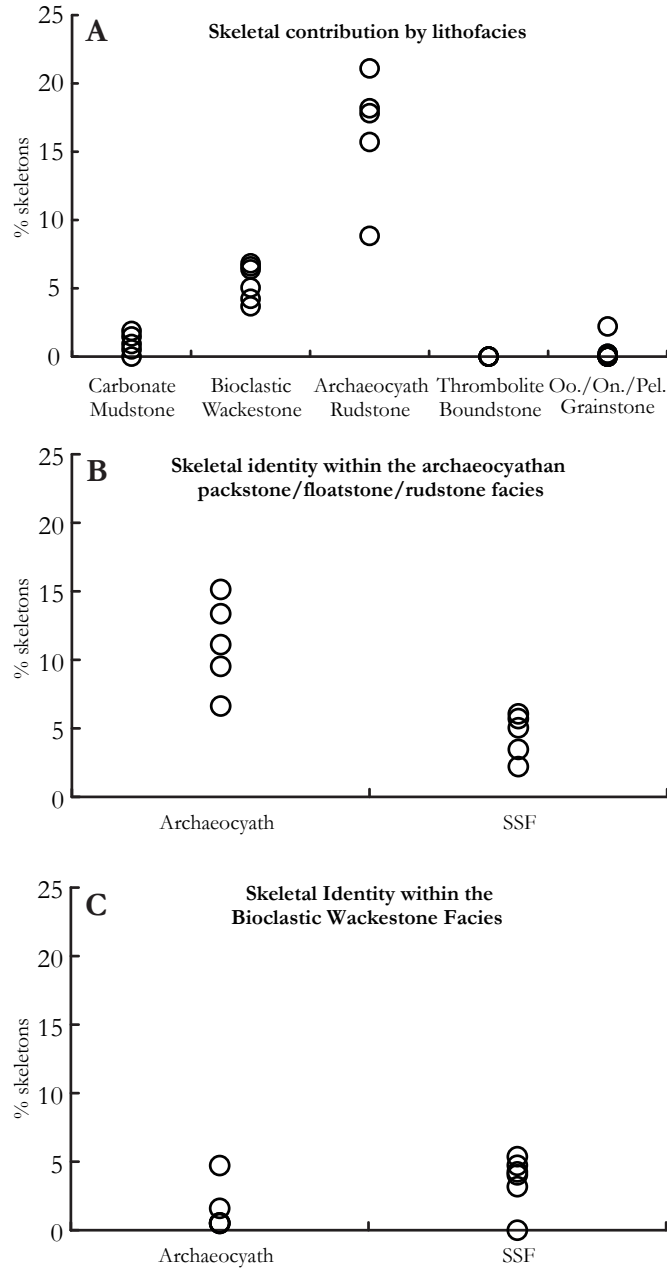


Figure 4.10: Percent skeletal contribution within the Pedroche Formation as determined from point counts of representative petrographic thin-sections (see Table 2 for data). Individual circles represent data from a single thin section. A) Percent skeletal contribution by carbonate lithofacies. Samples representative of the carbonate mudstone (n = 5), bioclastic wackestone (n = 6), and archaeocyath rudstone (n = 5) lithofacies derive exclusively from section LE. Samples representative of the thrombolite boundstone (n = 5) and ooid/oncoid/peloid grainstone lithofacies (n = 9) derive from sections AP and PR. B) Taxonomic identity of the skeletal contribution (i.e., archaeocyath versus small shelly fossil (SSF)) to the archaeocyath rudstone lithofacies and C) the bioclastic wackestone lithofacies.

facies is composed entirely of micritic clot textures ($37\pm 6\%$) set within a microspar matrix (herein interpreted as neomorphosed micrite; $49\pm 6\%$; Fig. 11b). Similarly, the ooid/oncoid/peloid grainstone lithofacies is composed almost entirely of either ooids, oncoids/peloids ($39\pm 18\%$ and $5\pm 9\%$, respectively) and sparry cement ($47\pm 9\%$; Fig. 11c).

4.6.2 SKELETAL CONTRIBUTIONS TO THE PEDROCHE FORMATION

The assignment of the Pedroche Formation to Cambrian Series 2, Stage 3 provides context for comparing its carbonate production in general, and skeletal contributions in particular, to contemporaneous carbonate platforms and archaeocyathan bioherms. First, however, we must address how well our point-count data estimate skeletal contributions to these lithofacies. All Pedroche samples reveal some evidence of fabric destructive diagenesis. The subset of thin-sections analyzed in detail display the least pervasive fabric-destructive diagenesis such that point counts of textural fabrics and fossil occurrences should best approximate the primary depositional texture. Nevertheless, the results presented here are necessarily minimum estimates of the primary carbonate constituents (e.g., skeletons, coated grains) or maximum estimates of secondary textures (e.g., cements). Even when primary matrix microfibrils are difficult to discern, however, original skeletal elements often retain their diagnostic features (e.g., Fig. 4a).

The most pervasive fabric-destructive events targeted the thrombolitic boundstone facies, hence our limited point-count observations ($n=5$). Despite field observation of archaeocyaths (and other skeletons) associated with the thrombolite boundstone lithofacies (Fig. 9d), none of the thin-sections analyzed included a quantifiable skeletal contribution (Fig. 10a, 11b). Likewise, only one thin-section from the grainstone lithofacies included a quantifiable skeletal contribution (Fig. 10a, 11c). It is possible

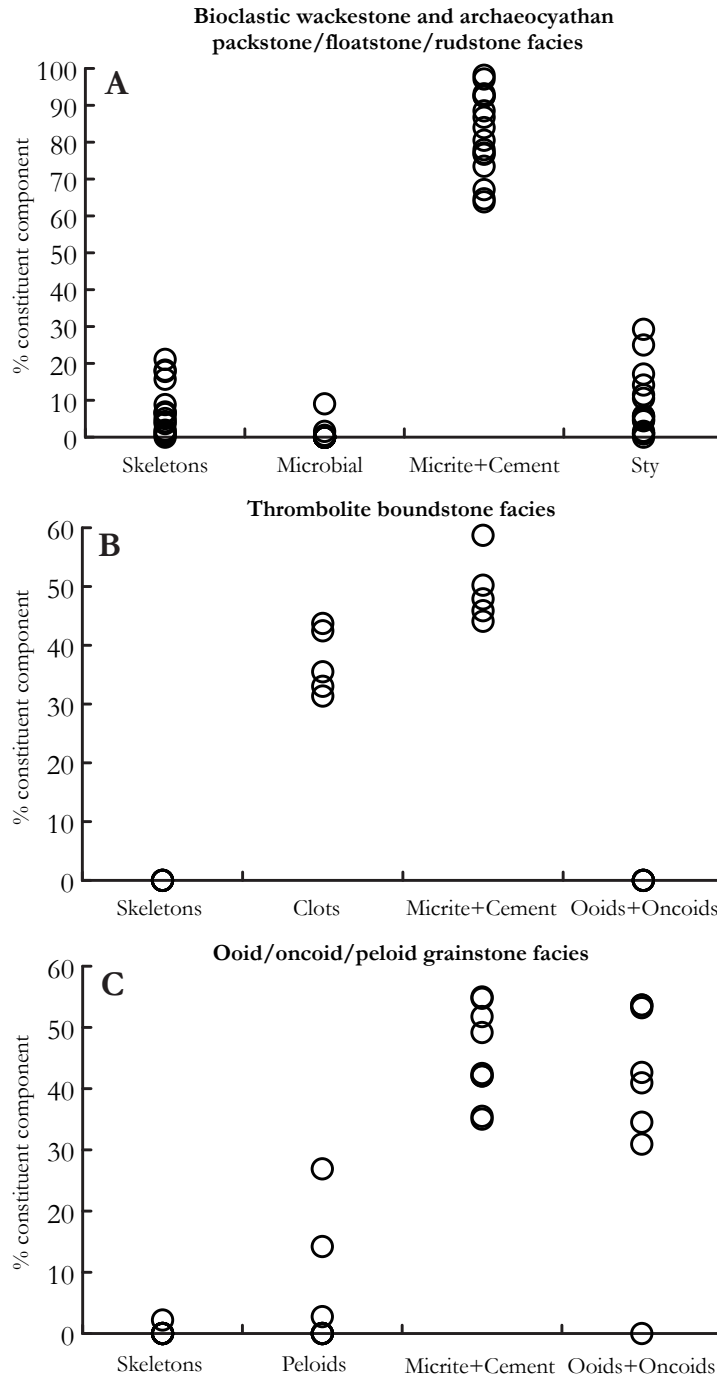


Figure 4.11: Percent constituent components of the carbonate lithofacies of Pedroche Formation as determined from point counts of representative petrographic thin-sections (see Table 2 for data). A) Constituent components of the bioclastic wackestone and archaeocyathan packstone–floatstone–rudstone lithofacies. B) Constituent components of the thrombolite boundstone lithofacies. C) Constituent components of the ooid/oncoid/peloid grainstone lithofacies.

that fabric-destructive recrystallization caused point count data to underrepresent skeletal contribution to these lithofacies. We prefer, however, the interpretation that while archaeocyath and other skeletal elements are present within this lithofacies, their absence (or low abundance) from point-count data correctly implies limited abundance or, at the most, a spatially-discrete enrichment in skeletal clasts that nevertheless reflects a low total skeletal volume in these lithofacies.

Total skeletal contribution within the archaeocyath-bearing reef facies at Las Ermitas is similar to that determined by Hicks and Rowland (2009) for microbial bioherms of the Cambrian Series 2, Stage 3–4 Xiannudong Formation, Yangtze Platform, southern China, as well as by Pruss et al. (2012) for archaeocyathan patch-reefs of the Cambrian Series 2, Stage 4 Forteau Formation, southern Labrador, Canada (Fig. 12a). Likewise, the percentage of total skeletal material representing archaeocyaths (Fig. 12b) versus all other fossils (Fig. 12c) is similar between these localities, with the notable exception of higher (up to 38%) archaeocyath abundance reported by Rowland and Gangloff (1988) within microbial-boundstone of the Cambrian Series 2, Stage 3 lower Poleta Formation, western Nevada, USA. We note, however, that the percent archaeocyath abundance determined by Rowland and Gangloff (1988) derives from volumetric determinations via tracing methods; thus, results from this method over-estimate skeletal contribution in comparison to the grain-solid point count method employed in both this study and by Pruss et al. (2012) and cannot be directly compared to these studies. More generally, Debrenne (2007) has estimated that while the percent contribution of archaeocyaths to lower Cambrian bioherms can be as high as the 38% reported by Rowland and Gangloff (1988) in high energy reef crests, it is more commonly 13% or less in lower energy settings similar to those interpreted for the Pedroche Formation.

Taken together, thin-section point-counts of fossil abundance and identity within

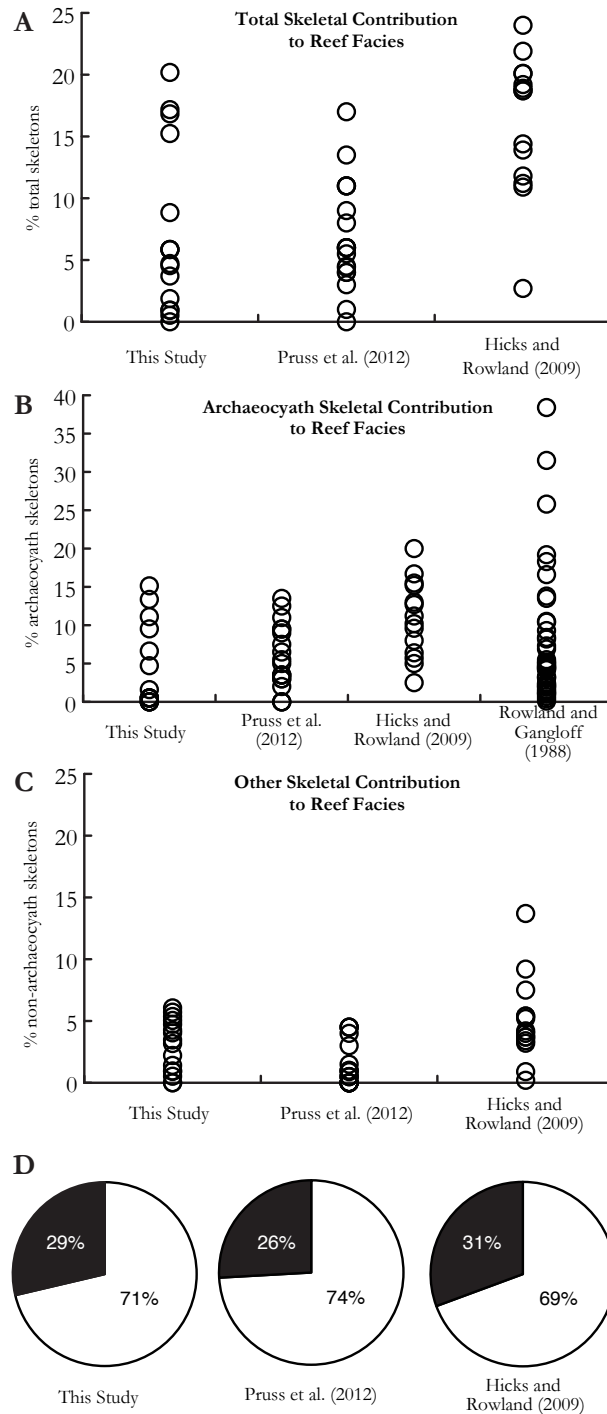


Figure 4.12: Comparison of the percent skeletal contribution to archaeocyath-bearing reef and inter-reef lithologies between the Pedroche Formation and other reef/inter-reef localities. A) Total skeletal contribution, B) archaeocyath contribution, and C) non-archaeocyath skeletal contribution to reef and inter-reef lithologies. D) Average proportion of archaeocyath versus non-archaeocyath skeletal material.

Cambrian archaeocyathan–microbial boundstone reef facies provide consistent views on reef ecology. Most lower Cambrian bioherms are microbialites that contain archaeocyaths. Maximum skeletal abundance is similar at the three localities for which quantitative data are available (Fig. 12a), confirming previous interpretations that archaeocyath-bearing microbial reefs represent important but spatially limited loci of carbonate production (Rowland and Gangloff, 1988; Hicks and Rowland, 2009; Pruss et al., 2012). Moreover, skeletal carbonate production is partitioned amongst archaeocyath and other skeletal taxa in a consistent ratio of $\sim 3:1$ for all three localities (Fig. 12d). Thus, if archaeocyaths were not actively displacing other taxa from ecological niches, the evolution and expansion of the Archaeocyatha during Cambrian Series 2 likely buoyed skeletal carbonate production beyond the low diversity, low abundance observed in other places and at other times in the Cambrian (Pruss et al., 2010).

One significant difference between the Pedroche and Forteau formations (Pruss et al., 2012) and, to a lesser extent, the Xiannudong Formation (Hicks and Rowland, 2009), is the minimal occurrence of skeletal material in Pedroche grainstone lithologies. Pruss et al. (2012) found up to 20.5% (average 12.4%) skeletal material in grainstone flanking archaeocyathan reefs, whereas we found skeletons in only one thin-section (of nine analyzed) with a total skeletal contribution of 2% (Fig. 10a). Grainstone shoals and sheets represent dynamic, high-energy depositional environments and rapidly changing wave-energies often winnow skeletal fragments into coarse lag deposits. Thus, for sedimentological reasons, we might expect high variance in the skeletal contribution to grainstone lithologies. Specifically, Pruss et al. (2012) identified echinoderms as the major constituent of grainstone skeletal debris, whereas no echinoderm fossils were observed in Pedroche thin-section. Both fossils and molecular clocks indicate an initial diversification of echinoderms during Cambrian Series 2 (Peterson et al., 2004; Bottjer et al., 2006), but early taxa appear to

have been facies bound, including, in the case of helicoplacoids, to siliciclastic facies (Smith, 1985; Dornbos and Bottjer, 2000). Thus, differences from one platform to another may well reflect environmental distinctions.

4.6.3 CARBONATE PRODUCTION ON THE PEDROCHE PLATFORM

The Pedroche Formation contributes to a strengthening picture of carbonate deposition on Cambrian shelves and platforms. Within the Arroyo Pedroche and Pilgrimage Road sections, microbialites are both the most conspicuous and most abundant contributors to platform deposition, comprising 55–60% of all carbonates. Coated grains account for 8–13% of carbonate accumulation, while the remaining 32–33% encompasses grainstone ‘ribbonites,’ recrystallized textures, and other, minor lithologies. Skeletons, especially archaeocyaths, are locally conspicuous and abundant, but because facies other than archaeocyath rudstones contain such a low skeletal component, the total measurable contribution of carbonate skeletons to the platform accumulation is low, perhaps 5–6% by volume. This is not too different from Cambrian samples measured in China, Newfoundland, Labrador, and the North American Cordillera, and well below skeletal abundances in most Middle Ordovician and younger deposits (Hicks and Rowland, 2009; Pruss et al, 2010, 2012). That is, despite the fact that Pedroche and coeval carbonates accumulated during the acme of Cambrian body plan diversification (Knoll and Carroll, 1999; Erwin et al., 2011), and despite the observation that most of the skeletal designed ever evolved by animals appeared during this interval (Thomas et al., 2000), skeletons remained a subsidiary component of carbonate deposits.

Clearly, Pedroche and other Cambrian carbonate accumulations are distinct from younger examples. How do they compare with older platform and shelf deposits? While countless stratigraphic sections transect Proterozoic carbonate platforms, few

studies compile the percentage of lithofacies at the outcrop-scale. Knoll and Swett (1990) reported that stromatolites, oncolites and microbial laminates make up $\sim 25\%$ of all carbonates of the ca. 800-750 Ma Akademikerbreen Group, with oolites contributing $\sim 15\%$, and the remaining $\sim 60\%$ consisting of micrite, arenites (carbonate grainstone), and rudites derived from the erosion and re-deposition of mostly micrite lithologies. Thus, even more than this Neoproterozoic succession, microbialites represent a significant component of Pedroche carbonate accumulation.

Proterozoic and Cambrian carbonates differ, of course, in the nature of constituent microbialites, being largely stromatolitic in older rocks and thrombolitic in the Cambrian (Grotzinger, 1990; Grotzinger et al., 2000). Indeed, in the Pedroche Formation, stromatolites, developed in a marginal restricted environment, make up only about 0.25% of the package as a whole. In modern settings, thrombolitic textures develop in subtidal environments where eukaryotic algae, especially macroscopic algae, colonize microbialite surfaces (Feldmann and McKenzie, 1998; Andres and Reid, 2006). The holdfasts of sessile benthic invertebrates might also disrupt microbial lamination (Grotzinger et al., 2000). Such observations provide a framework for interpreting Pedroche and other Cambrian thrombolites. These structures accreted subtidally, where the influence of traction load sediments was small (e.g., Pratt and James 1982, 1986). And, fossils and molecular clocks support the hypothesis that the diversification of green algae and sessile benthic animals contributed to the distinctive fabrics of subtidal Cambrian microbialites (e.g., Grotzinger et al., 2000). In general then, the introduction of animal and algal macrobenthos into early Phanerozoic marine communities modified the morphologies, fabrics, and facies distribution of microbialites, but did not result in their elimination from carbonate platforms and shelves. That occurred later, with the mid-Ordovician radiation of heavily skeletonized sessile macrobenthos.

Increasingly, then, the Cambrian stands out as a transitional interval of carbonate deposition, with carbonate production still linked to the physical and microbial processes that had governed carbonate deposition for billions of years, but with evolving algae and animals beginning to exert a quantifiable influence on the processes, loci and fabrics of shelf and platform carbonates.

4.7 CONCLUSIONS

Carbonate carbon isotope ($\delta^{13}C_{carb}$) data from three stratigraphic sections of the Pedroche Formation provide the first chemostratigraphic curve for Cambrian stratigraphy of the Ossa Morena geotectonic zone, Iberia. The Pedroche Formation captures the apex of an $\sim 3\text{‰}$ positive $\delta^{13}C_{carb}$ excursion preceding a plateau around -1.5‰ . Within the context of trilobite, small shelly fossil, and archaeocyath biostratigraphy, we correlate this isotopic variability to excursion IV of the Siberian chemostratigraphic framework, correlative to Cambrian Series 2, Stage 3.

Archaeocyath-bearing framework reefs, inter-reef, and flanking-reef talus represent loci for skeletal carbonate production and accumulation within the Pedroche Formation, with skeletal material comprising a maximum of 21% of total carbonate. Of the skeletal material quantified, archaeocyaths contributed an average of $\sim 71\%$, with the remainder attributable to small shelly fossils, trilobites, and calcitic brachiopods. The production and export of skeletal material beyond these depositional environments contributed little to coeval carbonate accumulation. Instead, microbial and abiotic carbonates dominate. Despite an important skeletal presence, carbonate accumulation and distribution within the Cambrian Pedroche Formation appears more similar to Neoproterozoic accumulations than Phanerozoic skeletal reef ecosystems.

ACKNOWLEDGMENTS

We thank the Agouron Institute for generous support.

4.8 REFERENCES CITED

- Andres, M.S., and Reid, P.R. 2006, Growth morphologies of modern marine stromatolites; a case study from Highborne Cay, Bahamas: *Sedimentary Geology*, v. 185, p. 319-328.
- Babcock, L.E., and Peng, S., 2007, Cambrian chronostratigraphy: Current state and future plans: *Palaeogeography, Palaeoclimatology, Palaeoecology*, v. 254, p. 62-66.
- Bottjer, D.J., Davidson, E.H., Peterson, K.J., and , Cameron, R.A. 2006, Paleogenomics of echinoderms: *Science*, v. 314. p. 956-960.
- Brasier, M.D., Rozanov, A., Yu., Zhuravlev, A. Yu, Corfield, R.M., and Derry, L.A., 1994, A carbon isotope reference scale for the Lower Cambrian succession in Siberia: report of IGCP project 303: *Geological Magazine*, v. 131. P. 767-783.
- Cowan, C.A., and James, N.P., 1993, The interactions of sea-level change, terrigenous sediment influx, and carbonate productivity as controls on Upper Cambrian Grand Cycles of western Newfoundland, Canada: *Geological Society of America Bulletin*, v. 105, p. 1576-1590.
- Dallmeyer, R.D. and Martínez García, E., (eds.), 1990, *Pre-Mesozoic Geology of Iberia*. Springer, New York, 416 p.
- Debrenne, F., 2007, Lower Cambrian archaeocyathan bioconstructions: *Comptes Rendus Palevol*, v. 6, p. 5-19.
- Dornbos, S.Q., and Bottjer, D.J., 2000, Evolutionary paleoecology of the earliest echinoderms: Helicoplacoids and the Cambrian substrate revolution: *Geology*, v. 28, p. 839-842.
- Eguíluz, L., Gil Ibarguchi J.I., Ábalos, B. and A. Apraiz, A., 2000, Superposed Hercynian and Cadomian orogenic cycles in the Ossa-Morena zone and related areas of the Iberian Massif: *Geological Society of America Bulletin*, v. 112, p. 1398-1413.
- Erwin, D. H., Laflamme, M. Tweedt, S.M., Sperling, E.A., Pisani, D., and Peterson. K.J., 2011, The Cambrian conundrum: early divergence and later ecological success in the early history of animals: *Science*, v. 334, p. 109–1097.
- Feldmann, M. and McKenzie, J., 1998, Stromatolite-thrombolite associations in a modern environment, Lee Stocking Island, Bahamas: *Palaios*, v. 13, p. 201-212.

- Fernández-Remolar, D.C., 2001, Latest Neoproterozoic to Middle Cambrian body fossil record in Spain (exclusive of trilobites and archaeocyaths) and their stratigraphic significance: *GFF*, v. 123, p. 73-80.
- Flügel, E., 2004, *Microfacies of carbonate rocks: Analysis, Interpretation, and Application*, Springer, New York, 976 p.
- Grotzinger, J.P., 1989, Facies and evolution of Precambrian carbonate depositional systems: emergence of the modern platform archetype: *Society of Economic Paleontologists and Mineralogists Special Publication 44*, p. 79-106.
- Grotzinger, J.P., 1990, Geochemical model for Proterozoic stromatolite decline: *American Journal of Science*, v. 290A, p. 80-103.
- Grotzinger, J.P., and Knoll, A.H., 1999, Stromatolites in Precambrian carbonates: Evolutionary mileposts or environmental dipsticks?: *Annual Review of Earth and Planetary Sciences*, v. 27, p. 313-358.
- Grotzinger, J.P., and James, N.P., 2000, Precambrian carbonates: Evolution of understanding: *Society for Sedimentary Geology (SEPM) Special Publication*, v. 67, p. 3-22.
- Grotzinger, J.P., Watters, W.A., and Knoll, A.H., 2000, Calcified metazoans in thrombolite-stromatolite reefs of the terminal Proterozoic Nama Group, Namibia: *Paleobiology*, v. 26, p. 334-359.
- Gubanov, A.P., Fernández-Remolar, D.C., and Peel, J.S., 2004, Early Cambrian molluscs from Sierra de Córdoba (Spain): *Geobios*, v. 37, p. 199-215.
- Hicks, M., and Rowland, S.M., 2009, Early Cambrian microbial reefs, archaeocyathan inter-reef communities, and associated facies of the Yangtze Platform: *Palaeogeography, Palaeoclimatology, Palaeoecology*, v. 281, p. 137-153.
- Hinz-Schallreuter, I., Gozalo, R., and Liñán, E., 2008, New bradorid arthropods from the Lower Cambrian of Spain: *Micropaleontology*, v. 53, p. 497-510.
- Holland, S.M., 1995, The stratigraphic distribution of fossils: *Paleobiology*, v. 21, p. 92-109.
- Jensen, S., Palacios, T., and Martí Mus, M., 2012, Revised biochronology of the Lower Cambrian on the Central Iberian zone, Iberian massif, Spain: *Geological Magazine*, v. 147, p. 690-703.

- Knoll, A.H., and Carroll, S.B., 1999, The early evolution of animals: Emerging views from comparative biology and geology: *Science*, v. 284, p. 2129-2137.
- Knoll, A.H., and Swett, K., 1990, Carbonate deposition during the late Proterozoic Era: an example from Spitsbergen: *American Journal of Science*, v. 290-A, p. 104-132.
- Kouchinsky, A., Bengtson, S., Pavlov, V., Runnegar, B., Torssander, P., Young, E., and Ziegler, K., 2007, Carbon isotope stratigraphy of the Precambrian–Cambrian Sukharikha River section, northwestern Siberian platform: *Geological Magazine*, v. 144, p. 1-10.
- Kouchinsky, A., Bengtson, S., Runnegar, B., Skovsted, C., Steiner, M., and Vendrasco, M., 2012, Chronology of early Cambrian biomineralization: *Geological Magazine*, v. 149, p. 221-251.
- Landing, E., and Geyer, G., In Review, Deficiencies of the first appearance datum (FAD) concept: relevance to lowest Cambrian correlation standards and diachroneity of the oldest trilobites: *Earth-Science Reviews*.
- Landing, E., Bowring, S.A., Davidek, K.L., Westrop, S.W., Geyer, G., and Heldmaier, W., 1998, Duration of the Early Cambrian: U-Pb ages of volcanic ashes from Avalon and Gondwana: *Canadian Journal of Earth Sciences*, v. 35, p. 329-338.
- Liñán, E., and Quesada, C., 1990, Rift Phase (Cambrian), in Dallmeyer, R.D. and Martínez García, E., (eds.), *Pre-Mesozoic Geology of Iberia*. Springer, New York, 416 p.
- Liñán, E., Dies, M.E., Gámez Vintaned, J.A., Gozalo, R., Mayoral, E., and Muñiz, F., 2005, Lower Ovetian (Lower Cambrian) trilobites and biostratigraphy of the Pedroche Formation (Sierra de Córdoba, southern Spain): *Geobios*, v. 38, p. 365-381.
- Liñán, E., Gozalo, R., Dies Álvarez, M.E., Gámez Vintaned, J.A., and Zamora, S., 2008, Nuevos trilobites del Ovetiense inferior (Cámbrico Inferior bajo) de Sierra Morena (España): *Ameghiniana*, v. 45, p. 123-128.
- Liñán, E., Perejón, A., and Sdzuy, K., 1993, The Lower-Middle Cambrian stages and stratotypes from the Iberian Peninsula: a revision: *Geological Magazine*, v. 130, p. 817-833.
- Maloof, A.C., Schrag, D.P., Crowley, J.L., and Bowring, S.A., 2005, An expanded record of Early Cambrian carbon cycling from the Anti-Atlas Margin, Morocco: *Canadian Journal of Earth Sciences*, v. 42, p. 2195-2216.

- Maloof, A.C., Porter, S.M., Moore, J.L., Dudás, F.Ö., Bowring, S.A., Higgins, J.A., Fike, D.A., and Eddy, M.P., 2010a, The earliest Cambrian record of animals and ocean geochemical change: *Geological Society of America Bulletin*, v. 122, p. 1731-1774.
- Maloof, A.C., Ramezani, J., Bowring, S.A., Fike, D.A., Porter, S.M., and Mazouad, M., 2010b, Constraints on early Cambrian carbon cycling from the duration of the Nemakit-Daldynian—Tommotian boundary $\delta^{13}C$ shift, Morocco: *Geology*, v. 38, p. 623-626.
- Myrow, P.M., Taylor, J.F., Runkel, A.C., and Ripperdan, R.L., 2012, Mixed siliciclastic-carbonate upward-deepening cycles of the upper Cambrian inner detrital belt of Laurentia: *Journal of Sedimentary Research*, v. 82 p. 216-231.
- Payne, J.L., Lehrmann, D.J., Wei, J., and Knoll, A.H., 2006, The pattern and timing of biotic recovery from the end-Permian mass extinction on the Great Bank of Guizhou, Guizhou Province, south China: *PALAIOS*, v. 20, p. 63–85.
- Peng, S., and Babcock, L.E., 2011, Continuing progress on chronostratigraphic subdivision of the Cambrian System: *Bulletin of Geosciences*, v. 86, p. 391-396.
- Perejón, A., 1986, Bioestratigrafía de los Arqueociatos en España: *Cuadernos de Geología Ibérica*, v. 9, p., 213-216.
- Perejón, A., 1989, Arqueociatos del Ovetiense en las sección del Arroyo Pedroche, Sierra de Córdoba, España: *Boletín de la Real Sociedad Española de Historia Natural (Geología)*, v. 84, p. 143-247.
- Perejón, A., 1994, Palaeogeographic and biostratigraphic distribution of Archaeocyatha in Spain: *Courier Forschungsinstitut Senckenberg*, v. 172, p. 341-354.
- Perejón, A., Moreno-Eiris, E., and Menendez, S., 2008, Los arqueociatos del Cámbrico Inferior de Navalcastaño (Sierra Morena, Córdoba, España: *Bol. R. Soc. Esp. Hist. Nat. Sec. Geol.*, v. 102, p. 93-119.
- Peterson, K.J., Lyons, J.B., Nowak, K.S., Takacs, C.M., Wargo, M.J., and McPeck, M.A., 2004, Estimating metazoan divergence times with a molecular clock: *Proceedings of the National Academy of Sciences, USA*, v. 101, p. 6536-6541.
- Pratt, B.R., 1984, Epiphyton and Renalcis – Diagenetic microfossils from calcification of coccoid blue-green algae: *Journal of Sedimentary Petrology*, v. 54, p. 948-971.
- Pratt, B.R., and James, N.P. 1982, Cryptalgal-metazoan bioherms of Early Ordovician age in the St-George Group, Western Newfoundland: *Sedimentology*, v. 29, p. 543-569.

- Pratt, B.R., and James, N.P., 1986, The St. George Group (Lower Ordovician) in western Newfoundland: tidal flat island model for carbonate sedimentation in shallow epeiric Seas: *Sedimentology*, v. 33, p. 313-343.
- Pruss, S.A., Finnegan, S., Fischer, W.W., and Knoll, A.H., 2010, Carbonates in skeleton-poor seas: New insights from Cambrian and Ordovician strata of Laurentia: *Palaios*, v. 25, p. 73-84.
- Pruss, S.A., and Clemente, H., 2011, Assessing the role of skeletons in Early Paleozoic carbonate production: Insights from Cambro-Ordovician strata, Western Newfoundland, in Laflamme, M., Schiffbauer, J.D., and Dornbos, S.Q., eds., *Quantifying the Evolution of Early Life, Numerical approaches to the evaluation of fossils and ancient ecosystems*: Springer, New York, 462 p.
- Pruss, S.A., Clemente, H., and Laflamme, M., 2012, Early (Series 2) Cambrian archaeocyathan reefs of southern Labrador as a locus for skeletal carbonate production: *Lethaia*, v. 45, p. 401-410.
- Rowland, S.M. and Gangloff, R.A., 1988, Structure and paleoecology of Lower Cambrian reefs: *Palaios*, v. 3, p. 111–135.
- Rožanov, A.Yu., Parkhaev, P.Yu., Demidenko, Yu., and Skorlotova, N.A., 2011, *Mobergella radiolata*—a possible candidate for defining the base of Cambrian Series 2 and Stage 3: *Museum of Northern Arizona Bulletin*, v. 67, p. 304–306.
- Sarmiento, J.L. and Gruber, N., 2006, *Ocean biogeochemical dynamics*: Princeton University Press, New Jersey, 503 p.
- Smith, A.B., 1985, Cambrian eleutherozoan echinoderms and the early diversification of edrioasteroids: *Palaeontology*, v. 28, p. 715-756.
- Steiner, M., Li, G., and Ergaliev, G., 2011, Toward a subdivision of the traditional Lower Cambrian: *Museum of Northern Arizona Bulletin*, v. 67, p. 306–308.
- Stoddart, D.R., 1969, Ecology and morphology of recent coral reefs: *Biological Reviews*, v. 44, p. 433-498.
- Thomas, R.D.K., Shearman, R.M., and Stewart, C.W., 2000, Evolutionary exploitation of design options by the first animals with hard skeletons: *Science*, v. 288, p. 1239-1242.
- Van der Plas, L. and Tobi, A.C., 1965, A chart for judging the reliability of point counting results: *American Journal of Science*, v. 263, p. 87-90.

- Vennin, E., Álvaro, J.J., Moreno-Eiris, E., and Perejón, A., 2003, Early Cambrian coelobiontic communities in tectonically unstable crevices developed in Neoproterozoic andesites, Ossa-Morena, southern Spain, v. 36, p. 53-65.
- Wood, R., 1998, The ecological evolution of reefs: *Annual Review of Ecology and Systematics*, v. 29, p. 179-206.
- Wood, R.A., Grotzinger, J.P., and Dickson, J.A.D., 2002, Proterozoic modular biomineralized metazoan from the Nama Group, Namibia: *Science*, v. 296, p. 2383–2386.
- Zeebe, R.E., and Westbroek, P., 2003, A simple model for the CaCO₃ saturation state of the ocean: The "Strangelove", the "Neritan", and the "Cretan" Ocean: *Geochemistry, Geophysics, Geosystems*, v. 4, 1104, doi:10.1029/2003GC000538.
- Zhu, M.Y., Babcock, L.E., and Peng, S.C., 2006, Advances in Cambrian stratigraphy and paleontology: integrating correlation techniques, paleobiology, taphonomy and paleoenvironmental reconstruction: *Palaeoworld*, v. 15, p. 217–222.

CHAPTER 5

A MECHANISM FOR OSCILLATORY TRUE POLAR WANDER IN DEEP TIME

ABSTRACT

Paleomagnetic studies [Mitchell et al., 2010; Maloof et al., 2006; Mitchell et al., 2010b; Van der Voo et al., 1994; Steinberger & Torsvik, 2008] of Paleoproterozoic to Cretaceous rocks propose a suite of large and relatively rapid (10s of degrees with duration ~ 10 -100 Myr) excursions of the rotation pole relative to the surface geography, or true polar wander (TPW), that may link together in an oscillatory, approximately coaxial succession about the center of the contemporaneous supercontinent [Evans, 1998, 2003; Steinberger & Torsvik, 2008]. Within the framework of the standard rotational theory [Gold, 1955; Goldreich and Toomre, 1969], in which a delayed viscous adjustment of the rotational bulge acts to stabilize the rotation axis [Ricard et al., 1993], geodynamic models for oscillatory TPW generally appeal to consecutive, opposite loading phases of comparable magnitude [Evans, 1998; Greff-Lefftz, 2004; Steinberger & Torsvik, 2010]. To revisit this issue, we adopt a non-linear rotational stability theory [Ricard et al., 1993], and incorporate into this theory the stabilizing effect of TPW-induced elastic stresses in the lithosphere [Willemann, 1984; Matsuyama et al., 2006]. We demonstrate that convectively-driven inertia perturbations acting on a nearly prolate nonhydrostatic Earth [Evans, 1998, 2003] with an effective elastic

lithospheric thickness (EET) of ~ 10 km yield oscillatory TPW paths consistent with paleomagnetic inferences. This estimate of EET can be reduced if the rotation axis was stabilized by long-term excess ellipticity in the plane of the TPW. We speculate that these sources of stabilization, acting on TPW driven by a time-varying mantle flow field [Greff-Lefftz, 2004; Steinberger & Torsvik, 2010; Spada et al., 1992; Rouby et al., 2010; Richards et al., 1999; Davaille, 1999], provide a mechanism for linking distinct, oscillatory TPW events proposed for the last few billion years of Earth history.

5.1 INTRODUCTION: THE PALEOMAGNETIC RECORD

Paleomagnetic inferences of TPW are complicated by the difficulty of disentangling polar motion and continental drift. However, independent inferences of five distinct episodes of large-amplitude TPW spanning the Paleoproterozoic to the Cretaceous [Mitchell et al., 2010; Maloof et al., 2006; Mitchell et al., 2010b; Van der Voo et al., 1994; Steinberger & Torsvik, 2008] suggest a marked tendency for pseudo-oscillatory reorientation of the rotation axis [Evans, 1998, 2003].

Figure 1a summarizes a suite of inferences of large amplitude TPW, based on paleomagnetic reconstructions of apparent polar wander (APW) paths, over a time period that extends from the Paleoproterozoic Orosirian period to the Cretaceous. The inferences plotted in the figure are taken directly from the primary literature cited below. Future, improved constraints on plate motions across these various time intervals will undoubtedly lead to a revision of the magnitude and duration of the inferred TPW events, but, taken together, they strongly suggest an inherent tendency toward oscillatory polar motion.

An edited form of this chapter is in review at *Nature* with co-authors: Jerry X. Mitrovica, Ngai-Ham Chan, Konstantin Latychev and Isamu Matsuyama.

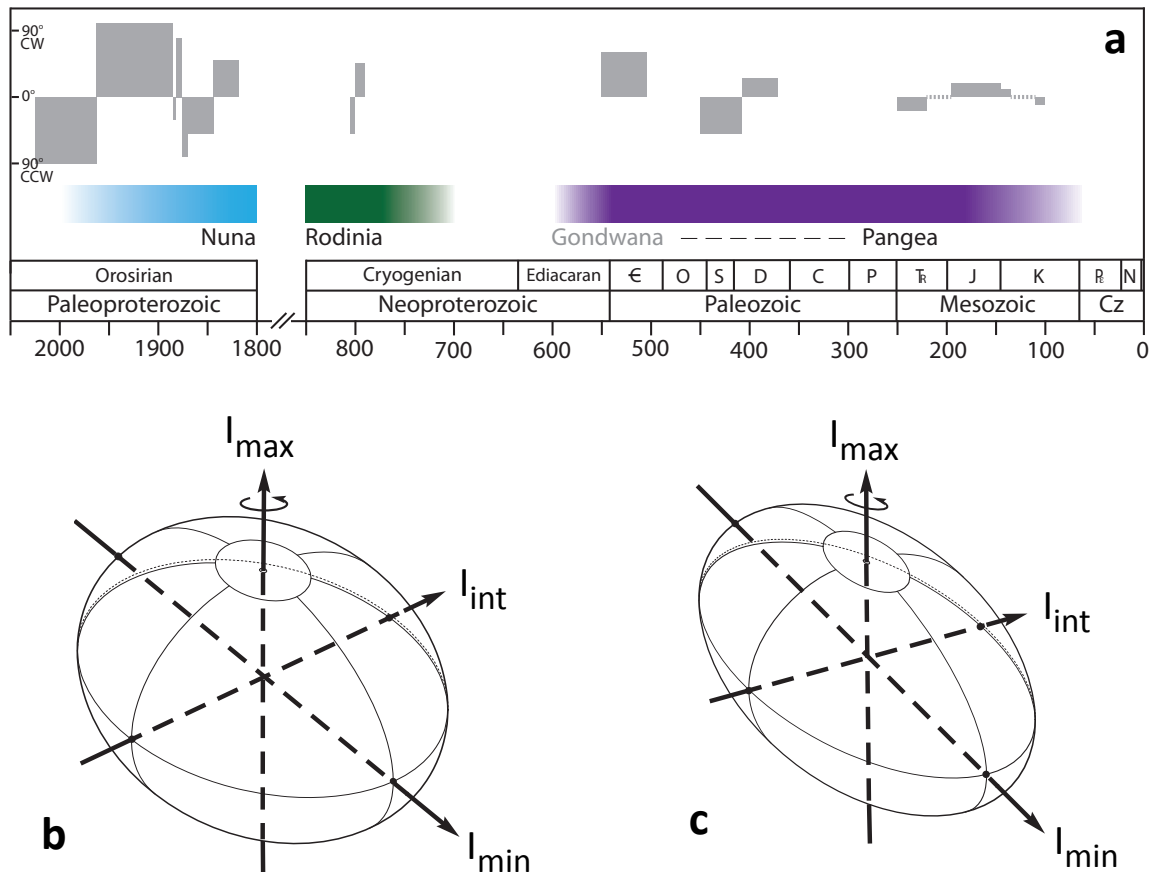


Figure 5.1: TPW, supercontinent phases and the Earth's figure in deep time. (a) Time line (in Myr ago) for paleomagnetically-inferred TPW events (shaded grey boxes) through the Proterozoic (not including the span from 1800-850 Myr ago) and Phanerozoic eons, together with the associated history of supercontinent aggregation, stability, and disaggregation. The Gondwanan superterrane is shown as a precursor to Pangea. The height of the grey boxes is proportional to the paleomagnetically-inferred TPW angle (legend at left). If the box is plotted rising above (below) 0° , the pole moved clockwise (counter-clockwise) relative to an observer on the contemporaneous supercontinent or superterrane. The abbreviations listing Phanerozoic periods represent, from left to right, the Cambrian, Ordovician, Silurian, Devonian, Carboniferous, Permian, Triassic, Jurassic, Cretaceous, Paleogene, and Neogene. The sequence of TPW oscillations in the Paleoproterozoic define the Coronation loop [Mitchell et al., 2010]; the Neoproterozoic TPW oscillation is taken from Maloof et al. [2006]; the Late Ediacaran - Early Cambrian TPW event is adopted from Mitchell et al. [2010b]; the Late Ordovician - Early Devonian oscillation is taken from Van der Voo et al. [1994]; and the pair of TPW oscillations spanning the Early Triassic - Cretaceous were inferred by Steinberger & Torsvik [2008]. The two dashed lines appearing within the latter two oscillations represent periods of relative stability in the pole position in the middle of each oscillation. (b) Schematic illustration of an Earth model with a triaxial non-hydrostatic figure. The rotation pole is coincident with the axis of maximum non-hydrostatic inertia. The maximum (I_{max}), intermediate (I_{int}) and minimum moments of inertia (I_{min}) are distinct. (c) A nearly prolate non-hydrostatic figure of the Earth. The maximum and intermediate moments of inertia are nearly equal and distinct from the minimum moment, i.e., $I_{max} \sim I_{int} > I_{min}$.

The complex, Paleoproterozoic event is adopted from a recent re-analysis by Mitchell et al. [2010] of the so-called Coronation APW loop. These authors argue, based on structural mapping of strike-slip fault systems within the Slave craton and numerous paleocurrent measurements from the Great Slave basin, that vertical axis crustal rotations were modest. Moreover, they claim that the inferred rates are incompatible with plate motions, and they thus interpret the rotation-corrected APW path as a sequence of oscillatory TPW episodes, as shown on the figure. (We note the final two oscillations only have dates on their initiation and termination, and in these cases we partition their duration equally.) Paleomagnetic records over this time interval from sites in the Kaapvaal Craton have led to contradictory conclusions for either a large amplitude, looping APW path from ~ 2.05 -1.87 Gyr ago [DeCock et al., 2006] or low rates of APW [Letts et al., 2011]. This inconsistency raises a potentially important caveat in regard to inferences of Orosirian TPW.

The Neoproterozoic TPW oscillation event (803-792 Myr ago) is taken from the Maloof et al. [2006] analysis of a carbonate succession in Svalbard. Their inference of a greater than $\sim 50^\circ$ displacement of the pole is based on data from a continuous stratigraphic section that was reproduced at three localities. The event is coeval with a large amplitude, negative carbon isotope excursion interpreted to be the Bitter Springs event. The authors use a thermal subsidence model of rifting to infer the absolute age of the event and provide an estimate of the duration (~ 11 Myr). Uncertainties in this modelling suggest an upper bound on the duration of ~ 25 -30 Myr. A variety of paleomagnetic tests (e.g., soft-sediment fold tests, regional-scale fold tests, correlation of magnetic reversals between sections) are used to argue that the magnetic remanence of the samples is primary. The regional fold test indicates that magnetic remanence was acquired before folding in the Silurian-Devonian. Since no Neoproterozoic to Devonian age orogenic event is known for this region, the results of

the tectonic fold tests suggest that thermal or deformational remagnetization is unlikely, but secondary remagnetization cannot be ruled out. Finally, the authors argue that the correlation between the TPW event and the globally observed Bitter Springs isotopic excursion, and the consistency of the event with coeval sea-level changes, lend support to their inference of oscillatory TPW.

The Late Ediacaran-Cambrian TPW event is based on the Mitchell et al. [2010b] analysis of sedimentary strata from the Amadeus Basin, central Australia. The age of the event is determined by intrabasin biostratigraphic and lithostratigraphic correlation. The authors quote TPW rates based on the assumption of a linear (in time) motion of the pole between inferred end points. These rates, and the associated integrated displacements ($61^\circ \pm 16^\circ$), would be higher in the case of a more circuitous pole path, but they would likely be lowered by correction for plate motions. Since Gondwana was fully formed by the Early Cambrian, any age controls on Australian APW/TPW would need to match age controls on any other part of Gondwana. In this regard, contradictory paleomagnetic evidence from Laurentia [McCausland & Hodych, 1998] maps into a significant uncertainty in the age, duration and veracity of the proposed TPW event.

Figure 1a adopts the Van der Voo et al. [1994] inference of an Ordovician to Devonian episode of APW. The inference of a total of $\sim 75^\circ$ of motion in ~ 75 Myr is based on paleopoles from Laurentia, Baltica and Gondwana, and it is consistent with less well-constrained paleopoles from South China and Siberia. Van der Voo et al. [1994] tentatively interprets the data as an oscillatory TPW event involving a 50° counter-clockwise rotation relative to Gondwana from 450-408 Myr ago followed by 25° clockwise motion from 408-372 Myr ago. The details of this inference may be susceptible to potential contamination from plate motions associated with the closing of the Rheic Ocean.

Steinberger & Torsvik [2008] use a global compilation of paleomagnetic data and hot spot records [Torsvik et al., 2008] to estimate mean continental motion over the last 320 Myr. One component of this coherent motion involved multiple rotations around a relatively stable equatorial axis located near the site of the triple junction at the focus of Pangean disaggregation. The authors interpret these rotations as a set of TPW events in the following sequence: (1) an 18° counter-clockwise rotation from 250-220 Myr ago, (2) a clockwise rotation of equal amplitude from 195-145 Myr ago, (3) a 10° clockwise rotation from 145-135 Myr ago, and (4) a counter-clockwise rotation from 110-100 Myr ago that brought the pole back to its original position.

5.2 THE ROTATIONAL STABILITY OF THE EARTH

5.2.1 THE FIGURE OF THE EARTH

Rotational stability is established, in part, by the non-hydrostatic figure of the Earth, that is, the figure after correction for the equilibrium hydrostatic form. The Earth's present-day triaxial figure [Goldreich and Toomre, 1969] (Figure 1b) is driven by convection associated with large thermochemical anomalies (henceforth, "superswells") beneath southern Africa and the Pacific and the circum-Pacific ring of subduction [Ritsema & Van Heijst, 2000; Zhang et al., 2010]. The minimum axis of inertia aligns with the superswells, and the moment difference $I_{max} - I_{int} \sim \frac{1}{2}(I_{max} - I_{min})$. Thus, mantle convection currently drives significant excess ellipticity along both equatorial axes, stabilizing the rotation pole [Goldreich and Toomre, 1969]. This stabilization may explain the more muted TPW in the last 100 Myr [Steinberger & Torsvik, 2008; Evans, 1998; Steinberger & Torsvik, 2010; Goldreich and Toomre, 1969; Zhang et al., 2010; Chan et al., 2011] (Figure 1a). However, superswells are dynamic structures [Davaille, 1999; Oldham & Davies, 2004; Zhong et al., 2007] subject to long-timescale

doming [Davaille, 1999]. Likewise, the geometry of subduction evolves [Spada et al., 1992; Rouby et al., 2010; Richards et al., 1999; Steinberger & Torsvik, 2010]. It is thus probable that there were times in Earth history when large-scale convective flow was more symmetric about the axis of minimum inertia, leading to a prolate figure [Ricard et al., 1993] (Figure 1c). This prolate form would have a strong propensity for TPW in the plane defined by I_{max} and I_{int} , and it has been identified as a favourable pre-condition for episodes of rapid, large magnitude "coaxial" TPW in deep time [Evans, 1998, 2003] (Figure 1a). However, while a prolate figure strongly favours TPW coaxial to the axis I_{min} , the mechanism(s) responsible for the oscillatory nature of the reorientations remain enigmatic.

5.2.2 THE PHYSICS OF TPW

One route to resolving this enigma may be provided by studies of planetary rotation [Willemann, 1984; Matsuyama et al., 2006] that revise the standard equilibrium rotational theory [Gold, 1955; Goldreich and Toomre, 1969] to argue that the rotating system can retain long term memory of previous pole orientations. In this section, we provide an overview of these issues using the schematic Figure 2.

Figure 2A is a schematic illustration of the physics associated with the canonical rotational stability theory of Gold [1955] and Goldreich and Toomre [1969]. An initially hydrostatic Earth (A1) is subject to a convective load (green dot) that pushes the pole away and moves the rotational bulge off the equator (A2). This reorientation acts as a second mass load that resists further TPW. This resistance is transitory because the bulge will ultimately relax perfectly (i.e., hydrostatically) to the new orientation of the rotation axis (A3). This allows further TPW and the system adjusts in incremental steps until the load reaches the equator (A4). At any stage in the evolution, the system loses memory of previous rotational states. If the load is removed

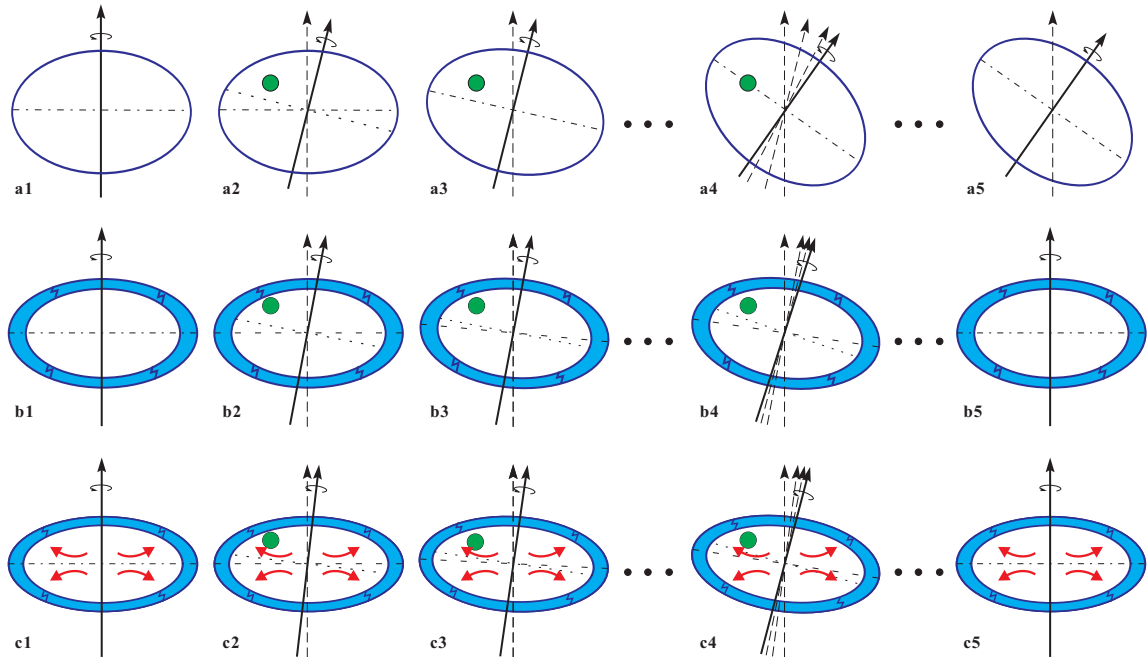


Figure 5.2: The physics underlying the (A) standard [Gold, 1955; Goldreich and Toomre, 1969] and (B) revised [Willemann, 1984; Matsuyama et al., 2006] rotational stability theories. The green dot represents an internal load and the black arrows represent either (solid line) the orientation of the rotation axis at the time associated with each frame (i.e., the current rotation axis), or (dashed line) previous orientations of this axis. The blue shell in rows B and C is a broken elastic lithosphere. The dashed and dotted lines within the figure of the Earth are the axis of the rotational bulge and the contemporaneous equator (i.e., 90° from the current rotation axis), respectively. Row C considers the case where the remnant bulge physics in row (B) is augmented by long-term excess ellipticity driven by a stable background convective flow (red arrows).

once it reaches the equator, no polar motion will ensue (A5). Although the schematic illustrates a time-dependent adjustment, the Gold [1955] theory predicts only the final, equilibrium position of the load (A4 and A5). A non-linear rotational stability theory that incorporates the time-dependent stabilization due to the viscously adjusting rotational bulge (that is, a theory that has quantified the time dependent evolution of the rotation axis from A2-A4) has been described by Ricard et al. [1993] (see below).

Next, we turn to the physics associated with an extended rotational stability theory that takes into account the potential stabilizing effect of a lithosphere with elastic strength [Willemann, 1984; Matsuyama et al., 2006; Daradich et al., 2008] (Figure 2B). The blue shell in these frames represents a broken, elastic lithosphere. Initially, the shell is unstressed and the Earth's figure is hydrostatic (B1). As in row (A), a convective load leads to TPW (B2) and the rotational bulge adjusts to this polar motion (B3). In contrast to the Gold [1955] scenario, the rotational bulge cannot adjust perfectly to the new orientation since the TPW introduces elastic stresses in the broken lithosphere and these stresses act to resist polar motion (note that the geographic equator is misaligned with the rotational bulge in frame B3). In this case, the system retains memory of its original state. TPW will continue in incremental, imperfect steps until the net elastic resistance - the so-called remnant bulge [Willemann, 1984; Matsuyama et al., 2006; Daradich et al., 2008] - balances the load's tendency to push the pole away (B4). The load does not reach the equator and, if the load is removed at any stage, the pole will return to the original orientation characterized by an unstressed lithosphere (B5). In the next section, we add a term to the non-linear theory of Ricard et al. [1993] to incorporate stabilization associated with the remnant rotational bulge.

In addition to the delayed viscous adjustment of the rotational bulge and the

remnant bulge, the rotation axis may be subject to a third stabilization mechanism linked to the convective forcing itself (Figure 2C). In particular, the convective pulse driving TPW may be superimposed on a background convective flow that is stable over much longer time scales than the pulse. If this stable background flow supports an excess ellipticity in the plane of the TPW, then it will introduce a memory of the original rotating state that persists for as long as the background flow remains stable. To consider this case, we begin in frame C1 with an Earth figure that is not hydrostatic (i.e., the oblateness of the figure in C1 is greater than the oblateness of the hydrostatic forms in A1 or B1). Frames C2-C4 show the TPW driven by the application of the convective pulse (green dot). If the stable background excess ellipticity acts in tandem with a remnant bulge (as is the case in row C), the rotational bulge will readjust even less perfectly to the new orientation of the pole than in row B, and the TPW will be even more muted (compare C4 with B4). If the short-term convective load is removed, then the stable background excess ellipticity will also provide a memory of the original rotational state and it will drive the pole back to its original location (C5) regardless of whether the remnant bulge stabilization is active (as it is, schematically, in row C) or not. In the next section, we derive a form of the non-linear rotational stability theory of Ricard et al. [1993] that explicitly treats the case of a stable background excess ellipticity.

5.2.3 A NON-LINEAR ROTATIONAL STABILITY THEORY

We begin by summarizing the expression for the time dependent inertia tensor derived by Ricard et al. [1993], which does not include stabilization due to elasticity in the lithosphere. Let us denote the inertia tensor on a spherical, non-rotating Earth as \mathbf{I}_o , and the inertia tensor perturbation associated with the advection of mantle density heterogeneities as $\mathbf{I}^{\mathcal{L}}(t)$, where t is time. The latter term includes the dynamic defor-

mation of all boundaries (i.e., dynamic topography). If we also denote the rotation vector as $\omega(t)$, with magnitude Ω , then the total inertia tensor is given by [Ricard et al., 1993]:

$$I_{i,j}(t) = I_o \delta_{i,j} + I_{i,j}^{\mathcal{L}}(t) + \frac{a^5}{3G} k^T(t) * [\omega_i(t)\omega_j(t) - \frac{1}{3}\omega^2(t)\delta_{i,j}] \quad (5.1)$$

where a is the radius of the Earth, G is the gravitational constant, δ is the Dirac-delta function, and $k^T(t)$ is the tidal (or tidal effective) viscoelastic k Love number at spherical harmonic degree 2. In writing the Love number, we have made its dependence on mantle viscosity (ν) and the elastic lithospheric thickness (EET) implicit. The term that includes the Love number is the contribution to the inertia tensor from rotation-induced deformation, and it involves a time-convolution (denoted by the asterisk) between the Love number and the evolving centrifugal potential (the term in the square brackets is proportional to this potential). This term introduces a time-dependent stabilization of the rotation vector associated with the delayed viscous adjustment of the rotational bulge [Ricard et al., 1993] (as in Figure 2A2-2A4), and it represents an important extension to the equilibrium physics described by Gold [1955].

In deriving their final expressions for long-term polar wander, Ricard et al. [1993] transformed the rotation contribution in the above equation into the Laplace transform domain (in which case the convolution becomes a simple multiplication), approximated the long-time behaviour of the (transformed) Love number using a Taylor series, and inverted the result to give:

$$I_{i,j}(t) = I_o \delta_{i,j} + I_{i,j}^{\mathcal{L}}(t) + \frac{a^5 k_f^T}{3G} [\omega_i(t)\omega_j(t) - \frac{1}{3}\omega^2(t)\delta_{i,j}] - \quad (5.2)$$

$$\frac{a^5 k_f^T T}{3G} [\dot{\omega}_i(t) \omega_j(t) + \omega_i(t) \dot{\omega}_j(t) - \frac{2}{3} \omega_k(t) \dot{\omega}_k(t) \delta_{i,j}]$$

In this expression, the superscript dot denotes time-differentiation, the parameter T is a constant involving combinations of the modal amplitudes and decay times of the viscoelastic k Love number (and is thus also dependent on ν and EET), and k_f^T is the so-called fluid Love number related to the long time limit of its viscoelastic counterpart. The physics governing the parameter T , and the time scale that controls TPW in the presence of stabilization due to the delayed viscous adjustment of the rotational bulge, has recently been discussed by Cambiotti et al. [2011]. The fluid Love number is a function of EET, but not of ν or t . Following arguments appearing in Ricard et al. [1993], in this long-time limit the Euler equation governing conservation of angular momentum reduces to an eigenvalue problem, and the orientation of the vector $\omega(t)$ may be approximated by the principal axis of maximum inertia. In practise, at each time step the rotation vector is tracked by diagonalizing the (non-hydrostatic) inertia tensor computed from the above equation [Ricard et al., 1993].

The above expressions incorporate no long-term memory of the original rotational state; that is, in the limit of infinite time, the inertia tensor of the Earth will adjust to reorient perfectly around the new rotational state. In this case, diagonalization of the inertia tensor is governed by the load term $\mathbf{I}^{\mathcal{L}}(t)$; this is equivalent to the equilibrium theory of Gold [1955], wherein the rotation axis reorients such that a positive load moves to the equator (as in Figure 2A4). In contrast, as we have discussed, the remnant bulge physics described in the last section (Figure 2B) introduces a memory of the original rotational state [Willemann, 1984; Matsuyama et al., 2006; Daradich et al., 2008]. If we adopt a reference frame such that the original (pre-loaded) rotation vector is given by $[0,0,\Omega]$, then, using results from Matsuyama et al. [2006] and Daradich et al. [2008], we can add a term to equation (2) to incorporate stabilization

due to the remnant bulge:

$$I_{i,j}(t) = I_o \delta_{i,j} + I_{i,j}^{\mathcal{L}}(t) + \frac{\Omega^2 a^5}{3G} (k_f^{T,*} - k_f^T) (\delta_{i,3} - \frac{1}{3}) \delta_{i,j} + \quad (5.3)$$

$$\frac{a^5 k_f^T}{3G} \left[\omega_i(t) \omega_j(t) - \frac{1}{3} \omega^2(t) \delta_{i,j} \right] - \frac{a^5 k_f^T T}{3G} \left[\dot{\omega}_i(t) \omega_j(t) + \omega_i(t) \dot{\omega}_j(t) - \frac{2}{3} \omega_k(t) \dot{\omega}_k(t) \delta_{i,j} \right]$$

where the fluid Love number $k_f^{T,*}$ is identical to k_f^T , except that it is computed using an Earth model with no elastic strength in the lithosphere (i.e., it governs the hydrostatic figure of the Earth). As described in Matsuyama et al. [2006], the strength of the remnant bulge stabilization is proportional to the difference in these two fluid Love numbers (i.e., $k_f^{T,*} - k_f^T$). At infinite time, the orientation of the rotation vector is governed by the diagonalization of the inertia contributions from the load term, $\mathbf{I}^{\mathcal{L}}(t)$, and from the remnant bulge (the third term on the right hand side of equation 3). In this limit, which is equivalent to the equilibrium theory derived by Willemann [1984] and Matsuyama et al. [2006], the orientation of the rotation vector is thus governed by a balance between load-induced TPW and stabilization due to the remnant bulge (Figure 2B4). We have verified that a diagonalization of the sum of the load and remnant bulge contributions in equation (3) yields the analytic expression for the final (equilibrium) pole position derived in Matsuyama et al. [2006].

In the introductory text above, we stated that the rotational stability is governed by the figure of the Earth after correction for the hydrostatic form (i.e., the non-hydrostatic figure). In the case when a remnant bulge is active (Figure 2B), it is more precise to say that the stability is governed by the figure of the Earth after correction for the so-called equilibrium form (i.e., the non-equilibrium figure) [Daradich et al., 2008]. The equilibrium form of a planet is defined as the figure that one would predict by considering a non-rotating planet with an elastic lithosphere, spinning

it up to its present angular velocity, and waiting an infinite time [Daradich et al., 2008]. The extension of the physics of rotational stability to a consideration of the non-equilibrium form is embedded in equation (3).

As discussed in the last section, the rotation axis may be subject to an additional stabilization associated with the convective forcing itself. In particular, if the convective pulse that drives the TPW is superimposed on a much longer-lived convective flow, then the latter may support a stable background excess ellipticity in the Earth's form. This special case can be accommodated by replacing the general expression for the inertia tensor perturbation due to the load in equations (1)-(3) by:

$$I_{i,j}^{\mathcal{L}}(t) = l_{i,j}^L(t) + \frac{\Omega^2 a^5}{3G} \left[\frac{1}{3}(\Delta k_1 + \Delta k_2)\delta_{i,j} - (\Delta k_1 \delta_{1,i} \delta_{1,j} + \Delta k_2 \delta_{2,i} \delta_{2,j}) \right] \quad (5.4)$$

where the first term on the right-hand-side is the inertia perturbation due to the time varying component of the convective load and the second term is the perturbation to the Earth's form due to the stable background component of the convective flow. The latter effectively introduces a memory of the original rotational state, and acts to stabilize the pole with respect to departures from this original state. The terms Δk_1 and Δk_2 are parameters that govern the stable background excess ellipticity in the planes defined by (I_{max}, I_{min}) and (I_{max}, I_{int}) , respectively. Given the symmetry of the load and the convective forcing, only the parameter Δk_2 enters into the predictions described in the text.

In the next section, we discuss the moment difference $\Delta I_{MD} = I_{max} - I_{int}$. Using equation (4), this difference is related to Δk_2 by:

$$\Delta I_{MD} = \frac{\Omega^2 a^5}{3G} \Delta k_2 \quad (5.5)$$

The numerical results described below are based on equations (3)-(5). These results will involve: (1) a sensitivity study in which we vary all the free parameters of the numerical modeling; and (2) a modeling study of the Mesozoic [Steinberger & Torsvik, 2008] (Figure 3a-d) and Neoproterozoic [Maloof et al., 2006] (Figure 4a) oscillatory TPW events included in Figure 1a. The Mesozoic event involves two oscillations of 18° and 10° amplitude and duration ~ 105 and 45 Myr, respectively [Steinberger & Torsvik, 2008], coaxial about an axis near the center of Pangea. The Neoproterozoic event is characterized by a $> 50^\circ$ oscillation with duration $\sim 11 - 30$ Myr coaxial about Rodinia [Maloof et al., 2006] .

5.3 RESULTS

5.3.1 THE NUMERICAL MODEL

Mantle convection simulations indicate that supercontinents reorganize flow into two antipodal superswells, one of which rises below the supercontinent and serves as the driving force for disaggregation [Zhong et al., 2007]. Accordingly, our numerical simulations align the minimum axis of inertia (and maximum excess ellipticity) with the center of the supercontinent (e.g., Figure 3b). We introduce a convective pulse comprised of downgoing and upwelling plumes symmetric about the plane of I_{max} and I_{int} . This placement, together with the symmetry in the Earth model, ensures that the predicted pole path will be confined to a great circle within this same plane. The numerical model has four free parameters: the moment difference (stable background excess ellipticity) of the Earth's figure, $\Delta I_{MD} = I_{max} - I_{int}$ (see equation 5); the effective elastic thickness of the lithosphere (EET; see below); the lower mantle viscosity (ν); and the peak perturbation in the product of inertia $\Delta I_{max,int}$ driven by the convective flow. We normalize both $\Delta I_{max,int}$ and ΔI_{MD} by the present day moment difference

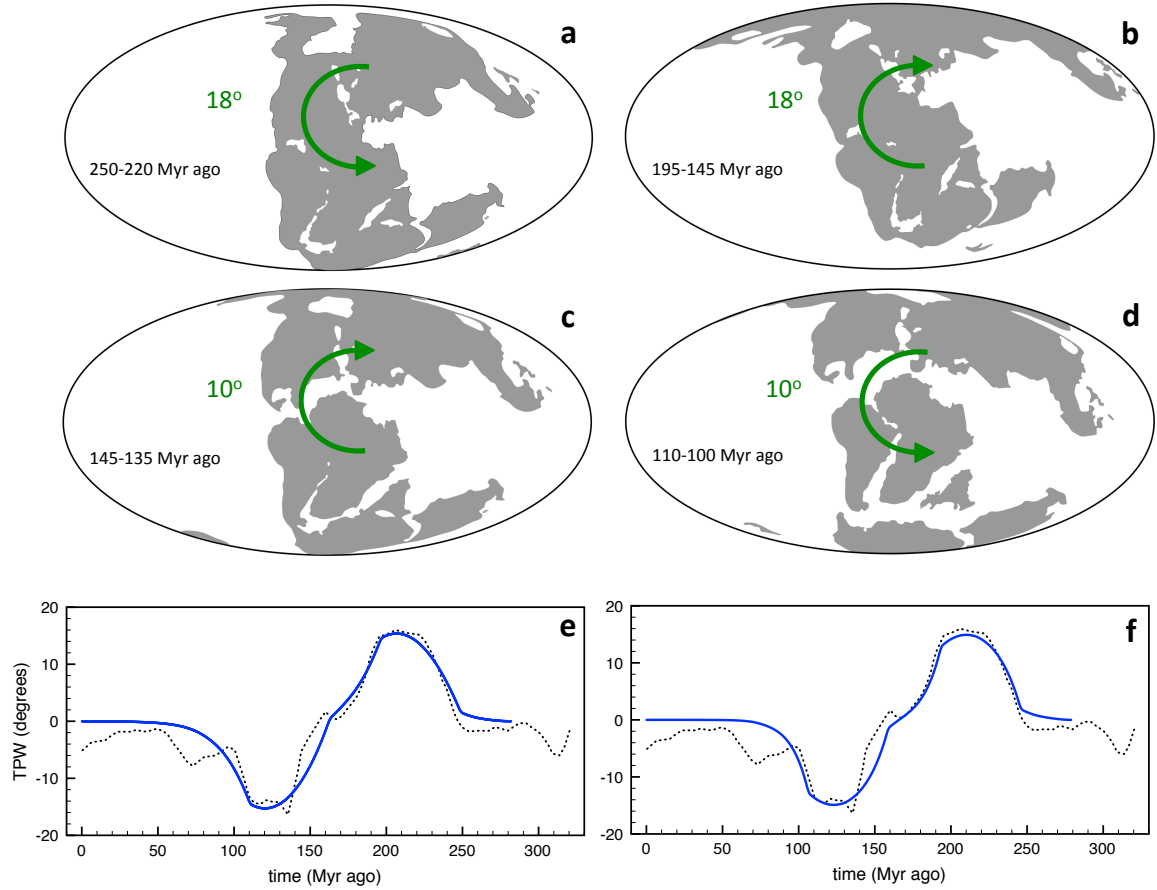


Figure 5.3: Modelling paleomagnetically-inferred TPW during the Mesozoic. (a-d) Continental locations in a paleomagnetic reference frame at the start of each time interval (as labeled), after Steinberger & Torsvik [2008]. Superimposed on each frame is the inferred (general) sense and amplitude of coherent continental motion (interpreted as TPW) in the paleomagnetic reference frame [Steinberger & Torsvik, 2008]. (e-f) Dotted line (same on both frames) shows the inferred, cumulative motion, averaged for all continents and interpreted as TPW, around an equatorial axis at a longitude coinciding with the center of mass of the continents in the paleomagnetic reference frame [Steinberger & Torsvik, 2008]. Positive slopes denote clockwise rotation about this axis, while negative slopes denote counter-clockwise rotation. The solid blue line on each frame is our numerical prediction of TPW, as discussed in the text. These predictions treat cases where the return of the rotation axis in response to convection-induced TPW is due to (e) a remnant bulge (i.e., elastic stresses in the lithosphere) or (f) stable excess ellipticity in the plane of I_{max} and I_{int} . In frame (e), $EET=12$ km, $\Delta^n I_{MD} = 0.0$, and two convective pulses, both of amplitude $\Delta^n I_{max,int} = 0.025$, are initiated at 282 Myr ago and 196 Myr ago. In frame (f), $\Delta^n I_{MD} = 0.11$, $EET = 0$ km, and the convective forcings are initiated at 279 Myr ago and 192 Myr ago, both with amplitude $\Delta^n I_{max,int} = 0.025$. The simulations adopt $\nu = 10^{22}$ Pa s.

[Chambat et al., 2010], $\Delta I_{PD} = I_{max}^{PD} - \Delta I_{int}^{PD}$ (i.e., $\Delta^n I_{max,int} = \Delta I_{max,int} / \Delta I_{PD}$ and $\Delta^n I_{MD} = \Delta I_{MD} / \Delta I_{PD}$).

The free parameters EET, ΔI_{MD} and ν , are linked to the three mechanisms that act to stabilize the rotation axis in the presence of a convective forcing: the remnant bulge, stable background excess ellipticity in the plane of TPW, and the delayed viscous adjustment of the rotational bulge, respectively. Moreover, EET and ΔI_{MD} introduce a memory of the original (pre-loading) orientation of the rotation axis and a tendency for the pole to return toward this initial position once the forcing ends.

Convective forcing within our model involves a pair of plumes upwelling from the core-mantle-boundary at 55° N and a second antipodal pair at 55° S. The plumes that comprise each pair are displaced by 60° in longitude, at locations symmetric about the plane defined by I_{max} and I_{int} . An equal number of downwelling plumes are also included in the model. These are located at positions defined by a 90° rotation about I_{min} from each of the upwellings. This configuration permits a maximum TPW of $\sim 60^\circ$. We also performed several test calculations where the plumes were placed at higher latitudes (75° N and 75° S) and found that the predicted peak TPW varied by $\sim 5^\circ$. Each plume has a radius of 6° . The speed of the plumes is given by Stoke's flow equations, and we use the method of images [Milne-Thomson, 1996] to account for the slowing of the plumes near boundaries. The fourth and final free parameter of the modelling is related to the strength of the convective forcing on TPW, which was varied from one simulation to another via the adopted density contrast (see below) between the plumes and surrounding mantle.

The evolving mantle flow field was converted to a time-dependent geoid anomaly (at spherical harmonic degree two) using depth-dependent kernels valid for a compressible, viscous Earth [Forte & Peltier, 2001]. We adopt kernels computed using free-slip boundary conditions at the core-mantle-boundary and no-slip conditions at

the surface; the latter is appropriate for plume-driven flow away from plate boundaries [Forte, 2007]. These kernels account for the geoid signal associated with both internal density heterogeneities and the dynamic topography of all density interfaces. Finally, the geoid perturbation at each time step is converted to an inertia tensor perturbation using a well-established mapping [Matsuyama et al., 2006], and the latter time series serves as the input to our extended non-linear rotational stability theory.

Our plume-model of mantle convective flow is highly simplified, however it allows us to quantitatively test the central hypothesis of this study, namely that stabilization associated with a remnant bulge and/or stable excess ellipticity would have been sufficient to return the rotation axis to its initial location after large amplitude, convectively-driven excursions. In designing the simulations, we were guided by several checks on the plausibility of the convective forcing. First, we distributed mantle buoyancy across a suite of plumes, rather than placing it in a single plume, so that the associated density contrast between the plume and mantle is reasonable. Furthermore, since the present-day, non-hydrostatic (excess) ellipticity of the Earth is presumably a consequence of mantle convection, our normalization of the plume-induced perturbation to the product of inertia, $\Delta I_{max,int}$, in terms of the observed excess ellipticity in the same plane ($\Delta I_{PD} = I_{max}^{PD} - I_{int}^{PD}$), provides a direct check on the size of the forcing. We note, in the results discussed below, that TPW excursions of order 40° are predicted for peak inertia perturbations of only 10 – 15% of ΔI_{PD} .

In modelling the paleomagnetically-inferred TPW events shown in Figures 3a-d and 4a, we consider Earth models with prolate, or nearly prolate forms. For this class of Earth models, the TPW path would be coaxial to I_{min} , or very nearly so, regardless of the orientation of the pulse of convective forcing. Thus, our placement of the plumes symmetric about the plane defined by I_{max} and I_{int} is made out of numerical convenience, and it does not imply that a nearly coaxial TPW path requires

a convective forcing of specific geometry.

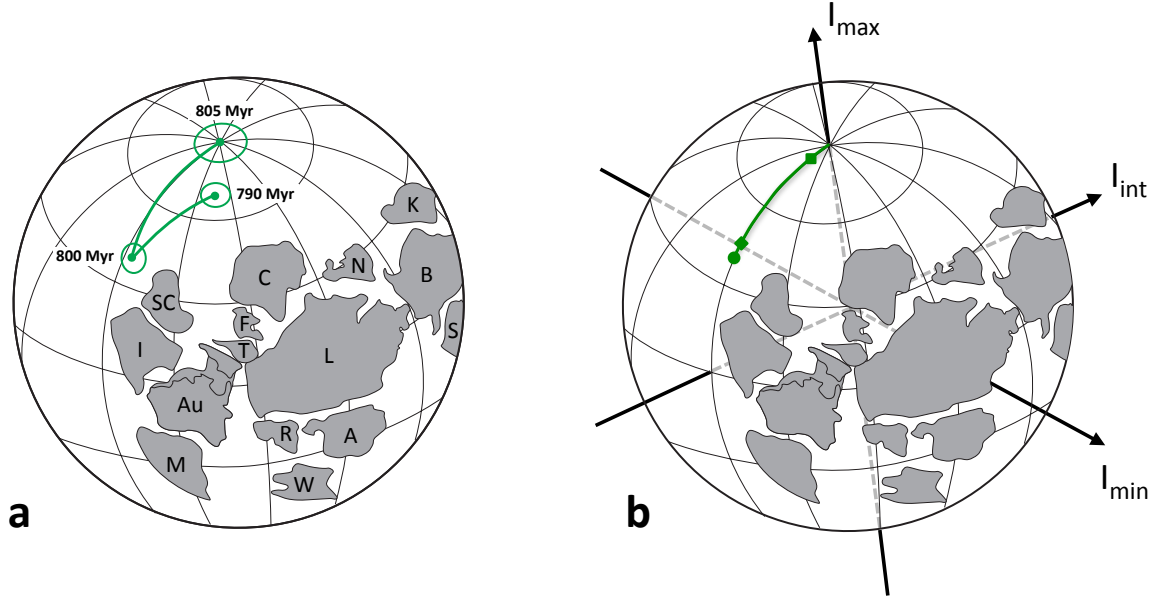


Figure 5.4: Modelling paleomagnetically-inferred TPW during the Neoproterozoic [Maloof et al., 2006]. (a) Rodinian supercontinent configuration prior to the pair of large amplitude TPW events shown by the green line with one- σ error ellipses, with total duration ~ 15 Myr, after [Maloof et al., 2006]. The labels on the continents and terranes are: A, Amazonia; Au, Australia; B, Baltica; C, Congo; F, Sao Francisco; I, India; K, Kalahari; L (Laurentia, including Svalbard); M, Mawsonland; N, North China; R, Rio Plata; S, Siberia; SC, South China; T, Tarim; W, West Africa. (b) Schematic showing the set-up of the numerical simulation of convection and TPW. An excess ellipticity is imposed along the axis of minimum non-hydrostatic inertia that intersects the middle of the supercontinent. The axis of maximum non-hydrostatic inertia is coincident with the rotation pole, and the axis of intermediate non-hydrostatic inertia lies on the equator, 90° from the remaining axes. A pulse of convective flow is driven by density heterogeneity (up or downwelling plumes) symmetric about the plane defined by I_{max} and I_{int} . This pulse drives TPW along a great circle in the same plane. The green line and symbols summarize results from two numerical simulations in which the return of the rotation axis in response to convection-induced TPW is due to either a remnant bulge ($EET=15$ km; $\Delta^n I_{MD} = 0$) or a stable background excess ellipticity in the plane of I_{max} and I_{int} ($\Delta^n I_{MD} = 0.1$; $EET=0$). In these simulations, the pole moves $\sim 44^\circ$ (diamond) and 51° (circle), respectively, in the first ~ 6 Myr. In both cases, the pole returns to a position $\sim 8^\circ$ (square) from the initial location in the next 20 Myr. The simulations adopt a convective forcing of $\Delta^n I_{max,int} = 0.3$ and $\nu = 10^{22}$ Pa s (see text).

For our "standard" simulation, we adopt values of $\Delta^n I_{max,int} = 0.1$ and $\nu = 10^{22}$ Pa s, the latter being at the lower bound of a joint inversion of ice-age and mantle convection data [Mitrovica & Forte, 2004]. The upper mantle viscosity is set to 5×10^{20} Pa s. We define two test cases based on the standard simulation. In the first, we adopt $\Delta^n I_{MD} = 0$ (i.e., a prolate spheroid) and an EET of 15 km. In the second, $\Delta^n I_{MD} = 0.1$ and EET = 0. These cases invoke stabilization by the remnant bulge or stable background excess ellipticity, respectively. The plume density contrast adopted in the standard simulation was 42.5 kg/m^3 . This value is less than 1% of the density of lower mantle material and it is consistent with inferences based on seismic tomography [Dziewonski et al., 2010]. Predictions of TPW described in this study are strongly dominated by the (2,3) component of the load inertia tensor perturbation $\mathbf{I}^L(t)$ in equation (4). Figure 5a shows the time series $I_{23}^L(t)$ for three different simulations. The solid line is the standard model simulation ($\Delta^n I_{max,int} = 0.1$; $\nu = 10^{22}$ Pa s). The dotted and dashed lines are analogous to the solid, with the exception that the convective forcing, $\Delta^n I_{max,int}$, is changed to 0.05 and 0.2, respectively. The periods of rapid change in each of these time series are associated with the traversal of the plumes through the low-viscosity upper mantle.

5.3.2 SENSITIVITY ANALYSES

The black lines in Figures 6a and 6e are predictions of TPW based on test cases #1 and #2, respectively. The perturbation to the inertia tensor driven by convective flow progressively increases in the first ~ 15 Myr of these simulations (see Figure 5a). The motion of the rotation pole lags behind this forcing, and reaches a maximum displacement of $\sim 34^\circ$ (case #1) or $\sim 40^\circ$ (case #2) in ~ 21 Myr. As the forcing diminishes, elastic stress in the lithosphere or the stable background excess ellipticity begin to dominate the rotational force balance. Once this resistance overcomes the

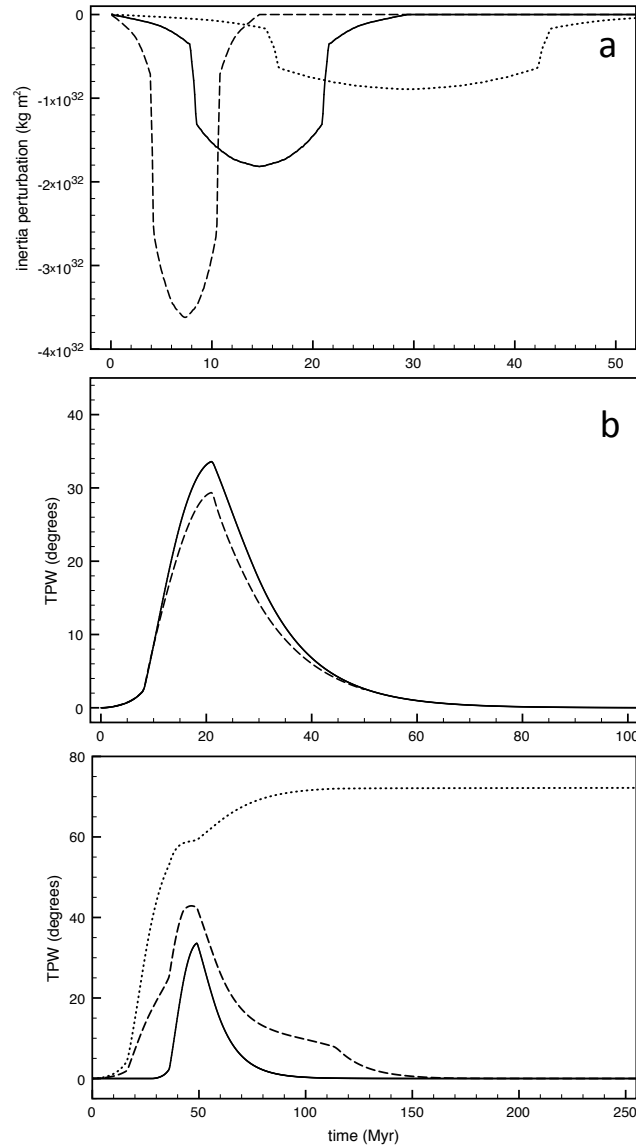


Figure 5.5: TPW predictions: Numerical experiments. (a) The perturbation to the product of inertia, $I_{23}^L(t)$, due to the plume-driven convective pulse described in the text. The solid line is the time-series associated with the standard model run ($\Delta^n I_{max,int} = 0.1$; $\nu = 10^{22}$ Pa s). The dotted and dashed lines are analogous time series, with the exception that $\Delta^n I_{max,int} = 0.05$ and 0.2 , respectively. (b) Solid line - TPW versus time computed for test case #1 of the standard simulation ($\Delta^n I_{max,int} = 0.1$, $\nu = 10^{22}$ Pa s, EET = 15 km, and $\Delta^n I_{MD} = 0.0$). The line is identical to the black line in Figures 6a-d. The prediction is based on the non-linear rotational stability theory described in the text. The dashed line is identical to the solid line, with the exception that TPW is computed using a linearized rotational stability theory [Chan et al., 2011]. (c) Solid line - as in frame (b). Dashed line - TPW predicted for a case including three separate convective forcings, $\Delta^n I_{max,int}$: 0.1; 0.05; and 0.02. The pulses are initiated at 28 Myr ago, 0 Myr ago, and 8 Myr ago, respectively. The simulation adopts EET = 15 km and $\Delta^n I_{MD} = 0.0$. Dotted line - as in the dashed line, except EET = 0 (i.e., the remnant bulge is absent).

driving force, the pole reverses direction and returns relatively rapidly toward its initial position. The net displacement of the pole drops to half the peak amplitude in ~ 9 Myr.

To investigate the sensitivity of the TPW predictions to the parameter choices listed above, we perform an analysis in which one of $\Delta^n I_{max,int}$, EET, $\Delta^n I_{MD}$ and ν is varied in the range 0.025-0.20, 0-50 km, 0.0-1.0, and 3×10^{21} Pa s to 30×10^{21} Pa s, respectively (Figures 6a-d,e-h). (An analysis in which these parameters are varied simultaneously is described below). We refer to three specific measures of the polar motion: the maximum displacement of the pole (TPW_{max}), the time required to reach this maximum displacement (t_{max}), and, subsequently, the time for the pole to return to a displacement of half of TPW_{max} ($t_{1/2}$). These values are, for the test case #1 (or #2): $TPW_{max} = 33.6^\circ$ (40.5°), $t_{max} = 21.0$ (20.7) Myr, and $t_{1/2} = 9.5$ (8.8) Myr.

We first explore the impact of varying the magnitude of the forcing, $\Delta^n I_{max,int}$ (Figures 6a,e). The velocity of the convective flow is proportional to the imposed density (buoyancy) perturbation. Accordingly, increasing the inertia tensor perturbation from 5% to 20% of ΔI_{PD} reduces t_{max} by a factor of ~ 4 . TPW_{max} increases with the size of the forcing, and it reaches 40° when the convection-induced inertia tensor perturbation $\Delta^n I_{max,int} = 0.15$ (case #1) or 0.1 (case #2). In contrast to both these sensitivities, the timescale of recovery, $t_{1/2}$, varies by only a few Myr for $\Delta^n I_{max,int} \geq 0.05$.

Next, we consider the two parameters that stabilize the rotation axis, $\Delta^n I_{MD}$ and EET. Varying EET in test case #1 (Figure 6b) or $\Delta^n I_{MD}$ in case #2 (Figure 6g) has a profound effect on TPW_{max} and $t_{1/2}$, but little effect on t_{max} . Moreover, introducing a stable background excess ellipticity in test case #1 (Figure 6c) or a remnant bulge in case #2 (Figure 6f) enhances the already existing stabilizations in these test cases, further decreasing the peak TPW and the recovery time. When EET

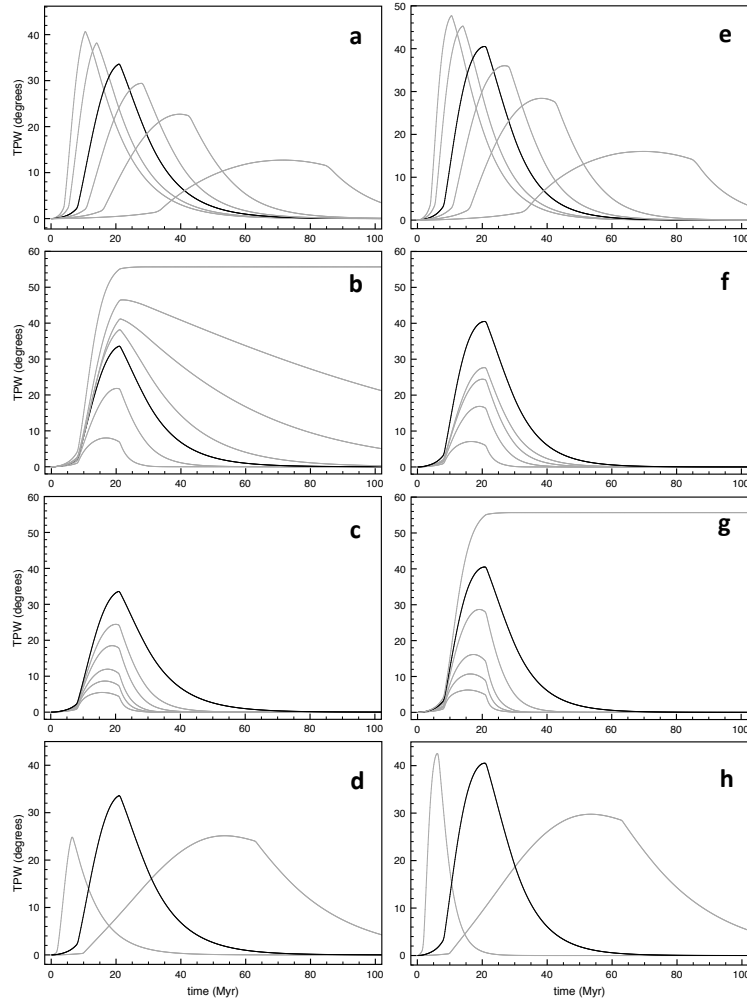


Figure 5.6: Sensitivity of numerical predictions of convectively-driven TPW to variations in standard model parameters. (a-d) The black line on each frame shows results based on test case #1 of the standard simulation, defined by the following parameter choices: $\Delta^n I_{max,int} = 0.1$, $\nu = 10^{22}$ Pa s, $\Delta^n I_{MD} = 0$ and EET = 15 km (see text). Each frame shows predictions of TPW in which one of these parameters is varied: (a) Normalized flow-induced inertia perturbation, $\Delta^n I_{max,int}$, of (from top to bottom) 0.2, 0.15, 0.1, 0.075, 0.05 and 0.025; (b) Effective elastic thickness of the lithosphere, EET, of (from top to bottom) 0, 2, 5, 10, 15, 25, and 50 km; (c) moment difference, $\Delta^n I_{MD}$, of (top to bottom) 0, 0.1, 0.2, 0.4, 0.6 and 1.0; (d) Lower mantle viscosity of (from left to right) 3×10^{21} Pa s, 10^{22} Pa s and 3×10^{22} Pa s. (e-h) The black line on each frame shows results based on test case #2 of the standard simulation, defined by: $\Delta^n I_{max,int} = 0.1$, $\nu = 10^{22}$ Pa s, $\Delta^n I_{MD} = 0.1$ and EET = 0 km. Each frame shows predictions of TPW in which one of these parameters is varied: (e) $\Delta^n I_{max,int}$ (0.2, 0.15, 0.1, 0.075, 0.05, 0.025); (f) EET (0, 10, 15, 25 and 50 km); (g) $\Delta^n I_{MD}$ (0, 0.1, 0.2, 0.4, 0.6 and 1.0); (h) ν (3×10^{21} Pa s, 10^{22} Pa s and 3×10^{22} Pa s).

$= 0$ and $\Delta^n I_{MD} = 0$ (Figures 6b,g) (i.e., a prolate Earth with no remnant bulge), only the delayed viscous adjustment of the rotational bulge acts to resist polar motion [Ricard et al., 1993] and the TPW has no return phase.

Finally, we consider simulations in which ν is varied from 3×10^{21} Pa s to 3×10^{22} Pa s (Figures 6d,h). The latter is a reasonable upper bound from modern inferences [Mitrovica & Forte, 2004], and the former is consistent with thermal history modelling [Crowley et al., 2011] suggesting that mantle viscosity was ~ 3 -10 times smaller than the present value ~ 1 Gyr ago. Since flow velocity is inversely proportional to mantle viscosity, t_{max} decreases by a factor of ~ 10 across this range. However, while the TPW rate is increased by this factor, the time scale across which the flow-induced perturbation is active decreases, and the net effect is a relatively small variation in TPW_{max} ; the sensitivity would be higher in models forced by continuous convective motion [Tsai & Stevenson, 2007; Chan et al., 2011].

The time for TPW to reach its peak value, t_{max} , is sensitive to the magnitude of the convective forcing and it is relatively insensitive to two parameters related to processes that stabilize rotation, the background excess ellipticity and the thickness of the elastic lithosphere (Figures 6b,c,f,g). Accordingly, in Figure 7 we plot t_{max} as a function of the inverse of the convective forcing for three different values of mantle viscosity considered in the main text. The fluid velocity in a Stoke's flow calculation is proportional to the buoyancy (i.e., the convective forcing), and therefore the higher the forcing, the faster the convective flow, and the shorter the time scale for the pole to reach maximum displacement. The results for each line in Figure 7 confirm this inverse proportionality. The fluid velocity is also inversely proportional to the mantle viscosity, and thus the time scale t_{max} is linearly related to the viscosity; this scaling is evident in the factor of ~ 10 increase in t_{max} for the case of $\nu = 3 \times 10^{22}$ Pa s relative to the case $\nu = 3 \times 10^{21}$ Pa s. The results in Figure 7 are computed using

values for the test case #1 defined in the main text, i.e., $\Delta^n I_{MD} = 0$ and EET = 15 km, but we have confirmed that the linear relationships evident in Figure 7 hold for $\Delta^n I_{MD}$ values up to 1.0 and EET values in the range 0-50 km.

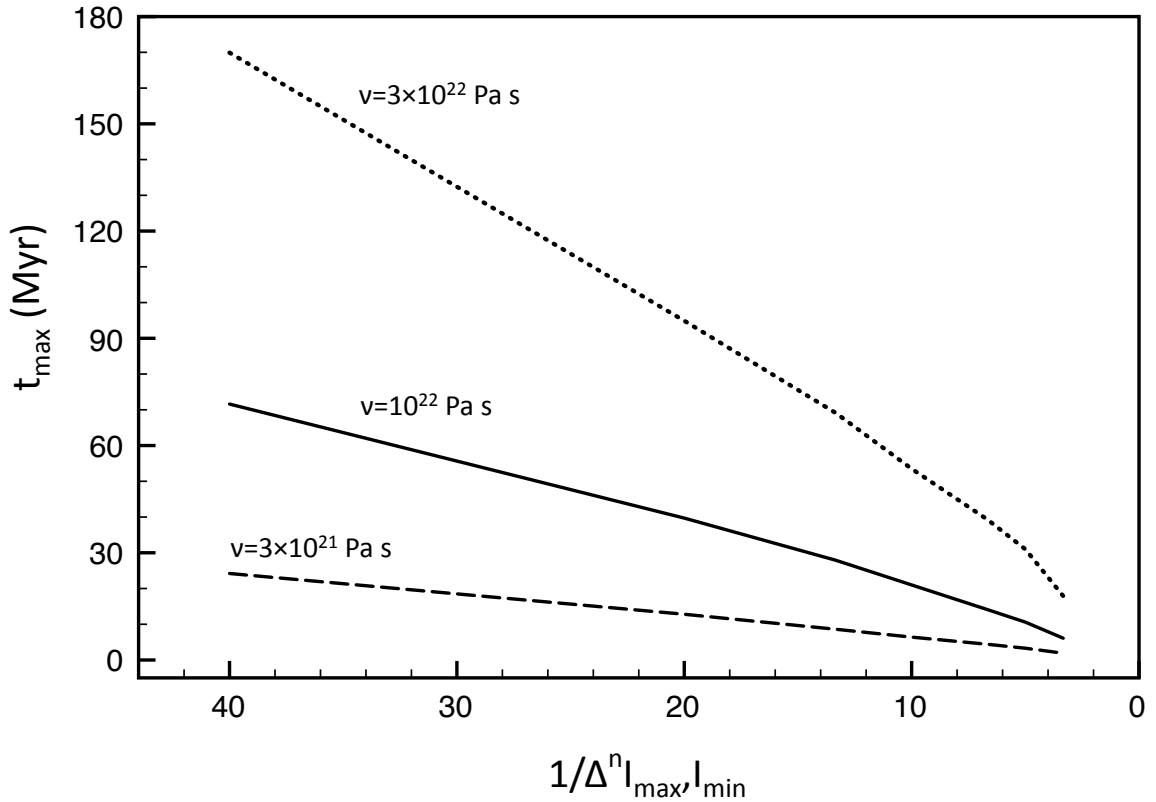


Figure 5.7: Predictions of t_{max} versus the inverse of the normalized convective forcing (i.e., $1/\Delta^n I_{max, int}$) for numerical simulations with a lower mantle viscosity of (dotted line) 3×10^{22} Pa s, (solid line) 10^{22} Pa s, or (dashed line) 3×10^{21} Pa s. All other parameters are adopted from the test case #1 simulation ($\Delta^n I_{MD} = 0$, EET = 15 km).

In Figure 8 we summarize a sensitivity analysis for predictions of both the peak displacement of the rotation axis, TPW_{max} (row A), and the recovery time scale, $t_{1/2}$ (row B). Each frame shows one of these predictions in a two-dimensional space defined by varying the two parameters that control processes that stabilize the rotation axis - the elastic lithospheric thickness, EET, and the normalized moment difference, $\Delta^n I_{MD}$. The figure also shows the sensitivity of the predictions to variations in the

normalized convective forcing, $\Delta^n I_{max,int}$ (each column shows results for a different forcing). All predictions in Figure 8 are based on $\nu = 10^{22}$ Pa s.

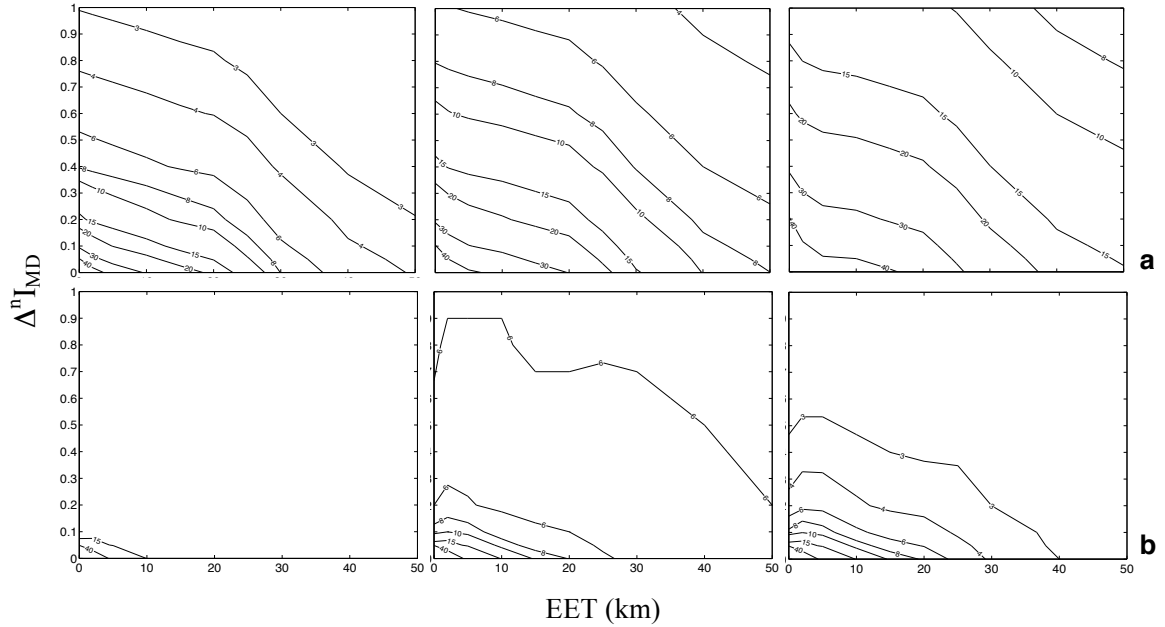


Figure 5.8: Sensitivity analyses for predictions of TPW_{max} (row A; contours are shown for 3° , 4° , 6° , 8° , 10° , 15° , 20° , 30° and 40°) and the time scale of recovery $t_{1/2}$ (row B, contours are shown for 3, 4, 6, 8, 10, 15 and 40 Myr) as a function of the elastic lithospheric thickness, EET, and normalized moment difference (stable excess ellipticity), $\Delta^n I_{MD}$, adopted in the numerical simulations. The columns on the figure refer to three different values of the normalized convective forcing, $\Delta^n I_{max,int}$: (left) 0.05, (middle) 0.1, and (right) 0.2. The simulations adopt $\nu = 10^{22}$ Pa s.

As one would expect, both TPW_{max} and $t_{1/2}$ generally decrease as either of the stabilizing effects, stable background excess ellipticity and the remnant bulge, increase (i.e., as one moves from bottom to top, or left to right, respectively, on each frame). For models that yield the highest predictions of TPW_{max} (bottom-left of each frame), the drop-off in the prediction of TPW_{max} as either the EET or $\Delta^n I_{MD}$ is increased is more gradual than the associated drop-off in $t_{1/2}$. For a convective forcing of $\Delta^n I_{max,int} = 0.05$ (left column), predictions of $TPW_{max} \sim 40^\circ$ are accompanied by recovery times, $t_{1/2}$, that exceed 40 Myr. In contrast, at a convective forcing of

$\Delta^n I_{max,int} = 0.2$ (right column), predictions of $TPW_{max} \sim 40^\circ$ may be accompanied by recovery times well below 10 Myr. Thus, paleomagnetically-inferred episodes of rapid, high amplitude TPW oscillations in deep time (e.g., Figure 4a) may be reconciled by a combination of a strong convective forcing and Earth models with a relatively thin lithosphere and a nearly prolate figure. Longer duration and shorter amplitude TPW oscillations (as in Figure 3) imply less restrictive conditions.

On the basis of the results in this section, we conclude that a relatively rapid pulse of mantle convection acting on an Earth with elastic lithospheric strength and/or an excess ellipticity that is stable over the time scale of the pulse, leads to an inherent tendency for oscillatory TPW events. Whether variability in downwelling [Steinberger & Torsvik, 2010; Spada et al., 1992; Rouby et al., 2010; Richards et al., 1999] or upwelling [Davaille, 1999; Greff-Lefftz, 2004] mantle flow is the dominant driver of TPW, these stabilization mechanisms remove the necessity for invoking load symmetry to explain a return of the rotation pole to a position near its original location [Evans, 1998; Greff-Lefftz, 2004; Steinberger & Torsvik, 2010; Richards et al., 1999]. (For mantle viscosity profiles characterized by a large, factor of > 30 , increase in viscosity with depth, a reversal in the sign of the associated geoid kernel may also contribute to the reversal in the direction of polar motion [Ricard et al., 1993].)

5.3.3 MODELLING PALEOMAGNETICALLY-INFERRED TPW

The sensitivity studies reveal a trade-off such that one can reduce the stabilization associated with the remnant bulge (i.e., lower EET) by increasing the stable background excess ellipticity (ΔI_{MD}). Consider, as an example, the paleomagnetically-inferred oscillation in pole position during the Neoproterozoic [Maloof et al., 2006] (Figure 4a). The large amplitude of the event can only be reconciled with an Earth model of nearly prolate form and relatively small EET. Figure 4b summarizes the results of

two simulations, both driven by a convective perturbation of $\Delta^n I_{max,int} = 0.3$. The first adopts a prolate Earth model ($\Delta I_{MD} = 0$) with EET=15 km, and the second adopts $\Delta I_{MD} = 0.1$ and EET=0. The simulations predict $\sim 44^\circ$ or $\sim 51^\circ$ of TPW, respectively, in ~ 6 Myr, followed by a return of the pole to within $\sim 9^\circ$ of the initial location in the next ~ 20 Myr, yielding good fits to the inferred TPW path [Maloof et al., 2006]. One could reduce the total duration of the modelled event by increasing EET or ΔI_{MD} . However, these changes would significantly reduce the predicted TPW amplitude. Thus, if large, rapid oscillatory TPW events occurred in the Paleoproterozoic through Paleozoic (Figure 1a), then their rarity in the geological record may reflect these restrictive constraints on the Earth's shape and rheology.

We next turn to the inference of two back-to-back episodes of oscillatory TPW during the Mesozoic [Steinberger & Torsvik, 2008] (Figure 3a-d). These events are more muted than those inferred for the Proterozoic and Paleozoic, and they are of longer duration than the Neoproterozoic TPW event (Figure 1a). To reduce the level of non-uniqueness, we only considered simulations in which the EET of the lithosphere and ΔI_{MD} are the same for both oscillations. Excellent fits to the inferred TPW path can be found for scenarios in which: (1) remnant bulge stabilization (EET=12 km) acts on a prolate ($\Delta I_{MD}^n = 0$) Earth model (Figure 3e); and (2) a background excess ellipticity ($\Delta I_{MD}^n = 0.11$) stabilizes an Earth model with an EET=0 (Figure 3f).

5.3.4 MISCELLANEOUS NUMERICAL TESTS

THE EFFECTIVE ELASTIC THICKNESS OF THE LITHOSPHERE

The paleomagnetically-inferred oscillatory TPW events were characterized by an approximately coaxial (back and forth) reorientation of the rotation pole about an axis through the center of the contemporaneous supercontinent, where the latter was

roughly aligned with the axis of minimum inertia [Evans, 2003]. In the context of this coaxial geometry, the term "effective elastic thickness" (EET) adopted in the modeling is defined as the thickness of a globally uniform elastic lithosphere that yields, for the convective forcing described above (i.e., a forcing symmetric about the plane defined by I_{max} and I_{int}), a time-dependent TPW prediction that matches a prediction based on a lithosphere with laterally varying strength (as in Figures 3a-d and 4). We have verified the appropriateness and accuracy of this connection by: (1) adopting a viscoelastic finite-element code [Latychev et al., 2005] to compute the time-dependent response to a centrifugal forcing of Earth models with an axisymmetric continental lithosphere of constant elastic thickness and radius 60° centred on the equator and an oceanic lithosphere of zero elastic strength; and (2) comparing these predictions to those generated using the same centrifugal forcing and a suite of Earth models with lithospheres of uniform elastic thickness.

While the adoption of uniform lithosphere models in the TPW predictions may be justified for the specific geometries considered in this study, the choice of EET appropriate for each of the deep time TPW events summarized in Figure 1a of the main text is highly uncertain. Much of this uncertainty stems from our incomplete knowledge of deep time paleogeography and lithospheric structure. For example, while a set of distinct continents will have an EET lower than an amalgamated supercontinent (see below), the difference will depend on the strength at continental sutures. Moreover, since elastic stresses associated with the remnant bulge will depend on the location of the supercontinent relative to the rotation axis and TPW direction, the EET will also be dependent on this relative position. Nevertheless, despite these uncertainties, observations of flexure at seamounts, basins and passive margins [Watts, 2001] indicate that the Earth's lithosphere retains non-zero elastic strength (i.e., $EET > 0$) on the 10-50 Myr time scale that typically characterizes the oscillatory TPW

events summarized in Figure 1a. Thus, a stable background excess ellipticity may have augmented, but likely did not entirely replace remnant bulge stabilization as a mechanism for oscillatory TPW in deep time.

In the face of the uncertainty in EET, the modelling exercises discussed above (Figures 3 and 4), are designed to estimate the EET of the lithosphere necessary to fit the suite of paleomagnetically-inferred episodes of oscillatory TPW. In this manner, we infer values of the EET in the range ~ 10 -15 km in cases where long-term background excess ellipticity in the plane of the TPW does not contribute to the stabilization of the rotation axis ($\Delta I_{MD} = 0$). If the long-term excess ellipticity is non-zero, the EET required to fit the observations is reduced considerably, even to zero (e.g., Figures 3f, 4b).

Are EET values of ~ 10 km plausible for the lithosphere during supercontinent phases in Earth history? To investigate this issue, we used a finite-element code that computes the strain energy stored within an elastic lithosphere of arbitrary thickness variation and plate boundary geometry subject to a centrifugal potential perturbation. Plate boundaries are modeled in the code as breaks through the entire lithosphere - that is, normal and tangential stresses vanish on the boundary. As an illustrative test, we considered a lithosphere characterized by a single continental plate with a geometry that matched the Pangean configuration at 220 Myr ago surrounded by oceanic lithosphere with zero elastic strength. The continental lithosphere was characterized by a uniform thickness, which served as a free parameter, a rigidity of 45 GPa and Poisson's ratio of 0.25. The centrifugal potential perturbation applied to the lithosphere was equivalent to a clockwise TPW event of 45° coaxial to the center of the supercontinent. Results obtained for average lithospheric thicknesses of 50 km and 100 km are given by the red arrows labelled P1 and P2, respectively, in Figure 9.

As a point of comparison, the solid blue line in Figure 9 is the total elastic strain

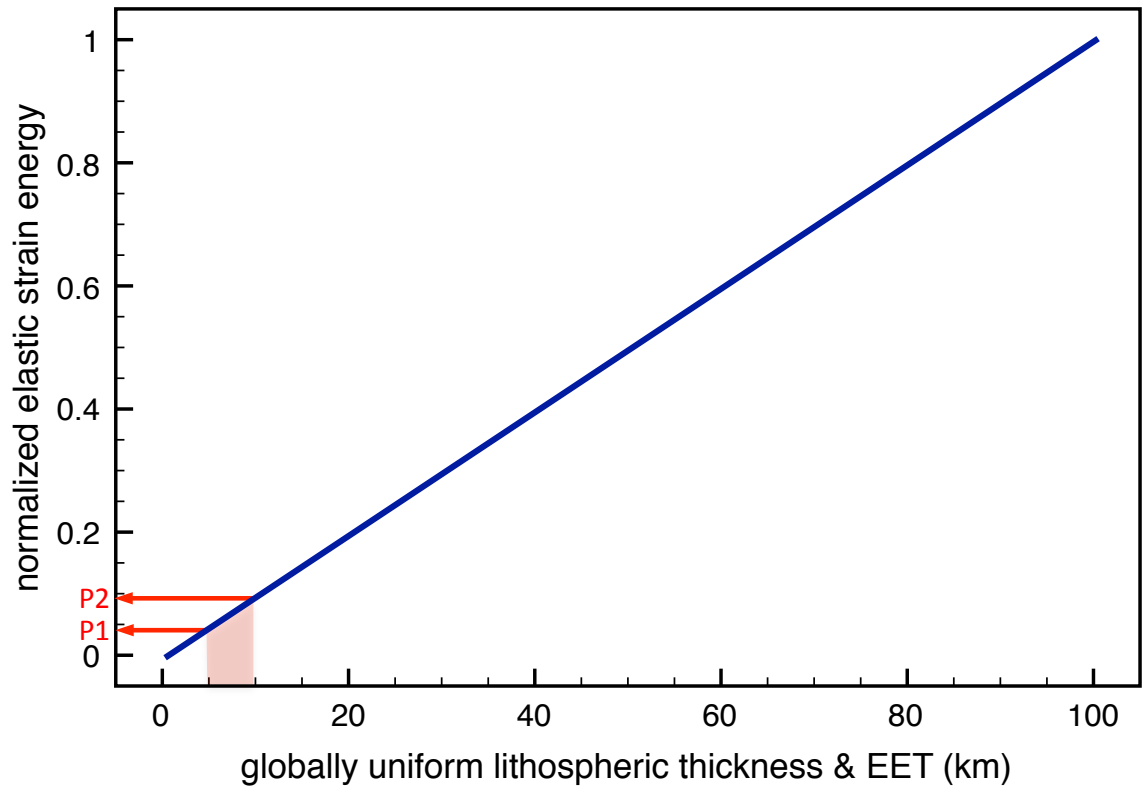


Figure 5.9: Calculation of the total elastic strain energy stored in response to a centrifugal potential forcing (see text) for various models of the lithosphere. Blue line: Total stored energy as a function of the thickness of a globally uniform elastic plate. P1 and P2 arrows: Total strain energy in an elastic plate with geometry given by the Pangean supercontinent configuration and thickness of 50 km or 100 km, respectively, surrounded by an oceanic lithosphere with no elastic strength. The shaded red region shows the range of EET values bounded by the P1 and P2 cases (see text). All values are normalized by the total strain energy computed for the globally uniform elastic lithosphere of thickness 100 km.

energy as a function of the thickness of a globally uniform lithosphere (i.e., no breaks) subject to the same centrifugal forcing. These results (as well as those for the Pangean supercontinent models P1 and P2) are normalized by the total elastic strain energy for the case of a globally uniform plate of thickness 100 km. The blue line, which was computed using an analytic solution, indicates that the total elastic strain energy is linearly proportional to the thickness of the globally uniform plate. The results on the figure (and, in particular, the intersection of the red arrows with the blue line) indicate that the total strain energy stored in the two models of the Pangean supercontinent lithosphere are equal to the total elastic strain energy stored in globally uniform lithospheres with elastic thickness of 4.8 km and 9.6 km (the range shown by the intersection of the shaded red region with the x-axis), respectively. Thus, the EETs associated with the P1 and P2 models for the Pangean supercontinent are about an order of magnitude smaller than their thickness. As discussed above, these EET estimates would decrease if any suture zones within the supercontinent were relatively weak; they would increase if either the elastic strength in oceanic regions contributed to the EET or the plate containing the supercontinent was not mechanically decoupled from the surrounding plates. In any case, we conclude on the basis of Figure 9 that EET values of up to ~ 10 km are plausible during supercontinent phases.

The memory of previous rotational states provided by a lithosphere will be partially lost (i.e., the remnant bulge stabilization will partially decay) if the timescale of the convective forcing approaches the relaxation time of the crust-lithosphere system. Moreover, the remnant bulge stabilization will be reset if the timescale of the convective forcing significantly exceeds the longest relaxation time of the lithosphere. The results in Figure 9 indicate that the disaggregation of the supercontinent would also have significantly reduced the total stored elastic strain energy and, thus, the remnant bulge stabilization. Finally, memory associated with excess ellipticity will

be lost as the Earth's background figure evolves. For these reasons, predictions of oscillatory TPW events need not fully return to the original pole location.

LINEAR VERSUS NONLINEAR APPROACHES

The solid line in Figure 5b, reproduced from the black line in each of Figures 6a-d, is the prediction of TPW based on test case #1 of the standard model simulation. That is, the prediction combines the inertia tensor perturbation in frame (a) (solid line) with stabilization associated with $EET = 15$ km, but no stable background excess ellipticity ($\Delta^n I_{MD} = 0$). The dashed line in Figure 5b is identical to the solid with the exception that the non-linear rotational stability described above is replaced by a linearized theory based on work in ice age rotation [Chan et al., 2011]. These TPW time series may be useful in future benchmarking efforts; furthermore, the relatively good agreement between the two predictions in Figure 5b is an indication of the robustness of the two distinct approaches to compute TPW.

A STASIS IN OSCILLATORY TPW?

The simulations of large amplitude, oscillatory TPW described above (e.g., Figures 6a and e, for convective forcings $\Delta^n I_{max,int} > 0.05$) have no significant delay between the back and forth phases of the predicted polar motion. However, paleomagnetic data, in combination with the carbon isotopic excursion that accompanied the Neoproterozoic TPW oscillation [Maloof et al., 2006], may suggest, at least for this event, a stasis of up to 10 Myr during which the rotation axis remained near its maximum excursion [D.A.D. Evans, pers. comm.] How might such a period of stasis be accommodated within the framework of our modelling of TPW?

The relatively simple geometry of TPW predicted by our simulations arises because we adopt a coordinated pulse of mantle convection as the driving force for

TPW. Deviations from this simple geometry likely require that stabilization due to the remnant bulge (or excess ellipticity) act on a more complex convective regime. For example, a stasis in the predicted TPW path may be introduced by including additional convective loads that are out of phase in both space and time with the main pulse. To illustrate this possibility, we begin with the results of test case #1 of the standard simulation (solid line, Figure 5c; $\Delta^n I_{max,int} = 0.1$, $\nu = 10^{22}$ Pa s, EET=15 km and $\Delta I_{MD} = 0.0$). Next, we set up a series of simulations in which smaller, additional convective loads were superimposed on this main pulse. The results of one such simulation are shown in Figure 5c (dashed line). This new simulation is characterized by secondary convective loads with $\Delta^n I_{max,int} = 0.05$ and 0.02 . Furthermore, the main convective pulse and the two additional load pulses were initiated at $t = 28$ Myr, 0 Myr and 8 Myr of the simulation, and at angles of 55° N, 75° N and 70° N, respectively. The resulting polar motion shows a more complex history than the standard simulation, including a period of relative stasis in which the pole remains within 2° of TPW_{max} for over 8 Myr.

The new simulation has a geometry such that all loads act to drive the rotation axis in the same direction. Thus, the return of the pole toward its original location in Figure 5c is, in this case, a result of remnant bulge stabilization, and not a result of introducing loading phases with opposing polarity. The dotted line on Figure 5c is a simulation identical to the dashed line, with the exception that the EET (and, thus, remnant bulge stabilization) is set to zero. The pole moves a total of $\sim 70^\circ$ and has no return phase. We conclude that even in the case where a suite of convective loads act in concert to drive the pole in one direction, stabilization by the remnant bulge (or a stable background excess ellipticity) will return the pole to its initial orientation. A secondary convective forcing that drives the pole in a direction opposite to the main pulse would act in tandem with stabilization via a remnant bulge (or a stable

background excess ellipticity) to bring the pole back to its original location, but this geometry of convective loading is not a necessary condition for the return of the pole.

5.4 FINAL REMARKS

There have been suggestions that the longevity of the present day superswells beneath Africa and the Pacific may extend uninterrupted to the Neoproterozoic. Numerical experiments suggest that the African superswells have persisted for the last ~ 200 Myr and the Pacific superswell much longer [Zhong et al., 2007], while a suite of observations suggest a life-span extending 500 Myr [Torsvik et al., 2010] or more [Dziewonski et al., 2010]. Indeed, the current equatorial location of the superswells [Spada et al., 1994] implies that any remnant bulge stabilization of TPW driven by these features has since relaxed. However, laboratory experiments on thermochemical convection suggest that long-lived superswells experience pseudo-periodic doming with timescales of 100-1000 Myr [Davaille, 1999], and such events may drive a relatively rapid pulse of subduction in the plane perpendicular to I_{min} (Figure 1c). This, or other classes of rapid, repetitive convective forcing [Tackley et al., 1994], acting on an Earth with a small elastic lithospheric thickness and/or a relatively stable background excess ellipticity, may provide an overarching physical framework linking the suite of paleomagnetically-inferred, oscillatory TPW events spanning the last few billion years of Earth history.

BIBLIOGRAPHY

- Cambiotti, G., Ricard, Y. & Sabadini, R., 2011. New insights into mantle convection true polar wander and rotational bulge readjustment, *Earth Planet. Sci. Lett.*, **310**, 538–543.
- Chambat, F., Ricard, Y. & Valette, B., 2010. Flattening of the Earth: Further from hydrostaticity than previously estimated, *Geophys. J. Int.*, **183**, 727–732.
- Chan, N.-H., Mitrovica, J. X., Matsuyama, I., Creveling, J. R. & Stanley, S., 2011. The rotational stability of a convecting Earth: Assessing inferences of rapid TPW in the Late Cretaceous, *Geophys. J. Int.*, **187**, 1319–1333.
- Crowley, J., Gerault, M. & O’Connell, R. J., 2011. On the relative influence of thermal and water cycles on planetary dynamics, *Earth Planet. Sci. Lett.*, **310**, 380–388.
- Daradich, A., Mitrovica, J. X., Matsuyama, I., Perron, J. T., Manga, M. & Richards, M. A., Equilibrium rotational stability and figure of Mars, *Icarus*, **193**, 463–475.
- Davaille, A., 1999. Simultaneous generation of hotspots and superswells by convection in a heterogeneous planetary mantle, *Nature*, **402**, 756–760.
- DeCock, M. O., Evans, D. A. D., Dorland, H. C., Beukes, N. J. & Gutzmer, J., 2006. Paleomagnetism of the lower two unconformity-bounded sequences of the Waterburg Group, South Africa: Towards a better-defined apparent polar wander path for the Paleoproterozoic Kaapvall Craton, *South African J. Geol.*, **109**, 157–182.
- Dziewonski, A., Lekic, V. & Romanowicz, B. A., 2010. Mantle anchor structure: An argument for bottom-up tectonics, *Earth Planet. Sci. Lett.*, **299**, 69–79.
- Evans, D. A. D., 1998. True polar wander, a supercontinental legacy, *Earth Planet. Sci. Lett.*, **157**, 1–8.
- Evans, D. A. D., 2003. True polar wander and supercontinents, *Tectonophysics*, **362**, 303–320.
- Forte, A. M., 2007. Constraints on seismic models from other disciplines - implications for mantle dynamics and composition, *Treatise of Geophysics*, **1**, 805–858.

- Forte, A. M. & Peltier, W. R., 2001. Viscous flow models of global geophysical observables: 1. Forward problems, *J. Geophys. Res.*, **96**, 20,131–20,159.
- Gold, T., 1955. Instability of the Earth's axis of rotation, *Nature*, **175**, 526–529.
- Goldreich, P. & Toomre, A., 1969. Some remarks on polar wandering, *J. Geophys. Res.*, **74**, 2555–2567.
- Greff-Lefftz, M., 2004. Upwelling plumes, superswells and true polar wander, *Geophys. J. Int.*, **159**, 1125–1137.
- Latychev, K., Mitrovica, J. X., Tromp, J., Tamisiea, M. E., Komatitsch, D. & Cristara, C. C., 2005. Glacial isostatic adjustment on 3-D Earth models: a finite volume formulation, *Geophys. J. Int.*, **161**, 421–444.
- Letts, S., Torsvik, T. H., Webb, S. J. & Ashwal, L. D., 2011. New Paleoproterozoic palaeomagnetic data from the Kaapvaal Craton, South Africa, *Geol. Soc. Lond.*, **357**, 9–26.
- Maloof, A. C., Halverson, G. P., Kirschvink, J. L., Schrag, D. P., Weiss, B. P. & Hoffman, P. F., 2006. Combined paleomagnetic, isotopic, and stratigraphic evidence for true polar wander from the Neoproterozoic Akademikerbreen Group, Svalbard, Norway, *GSA Bulletin*, **118**, 1099–1124.
- Matsuyama, I., Mitrovica, J. X., Perron, J. T., Manga, M. & Richards, M. A., 2006. Rotational stability of dynamic planets with elastic lithospheres, *J. Geophys. Res.*, **111**, doi:10.1029/2005JE002447.
- McCausland, P. J. A. & Hodych, J. P., 1998. Paleomagnetism of the 550 Ma Skinner Cove volcanics of western Newfoundland and the opening of the Iapetus Ocean, *Earth Planet. Sci. Lett.*, **163**, 15–29.
- Milne-Thomson, L. M., 1996. *Theoretical Hydrodynamics*, Courier Dover Pub., p. 743.
- Mitchell, R. N., Evans, D. A. D. & Kilian, T. M., 2010. Rapid Early Cambrian rotation of Gondwana, *Geology*, **38**, 755–758.
- Mitchell, R. N., Hoffman, P. F. & Evans, D. A. D., 2010. Coronation loop resurrected: Oscillatory apparent polar wander of Orosirian (2.05–1.8 Ga) paleomagnetic poles from Slave craton, *Precambrian Res.*, **179**, 121–134.
- Mitrovica, J. X. & Forte, A. M., 2004. A new inference of mantle viscosity based upon a joint inversion of convection and glacial isostatic adjustment data, *Earth Planet. Sci. Lett.*, **225**, 177–189.

- Oldham, D. & Davies, J. H., 2004. Numerical investigation of layered convection in a three-dimensional shell with application to planetary mantles, *Geochem. Geophys. Geosys.*, **5**, doi:10.1029/2003GC000603.
- Ricard, Y., Spada, G. & Sabadini, R., 1993. Polar wandering of a dynamic Earth, *Geophys. J. Int.*, **113**, 284–298.
- Richards, M. A., Bunge, H.-P., Ricard, Y. & Baumgardner, J. R., 1999. Polar wandering in mantle convection models, *Geophys. Res. Lett.*, **26**, 1777–1780.
- Ritsema, J. & Van Heijst, H. J., 2000. Seismic imaging of structural heterogeneity in Earth's mantle: evidence for large-scale mantle flow, *Sci. Prog.*, **83**, 243–259.
- Rouby, H., Greff-Lefftz, M. & Besse, J., 2010. Mantle dynamics, geoid, inertia and TPW since 120 Myr, *Earth Planet. Sci. Lett.*, **292**, 301–311.
- Spada, G., Ricard, Y. & Sabadini, R., 1992. Excitation of true polar wander by subduction, *Nature*, **360**, 452–454.
- Spada, G., Sabadini, R. & Boschi, E., 1994. True polar wander affects the Earth dynamic topography and implies a highly viscous lower mantle, *Geophys. Res. Lett.*, **21**, 137–140.
- Steinberger, B. & O'Connell, R. J., 2002. The convective mantle flow signal in rates of true polar wander, in *Ice Sheets, Sea Level and the Dynamic Earth*, eds. Mitrovica, J. X. & Vermeersen, L. L. A., *AGU Geodyn. Ser. 29*, 233–256.
- Steinberger, B. & Torsvik, T. H., 2008. Absolute plate motions and true polar wander in the absence of hotspot tracks, *Nature*, **452**, 620–624.
- Steinberger, B. & Torsvik, T. H., 2010. Toward an explanation for the present and past locations of the poles, *Geochem. Geophys. Geosys.*, **11**, doi:10.1029/2009GC002889.
- Tackley, P. J., Stevenson, D. J., Glatzmaier, G. A. & Schubert, G., 1994. Effects of multiple phase transitions in a 3-dimensional spherical model of convection in the Earth's mantle, *J. Geophys. Res.*, **99**, 15877–15901.
- Torsvik, T. H., Muller, R. D., Van der Voo, R., Steinberger, B. & Gaina, C., 2008. Global plate motion frames: Toward a unified model, *Rev. Geophys.*, **46**, RG3004, doi:10.1029/2007RG000227.
- Torsvik, T. H., Burke, K., Steinberger, B., Webb, S. J. & Ashwal, L. D., 2010. Diamonds sampled by plumes from the core-mantle boundary, *Nature*, **466**, 352–355.
- Tsai, V. C. & Stevenson, D. J., 2007. Theoretical constraints on true polar wander, *J. Geophys. Res.*, **112**, doi:10.1029/2005JB003923.

- Van der Voo, R., 1994. True polar wander during the middle Paleozoic?, *Earth Planet. Sci. Lett.*, **122**, 239–243.
- Watts, A. B., 2001. *Isostasy and flexure of the lithosphere*, Cambridge Univ. Press, New York.
- Willemann, R., 1984. Reorientation of planets with elastic lithospheres, *Icarus*, **60**, 701–709.
- Zhang, N., Zhong, S., Leng, W. & Li, Z.-X., 2010. A model for the evolution of the Earth's mantle structure since the Early Paleozoic, *J. Geophys. Res.*, **115**, doi:10.1029/2009JB006896.
- Zhong, S., Zhang, N., Li, Z.-X. & Roberts, J. H., 2007. Supercontinent cycles, true polar wander, and very long-wavelength mantle convection, *Earth Planet. Sci. Lett.*, **261**, 551–564.